Calibration & Optimization Procedures for an Ultrafast DEPFET based Electron Detector (EDET)

Dr. Eduard Prinker

MAX PLANCK
HALBLEITERLABOR

München 2022

Calibration & Optimization Procedures for an Ultrafast DEPFET based Electron Detector (EDET)

Dr. Eduard Prinker

Dissertation
an der Fakultät für Physik
der Ludwig-Maximilians-Universität
München

vorgelegt von Dr. Eduard Prinker
aus Steyr

München, 6. April 2022

Erstgutachter:	Prof. Dr. Christian Kiesling
Zweitgutachter:	Prof. Dr. Jochen Schieck
Tag der Einreichung:	6. April 2022
Tag der mündlichen Prüfung:	24. Mai 2022

Zusammenfassung

HLL[1] und MPSD[2] entwickeln einen neuartigen Elektronen-Detektor, der mit einer bislang unerreichten Bildfrequenz von 80 kHz, schnell ablaufende biologische und chemische Prozesse aufzeichnen wird. Maßgefertigt für die Fokalebene eines Transmissionselektronenmikroskops, sollen verschiedenste Proben bei unterschiedlichen Vergrößerungen abgebildet und ihre Dynamik erfasst werden. Aufgrund seiner exzellenten Zeitauflösung eignet sich dieser Detektor hervorragend dazu, Filme von Streuungs- oder Schattenbildern aufzuzeichnen. Die zu beobachtenden, schnellen dynamischen Prozesse laufen in eigens dafür entwickelten Gefäßen, den „environmental cells“ ab. Der Sensor selbst basiert auf der DEPFET Technologie. Jeder Pixel besteht aus einem MOSFET mit eingebauter Verstärkung für das Ladungssignal. Abgesehen von einer hohen Ladungssammlungskapazität zeichnet sich dieser durch eine zweistufige Verstärkung aus: ein hoher Verstärkungsfaktor für niedrige Signalamplituden und ein reduzierter für starke Signale. Auf diese Weise liefert der Detektor eine hohe Auflösung auch für kleine Signale bei gleichzeitiger Erhaltung eines großen dynamischen Bereiches.

Aufgrund von Prozessvariationen weichen die individuellen Pixel-Antwortsfunktionen mehr oder weniger stark voneinander ab. Für einen Detektor, bestehend aus über 1 Million Pixeln, stellt dies eine große Herausforderung für eine effiziente Pixelkalibrierung dar. Zur Erreichung der bestmöglichen Signalqualität muss auch die hohe Zahl von Bias- und Timing-Parametern für die Ausleseelektronik optimiert werden.

In der vorliegenden Arbeit werden die entwickelten Algorithmen und Prozeduren zur Kalibrierung und Optimierung der Detektoren vorgestellt. Ihre Anwendung auf ein Prototyp-Testsystem wird beschrieben, wo sie sich als effizient, effektiv und als übertragbar auf ein großes Modul erwiesen.

---

[1] Halbleiterlabor der Max-Planck Gesellschaft, München

[2] Max-Planck Institut für Struktur und Dynamik der Materie, Hamburg

Abstract

A novel electron detector, with an unprecedented frame rate of 80 kHz envisages the observation of the fast dynamics occurring in chemical and biological processes. Assembled into the focal plane of a transmission electron microscope (TEM), the detector will record magnified projections of the inserted sample. Due to its outstanding time resolution, the detector is well suited to record movies (scattering or shadow image sequences) of fast processes, taking place in a specific developed specimen capsule (liquid cell). The sensor itself is based on the DEPFET technology, consisting of a MOSFET structure with built-in internal amplification for the charge signal. It offers an extensive charge storing capacity with a two-tier linear response: high amplification of weak signals in the first stage and a lower gain for strong signals. By this means, the detector conserves high energy resolution at low signal charge in combination with a high dynamic range.

To create a homogeneous flat-field response, calibration of all detector channels is mandatory, as due to process variations the individual pixel response functions vary within a certain range. For a 1 megapixel sensor, this presents a major challenge to the selected calibration technique. Bias- and timing parameters of the readout electronics need to be adjusted and optimized to provide for an optimal signal quality. Furthermore, the readout electronics significantly affects the quality of the recorded data and must be optimized.

In the scope of this thesis, suitable procedures and algorithms were developed using a prototype test system, which have to be applied to the final large sensor modules.

Contents

1 Introduction

Scientific progress requires – among other things – the development of new instrumentation. Exemplarily, consider the advances in optics and the revolutionary impact of what knowledge could be produced for early astronomy and microscopy. Nevertheless, these fields witnessed other giant leaps with the advent of electron beam based microscopy and optical and non-optical progress. One observes an increasing trend towards interdisciplinary approaches, where, for instance, techniques and instrumentation developed by the needs of one field, finds a sudden application in entirely different scientific disciplines. Particle detectors from high energy physics, for example, have significantly impacted medical imaging [1, 2] and the accelerator technology was successfully established in the medical cancer therapy [3, 4]. This knowledge transfer between distinct domains stimulates innovation, potentially creates new fields of expertise and occasionally generates a direct benefit for the mankind.

Presently, the majority of transmission electron microscopes (TEM) employ an indirect electron detection mechanism [5]: the beam electrons are converted to photons in an appropriate scintillator, which itself is optically coupled to a Charge-Couple Device (CCD) or a CMOS[1] sensor. When using scintillation screens, however, image sharpness is conceptually compromised [5], as multiple scatterings of the primary electrons in the scintillator and the isotropic nature of photon radiation cause an expansion of the point spread function (PSF), i.e. the response of an imaging system to a point source, in the final image. On top of that, the frame rate of indirect detection systems is constrained by the scintillator's time constant, which is the decay time of the optical excitation of typically ms and longer. Additionally, compared to direct detectors a worse signal-to-noise ratio can be expected.

Recently, direct detection approaches significantly improved the information efficiency but allowed for the recording of mostly a few hundred frames per second (fps). The challenging capture of dynamic processes by means of electron microscopy at superior spatial resolution is hence restricted to ms and above by the speed of the employed detectors. Accordingly, the imaging potential of TEMs was, for the most part, restricted to provide morphological, compositional and crystallographic information on samples with limited dynamical or time information. One exception to this limitation concerns ultrafast phenomena which are investigated by a "pump – probe" scheme: two laser pulses, one responsible for triggering structural changes in the investigated sample, the second with an adjustable delay, catch the dynamics on a molecular scale as a function of the delay. However, intermediate physical processes like in situ studies of colloidal particles growth or chemical processes like the growth processes of nanorods or the corrosion of alumin-

[1] Complementary Metal Oxide Semiconductor (CMOS) is the most popular type of the Metal Oxide Semiconductor Field Effect Transistor (MOSFET) technology. It uses complementary p-type and n-type MOSFETS for logic functions.

ium are yet to be explored with sufficient time resolution. The same is true for bio-chemical processes as for example bacterial infections by bacteriophages or molecular self-assemblies (e.g. DNA origami or protein folding, each of which happens during intervals in the order of milliseconds). Though the chemical reactions on the molecular scale are well understood, the temporal coordinated behavior of such structures (if falling below the resolution of a light microscope) remain, for the most part, unobservable. Every push on the temporal resolution will grant access to a hitherto inaccessible “terra incognita” with unpredictable consequences on the information which could be gained.

It is hence intriguing to close this gap with advanced detector technology. At HLL, an additional stimulus came from the development of the PiXel Detector (PXD) for the BELLE II project [6], which inspired scientists entrusted with this task to roll out the particle detection technology for the high-energy particle collider to the electron microscopy field.

The new detector envisages a frame rate of up to 80,000 fps. This unprecedented time resolution of the new Electron DETector (EDET) aims to visualize hitherto temporally inaccessible processes. Each pixel is designed to produce a non-linear response function: a high amplification of weak signals in the first stage and a lower gain for strong signals (see Figure 5-1). This feature is especially helpful for high contrast images, where signal compression allows to combine high energy resolution for areas obtaining low signal charge with a high dynamic range. On the other hand, the individual pixel gain calibration, which is necessary due to imperfect detector fabrication processes, gets considerably complicated. The developed method is innovative, time-efficient, yields stable pixel gain curves and can in any case be used for large sensor surfaces.

The second central focus of this thesis concerns the operation and characterization of the new detector, especially the optimization of the communication and synchronization between readout electronics and sensor, the data acquisition and the optimal powering. It requires the establishment of appropriate control checks and procedures associated with a suitable software.

The sensor’s sensitive area is thinned down to 50 µm or even 30 µm, which reduces blurring by electron scattering significantly. In this way, EDET will contribute to new scientific insights and evoke new ideas and new fields of research.

The presented thesis focuses on enabling a technology from high energy physics for an entirely different field of electron microscopy with very different needs. The characterization, optimization, calibration and development of novel operation points of the new sensor for microscopy is the main contribution of this work.

The structure of this thesis can be summarized as follows:

Chapter 2 motivates the application of the new detector to the underlying physical, chemical and biological processes.

Chapter 3 provides an overview of the principles and the operation modes of TEMs. The innovative environmental cell for in vitro measurements of biological samples is presented as well as different TEM detector concepts. The chapter ends with an outlook how the new EDET detector could be used for recording fast, highly time resolved image sequences (movies) of biological processes.

Chapter 4 shortly summarizes the electromagnetic interactions in matter. This includes photon interactions in form the infrared over the visible to the low energy X-ray spectral range. Photons are indispensable for the detector calibration. The interaction of TEM electrons directly influences the image quality of the detector. For thin detectors, the energy deposition of the TEM electrons generates a Landau-like distribution instead of a Gaussian one. Finally, TEM electrons produce various secondary signals from the radiated specimen which can be exploited by different detection techniques.

Chapter 5 introduces the electron detector direct hit 80 kframes/s project “EDET DH80k” or short “EDET” and gives insight to the DEPFET technology and its operational principles. A short mathematical section outlines the elementary electrical properties of a DEPFET pixel. The key EDET design components are described in the last section.

Chapter 6 presents a key development of this thesis, the EDET Hybrid Board for small prototype sensors and gives an overview of the key testing procedures.

Chapter 7 is dedicated to the sensor calibration. Different instruments and methods are investigated, especially with respect to their accuracy and efficiency. The developed method is generally applicable, also for the final system, and implements a two-step approach: a ^{109}Cd X-ray source is used to calibrate the charge injected by a LED light source, whose intensity can be increased in an almost linear fashion. In the second step, the diffuse light characteristics of LEDs allow for a simultaneous calibration of all pixels and the generation of individual charge curves. An algorithm was developed to map all individual charge values to a common benchmark curve for all pixels.

Chapter 8 deals with the characterization of the detector. Performance gauges like the Modulation Transfer Function (MTF) permit an assessment of the detector’s image quality and enable a comparison of EDET to other detectors. Additionally, a further setting optimization attempt was made to minimize an adverse effect, which especially occurs in combination with large charge injections producing an unwanted extra pixel current (“ghost charge effect”). Finally, the optimal powering conditions for the sensor are briefly investigated.

Chapter 9 includes first results from TEM measurements collected from two measurement campaigns at the MPSD TEM in Hamburg.

Chapter 10 finishes with a conclusion and outlook.

Some standard optimization routines, which are nevertheless key for the detector operation are described in the APPENDIX.

Technical terms, displayed in bold caption can be found in the Glossary.

2 Beyond Motion-Pictures

2.1 Chemical and Biological Movie

Transmission electron microscopy has pushed the resolution limits to the atomic scale. In the early days, photographic films were used for the image recording. However, photographs are associated with static pictures, a serious deficiency since this does not answer how dynamic processes have evolved. As an allegorical example, imagine a football match where the TV provider broadcasts a picture only every 30 seconds instead of a continuous movie. If a goal was scored, everybody would notice the score but nobody would know how this result was achieved.

Dynamic processes proceed with a certain speed. If the image recording time was set too long, the images get blurred. On the other hand, if the time interval between two images was chosen too long, a lot of movement information gets lost. A stroboscopic movie consists of a stack of consecutive frames where each picture records only a fraction of the whole movement. The readout frequency and exposure time should match in agreement with the observable process. As an example, the composite stroboscopic images of a serving tennis player are shown in Figure 2-1.

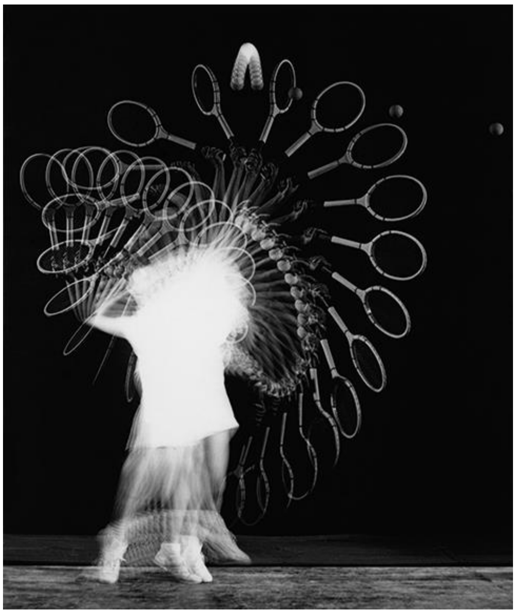

Figure 2-1: Stroboscopic Imaging: "Gussie Moran, Tennis Serve Multiflash" (1949 at Longwood Tennis), © Dr. Harold Edgerton/MIT, courtesy of Palm Press, Inc.[1]

Figure 2-2 ranks several processes in biology, chemistry and materials science according to their typical temporal and spatial resolution. Different magnification and imaging

[1] A caption by Gus Kayafas, president of Palm Press Inc., can be found in the Glossary section under **Multiflash**.

techniques give access to different regions displayed on this graph. Under certain conditions[2], for ultrafast timescales (< 1ns) the “pump-probe” technique can be applied [7]: at time t_0 a laser pulse (“pump”) induces an excitement or stimulates a chemical reaction. Then sequential (“probe”) pulses at variable time delays relative to t_0 capture different snapshots of the sample response. The linear series from the accumulated time-resolved snapshots finally deliver a “molecular movie”.

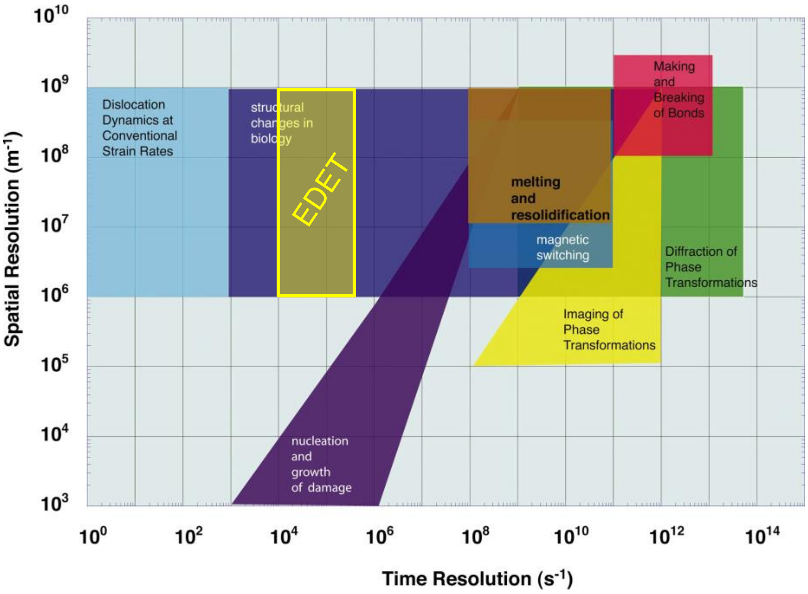

Figure 2-2: Various processes in chemistry, biology and physics together with their corresponding spatial and temporal resolution, adapted from [8]. The EDET project predominantly envisages nanoscale structures and their corresponding dynamic processes in the sub-millisecond range.

The availability of liquid (or gaseous) cells/capsules[3] (see section 3.3) facilitates observations of the chemical, morphological or crystallographic evolution of specimen over time. Especially in biology, whole cells or the structure of proteins can be imaged in their native environment. Other applications involve some external stimulus such as radiation induced effects (see chapter 9.3), mechanical deformation or temperature change. The complementary fast EDET sensor enables the recording of these fast dynamical processes.

Conventional direct detectors deliver standard video frame rates of 30 fps or 33 ms per frame [9]. An advanced high-speed camera at low dose rates (counter[4]) even acquires images up to 1,500 fps or 666 µs (see section 3.2.5). By contrast, EDET can be used for high contrast (high dose) applications and provides 50 consecutive frames at a frame frequency of 80 kHz or equivalently 12.5 µs per frame (duty cycle of 10% or 100 Hz).

[2] Reversible processes that reset rapidly, i.e. the processes are repeatable and the specimen must relax to the identical state between the shots [64].

[3] Electron-transparent, hermetically sealed enclosures.

[4] Electron detectors operated in counting mode identify single electron events, while if they are operated in integration mode the total charge produced is recorded.

Accordingly, EDET specifically addresses processes with time scales in the 1 ms range.

In combination with a TEM, the main usage is directed towards structural changes in biology[5] taking place at sub-millisecond timescales, as well as intermediate physical processes like in situ studies of colloidal particles growth or chemical processes like the growth processes of nanorods or the corrosion of aluminium. Typical examples, carried out by living organisms are intracellular regulation (e.g., conformational changes), protein folding, ligand binding, ATP diffusion[6], protein diffusion across E. coli bacteria or one step in DNA polymerase [10, 11].

The basic processes of all biological phenomena consist of chemical reactions. The initial binding or bond breaking events are quantum mechanical by nature and occur over atomic length scales [12]. In order to perform biological functions like protein folding, binding or dissociations of ligands or unwinding of DNA, these events must interact in a certain sense over mesoscale dimensions. It's like the "invisible hand" as an analogy for the unseen forces, that move the free market economy. Or using a much nicer metaphor from [12]: "Imagine you are attending a magnificent symphony for which some 10,000 different musicians have been assembled and who are all warming up their instruments as you enter a massive concert theatre. The sounds you would hear would be quite chaotic. Then the maestro steps forward, taps his baton and this marvellous music, the music of life (to overextend the metaphor), bursts forward. What just happened? The different degrees of freedom, the musicians, all agreed to be correlated through space by visual inspection of the conductor's baton".

What an exciting imagination, to observe how "mother nature" orchestrates a well ordered process of strongly correlated atoms.

2.2 *In-situ* TEM Application Fields

Recent advances in detector technology allow the usage of transmission electron microscopy for studying dynamic processes. If the experimenter aims to modify the specimen in a controlled way, while observing its reaction[7], this is referred to as *in-situ* microscopy [13]. A wide range of external stimuli can be applied, starting from a simple beam heating to controlled sample heating, interaction with optical light triggers, application of a voltage or a magnetic field up to changing the sample's environment by exposing it to a reactive gas. A variety of areas (listed in Table 2-1) are currently investigated, which would profit largely from high-time-resolution TEM as provided, e.g. by the EDET technology [13]:

[5] TEM electrons are comparatively better suited than high energy X-rays in their application to biological specimens since the average deposited energy per inelastic scattering event is just 20 eV (8 keV for 0.15 nm X-rays) and the ratio of inelastic/elastic scattering events is about 3 (10 for 0.15 nm X-rays) [239].

[6] ATP supplies body cells with energy by diffusion within milliseconds through cell volumes ranging from several micrometers up to millimeters.

[7] Potential change of its structure and properties.

FIELDS	OBSERVABLES	APPLICATIONS
Phase Transformations	➢ Melting ➢ Crystallization ➢ Transformations between Crystal Structures ➢ Formation of new Phases by solid state Diffusion	➢ Alloy Processing ➢ Development of new Materials: extreme Hardness, superplastic, magnetic or shape Memory Properties
Surface Reactions & Crystal Growth	➢ Heating or Exposure to an reactive Environment or Deposition Flux	➢ Understanding of Surface Reactions
Magnetic, Ferroelectric & Superconducting Materials	➢ Dynamics of ferromagnetic Domain Switching ➢ Phase Transformations with magnetic, ferroelectric and superconducting Materials	➢ Storage Media ➢ Memory Elements ➢ Motion of flux Vortices through Superconductors
Elastic and Plastic Deformation	➢ Impose a known Stress (straining stage, inbuilt Stress, thermal Expansion mismatch) on the Sample	➢ Bringing the Understanding of the mechanical Properties of Nanostructures, thin Films and Surfaces to a new Level of Precision
Ion and Electron Beam induced Phenomena	➢ Irradiation Damage ➢ Ion beam assisted Depositions ➢ Ion Implantations	➢ Model Neutron Damage in the context of nuclear electric Power Generation ➢ Development of host Materials for long term nuclear Waste Storage ➢ Materials Processing: Development of Semiconductor Devices
Liquid Phase Processes	➢ Polymer Growth ➢ Biomolecular Imaging ➢ Electrochemical Deposition	➢ Drug Delivery ➢ Data Storage

Table 2-1: In-situ TEM application fields

2.3 Recording Dynamical Processes - Examples

2.3.1 Order-Disorder Phase Transformation

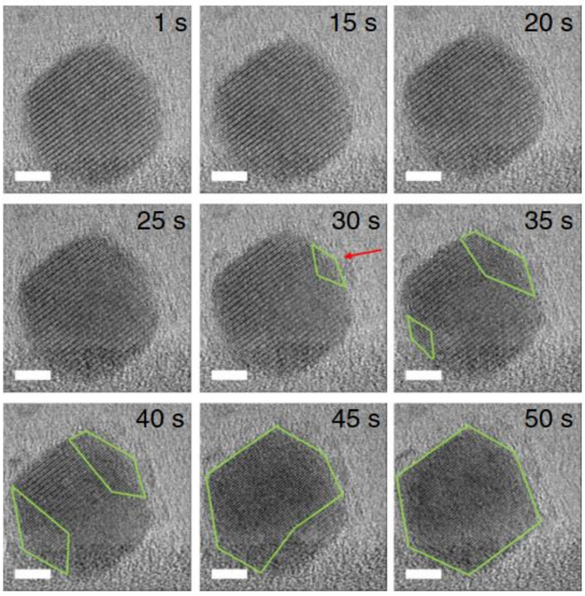

Figure 2-3: Selected TEM movie frames (extracted from [14]) of a hexagonal-shaped $Cu_{2-x}Se$ nanoparticle (HNP) undergoing a transition from the vacancy-ordered phase to the superionic (SI) phase. The time relative to the start of the movie is indicated for each frame. At t =30 s, a red arrow labels the nucleation of a cation-disordered region (marked by green outlines) growing across the HNP over time. Scale bars correspond to 5 nm in length.

Fast-ion conducting solids like cuprous selenide, Cu_2Se or $Cu_{2-x}Se$, offer a potential as solid electrolytes for Li-ion batteries [14]. At room temperature they are crystalline, however at elevated temperatures (> 140 °C) they exhibit a disordered sub-lattice with high cation (Cu^+) mobility (superionic phase – SI) leading to fast-ion conduction.

Figure 2-3 presents a section of a TEM movie recorded on a single Cu_2Se nanoparticle undergoing an electron beam induced transition from the ordered crystalline phase to the superionic phase. The phase transition was found to be positively correlated with the electron energy and the applied electron dose. *In-situ* TEM contributes to a better understanding of the temperature-induced transition from the ordered phase to the SI phase and ultimately may lead to the development of strategies for enhancing the ion transport and for reducing the necessary temperature to the operating range of Li-ion batteries.

With respect to non-biological measurements, a better time resolution as provided by the EDET system, will allow the study of shorter phase transformations and their kinetics, e.g. homogeneous (spontaneous & randomly without a preferential nucleation site) vs. heterogeneous (occurs at preferential sites such as grain boundaries) nucleation.

2.3.2 Vapor-liquid-solid Growth in the Formation of Nanowires

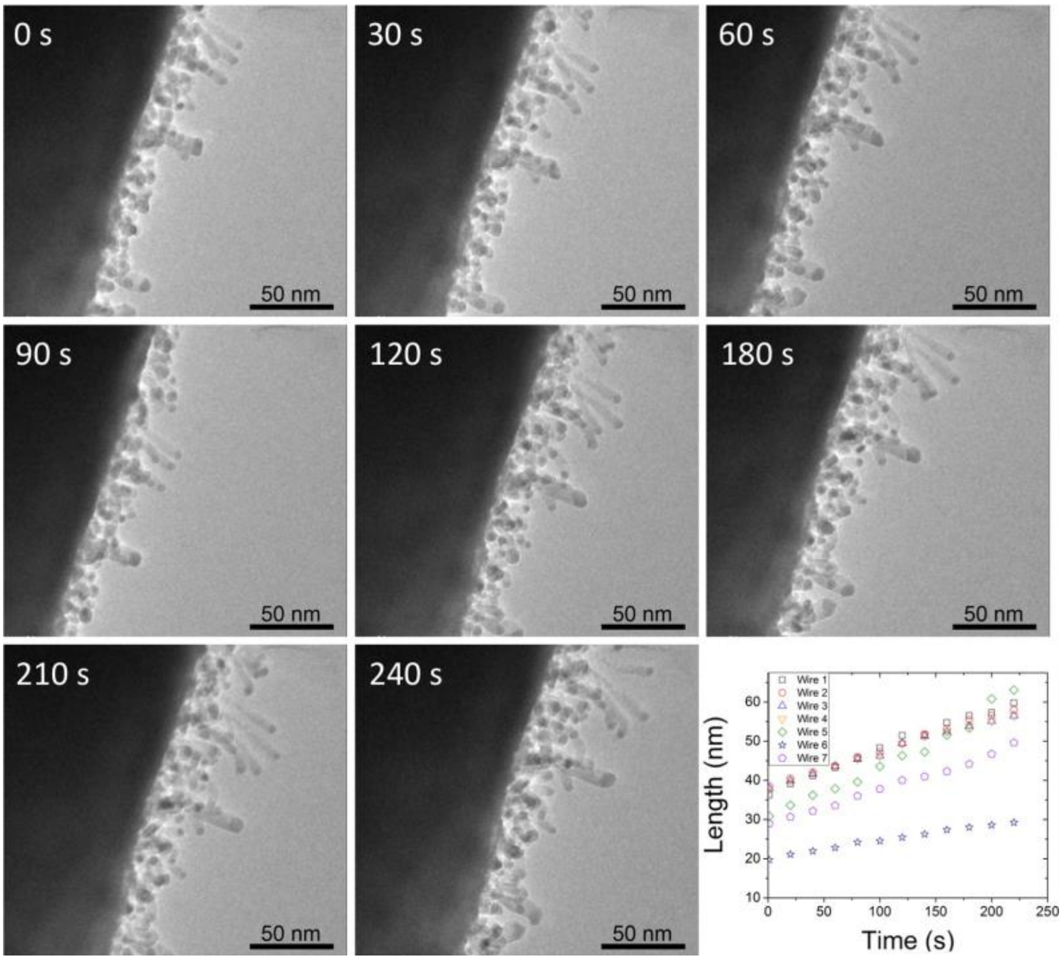

Figure 2-4: Time-lapse in situ TEM images of Fe_3O_4 nanowire growth catalyzed by Pd nanoparticles at ≈500 °C. The growth kinetics of several single nanowires are plotted in the lower right, from [15].

Nanowires are essential for the fabrication of various nanodevices for electronics and sensors. A common technique, the vapor-liquid-solid method, uses precursors supplied from the gas phase, which diffuse and form a liquid phase with the solid seed to finally form a nanowire up to several micrometers (vapor-liquid-solid method) [16]. A similar, low-cost technique is based on catalyzed oxidation [17]. Figure 2-4 depicts an *in-situ* TEM of catalyzed metal nanowire growth due to an oxygen reduction reaction at ≈500 °C.

The mentioned approach supplies a new class of nanowire growth methodology that may be applied to a broad range of systems.

2.3.3 Controlling Nanoparticle Nucleation and Growth

Nucleation and growth directly affect the morphology and size of nanocrystals and herewith, also their physicochemical properties [18]. In particular, the ability to synthesize nanocrystals as a function of size has established interesting applications such as UV protection films, fluorescent sensors in biological applications, nano-tweezers, optical switches and other optoelectric devices [19]. Conventionally, nanoparticles are grown by phase-controlled wet-chemical synthesis, e.g. Au can be attached to oleylamine[8] and then reduced to form Au nanocrystals [20]. A major issue with this approach concerns the optimal reaction conditions and parameters (nucleation rate, induction time, growth rate etc.) which are not fully understood but rather derived in an empirical and intuitive matter [19].

In situ electron microscopy might shed a light on this, allowing the direct observation of the growth dynamics of nanocrystals induced by an electron beam. In the underlying process, the incident beam electrons create free radicals (H_3O^+, H^*, H_2, OH^*, H_2O_2) and aqueous electrons, that reduce soluble metallic precursors (e.g. solution of silver nitrate $AgNO_3$) into solid metal atoms ($Ag^+ + e^-_{aq}, H^* \rightarrow Ag^0$). The latter aggregate to form nuclei and subsequently grow into nanocrystals as shown in Figure 2-5 [18].

By varying several beam parameters, especially the beam intensity and exposure time, valuable information could be gained: first of all, a certain threshold electron dose rate, the so-called nucleation growth threshold[9] must be maintained, below no nucleation was observed.[10] Following the nucleation, the beam current largely influences the growth and final morphology in the same way that the concentration of the reducing agent does for conventional colloidal synthesis. At a beam current near the growth threshold, the nanocrystals grew by a reaction limited mechanism, characterized by faceted plates or bipyramidal structures and a radius growth at $r{\sim}t^{1/2}$, while higher beam currents encourage diffusion limited growth ($r{\sim}t^{1/3}$) yielding polyhedral or near spherical nanocrystal shapes.

[8] Organic compound, an unsaturated fatty amine, *cis*-1-aminio-9-octadecene: $C_{18}H_{37}N$

[9] Knowledge of the growth threshold will allow researchers in future studies, to separate electron beam induced growth from typical electrochemical reduction growth.

[10] Nanocrystals did not grow immediately upon irradiation but became visible after a few seconds.

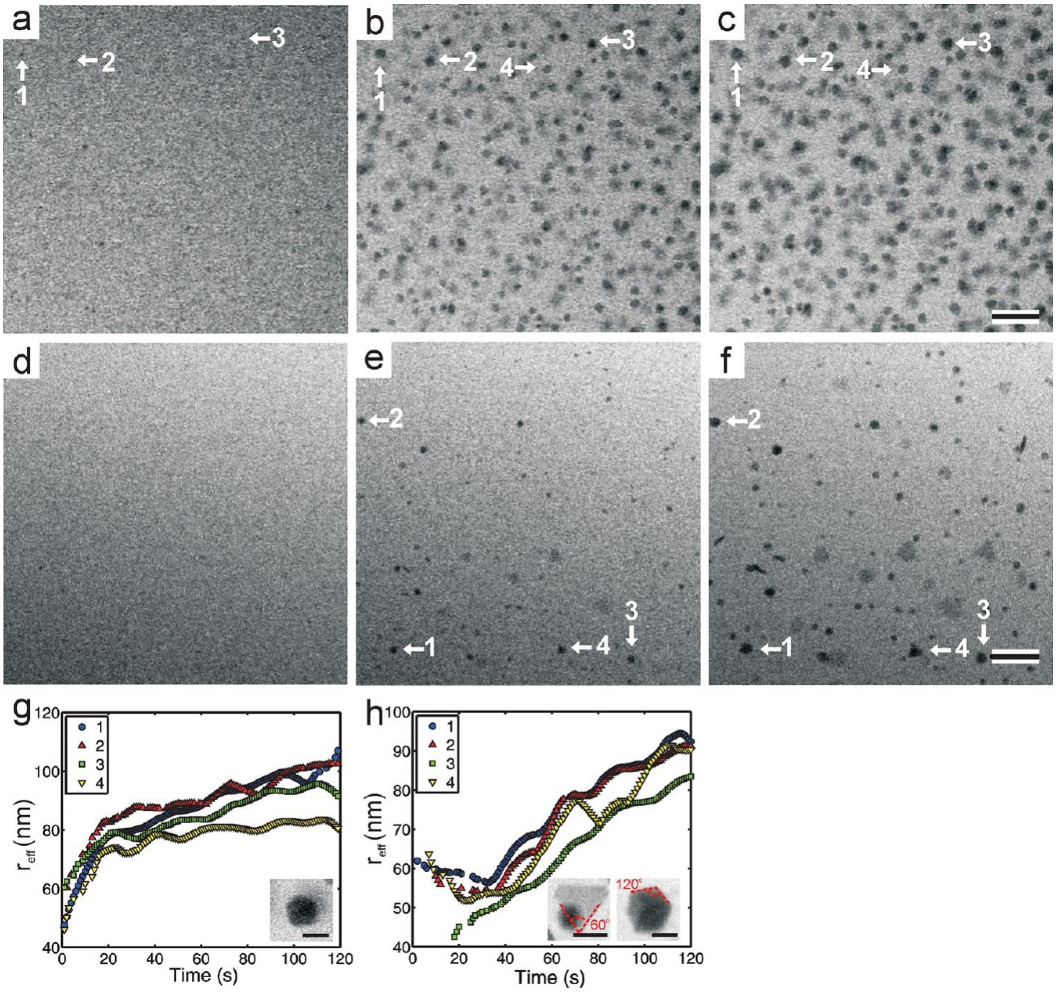

Figure 2-5: (a-c) Time series of scanning transition electron microscope (STEM)[11] images taken at t = 0 (a), 60 (b), and 120 s (c), resulting in an electron dose rate of 3.37 electrons/(Å^{2}s). (d-f) Dose rate of 0.59 electrons/(Å^{2}s). The scale bar for both time series is 200 nm. (g) Plot of the effective radius (r_{eff}) as a function of time for four individual nanocrystals indicated in panels a-c with arrows. (h) Plot of the effective radius (r_{eff}) as a function of time for four individual nanocrystals indicated in panels d-f with arrows. Insets are higher magnification images showing the different morphologies of the resulting nanocrystals; the scale bars are 100 nm. Pictures from [18].

Other nanoparticle growth processes experience a burst nucleation (e.g. iron oxide Fe_3O_4, synthesized through oxidizing $Fe(CO)_5$ with meta-chloroperoxybenzonic acid in the presence of tridecanoic acid in dioctyl ether [21]): the oxidation reaction takes one hour with no measurable formation of particles. All of a sudden, an extremely fast particle growth occurs. Such transformation phases can be much better investigated by a fast electron detector.

[11] A STEM combines the principles of a TEM and a scanning electron microscope (SEM). If a TEM is switched to the STEM-mode, the beam is finely focused and scans the sample area, while the image is generated by the transmitted electrons.

2.3.4 Plasmon-Mediated Nanocrystal Synthesis

Some physical and chemical properties of nanoscale materials are closely connected to their size and shape. Colloid chemistry already achieves good control over particle size for several spherical metal and semiconductor compositions [22]. Notwithstanding several approaches for non-spherical shapes, e.g. Pt cubes and pyramids [23], these are traditionally based on thermal processes and yield relatively small quantities of the desired particle shape. The discovery of localized surface plasmon resonances (LSPRs), i.e. the collective oscillation of nanocrystal electrons caused by incident light, allows an efficient control over size and shape of the nanocrystals [24].

The underlying mechanism is based on redox chemistry: excitation of LSPRs of nanoparticles by high-energy electrons in an aqueous solution catalyzes the reduction of ions by the citrate, the speed of which influences the dominant facets (and hence the shape) of the growing crystals [25]. As an example, Figure 2-6 shows the photoinduced[12] synthesis of large quantities of spherical silver nanoparticles into triangular nanoprisms.

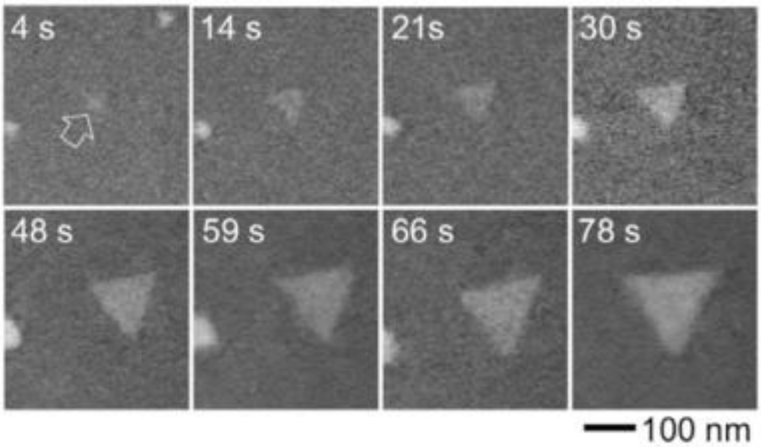

Figure 2-6: Time-lapse sequence (from [26]) of in situ STEM images showing the conversion of Ag nanoparticles (30 nm in diameter, originally dissolved by oxidative etching) into triangular nanoprisms. The nanoparticles were embedded in a liquid cell containing sodium citrate. The process was driven by the white-light excitation of the scanning electron beam.

Again, *in situ* electron microscopy provides the necessary tools for the quantitative understanding of these growth processes. The unusual optical properties of silver plasmon-resonant particles have been exploited in the development of biodiagnostic applications [27].

2.3.5 Biomolecular Imaging

Cryo-electron microscopy (cryo-EM) accomplished significant progress to the understanding of small biological samples (e.g. protein structures) and some fundamental dynamic processes. As an example, the first stages of bacteriophage infections of bacterial host cells was well described by [28].

[12] Using monochromatic light.

Figure 2-7 pictures 5 distinct conformations during T4 phage infection. At the beginning, some of the six long tail fibers (LTF) of the virion are retracted ("up" or capsid bound), some are extended ("down") to contact the outer membrane of the *E. coli* cell. The next step, the baseplate transits to its star configuration, triggering a contraction of the sheath and a release of the remaining LTF. This tail contraction pushes a needle through the cell membrane and releases the phage DNA from the capsid into the cytoplasm of the *E. coli* cell.

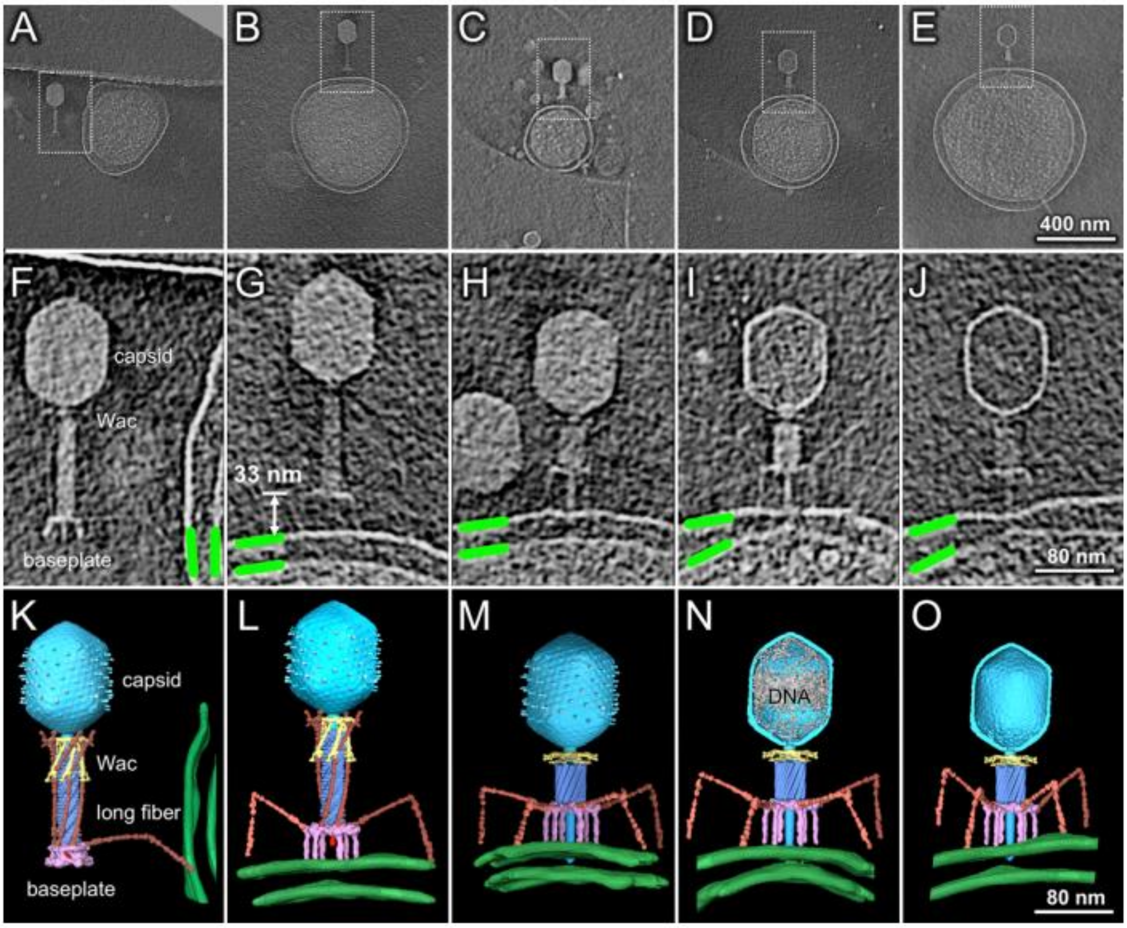

Figure 2-7: Several stages of bacteriophage infection of an E. coli minicell as a host. The 3D tomograms show individual virions after 30 s (A and F), 1 min (B and G), 3 min (C and H), 5 min (D and I), and 10 min (E and J) of infection. Boxed areas in A–E are enlarged in panels F–J and also rendered in 3D in K–O; the outer and inner membranes (green) were segmented manually. The baseplate (purple) changes conformation from hexagonal (A, F, and K) to star (B–E, G–J, and L–O), releasing the short tail fibers (STF). The capsid is in cyan, tail sheath in blue, whisker antigen control (Wac) in yellow, and the long tail fibers (LTF) in orange. DNA remaining in the capsid in N is in gray. Picture from [28].

Similar studies might deliver important model systems for viral infection, replication, gene transfer or protein folding and assembly. Every year, a lot of people become infected with bacteria, that are resistant to antibiotics. Phage therapies might contribute to solve this problem.

The five pictures presented above were established by a very time-consuming and complex method. Additionally, the freezing process employed during sample preparation is not conducive for dynamic observations, or to be more precise only allows for snapshots of longer time intervals restricted to a millisecond temporal resolution.[13]

For faster biological dynamics, the samples need to be observed in a fully hydrated state. Liquid *in-situ* scanning transmission electron microscopy can be used to get a better understanding of the structure/function relationship of macromolecular protein complexes [29]. To be sure, liquid cell electron microscopy (LC-EM) offers reduced resolutions compared to conventional EM due to increased scattering and absorption by the liquid cell membrane as well as by the aqueous medium [30]. Faster read-out speeds (provided by the novel EDET) will limit blurring artifacts due to particle mobility during imaging. Furthermore, since biological structures are in general sensitive to radiation damage, a faster readout would also mitigate this problem.

2.3.6 DNA Origami

DNA origami is the nanoscale folding of DNA to create arbitrary 2- and 3-D shapes at the nanoscale [31]. Usually, it uses long, single-stranded viral DNA macromolecules (“scaffold”). The necessary folding via self-assembly is achieved by adding short oligonucleotides (“staples”) in a buffer solution. A profound understanding of the base-pairing dynamics of DNA interactions can be exploited to produce tailor-made structures, capable of being used as shuttles to transport drugs or dyes into live cells or for data storage in electronic devices [32].

Traditional DNA origami is size limited to about 100 nm, which hampers plasmonics applications[14] [33]. The inclusion of gold nanoparticles (AuNPs) helps to overcome the size limitation and provide an enhanced *z*-contrast[15] in electron microscopy [32]. The specificity of the hybridization[16] and the observation of the real-time dynamics are very important for many fields in chemistry and biology.

Figure 2-8 shows two snapshots of a movie, picturing the real-time clustering dynamics of DNA-AuNP conjugates in water with nanometer spatial (scale bar represents 100 nm) and 200 ms temporal resolution.

[13] Time-lapse cryo-EM uses laser flash photolysis or microfluidic mixing.

[14] Investigation of electron oscillations in metallic nanostructures and nanoparticles. Surface plasmons exhibit specific optical properties, e.g. the capacity to confine light at the nanoscale. Surface plasmon resonances can be controlled by adjusting the size, shape, periodicity of the nanocrystal [211].

[15] Soft materials offer weaker electron scattering from their low atomic number atoms.

[16] In aqueous solutions, the four nucleobases adenine, cytosine, guanine and thymine form base pairs via hydrogen bonds. On a large scale, hybridization describes the process where a single-stranded DNA anneals to a complementary DNA.

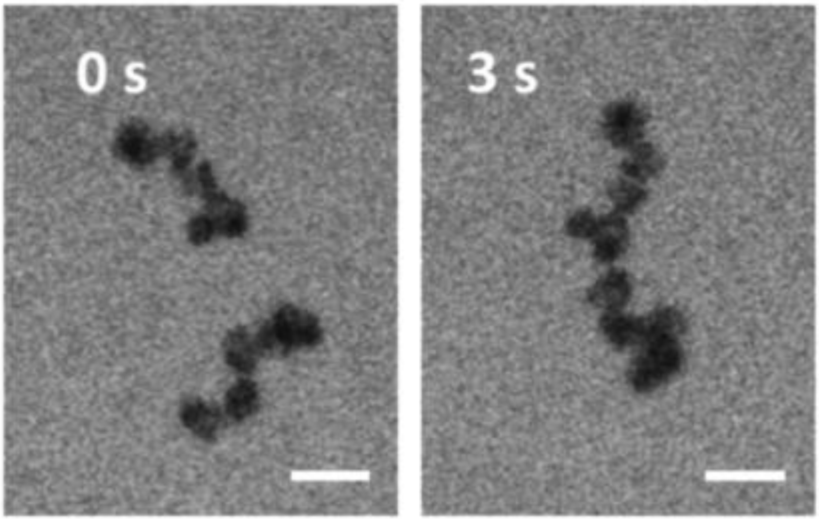

Figure 2-8: In-liquid TEM images of two clusters before and after merging, from [32].

For all bio-chemical processes the importance of in-liquid TEM must be emphasized. As mentioned, although Cryo-TEM has enjoyed considerable achievements, it uses series of frozen samples at different stages of the process and hence, only delivers static images, where the inherent correlated motions are lost. The freezing process may also affect gross morphologies or sub-cellular structures [30]. By contrast, *in-situ* TEM not only preserves the liquid state of the specimens inside the TEM vacuum, but also allows the observation of fast biological processes of even unstained and unlabeled samples (exemplarily shown for liposomes in [34]), thereby minimizing chemical perturbances.

On the downside, electron-water interactions (creation of reactive species such as solvated electrons, hydrogen radicals and hydroxyl radicals) are inevitable, leading to potential alterations of the subcellular structures of biological specimens [30].[17] Additionally, bubbles may form and compromise the spatial resolution as well as affect the behavior of the biological system. Specific care has to be given to the dose in order to prevent unintended chemical changes in the sample [35]. Structural damage effects to biological samples at a sub-nanometer scale can already occur at dosages of below $1\ e^{-}\text{Å}^{-2}$ [36].[18]

With the envisaged rate of 80,000 frames per second, EDET will possibly allow the observation of macromolecular dynamics on time scales relevant to conformational fluctuations that play a key role in their basic function.

[17] A mitigation of this problem can be achieved by the usage of graphene membranes, for their ability to efficiently scavenge reactive radical species, especially the hydroxyl radicals [284].

[18] On the other hand, microtubule proteins can maintain their structural features down to 5 nm for an electron density of up to $7.2\ \pm 1.4 \times 10^{2}\ e^{-}\text{Å}^{-2}$ by usage of graphene encapsulated liquid cells [286].

3 Transmission Electron Microscopy

3.1 TEM Resolution

The resolving power of transmission electron microscopes (TEM[1]) is superior to diffraction limited light microscopes. While light microscopes can easily resolve blood cells (~10 µm) or bacteria (~1 µm), smaller structures like the corona virus (~100 nm) and molecules down to single atoms are exclusively reserved to TEMs.

The German physicist Ernst Abbe discovered the resolution limit of a microscope and published the following formula[2] for the minimum distinguishable distance d or resolution:

Equation 3-1

$$d = \frac{\lambda}{2n\sin\theta} = \frac{\lambda}{2NA}$$

with λ the wavelength, traveling in a medium with a refractive index n. θ denotes the half collection angle of the magnifying lens, which in turn depends on the focal length and the diameter of the aperture. The numerical aperture NA is defined by $NA \equiv n\sin\theta$. According to Equation 3-1, it is possible to improve the resolution by the following measures:

- Expansion of the numerical aperture: the maximum half-angle of the numerical aperture equation is theoretically 90 degrees corresponding to $NA = 1n$. However, angles larger than 70 to 80 degrees are only found in the highest performance objectives [37]. Another option to increase NA consists of a stronger refractive index. The use of oil immersion liquids with a refractive index similar to glass ($n = 1.52$, in order to eliminate reflections to the greatest possible extent) can improve the resolution by about 50%.[3]
- The resolving power of a microscope is also influenced by the numerator of the equation: with a numerical aperture of 0.95 and the shortest visible wavelength at 400 nm (violet), the maximum achievable resolution of a visible light microscope is about 210 nm [38].[4] This corresponds to a magnification of roughly $1{,}000 \times$ compared to the resolution of the human eye. Though X-rays involve significant shorter wavelengths, they weakly interact with matter and are thus difficult to focus for imaging.

[1] In the following the term TEM is interchangeably used for the transmission electron microscope and the transmission electron microscopy.

[2] The similar Rayleigh criterion (named after the British physicist Lord Rayleigh) deviates slightly from Abbe's formula. The difference can be attributed to differing definitions for what is meant resolving two objects from each other.

[3] The effective resolving power also depends on the existence of optical aberrations.

[4] This value is hardly to achieve in real world applications, since other factors like low specimen contrast and improper illumination also contribute to the resolution.

The French physicist Louis de Broglie postulated wave properties for all particles and published in 1924 his well-known matter wave equation:

Equation 3-2
$$\lambda = \frac{h}{p}$$

with h the Planck constant and p the (relativistic) momentum. For TEM investigations, the acceleration voltages typically vary from 60 keV to 300 keV. The corresponding electron wavelengths range between 4.86 pm to 1.97 pm (equivalent to 0.45 – 0.77 the speed of light). However, spherical and chromatic aberrations of the electron lenses deteriorate the resolution level significantly. As an example, the JEM-2100 used for the TEM measurements in this thesis specifies the lattice resolution to 140 pm and the point resolution between 194 pm (in ultrahigh resolution – UHR configuration) and 310 pm (in high contrast – HC configuration). Efforts with aberration-corrected electron optics and a monochromated (energy-filtered) high-brightness source have pushed the spatial resolution to below 0.5 Å or 50 pm [39].

3.2 TEM Instrumentation & Working Principle

A TEM layout is schematically shown in Figure 3-1. Though the external appearances can differ substantially, the basic design and operation principles are similar:

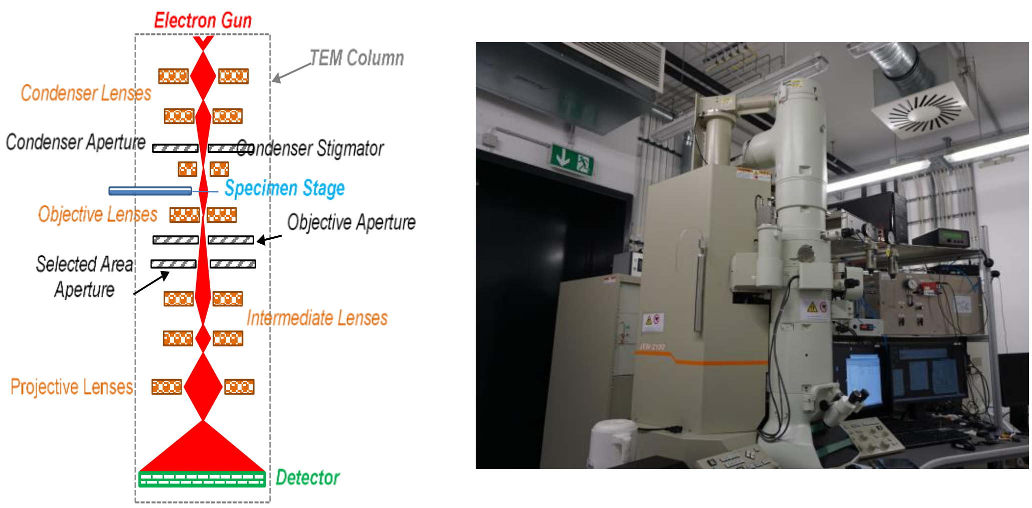

Figure 3-1: Left: TEM schematic diagram. The electrons, emitted by the electron gun at the top are shaped by the condenser lenses and the condenser aperture before passing the specimen. Subsequent series of lenses and apertures serve for magnification and control of the beam diameter. The detector at the bottom converts the electron energies to a real image. The TEM column, which houses all mentioned parts, must be evacuated to minimize the collision frequency of electrons with the gas atoms. Right: JEM-2100 TEM (JEOL) used for the measurements in Hamburg.

The market for TEMs is dominated by a few companies, among them the leading players are Thermo Fisher Scientific, JEOL Ltd and Hitachi High-Technologies. A typical TEM consists of 5 distinct components [40, 41, 42, 43, 44]:

3.2.1 Electron Gun

Basically, there are two types of electron guns prevalent: a thermionic gun uses a filament (tungsten, LaB_6 or CeB_6), which is heated up to high temperatures and usually embedded in a **Wehnelt cylinder**. A bias voltage of a few hundred volts extracts the electrons which are then accelerated to an anode plate. By contrast, field emission guns (FEGs) need several thousand volts for extraction in exchange for a much higher brightness, smaller beam spot size and higher coherency (and of course they are offered with a much higher price tag). All TEM images are subject to shot noise. It arises due to variations in the number of emitted electrons obeying poisson statistics with $\sigma \sim \sqrt{N}$, where N corresponds to the average number of primary electrons.

3.2.2 TEM Lens System

Unlike optical microscopes, a TEM uses electromagnetic lenses, usually made of a solenoid copper coil surrounded by a soft iron core[5]. The magnetic field and the related focusing power can be adjusted by changing the current flow through the coils. The ability to variate the focal length provides a lot of operational flexibility, especially for assemblies of independent lenses which are typical for a TEM system. The lens stages can be distinguished according to their different functionality:

- <u>Condenser Lens System</u>: located above the specimen, it contains at least two electron lenses responsible for converging the electron beam to a focus at or near the plane of the specimen. Additionally, small circular holes form a fixed or changeable condenser aperture which allows to regulate the beam intensity. Finally, a stigmator (also an electromagnetic piece) corrects for some residual **astigmatism** of the condenser lenses.
- <u>Imaging Lens System</u>: the objective lens strongly focuses and magnifies the beam exiting the sample. The downstream intermediate lens system is used for the selection of the operational mode (imaging or diffraction, depending on whether an image or diffraction pattern is projected onto the detector) and further magnification. The projector lens resides at the end of the TEM lens stack. It is responsible for another magnification of the beam to the detector. Additional apertures fulfill different functions as higher contrast provision, stabilization of nonconductive samples, selection of specific areas of electron diffraction and limiting the X-ray generation.

The lens system can be significantly improved by additional stigmators, customized lens configurations to minimize **spherical aberrations** and energy filters to reduce electron **chromatic aberration**.

[5] Should not retain magnetization when the applied magnetic field is turned off (low hysteresis).

3.2.3 TEM Specimen Stage

TEM specimens are standardized to a circular shape with a diameter of 3 mm. The rod-shaped specimen holder can be introduced into the TEM column via a small chamber (airlock), which is evacuated before the specimen enters the TEM vacuum zone. The holder is designed to move the specimen in all spatial directions (sometimes it even allows for rotations). It also provides a stable environment for the specimen to avoid any drift or vibration which would be magnified in the final image.

3.2.4 TEM Vacuum System

Different pumps are used to evacuate the TEM column to pressures below 10^{-5} Pa. The TEM vacuum improves most aspects of TEM performance: first, it reduces the frequency of scatterings with gas molecules which inevitably would shorten the electron mean free path. Second, it prohibits a high-voltage discharge and third, it prevents the specimen from contamination.

3.2.5 TEM Detectors

A useful tool for in-situ observation of the final image is a fluorescent screen, which can be tilted into the TEM beam. A viewing window made of lead glass shields the hard X-rays generated in the TEM. Alternatively, especially for higher beam intensities a closed-circuit TV (CCTV) transfers the image to an external monitor [45]. The imaging camera is situated at the bottom of the TEM column. In the early days, photographic emulsions or imaging plates were used. These got more and more replaced by indirect detectors with an upstream scintillator and a CCD or a pixel detector behind. Nowadays, direct pixel detectors are dominating the market.

3.3 Liquid Cell

In the past, TEM investigations were restricted to thin and vacuum compatible, mostly solid samples. The inelastic mean free path (IMPF) of electrons, defined as the mean distance traveled by an electron between consecutive inelastic collisions, highly depends on the electron energy and the sample material. For water, which can be used as a proxy for organic substances, the IMPF of 120 keV electrons extends to 180 nm [46]. In order to reduce scattering cross sections, TEM samples must be cut into very thin slices[6] of less than 30 nm (assuming 100 keV electrons and $Z < 30$), in case of higher energies (or higher atomic numbers) somewhat thicker [44].

Biological samples need a variety of special treatments [47]:

- Fixation: preserves the structure by adding a fixative like glutaraldehyde.
- Staining: addition of some radiopaque material to improve the mass contrast.

[6] This is a science in its own.

- Sample Drying: the sample has to be dried before brought to the vacuum. Otherwise, the evaporation of the residual water induces a sample damage.

The samples are typically embedded in plastic resin (alternatively, they are cryogenically frozen) and sliced to thin sections. However, there is always a risk that the object of interest gets deformed in the freezing or slicing process. Apart from that, static and frozen specimen severely limit the observation of correlated and uncorrelated motions.

By contrast, liquid phase based experiments open the field for dynamic studies while keeping atomic or molecular resolution. The conventional sample geometry consists of a liquid layer, encapsulated between two amorphous silicon nitride (Si_3N_4) membranes of 10–50 nm thickness.[7] A special type of these so-called liquid cells involves a microfluidic flow system, schematically presented in Figure 3-2. The overall cell dimension of $7 \times 4 \times 0.6\ \mathrm{mm}^3$ hosts two silicon microchips with a viewing window of $50 \times 50\ \mathrm{\mu m}^2$ [48], where the electron beam passes through the membrane onto a specimen. A rigid spacer defines the height of the fluid chamber (about 0.5 to 5 µm) which is sandwiched between the Si_3N_4 membranes.

The cell dimensions as well as the inlet and outlet port for the liquid require a custom designed TEM holder arm. A special pump outside the TEM column transports the fluid samples via feedthroughs to the nano-cell. The design guarantees, that any sample flow passes the narrowed 0.25 pico liter imaging volume ($50 \times 50 \times 0.1\ \mu m^3$) of the radiation window.

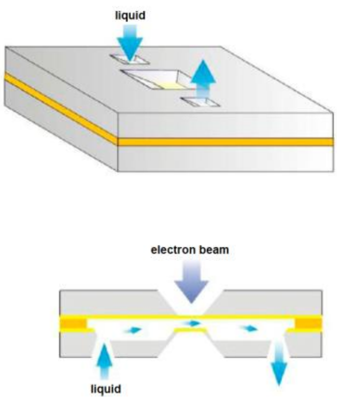

Figure 3-2: Liquid cell for TEM applications (cross-sectional view). The grey color represents the silicon housing, the orange color the spacer material and the yellow color shows the silicon nitride membranes. Image taken from [48].

Liquid cells are routinely used in material science to study the growth of metal nanoparticles. However, effects such as bulging of the silicon nitride window, evoked by pressure differences between the inside fluid and the outside TEM vacuum [49], adversely affect

[7] To minimize electron scattering, the membrane material should contain light elements and should be as thin as possible. Si_3N_4 is especially well suited for some stringent materials requirements: high vacuum stability, electron transparency as well as minimal susceptibility to charging or thermal effects. As an alternative material, graphene offers promising properties [186].

the imaging contrast and resolution of weakly scattered organic substances. For a window with favorable short dimensions like above, bulging amounts to approximately 1µm [50].

Moreover, the membranes can experience a stronger scattering than the objects of interest. A new environmental liquid cell (ELC) generation [51] uses thinner membranes (20 nm) and adds a 10 µm polyimide spacer in between. Since bulging also depends on the window width, the nano-fluidic cell dimensions were modified from $50 \times 50 \times 0.05\ \mu m^3$ to $200 \times 30 \times 0.02\ \mu m^3$. The liquid layer thickness is controlled by adjusting the flow rate of humid air. By means of a glow discharger, the surface of the bottom membrane is made hydrophilic. The inlet port is connected to a humidity reservoir, whereas the outlet drains to a vacuum pump. Two fine-tuning valves allow to adjust flow speed and pressure and the related liquid layer thickness via liquid displacement and condensation/evaporation effects.

3.4 Different Electron Detector Systems

3.4.1 Indirect Detection Systems

Until recently, indirect detection systems dominated TEM applications. Usually, an interposed scintillator converts the impinging TEM electrons into optical photons. The downstream detector (CCD or CMOS camera), connected by a fiber optic plate, subsequently registers only parts of the generated optical photons.[8] Since the scintillator-generated optical photons spread isotropically in all directions, a generally more blurred and noisier image is processed compared to a direct detection system [52, 53]. Mathematically, this is expressed by a lower signal-to-noise ratio (SNR):

Equation 3-3

$$SNR = \left(\frac{A_{signal}}{A_{noise}}\right)^2 = \frac{P_{signal}}{P_{noise}}$$

where, A is the root mean square amplitude and P references the average power. Additionally, indirect detectors are intrinsically slower due to the scintillator time constant.

3.4.2 Direct Detection Systems

The considerable advantages of direct electron detectors with respect to SNR and spatial resolution are somewhat counterbalanced by radiation damage. As a consequence, one can expect higher downtimes and additional repair and replacement costs. Basically, two different direct detector designs prevail: on the one hand, detectors with hybrid pixels. Each of them is composed of a sensitive semiconductor and an attached readout chip. Both parts are manufactured independently and connected via bump bonding. The alternate concept are monolithic pixel detectors (e.g. MAPS, DEPFET), which integrate part or the whole readout circuitry into one piece of silicon.

[8] A typical scintillator (LYSO) produces about 3,000 visible photons per one 100 keV electron.

3.4.2.1 CMOS Active Pixel Sensors (MAPS)

When asked for an evaluation of a specific digital photo camera, the layman would typically mention the price, the number of pixels, the overall size and perhaps even the video performance (expressed by number of photos/frames per second – fps). However, most times the number of megapixels is mentioned as the top criteria for a camera's image quality. But this is misleading, since also the size of the image sensor has to be taken into account. In that sense, a digital single lens reflex (DSLR) camera with 24 megapixels is superior to a fancy new smartphone camera with 48 megapixels because both the DSLR sensor and its pixel size are much bigger, hence the more light they can capture especially in a poor lighting environment. The ongoing pixel miniaturization reduces the light collection efficiency accompanied by a drop in the sensitivity. Also a higher fps rate can be useless in certain circumstances, e.g. if not coupled with a good autofocus tracking sensitivity. It is therefore advisable, to keep an eye on the whole detector system before drawing conclusions too quickly on specific parameters.

Monolithic Active Pixel Sensors (MAPS) can be regarded as an offspring of consumer cameras [54]: each pixel is composed of a silicon photodetector with an attached CMOS transistor (basic design) used for the discharge and amplification.

The structure of a MAPS pixel usually includes a lightly doped p-type epitaxial layer (typical thicknesses between 5-20 µm) over a highly doped silicon substrate (also p-type) and the readout electronics on top [55], as illustrated in Figure 3-3.

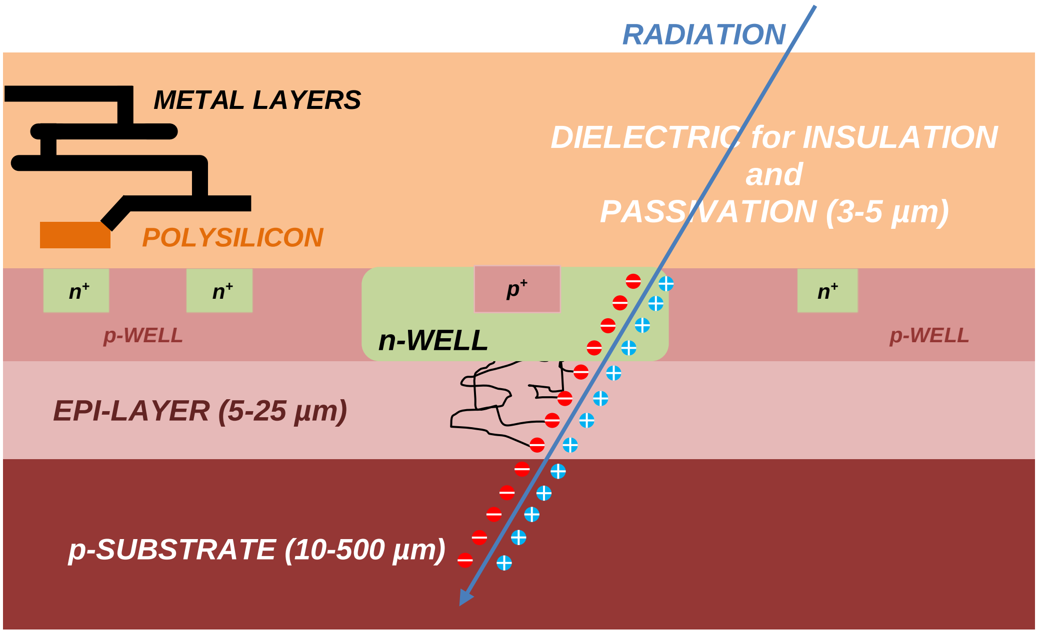

Figure 3-3: Cross-sectional schematic view of a CMOS pixel, adapted from [56] (distances are not to scale). High-energetic TEM electrons easily penetrate the metal layers of the readout electronics which are just a few microns thick. The epitaxial (epi)-layer can be considered as the detecting volume. As an example, one of the first direct detectors, the prototype Direct Detection Device (DDD) had a sensitive p-epitaxial layer of just 8 µm [57]. Thicker charge generating epi-layers will yield more signal.

Via backthinning of the p-substrate (down to whole sensor thicknesses of ~30 µm), the effect of **backscattered electrons** can be substantially reduced. The top layer harbors a dielectric for the insulation and passivation as well as the electronics and interconnects for the readout. An incident high-energy electron loses energy by optical phonons and impact ionization, fabricating electrons within the depleted epi-layer. The generated electrons are attracted by a positive diode potential (n-well) in a mix of drift and diffusion processes. The doping differences at the other boundaries of the p-epi-layer (p-wells & p-substrate) act as a potential barrier for the originated electrons. The discharge of the diode (removal of electrons from the n-well) and the amplification by the attached transistors constitute the signal. Typically, the readout occurs row by row for all corresponding pixels in all columns, this is why this readout mechanism is also called a rolling-shutter mode. Analog-to-digital converters (ADC, on-chip or external) digitize the voltage differences, which are proportional to the collected charge in each pixel.

The radiation hardness can be increased by special design features [58], but also by a higher frame rate [59]. The latter reduces the integration time and hence the relevant build-up of leakage current, making radiation damage relatively less important.

A CMOS design offers several advantages [56]:

- Complementary Metal Oxide Semiconductor (CMOS) technology is a worldwide industrial standard, any miniaturization progress benefits the MAPS technology
- lower cost per area from mass production
- very low power consumption
- higher radiation tolerance because of shrinking transistor sizes and corresponding thinner insulators and oxides [60]
- shrinking transistor sizes allow additional functionalities to be integrated in the same pixels

The market for direct detectors is dominated by 3 companies: Direct Electron, Gatan and FEI (now ThermoFisher Scientific) [61]. The specific properties of their flagship cameras are presented in Table 3-1:

DETECTOR	***DE-16***	***K3***	***FALCON 4***
PIXEL ARRAY	*16.8 MP (4,096 x 4,096)*	*23.6 MP (5,760 x 4,092)*	*16.8 MP (4,096 x 4,096)*
PIXEL PITCH	*6.5 µm*	*5 µm*	*14 µm*
SENSOR AREA	*7.09 cm^2*	*5.89 cm^2*	*32.88 cm^2*
FULL FRAME RATE	*92 fps*	*1,500 fps*	*320 fps*
INTEGRATION/COUNTING	*YES/YES*	*NO/YES*	*YES/YES*

Table 3-1: Most actual direct electron detectors from different vendors. Various datasheets DE-16 from Direct Electron [62], K3 from Gatan (AMETEK) and Falcon 4 from FEI.

In principle, direct electron detectors can be operated by two different readout modes: counting of all hit events above a certain threshold per pixel (counting mode) or integration of the generated charge carriers deposited in the sensor (integration or charge summing mode). MAPS detectors are mainly operated as counters at low electron dose rates, e.g. in the scientific area of cryo electron microscopy (cryo-EM) to provide high-quality images. The effective frame rate has to be substantially reduced in order to make it comparable with an integrating mode (large number of summed frames to form an electron counting image, e.g. each frame contains only one electron event per approximately 50 pixels [63]).

The total of generated electron hole pairs have to surpass a certain threshold to be counted as a hit. In case of a charge spread to neighboring pixels, caused by incident electron scatterings, the final event is attributed to the pixel with the highest charge [64]. To form an electron counting image, a large number of frames has to be accumulated, which makes the counting mode substantially slower compared to the integration mode.

The thickness of the sensitive layer represents a compromise between two diverging goals: signal variance (amplitude noise) and signal spatial resolution. The first decreases with the active layer thickness, the latter improves with a thinner active layer [61]. A general rule applies: a small pixel area requires a thin sensor to avoid signal spreading across several pixels.

The bottom of the camera housing should be equipped with low-atomic weight material like Carbon or Beryllium, in order to reduce an unwanted backscattering of electrons to the sensor.

3.4.2.2 Hybrid Active Pixel Sensors (HAPS)

An alternative detection approach uses a hybrid technology: Hybrid Active Pixel Sensors (HAPS) or also called Hybrid Pixel Array Detectors (HPADs), as for example the Medipix detector series. Originally developed for the LHC photon and particle detection [65], the sensor and the read out electronics consist of two different substrates, connected by bump bonding. A sensor thickness of 300 µm for Medipix based devices up to 500 µm for the EMPAD detector is able to absorb the full energy of the arriving TEM electrons.[9] Additionally, this makes the detector resilient to radiation damage[10], since the complete energy of the incident electrons is dissipated within the (at least to a large extent) damage-resistant silicon layer serving as a radiation shield for the electronic circuits on the bump-bonded readout integrated circuit (IC).

As explained in sections 4.2.4 and 8.2.2.5, the impinging electrons can also travel a significant lateral distance due to multiple scattering. Hence, in order to allocate as much

[9] The range of a 300 keV electron in silicon is close to 300 µm.

[10] For example, the EMPAD detector from ThermoFisher Scientific officially withstands > 10^{12} e^-/pixel @300 keV [174]. This compares to an accumulated dose of > 3.3 x 10^6 e^-/pixel for the original DDD [23].

of the deposited energy to a single pixel, large pixels are necessary. Ultimately, this limits the resolution for a given **field of view (FOV).**[11]

The active part of the Medipix 3 detector covers an area of about 66k pixels at 55 µm pitch. Each of them provides its own electronic circuitry consisting of around 1,100 transistors [66]. Additional electronics mitigate the effects of charge sharing. Some HAPS detectors are also operated as event counters: if the deposited energy exceeds a preset threshold, a hit is recorded and the counter is incremented. The specific properties of different HAPS camera producers are presented in Table 3-2:

DETECTOR	***EMPAD***	***MEDIPIX 3***	***DECTRIS ELA***
PIXEL ARRAY	*16 KP* *(128 x 128)*	*66 KP* *(256 x 256)*	*526 KP* *(1,028 x 512)*
PIXEL PITCH	*150 µm*	*55 µm*	*75 µm*
SENSOR AREA	*3.69 cm^2*	*1.98 cm^2*	*29.6 cm^2*
FULL FRAME RATE	*1,100 fps*	*~2,000 fps*[12]	*4,500 fps*
MAX COUNT RATE	*1 x 10^6 e^-/px/fr*	*~2.5 x 10^6 e^-/px/s*	*1 x 10^7 e^-/px/s*
INTEGRATION/COUNTING	*YES/NO*	*NO/YES*	*NO/YES*

Table 3-2: Hybrid direct electron detectors from different vendors. Various datasheets EMPAD from ThermoFisher Scientific with its high dynamic range of 1 Mio. e^- per pixel and per frame, MEDIPIX 3 from MEDIPIX Collaboration and DECTRIS ELA from DECTRIS AG. EMPADs exhibit a maximum beam current per pixel of ~4.5 pA in the integrating mode [67]. For comparison, the respective value for an EDET pixel is at least 6 pA[13], whereas just ~7 fA for the DE-16 sensor [63].

In contrast to MAPS, the individual pixel detection circuitry can be directly accessed by a much faster repetition rate than the overall frame readout rate (separate event counters) [68]. This is especially helpful for higher electron doses. For the Medipix detector even a continuous operation is possible: while one counter is read out, the other counter is still incremented [69].

[11] In order to limit lateral electron spreading, heavier materials are explored such as GaAs:Cr and CdTe for the use in HAPS [67].

[12] 200 MHz clock, 8 LVDS lines, 12 bit counters

[13] Assumptions: 200 keV electrons, 500 electrons per pixel/frame, 80,000 fps

4 Electromagnetic Interactions in Matter

Before turning to EDET a brief overview of electromagnetic interactions in matter should be given. Without a profound understanding of the fundamental relationships it is not possible to efficiently calibrate and optimize the detector.

Apart from that, electrons are elementary to all electron microscopy. Nothing can be observed unless the specimen scatters the electrons in some way.

When electrons or photons collide with matter, they deposit energy via electromagnetic (or nuclear) processes inside the medium. The way these particles lose their energy dominantly depends on their energy level.

4.1 Interactions of Photons with Silicon

For a homogeneous material of mass thickness t, a beam of mono-energetic photons of initial intensity I_0 emerges with intensity I according to the Beer-Lambert law:

Equation 4-1

$$I = I_0 e^{-(\mu/\rho)t}$$

where $\mu/\rho\ [cm^2/g]$ is the mass attenuation coefficient. In the above equation the mass thickness t is defined as the mass per unit area, therefore the thickness of the material x must be multiplied by its density ρ: $t = \rho x$.

The National Institute of Standards and Technology (NIST), a subdivision of the U.S. Department of Commerce, provides tabulated data of μ/ρ for various elements/compounds and different photon energy levels. Additionally, these coefficients are split up depending on their contributions from the following principal photon interactions[1]:

- photoelectric effect
- coherent or elastic scattering (Rayleigh)
- incoherent or inelastic scattering (Compton)
- pair production

The minimum energy required for the production of a charge carrier pair in silicon equals 1.12 eV at 300K.

Since the photon energy E_{ph} is inversely proportional to the wavelength λ:

Equation 4-2

$$E_{ph} = \frac{hc}{\lambda}$$

with $hc \approx 1.24\, eV \cdot \mu m$ (h the Planck constant, c the speed of light) the corresponding maximum wavelength amounts to about 1.1 µm in the infrared area. Beyond that, silicon

[1] Other less probable photon-atom interactions like photonuclear absorption, nuclear-resonance scattering or Delbrück scattering are neglected. Photonuclear absorptions usually result in the ejection of neutrons or protons from the atomic nucleus and can amount to almost 10% of the total photon interaction cross section. They are not included in the tabulated data and occur somewhere between 5 MeV and 40 MeV, well beyond the used photon energies in this thesis (maximum of 88 keV) [198].

is said to be transparent. If the wavelength is constricted to the visible light zone, only one electron hole pair per photon can be generated, the residual energy is absorbed by lattice excitation (phonon scattering) [70]. For high energetic photons like X-rays, multiple charge pairs are created (impact ionizations) and the mean energy loss (including phonon collisions) for one electron hole pair reaches an asymptotic value of about 3.6 eV.

As shown in Figure 4-1, the dominant absorption process for energies up to 30 keV is the photoelectric effect. Elastic scatterings and pair production are negligible, while inelastic scatterings begin to dominate at photon energies above 60 keV.

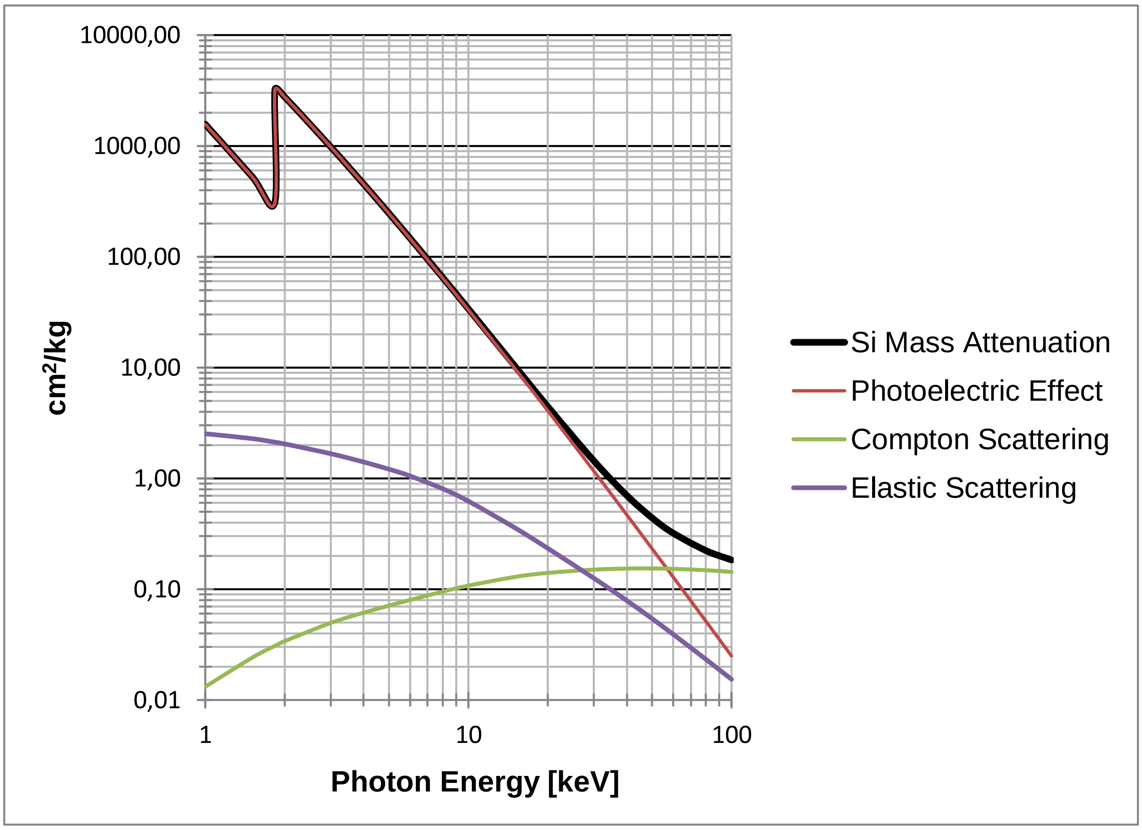

Figure 4-1: Silicon Mass Attenuation Coefficients for the three most relevant processes up to an energy of 100 keV (NIST data). The sharp spike at around 1,839 eV marks the X-ray response at the K-edge.

4.2 Interactions of Electrons with Matter

4.2.1 Collision Losses of Electrons in Matter

At energies below 1 MeV, an electron travelling through matter loses its kinetic energy dominantly by collisions, inducing ionizations or excitations of atomic electrons. Mathematically, this can be expressed by the average collision energy-loss or linear electronic stopping power $\langle dE/dx \rangle$ $[\mathrm{MeV/cm}]$, the first moment of the Møller cross section [71]:

Equation 4-3
$$\langle -dE/dx\rangle = \frac{1}{2}K\rho\frac{Z}{A}\frac{1}{\beta^2}\left[\begin{array}{c}\ln\frac{m_ec^2\beta^2\gamma^2\left\{\frac{m_ec^2(\gamma-1)}{2}\right\}}{\hat{I}^2}+\\(1-\beta^2)-\frac{2\gamma-1}{\gamma^2}\ln 2+\frac{1}{8}\left(\frac{\gamma-1}{\gamma}\right)^2-\delta\end{array}\right]$$

$K = 4\pi N_A r_e^2 m_e c^2 = 0.307075\ \text{MeV mol}^{-1}\,\text{cm}^2$,

ρ: the density in g/cm^3,

$N_A = 6.022140857(74)\times 10^{23}\text{mol}^{-1}$: Avogadro's number,

$r_e = e^2/4\pi\epsilon_0 m_e c^2 \approx 2.82\times 10^{-15} m$: the classical electron radius,

$m_e c^2 \approx 0.511\ Me$V: the electron rest mass,

β,γ: with their usual relativistic meanings,

Z: the atomic number of the absorber,

A: the atomic mass of the absorber,

$\hat{I}[eV]$: the mean excitation energy,

$\delta(\beta\gamma)$: the density effect correction to the ionization energy loss

Equation 4-3 is strongly related to the famous Bethe formula for heavy particles. The main difference concerns the maximum allowable energy transfer, which is limited to half of the kinetic energy of the incident electron, because of the identity with the electrons it ionizes. The negative sign for $\langle -dE/dx\rangle$ indicates, that the incident electron loses energy.

The term in brackets delivers a dimensionless number and is sometimes referred to as the stopping power, containing the essential physics of the process [72]. In silicon ($\rho = 2.329\ g/cm^3$), $\langle -dE/dx\rangle$ amounts to 5.2062 MeV cm^{-1} @ 200 keV e^- and reaches a minimum level of 3.5038 MeV cm^{-1} @ 1.303 MeV e^- (at $\beta\gamma = 3.55$). Thereafter, the values are slightly increasing to 4.4727 MeV cm^{-1} @ 100 MeV and 4.8888 MeV cm^{-1} @ 1 GeV e^- (own theoretical calculations).

The mean excitation energy values $\hat{I}$ are determined experimentally, for instance $\hat{I} = 75$ eV for water, $\hat{I} = 173$ eV for Silicon and for Lead $\hat{I} = 823$ eV (NIST data). The density effect correction parameter $\delta(\beta\gamma)$, itself dependent on material specific parameters, is related to a polarization effect: the atoms close to the particle path shield the electrical field strength for electrons at large distances. However, this factor becomes more relevant for higher energies (high $\beta\gamma$) [72]. With respect to the parametrization of this value a lot of work was done by Sternheimer [73, 74, 75]: the introduction of a variable $X \equiv \log_{10}(\beta\gamma)$ permits a simple calculation of the numerical values of $\delta(X)$.

Equation 4-4
$$\begin{array}{ll}\delta(X) = \delta(X_0)\cdot 10^{2(X-X_0)}, & X \le X_0\\ \delta(X) = 4.6052X + a(X_1 - X)^m + C, & X_0 < X < X_1\\ \delta(X) = 4.6052X + C, & X > X_1\end{array}$$

The parameters are material specific and can be looked up in tables. For silicon, one can find $X_o = 0.2014$, $X_1 = 2.8715$, $\delta(X_0) = 0.14$, $a = 0.14921$, $m = 3.2546$ and $C = -4.4351$.

Equation 4-3 can be separated into 4 different parts, as presented in Table 4-1 for silicon. The corresponding values for selected energies between 80 keV and 1 GeV demonstrate, that for TEM energies the Lorentz term ($\beta\gamma$) and the density effect parameter can be neglected.

Energies (MeV)	***1st -term***	***$\ln$-term***	***$\beta\gamma$-term***	***$\delta(\beta\gamma)$-term***
0.080	0.71	12.35	0.07	0.02
0.150	0.44	13.67	-0.05	0.04
0.200	0.37	14.28	-0.11	0.05
0.300	0.3	15.17	-0.18	0.08
1.000	0.20	18.01	-0.22	0.29
100.0	0.18	31.13	0.12	6.15
1000.0	0.18	38.03	0.12	10.72

Table 4-1: Selected terms of the electron loss formula for typical TEM energies. The slight increase after the ionization minimum can be mainly attributed to the $\ln$-term, which is to a large extent counterbalanced by the $\delta(\beta\gamma)$-term.

4.2.2 Radiation Losses of Electrons in Matter (Bremsstrahlung)

Radiation losses from electron interactions in matter occur in the form of Bremsstrahlung. Whenever an electron advances close to the atomic nucleus of a material, it can interact inelastically by experiencing a deceleration in the Coulomb field of the nucleus. Due to the conservation of energy law, this electron releases an electromagnetic radiation with a continuum spectrum up to the original beam energy. The radiation emitted per unit of time increases with the square of the absorber's atomic number Z and is inversely related to the electron's squared rest mass m_e^2 [72]:[2]

Equation 4-5
$$\langle\frac{dE}{dt}\rangle_B \propto Z^2/m_e^2$$

For electron energies above 50 MeV some analytical theories properly explain the Bremsstrahlung process of an electron in the vicinity of an unscreened atomic nucleus (e.g. Born-approximation theory of Bethe and Heitler, Coulomb correction factor from Elwert or the DBMO formulas [76]). Below 2 MeV, Pratt et al. [77] carried out numerical partial-wave calculations.[3]

[2] Therefore, it is much less probable that a proton of the same energy radiates photons compared to an electron when traversing matter.

[3] The tabulated energy losses (E.L.) cannot be directly compared to NIST data but must be first converted with the given formula.

The spectral intensity I_{sp} (number of Bremsstrahlung photons of energy E_x) of the Bremsstrahlung emission can be approximately quantified by the following equation [78], originally developed for X-ray tubes:

Equation 4-6
$$I_{sp} = CZ(E_0 - E_x)^{\alpha} \quad (\text{energy/keV})$$

where E_0 is the initial energy of the electron, E_x the produced photon energy and C, α are material specific constants with values of $C = 2.2 \times 10^{-6}\text{keV}^{-1}$ and $\alpha = 1$ in the original theory of Kramers [79].[4] An integration over E_x delivers the total emission efficiency coefficient η, which can be considered as an alternative method for determining the radiation yield, the average fraction that is converted to Bremsstrahlung energy as the electron slows down to rest:

Equation 4-7
$$\eta = \frac{CZE_0^{\alpha}}{(\alpha + 1)} \approx 0.84 \times 10^{-6} ZE_0$$

Note, that η solely depends on the atomic number of the material and the initial electron energy.

Radiation losses play only a minor role for energies below 1 MeV, as can be seen in Table 4-2.

Energy [keV]	***Radiation Yield***	$\boldsymbol{\eta}$
80	*0.13%*	*0.09%*
150	*0.2%*	*0.18%*
200	*0.24%*	*0.24%*
300	*0.32%*	*0.35%*
1,000	*0.83%*	*1.18%*
5,000	*3.94%*	*5.88%*

Table 4-2: Initial electron energies and the corresponding radiation yields. Radiation yield data from NIST using Pratt et al. [77] and suitable interpolations for energies between 2 MeV and 50 MeV. The efficiency coefficients η from Kramers' equation do not much deviate from the radiation yield factors, especially within the energy range for TEM electrons.

The critical energy E_c indicates the energy, where ionization losses and losses by Bremsstrahlung are equal. An approximate formula for E_c is given in [80]:

Equation 4-8
$$E_c \cong \frac{800 \text{ MeV}}{Z + 1.2}$$

For silicon, E_c can be found at around 53 MeV.

[4] X-ray energies below 2 keV are increasingly absorbed in the absorber material and hence are not detected.

4.2.3 Scattering Losses of Electrons on Atomic Nuclei

Electrons can also lose energy by direct head-on collisions with the atomic nucleus. However, the nuclear stopping power is much lower (by a factor of about 10,000 compared to ionization losses [81][5]) and thus insignificant for electron energy loss considerations.

4.2.4 Most Probable Energy Loss of Electrons traversing thin Absorbers

Landau noise is characterized by fluctuations around the mean energy loss and is the most influential noise source for thin detectors operated in integration mode[6] [63].

If a mono-energetic electron beam travels through matter, the resulting distribution from the mean energy loss formula would ideally resemble a simple delta function. Far from that, the total energy loss Δ of the electrons undergoes significant statistical fluctuations, strongly dependent on the thickness of the traversed material. The thinner the absorber element, the more the energy distribution varies and gets skewed with a long tail towards higher energies.

The corresponding probability density function $f(\Delta)$ is conventionally referred to as the straggling function[7]. Landau [82] wrote a first theoretical essay on energy loss straggling and set up an asymmetric probability density function with a long upper tail, expressing a higher probability for the deposition of comparatively large amounts of energy losses in a thin sensor. Therefore, the moments of $f(\Delta)$ like mean value and standard deviation do not characterize the distribution accurately, instead, the most probable energy loss Δ_{mp} and the full width at half maximum (*FWHM)* should be used [83] . The latter is simply the width of the distribution curve, measured between those points on the y-axis which are located at half of the maximum peak value.

For the Landau model it is convenient to define two parameters: ξ, denoting the product of the numerical coefficient before the square brackets of Equation 4-3 with the absorber thickness x:

Equation 4-9
$$\xi = x \cdot \left(\frac{1}{2} K\rho \frac{Z}{A}\frac{1}{\beta^2}\right)$$

and the maximum possible energy transfer ε_{max} in a single collision, which is for electrons [71]:

Equation 4-10
$$\varepsilon_{max} = m_e c^2(\gamma - 1)/2$$

[5] Silicon: between 2.3 x 10^{-4} MeV cm^2 g^{-1} and 3.6 x 10^{-4} MeV cm^2 g^{-1} for energies between 200 keV and 1 TeV with the minimum at around 1 MeV (for comparison, the minimum stopping power for electrons in silicon is around 1.52 MeV cm^2 g^{-1}).

[6] In contrast to the counting mode.

[7] Considered mathematically, the straggling functions are solutions to the transport equation under certain assumptions (neglect distant collisions, negligible electron energy losses in a collision).

Since ε_{max} solely depends on the Lorentz factor γ, the denominator can be easily determined. Using the relativistic energy-momentum relation $E^2 = (pc)^2 + (m_0c^2)^2$ and the energy of an accelerated electron $E = eV_a + m_0c^2$, where V_a stands for the TEM acceleration voltage, after some transformations one gets the following expressions for β, γ:

Equation 4-11
$$\beta = \sqrt{1 - \left(1 + \frac{eV_a}{m_0c^2}\right)^{-2}}$$

Equation 4-12
$$\gamma = 1 + \frac{eV_a}{m_0c^2}$$

$\varepsilon_{max} = 150\ \mathrm{keV}$ for 300 keV electrons and $\varepsilon_{max} = 60\ \mathrm{keV}$ for 120 keV electrons.

A generalization of the Landau distribution was provided by Vavilov [84]. He also introduced a new parameter κ, which is proportional to the ratio between ξ and the maximum possible energy transfer

Equation 4-13
$$\kappa = \frac{\xi}{\varepsilon_{max}}$$

Kappa tends towards large values for thick absorbers and/or low energetic electrons (low β). Likewise, kappa tends towards zero for very thin absorbers and/or high energetic electrons ($\beta \to 1$). Accordingly, three different regions of sensor thickness can be distinguished [85, 72, 86][8]:

- $\kappa < 0.01$: thin sensor → Landau Distribution
- $0.01 < \kappa < 10$: intermediate sensor → Vavilov Distribution
- $\kappa > 10$: thick sensor → Gaussian Distribution

Table 4-3 presents kappa values for selected TEM energies and two typical EDET sensor thicknesses.

TEM energies	***30 µm***	***50 µm***
160 keV	*0.016*	*0.027*
200 keV	*0.011*	*0.018*
300 keV	*0.006*	*0.01*

Table 4-3: Vavilov κ-values for different electron energies incident on 30 µm and 50 µm silicon absorbers.

In order to find an expression for the energy loss distribution, Landau was first setting up a differential transport equation by combining the differential collision probability (i.e. Rutherford cross section) with the probability of an infinitesimal energy loss $d\Delta$, when an

[8] κ is equivalent to Rossi's *G*.

infinitesimal absorber length dx was traversed. A solution to this integro-differential equation is the straggling function $f(\mathrm{x},\Delta)_L$, “the probability that a particle of a given initial energy E_0 on traversing a layer x will lose an amount of energy lying between Δ and $\Delta + d\Delta$ (the function f is normalized so that $\int f d\Delta = 1$)” [82].

Equation 4-14
$$f(\mathrm{x},\Delta)_L = \frac{\phi(\lambda)}{\xi}$$

where λ is Landau’s universal variable:

Equation 4-15
$$\lambda = \frac{(\Delta - \langle\Delta\rangle)}{\xi(x)} - 1 - \beta^2 + C_E - \ln \varkappa$$

with $C_E = 0.577215$ the Euler constant, $\varkappa = \xi/\varepsilon_{max}$ and $\langle\Delta\rangle = x \cdot \langle dE/dx\rangle$, assuming a constant mean energy loss. λ has a maximum at $\lambda_0 = -0.222782$ ... [87][9], representing the most probable energy loss.

Finally, after several Laplace transformations, Landau derived the following distribution density [88]:

Equation 4-16
$$\begin{aligned}\phi(\lambda(\Delta)) &= \frac{1}{2\pi i}\int_{r-i\infty}^{r+i\infty} e^{[u\ln u + \lambda(\Delta)u]}\, du \\ &= \frac{1}{\pi}\int_0^{+\infty} e^{-u\ln u - \lambda(\Delta)u}\sin(\pi u)\, du \\ &= \frac{1}{\pi}\int_0^{+\infty} e^{(-\pi u/2)}\cos[u(\ln u) + \lambda(\Delta)]\, du\end{aligned}$$

where r is an arbitrary positive number. The second, not so popular real integral uses a different method for the derivation of the Landau distribution and can be found in [72]. The computational implementation of this integrand by numerical integration is not convenient, since it delivers occasionally odd results (singularities, fast variation of the phase angle [88]). Alternatively, one can use accurate parametrizations of the asymptotic formulae for $\phi(\lambda)$ as for example given in [89] or in [90, 87].[10]

The most probable energy loss Δ_{mp} can be determined for $\lambda = \lambda_0$ and by solving Equation 4-15 for Δ:

Equation 4-17
$$\begin{aligned}\Delta_{mp} &= \langle\bar{\Delta}\rangle + \xi \cdot [\lambda_0 + 1 + \beta^2 + \ln\varkappa - C_E] \\ &= \langle\bar{\Delta}\rangle + \xi \cdot [\beta^2 + \ln\varkappa + 0.2]\end{aligned}$$

Figure 4-2 depicts the Landau curve for a 30 µm thick sensor and electron energies of 300 keV. The mean energy loss value deviates significantly from the most probable energy loss (for a Gaussian shape both would coincide).

[9] Note, in literature one can find slightly different values: the tabulated maximum in [52] is -0.225 and in [37] it is -0.229.

[10] The latter is implemented in the *pylandau* Python module.

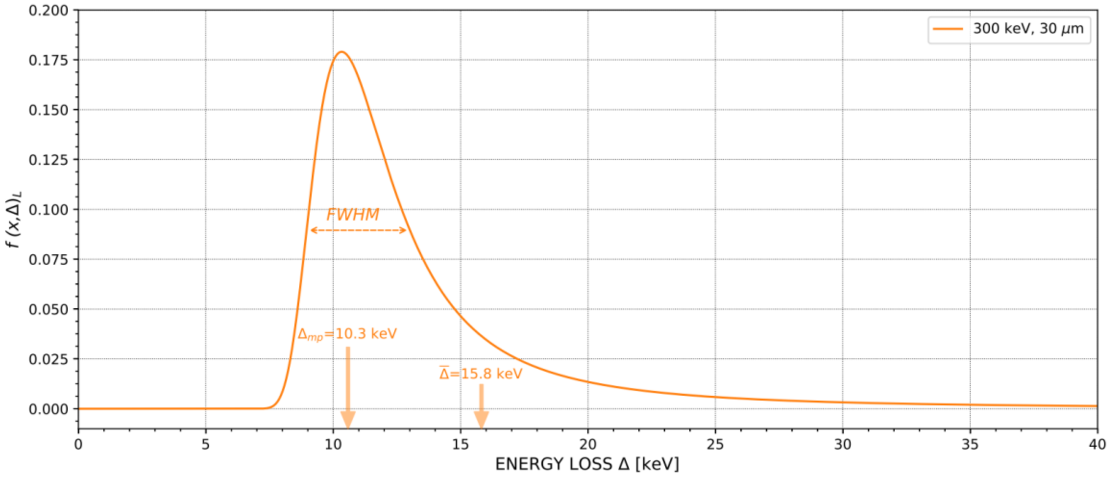

Figure 4-2: Landau-shaped Energy Loss distributions for a 300 keV electron beam on a 30 µm silicon absorber thickness. The full-width-half-maximum (FWHM) amounts to 4.1 keV.[11]

Table 4-4 compares the calculated means and the most probable energy losses, determined by GEANT4 simulations[12], with and without entrance layer for different electron energies. As one can see, the applicability of the Landau distribution increases (κ decreases) with higher energies and thinner material, i.e. the calculated data converges to the simulated data.

Energy [keV]	MV – Geant4 [keV] w/o entrance layer	MV – Geant4 [keV] with entrance layer	MV – calc. [keV]	MPV – Geant4 [keV] w/o entrance layer	MPV – Geant4 [keV] with entrance layer	MPV – calc. [keV]
30 µm						
160	30.5	36.2	20.9	18.2	20.1	14.5
200	22.1	25.5	18.7	14.6	15.6	12.7
300	14.9	16.0	15.8	10.8	11.2	10.3
50 µm						
160	68.8	75.0	34.5	37.5	41.6	26.0
200	49.7	55.5	31.0	28.7	29.7	22.2
300	29.2	31.6	26.3	20.2	20.9	18.1

Table 4-4: Comparison of Geant4 simulated and calculated mean & most probable values (expressed in keV) for different electron energies on 30 µm and 50 µm thick Silicon sensors with and without entrance layers.

[11] [177] found a relation for $FWHM = 4.02\xi$. Accordingly, the $FWHM$ should theoretically achieve 3.57 keV.

[12] Simulations performed by Ibrahym Dourki. To be correct, for the 50 µm thick sensor and electron energies below 200 keV, the simulated most frequent loss was observed close to the total energy loss due to the Bragg peak effect. Since the energy lost by charged particles is inversely proportional to the square of their velocity, the stopping power rises to a maximum when the electron has lost almost all of its energy.

The Landau theory has some limiting assumptions [82, 91]:

- $\xi \ll \varepsilon_{max}$: the total ionization energy loss is much lower than the maximum transferrable energy loss in a single collision
- $\xi \gg \varepsilon_0$: the total energy loss is much higher than the characteristic binding energy ε_0 of the most tightly bound atomic electrons
- the particle velocity remains approximately constant

As mentioned, the Landau integrals are difficult to handle numerically. The calculated energy losses also depend on the step size used for the computations.

For intermediate sensors, the Vavilov distribution [84] more accurately describes the energy straggling of electrons.[13] Vavilov further showed that in the limits $\kappa \rightarrow 0$ and $\kappa \rightarrow \infty$[14] the Vavilov distribution converges to a Landau resp. Gaussian distribution. However, for its more difficult analytic form the Vavilov model requires some challenging numerical computations (a computer program for its evaluation is given by [92] and [93], algorithms for the ”rapid calculation” can be found in [94]). Various refined straggling models were developed as for example by Talman [95], Wilkinson [96] and Bichsel [83].

4.3 Signals generated from Electron Interactions with Matter

If a TEM electron beam impinges on matter, various physical reactions are possible as depicted in Figure 4-3.

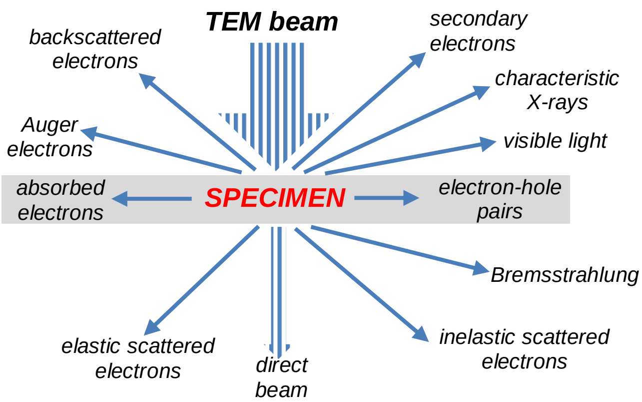

Figure 4-3: Interaction of a TEM beam with a thin specimen. The incident electrons induce a wide range of secondary signals. Adapted from [44].

These secondary signals are used for a wide range of applications in the field of Analytical Electron Microscopy (AEM): e.g. X-ray Energy Dispersive Spectroscopy (XEDS), Electron Energy Loss Spectroscopy (EELS), Reflection Electron Microscopy (REM) or Auger-Electron Spectroscopy (AES). In case of a high-quality TEM electron beam[15], the

[13] Furthermore, some hybrid forms exist like Landau convolved with a Gaussian distribution or Vavilov convolved with a Gaussian distribution [197].

[14] In this case the central limit theorem applies.

[15] Characterized by a relative narrow energy range.

likelihood of a scattering event increases mainly with the density and thickness of the absorber or specimen.

The following section provides only a qualitative description of the different phenomena and their relevance in the transmission electron microscopy (apart from a few approximation formulas). For a detailed analysis the interested reader might consult the following textbooks [44, 97, 42, 9, 40, 98].

4.3.1 Elastic Scattering of Electrons

An elastic scattering event on a heavy target changes the direction but not the wavelength of the electron. The electron gets deflected by the electrostatic field of a single atom and there is no loss of energy. To be precise, the total kinetic energy and momentum must be conserved, so a small energy transfer is always possible. The elastic interaction of an electron with the Coulomb cloud of the atom usually results in low-angle scatterings. By contrast, if the electron approaches the attractive force of the nucleus, much higher scattering angles are possible (and in rare cases lead to a complete backscattering).

The energy loss transfer from the primary electron to the nucleus can be obtained according to the following equation with $Mc^2 = Am_u$ the rest mass of the nucleus and $m_u = 931.4941\ \mathrm{MeV}$ the atomic mass unit [42]:

Equation 4-18

$$\Delta E = \frac{2E(E + 2m_0c^2)}{Mc^2}\sin^2\frac{\theta}{2} = \frac{E(E + 1.02)}{466A}\sin^2\frac{\theta}{2}$$

where the energies are expressed in MeV and the scattering angle θ in radians. Since most elastic scattering occurs below $\theta < 1°$, a scattering of a 200 keV electron at a Carbon nucleus ($A = 12$) would result in an electron energy loss of just 3.3 meV (and 43.6 eV for the rare 180° scattering event[16]). For Lead ($A = 208$), the corresponding numbers are just 0.19 meV and 2.5 eV respectively.

The figure of merit for all electron scattering processes is the cross section σ, the probability that an incident electron reacts with the target in a specific way. The basic dimension for particle cross sections indicates the effective area (proportional to the specific electron–target interaction probability), conventionally expressed in barn $(10^{-28}\mathrm{m}^2)$. Instead, the NIST database uses the squared Bohr radius ($a_0^2 = 2.800\ 285\ 2\ \times 10^{-21}\ m^2$) as the basic unit. ‘Area’ in the context of particle scattering has not the general accepted meaning, but rather expresses the probability of a scattering event.

The differential cross section records the scattering into a differential solid angle $d\Omega$ at a polar angle θ as depicted in Figure 4-4. An incremental increase of the scattering angle $d\theta$ leads to an incremental increase of the solid angle $d\Omega$.

[16] In this specific case, the energy transfer would be higher than the displacement energy of about 10-30 eV. This is bad news for biological substances with respect to early radiation damages, since carbon nuclei would be displaced from their lattice point to interstitial sites.

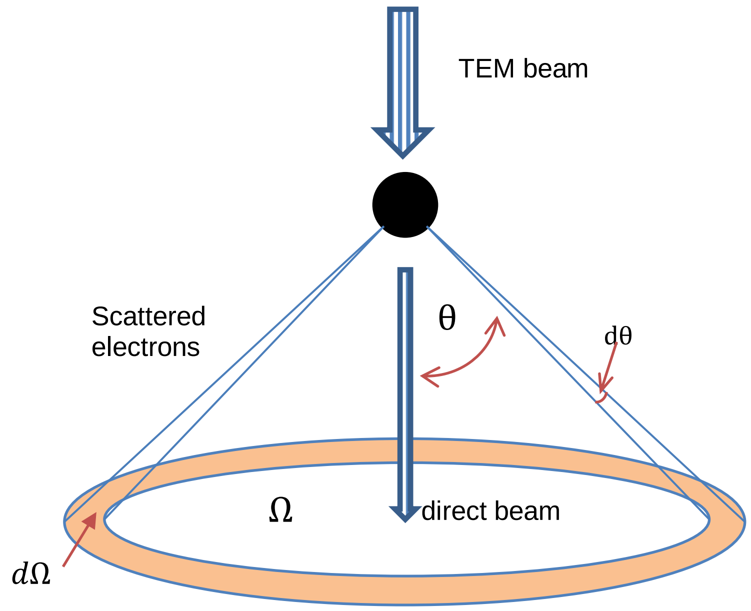

Figure 4-4: TEM beam scattering by a single atom (black ball). The total cross section expresses the probability of a reaction with a single atom. The differential cross section expresses the distribution of the interaction probability into different solid angles.

A very rough, but quick and instructive estimation of the elastic scattering cross section for TEM electrons is provided by the two following simple equations, segmented by the electron cloud σ_e and the nucleus σ_n scattering cross sections [44]:

Equation 4-19

$$\sigma_e = Z\pi\left(\frac{e}{V_a\theta}\right)^2$$

$$\sigma_n = \pi\left(\frac{Ze}{V_a\theta}\right)^2$$

with Z the atomic number, V_a the acceleration voltage and e the electron charge. Though these formulas do not exactly reproduce reality[17], the elementary dependencies are singled out quite well: the cross section for scattering at the nucleus increases strongly with the atomic number[18] and is inversely related to the electron beam energy and the scattering angle. The expression within the parenthesis can be considered as a radius, so the base unit has to be expressed in cgs-esu:

$$1\ e \approx 4.8\times 10^{-10}\ \mathrm{cm}^{3/2}\mathrm{g}^{1/2}\mathrm{s}^{-1}$$

and since

$$1V = 0.00333564\ \text{statvolts}\ \left[\mathrm{cm}^{1/2}\mathrm{g}^{1/2}\mathrm{s}^{-1}\right]$$

$$V_a = 300\ kV \approx 1{,}000\ \mathrm{cm}^{1/2}\mathrm{g}^{1/2}\mathrm{s}^{-1}$$

[17] For instance, the cross section would explode for scattering angles approaching 0.

[18] Also the Rutherford cross section for nucleus scatterings shows a proportional dependency $\sim Z^2$.

The cross sections added together and multiplied by $N_A \varrho x / A$ deliver a coarse estimate of the elastic scattering through a thin specimen of thickness x. In order to get more accurate results, one can again turn back to the NIST database. The newest version 4.0 [99] provides differential and total elastic cross sections for energies between 50 eV and 300 keV and for elements with atomic numbers from 1 to 96. Methodologically, the NIST cross sections are calculated using the relativistic Dirac partial-wave method as described by [100] whereas the scattering potentials are obtained from the Dirac-Hartree-Fock electron densities for free atoms (see [101]). Values of cross sections depend on the type of reaction and on the energy of the incident electrons. A comparison between Carbon an Lead is presented in Figure 4-5 for 200 keV electron energies.

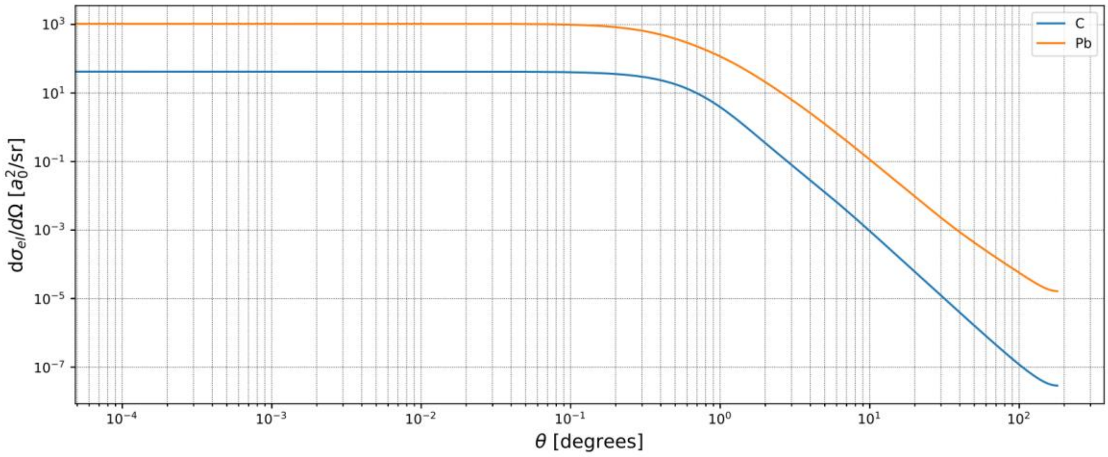

Figure 4-5: Differential elastic cross sections $d\sigma_{el}/d\Omega$ versus scattering angle θ for Carbon ($Z = 6$) and Lead ($Z = 82$) and incident electron energies of 200 keV. The numbers are to be interpreted in the following way: if the incident electron of the given energy hits an area of a_0^2 perpendicular to its path and is centered at the target nucleus or particle, the specific elastic reaction occurs. The differential cross sections are relatively stable for very small scattering angles until 0.3°. Additionally, they show a strong Z-dependency. The total cross sections amount to $0.018\ a_0^2$ for Carbon and for Lead $0.576\ a_0^2$ [99].

If the deflection angles are relatively low (1-10°), the electron beam remains coherent and can be used to analyze crystal structures from electron diffraction [102]. More importantly, elastic scatterings of the electrons by the Coulomb potential of a nucleus constitute the main contribution for the TEM image contrast.

4.3.2 Inelastic Scattering of Electrons

Inelastic scattering turns out principally incoherent and causes an energy loss of the incident electron, leading to ionizations or electron–atom excitations. The amount of energy lost in a single collision can range up to half of the kinetic energy for interactions with the atomic electrons of the material. The single deflections are characterized by very low angles (typically of the order of a few mrad).

Inelastic scatterings offer advantages and disadvantages: on the one hand, they generate a wide range of secondary signals (X-rays, secondary electrons or cathodoluminescence) and thus, also transport information about the chemistry of the specimen. This stimulated the establishment of the AEM with the main applications in XEDS and EELS. On the other hand, inelastic scatterings increase the background intensity and deposit radiation energy contributing to specimen damage.

The total inelastic cross section dominates the scattering for low atomic number materials [103]. If one assumes energy losses higher than 50 eV (typical for K-, L or M-shell ionizations), the following approximate equation can be used for the total inelastic cross section [43]:

Equation 4-20

$$\sigma_{inel} = \int_{50eV}^{E} \frac{\pi e^4}{(4\pi\varepsilon_0)^2 E \Delta^2} d\Delta \approx 26 \times \frac{10^{-20}\mathrm{m}^2}{E}$$

where the Coulomb constant $k_e = 1/4\pi\varepsilon_0 = 14.3996\, eV \cdot e^{-2} \cdot 10^{-10}\mathrm{m}$. For a 200 keV electron, the total inelastic cross section would result in $\approx 1.3 \times 10^4$ barns.

As mentioned, typical scattering cross sections are dependent on the incident electron energy and the used material. To get some feeling for the relative importance of elastic and inelastic scatterings in TEM: assuming 100 keV electrons impinging on carbon, inelastic scattering begins to dominate up to several orders of magnitude below a scattering angle of 10 mrad (~0.57°) [43, 103]. For large scattering angles, the ratio

Equation 4-21

$$\frac{\sigma_{inel}/d\Omega}{\sigma_{el}/d\Omega} = \frac{1}{Z}$$

only depends on the atomic number [42].

L-shell ionizations occur by a factor of one order of magnitude higher than K-shell ionizations [44]. Both, L- and K-shell ionizations are negatively correlated to the atomic number of the specimen: for Carbon, 200 keV electrons produce a total K-shell ionization cross section of 1.453×10^4 barns, the corresponding cross section for a Cd-Atom arrives much lower at 47.33 barns [104]. An in depth analysis and comparison of different inner shell ionization cross section models is provided by [105].

As the electrons pass through the specimen, they remain either undeviated or get scattered by elastic or inelastic processes. Accordingly, the resulting distribution is non-uniform, containing all the structural, chemical and other information about the specimen. The final image can be either observed with varying intensities as image contrast (spatial distribution) or as a scattering/diffraction pattern (angular distribution) [44].

4.3.3 Direct Beam

As is known, the mean free path expresses the average distance over which an electron does not experience any substantial change of its direction and energy. It is inversely related to the total (elastic + inelastic) scattering cross section. The undeviated electron beam, passing the specimen without interaction is termed the direct beam.[19] Since the scattering intensity decreases with increasing scattering angle θ, most scattered electrons point in forward direction inside $\pm 5°$ of the direct beam. The measurement of the undistorted, direct electron beam intensity can be used for precise measurements of the sample thickness.

4.3.4 Backscattered Electrons (BSE)

As the absorption material gets thicker, the probability increases, that an electron will experience multiple, elastic scattering events or even that an electron gets backscattered from the material. Backscattered electrons from the specimen are very important for Scanning Electron Microscopy (SEM) applications.

4.3.5 Characteristic X-Rays & Auger Electrons

If an inner shell electron is expelled by an incident electron, this leaves a vacancy. An electron from a higher energy level will then fill this hole, while the energy difference must be simultaneously released. It can be basically issued in two forms:

- An emitted photon with a material specific, characteristic energy (X-ray spectrum). As an example, the spectra of very small regions of the specimen allow to draw conclusions about the composition of an inhomogeneous microstructure.
- Alternatively, the energy is transferred to a third electron, the Auger electron, which is ejected from the atom, kinetically absorbing the excess energy in this radiation-less process. In other words, the Auger electron's kinetic energy corresponds to the difference between the original excitation energy and the binding energy from which the electron was ejected. The fluorescence yield from the K-shell ω_K describes the probability of an X-ray versus an Auger electron emission and can be approximated by the following third degree polynomial [106]:

Equation 4-22

$$\left(\frac{\omega_K}{1-\omega_K}\right)^{\frac{1}{4}} = -0.044 + 0.0346Z - 1.35 \times 10^{-6} Z^3$$

$$\Rightarrow \omega_K = \frac{(-4.4 + 3.46Z - 0.000135Z^3)^4 \times 10^{-8}}{1 + (-4.4 + 3.46Z - 0.000135)^4 \times 10^{-8}}$$

One notices the strong Z dependency. As a consequence, for low Z materials one rather uses EELS (instead of XEDS) for the structure analysis: e.g. for Carbon material about 1,400 atoms must be ionized in order to get a single C K_α X-ray, whereas for Lead ω_K almost reaches 1.

Since the energy difference is comparably low, only Auger electrons from the specimen surface are able to escape. Accordingly, the Auger Electron Spectroscopy (AES) has its main application in surface-chemistry.

[19] Sometimes, a secondary scattering event can redirect the electron back into the direct beam.

4.3.6 Secondary Electrons

In contrast to backscattered electrons, secondary electrons originate from the atoms of the sample as a result of inelastic interactions between the electron beam and the atomic electrons of the material. More specifically, only electrons which are ejected from the conduction or valence band are counted as secondary electrons. This distinguishes them from Auger electrons and limits the typical energies to below 50 eV with a maximum at around 5 eV. The secondary electron yield is comparably low within the inelastic scattering process and the low energy limits its applications to surface analysis.

4.3.7 Visible Light

If the electron beam impinges on a luminescent material, as for example a scintillator or a semiconductor, the orbital electrons get excited to a higher energy level. When they de-excite to the original energy level, they emit energy in the form of light of a certain color (cathodoluminescence – CL). CL-Spectroscopy is used for the analyzation of semiconductors and their impurities.

4.3.8 Plasmons and Phonons

Both, plasmons and phonons result as a consequence of the inelastic scattering process. Plasmons are collective oscillations of free electrons, when an electron beam interacts with the free electron gas, just as phonons are collective oscillations of atoms with the atomic lattices respectively. Plasmon peaks (energy loss range between 3-25 eV) are strong features of metallic EEL spectra and the number of plasmon excitations is frequently used to measure the specimen thickness. Phonon excitations (energy losses in the order of 20 meV to 1 eV) only contribute to a diffuse background and mainly increase the temperature of the specimen.

5 “EDET DH80k”-Project

The direct hit 80 kframes/s project “EDET DH80k” or short “EDET” serves as a working title for a collaboration established between the Halbleiterlabor (HLL) of the Max Planck Society in Munich and the Max Planck Institute for the Structure and Dynamics of Matter (MPSD) in Hamburg. The original intention envisaged two goals: first, the development of a detector, capable to record images of biological and chemical processes with a time resolution of 0.1 MHz, “while maintaining a spatial resolution in the nanometer range” [107]. Second, the fast frame rate should substantially enhance Ultrafast Electron Diffraction experiments (UED).

To minimize development costs, the project initially relied on the existing platform for the BELLE II detector (see [108]). However, little by little a series of adjustments were necessary. First and foremost, the basic charge storage volume of a single pixel had to be significantly increased. While for the BELLE experiment the required charge handling capacity (CHC) could be easily satisfied with a maximum of 6 x 10^4 electron-hole pairs per pixel, for higher particle flux experiments like EDET this number was regarded as far too low. Additionally, to cope with the new requirements, the existing ASIC chips had to be replaced or redesigned. Special emphasis had to be put to the fast storage of data, unlike for BELLE; the use of suppression schemes[1] is not effective for scattering or shadow images. On the other hand, the data does not have to be recorded on a continuous basis. As an example, biological dynamics often occur on timescales of just a few milliseconds [109].[2] It goes without saying, that the project also required a complete new power supply and data acquisition system.

Last but not least, the spatial extension of the sensor as well as the pixel size had to be fixed in advance, as this determines the maximal magnification of a specimen in a TEM.

5.1 DEPFET Pixel Structure

Like for the BELLE vertex tracker, DEPFET based devices were selected for the use as sensors for EDET as well. The DEPFET technology was preconceived by G. Lutz and J. Kemmer in 1987 [110] and developed by the Semiconductor Laboratory (HLL) of the Max Planck Society in Munich. It is based on a p-channel MOSFET, implanted on a highly-resistive, depleted n-type silicon substrate. The depletion is a necessary condition to assure that the electron hole pairs, which were generated by ionizing radiation do not recombine immediately.

Typical for a MOSFET structure, two highly conducting p-type electrodes, source (S) and drain (D) with a potential difference of several volts are isolated by the n-type substrate. A poly-silicon gate, which is separated from the bulk by a gate oxide covers the region

[1] Filtering signal data above a certain threshold, i.e. only data from pixels above a certain threshold are sent to the data acquisition system.

[2] The elementary bond formation/breaking processes occur during femto- to pico-second intervals.

between source and drain. If a negative voltage is applied to the gate contact and exceeds a certain threshold, an inversion layer at the oxide-semiconductor interface forms out, creating a hole channel between source and drain [111]. The strength of this hole channel is controlled by the (negative) voltage applied to the gate.

In contrast to ordinary MOSFET transistors, a DEPFET pixel contains a two-staggered attractive potential for electrons by means of various doping concentrations close to the MOSFET structure on the surface. The first potential is situated a few hundred nanometers below the external gate. If the bulk gets a certain exposure and the generated electrons move to this potential minimum[3], they will induce an extra charge of roughly the same amount in the channel, thereby increasing the transistor current [112]. Accordingly, the potential below the gate transistor channel is called the “internal gate” (IG).

As a consequence, a DEPFET integrates signal detection and amplification within a single silicon pixel structure. While for MAPS the discharged diode electrons are amplified by the integrated transistor electronics on top of the pixel, the first stage amplification for DEPFETs occurs intrinsically by direct modulation of the drain current. The CHC of the internal potential is, however limited. Each additional electron decreases the internal gate potential. The IG’s total capacity is limited to about 80,000 to 200,000 electrons, depending on the external gate area and the provided doping depth and doping concentration. However, a good contrast for TEM shadow images requires up to 800 thousand electrons per pixel and per readout frame.

To solve this problem, the source dimensions could be substantially increased, although this would come at a cost: since the internal amplification g_q is inversely proportional to the gate length (L) by $g_q \sim L^{-3/2}$ (see Equation 5-14) this would equivalently reduce the signal amplification. A much better solution uses the volume below the source area as an “overflow region” (OF) by additional implantations. The result involves a two-tier structure: a strong amplification from the internal gate region to detect weaker signals combined with a – by a factor of around 3 to 4 – weaker signal compression in the overflow region. This feature is especially helpful for high contrast images: signal compression allows to combine high energy resolution for areas obtaining only low signal charge with a high dynamic range.

Since a charge-less internal gate potential resides between 4 V with respect to the referencing source potential, the initially generated electrons are first attracted by the internal gate before the much lower potential from the overflow region (about 1 V above source) becomes attractive. Figure 5-1 shows the different gain slopes of an EDET pixel, capable of a strong amplification for weaker signals and in addition, a significant increased charge storage area for stronger signals.

[3] The holes are extracted by a negative p-backside contact.

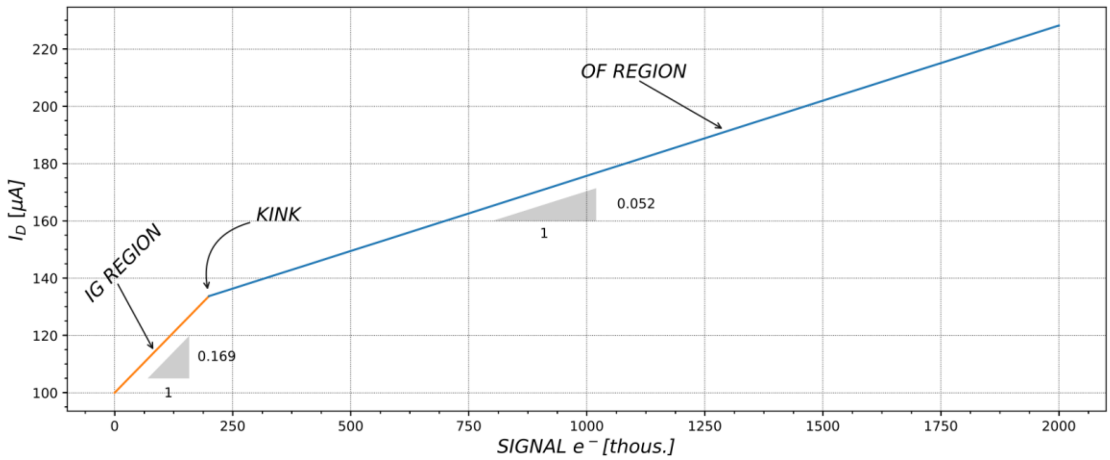

Figure 5-1: Non-linear response curve of an EDET pixel. The internal gate charge storage region offers strong amplification to detect weaker signals. By contrast, the overflow region can absorb significant more charge at a lower gain. The amplification is also influenced by the basic drain current, which is generally set to 100 µA and controlled by the gate voltage.

The dimensions of an EDET-DEFPET pixel comprises an area of $60 \times 60\ \mu m^2$ and a thickness of 30 or 50 µm. Figure 5-2 depicts the schematics of a minimum cell, consisting of 4 EDET pixels without the overlying metal layers for the electrical connections.

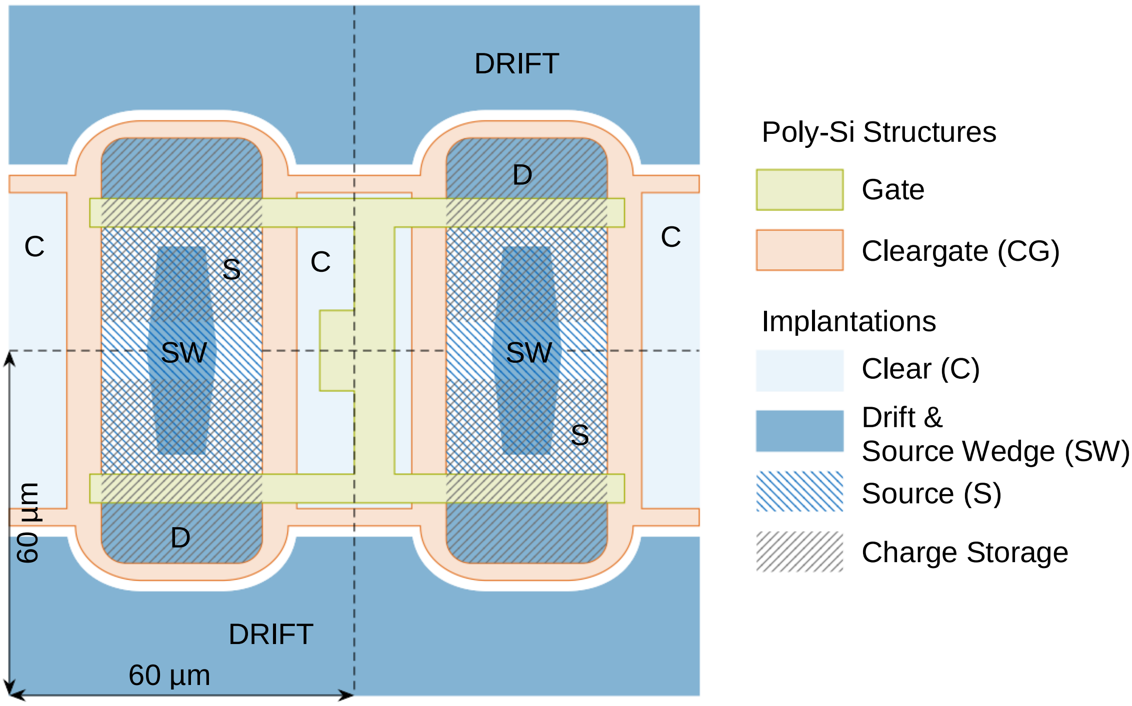

Figure 5-2: Layout of a minimum cell, comprising 4 EDET pixels (top-view). Two opposite pixels share the same source contact, while gate and clear structures are completely shared. The typical gate length (measured in north direction) variates between 4-6 µm, the gate width extends to about 22 µm. The volume below the source wedge (SW) area offers the lowest potential and is filled up at last.

Since there are only two aluminium layers for electrical connections, the pixels in the minimum cell share the gate and clear structures, while the source is only shared by the pixels framed by the cleargate.

The MOSFET structure is achieved by means of various implantations and isolation layers. The drift regions get negatively biased and take care for the horizontal transport of the generated electrons to the charge storing regions. If a very high charge was injected, a spill-over to an empty neighboring pixel is possible.

Figure 5-3 shows the schematic cross section of a simplified EDET structure. Ionizing radiation creates electron hole pairs in the fully depleted silicon bulk. The electrons are collected by two attractive potentials, starting with the internal gate volume thereby modulating the drain current (first stage amplification).

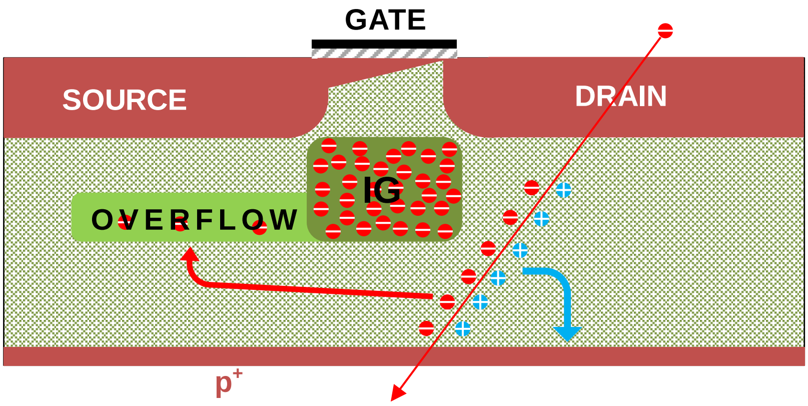

Figure 5-3: Schematic cross section of a DEPFET pixel with a MOSFET structure on top. The polysilicon gate electrode is isolated by a thin SiO_2 layer (shaded area). Impinging TEM electrons generate electron-hole pairs, which are first attracted by the higher internal gate potential directly below the external gate, then to the (much larger) overflow region. The holes drift to the p^+ back contact. Dimensions are not to scale.

High accumulated pixel charge carriers would quickly neutralize the internal gate potential and at a certain point, also the storage capacity of the overflow region. As a result, the detector would become insensitive. To avoid such situations, the collected electrons must be regularly extracted by a clearing mechanism. Two additional implantations are necessary: on the one hand, the clear structure consisting of a highly doped n-clear implant and the polysilicon cleargate. On the other hand, a deep boron implantation below the clear contact, also called p-well. It hinders the electrons from moving directly to the clear implant during the charge collection process.

A positive clear pulse, which is periodically applied to the clear contact, removes the accumulated electron charge from the internal gate and the overflow region. The principal task of the cleargate is to maintain a potential barrier, shielding the stored electrons in the IG and OF regions from moving directly to the clear electrode. Both, the clear and the cleargate must be perfectly synchronized with the readout process. Two positive pulses allow an erasure of the stored charges with relative low voltages. On the negative side, this mechanism adds to the design complexity. As a special solution, a common cleargate was introduced and capacitive coupled (see Equation 5-1) to the clearing pulse. It is placed peripherally on both sides of the internal gate to facilitate a very fast and efficient clearing mechanism.

Equation 5-1
$$\Delta V_{CLG} = \Delta V_{CL} \cdot \frac{C_{CL-CLG}}{\sum C_{CLG}}$$

with V_{CL} and V_{CLG} the clear and cleargate voltages, $\sum C_{CLG}$ the total cleargate capacity and C_{CL-CLG} the relative share of clear and cleargate capacities. The sigma sign denotes the total cleargate capacitance (including the capacitive coupling to the clear). In effect, a capacitive coupling between the clear and the cleargate voltage of 25-30% is achieved, i.e. a difference between clear low and clear high of 15 V would result in an uplift of the clear gate potential of 5 V. During the readout operation, all pixels of the minimum cell are enabled in parallel and the collected charge is removed by the common clear contact.

The readout process of a single DEPFET pixel follows an iterative loop:

- *Collection process:* the pixel is in an off-state, i.e. the clear and the external gate voltages are both kept in on position[4] (typically +1 V and +5 V respectively, referenced against the source potential). The silicon bulk remains sensitive to ionizing radiation and the generated electrons will accumulate in the internal gate or overflow region.
- *Readout:* by applying a voltage (e.g. -2 V depending on the gate length and potential radiation damage) to the external gate, the transistor is switched to the active state. The source–drain current, composed of the basic offset current (as mentioned, about 100 µA per pixel) and the induced current from the internal gate and overflow region is measured. The net signal is calculated by subtracting the offset value.
- *Clear:* a clear high voltage pulse, which is applied to the clear contact simultaneously, lifts also the cleargate voltage and paves the way for the electrons to get removed from their storing regions.

An overview over the key EDET system specifications is given in Table 5-1.

DETECTOR	***EDET***
PIXEL ARRAY	*1.048 MP (1024 x 1024)*
PIXEL PITCH	*60 x 60 µm²*
SENSITIVE SENSOR AREA	*37.75 cm²*
FULL FRAME RATE	*80,000 fps*
INTEGRATION/COUNTING	*YES/YES*

Table 5-1: EDET system specifications.

More about EDET sensor pixels can be found in [113].

[4] The terminology clear (gate) high/low or clear (gate) on/off is interchangeably used.

5.2 Electrical Properties of the DEPFET Sensor

The external gate of a DEPFET does not differ from a conventional PMOS transistor. The model of the linear gradual-channel approximation neglects changes in the longitudinal direction $(\partial E_x/\partial x)$[5] when the changes in the transverse direction $(\partial E_y/\partial y)$[6] of the channel is much stronger[7]. This is in general the case when the channel length $L \gg d_{ox}$, the thickness of the dielectric. A derivation of the following one-dimensional equation for the drain current I_D (linear region) can be found in [114]:

Equation 5-2
$$I_D = -\frac{W}{L}\mu_p C_{ox}\left[\left(V_G - V_T - \frac{V_D}{2}\right)V_D\right]$$

with W, L the gate width and the gate length[8], V_D the drain–source voltage[9], V_G the gate voltage and V_T the transistor's threshold voltage[10].

The hole drift mobility μ_p is defined by the drift velocity v_d, caused by the average electrical field E in the MOS transistor channel:

Equation 5-3
$$v_d = \mu_p E$$

$C_{ox} = \epsilon_{ox}\epsilon_0/d_{ox}$ expresses the oxide capacitance[11] per unit area. If the electrical field gets high enough, that the electron/hole energies sufficiently exceed the thermal energies within the silicon material, the drift velocities become independent from the electrical field and converge to their saturation values.[12]

In the ideal case, the saturation drain Voltage $V_{D,sat}$ follows the condition $\partial I_D/\partial V_D = 0$. The number of carriers flowing from source to drain is essentially independent of the drain voltage. Applied to Equation 5-2 this implies that $V_D = V_G - V_T$. In spatial terms this would mean, that the thickness of the inversion layer at the drain electrode is reduced to zero (“pinch-off” condition). Inserted into Equation 5-2 gives:

Equation 5-4
$$I_{D,sat} = -\frac{W}{2L}\mu_p C_{ox}(V_G - V_T)^2$$

---

[5] Field between source and drain.

[6] Perpendicular to the channel, created by the gate electrode. The term gradual is used since the voltages vary gradually along the channel from the drain to the source, whereas they vary quickly in the perpendicular direction from the gate to the bulk semiconductor.

[7] Additionally, the following idealized conditions are assumed: (1) the gate structure corresponds to an ideal MOS capacitor (no interface traps, no mobile oxide charge, no difference of the work function), (2) only the drift current is considered, (3) a uniform channel doping and (4) a negligible reverse leakage current.

[8] Typical gate lengths for the EDET pixels are between 4-6 µm, the gate widths are about 22 µm.

[9] Hereinafter everything is referred to the source as the ground potential, hence instead of writing V_{DS} or V_{GS} the first subscript will do.

[10] The threshold voltage is the gate voltage necessary for the formation of an inversion layer (channel) at the interface of the dielectric and the substrate (in the case of an empty internal gate).

[11] ϵ_0 the vacuum permittivity $\approx 8.854 \times 10^{-12} F \cdot m^{-1}$, $\epsilon_{ox} = 3.9$ the relative permittivity for the silicon oxide expressed as a ratio to the vacuum permittivity and d_{ox} the thickness of the silicon oxide.

[12] $\sim 1 \times 10^7 cm/s$ for electrons and $\sim 8.4 \times 10^6 cm/s$ for holes.

At the saturation voltage, the conductivity of the hole channel exhibits a quadratic dependency

$$I_{D,sat} \sim (V_G - V_T)^2$$

To incorporate the induced current from an internal gate charge Q_{sig} for DEPFET sensors, the following considerations were made [115]: at a given gate voltage V_G the number of holes N_h in the MOS channel is constant and defined by both the potential along the channel and the gate-channel capacitance. If a single electron is collected in the internal gate, this induces one additional hole (mirror charge) in the channel moving at the same velocity as the others. Accordingly, the transit time τ of a hole is:

Equation 5-5
$$\tau = \frac{L}{v_d}$$

The charge transconductance or charge gain g_q is defined as the number of holes, influenced by the electrons transiting from the source to the drain contact per second[13]:

Equation 5-6
$$g_q = \frac{1}{\tau} = \frac{\mu_p \cdot E}{L}$$

Note, g_q only depends on the channel carrier velocity and on the channel length.

At saturation voltage, the electric field can be approximated by:

Equation 5-7
$$E = \frac{V_{D,sat}}{L} = \frac{V_G - V_T}{L}$$

therefore, the internal gate gain can be expressed by:

Equation 5-8
$$g_q = \frac{\mu_p \cdot |V_G - V_T|}{L^2}$$

The internal gate’s collected signal charge Q_{sig} induces an equal charge with opposite sign in the neighboring conductors, depending on the respective capacitances as there are the source, the drain, the channel and the backside contact. Since the electrons in the internal gate are pushed towards the source electrode by the negative drain voltage, only a fraction f will be induced into the p-channel. Apart from the parasitic correction factor f, another factor $k = g(d_{ox})$ corrects for the coupling loss at the pinch-off region. The thicker d_{ox} the lower k!

Equation 5-9
$$g_{q_{corr}} = \frac{f \cdot k \cdot \mu_p \cdot |V_G - V_T|}{L^2}$$

For the drain current in the saturation regime a separated treatment of the classical MOS transistor current has to be made

Equation 5-10
$$I_{D,sat} = I_{offs} + I_{sig}$$

where I_{offs} is the transistor current with an empty internal gate and I_{sig} references the induced current by Q_{sig}.

[13] Note $g_q$is a frequency and only depends on the channel carrier velocity and the channel length.

Equation 5-11
$$I_{D,sat} = -\frac{W}{2L}\mu_p C_{ox}(V_G - V_T)^2 + g_{q_{corr}} \cdot Q_{sig}$$

The transconductance g_m of the external gate relates the change of the drain current I_D to the change of the gate voltage [116]:

Equation 5-12
$$g_{m,sat} = \frac{\partial I_{D,sat}}{\partial V_{D,sat}} = -\frac{W}{L}\mu_p C_{ox} V_{D,sat} = \sqrt{\frac{2W\mu_p C_{ox}}{L}}\sqrt{-I_{D,sat}}$$

Note the negative sign for I_D which is by convention positive when it flows into the drain: the drain current of a p-channel device runs into the opposite direction and increases with the gate voltage changed in negative direction. Furthermore, g_m is proportional to the square root of the gate width and inversely related to the gate length and the silicon oxide thickness.

Rearranging Equation 5-12, an expression for the drain voltage can be found:

Equation 5-13
$$V_{D,sat} = V_G - V_T = \sqrt{\frac{2L}{W\mu_p C_{ox}}}\sqrt{-I_{D,sat}}$$

Inserted in Equation 5-9 finally gives:

Equation 5-14
$$g_{q_{corr}} = f \cdot k \cdot \sqrt{\frac{2\mu_p}{WL^3 C_{ox}}}\sqrt{-I_{D,sat}}$$
$$g_{q_{corr}} \sim W^{-1/2}, L^{-3/2}$$

One efficient way to increase the charge amplification is to reduce the channel length L.

5.3 EDET Design Components

5.3.1 Sensor Layout and Operation Scheme

The DEPFET pixels for the EDET sensor are arranged in a $N \times M$-matrix structure (N rows and M columns). In addition to the large matrix devices, which will be used to furnish the focal plane arrays (FPAs), also small devices were produced, whose properties were investigated in the course of this thesis. For a small matrix, $N \times M = 128 \times 64$ (8,192 pixels), for the final sensor $N \times M = 512 \times 512$ (262,144 pixels) per one module (total of 4 modules).

Four physical matrix rows are combined together to form an electrical line which is controlled by a steering chip (Switcher) via two metal lines: one for the activation of the external pixel gates and one for the clearing of the accumulated charge. All pixels of an electrical row are switched on/off together and are collectively erased by a clear pulse (V_C^{on}) after the readout. This design speeds up the sensor readout by a factor of 4. In exchange, the number of necessary drain lines must be quadrupled compared to the physical matrix columns.

As shown in Figure 5-4, another metal layer is oriented in column direction and connects the pixel drain outputs to the input nodes of the readout chip (DCDE). As a result, the pixels in the same electrical column are read out sequentially, whereas pixels in the same electrical row are read out in parallel.

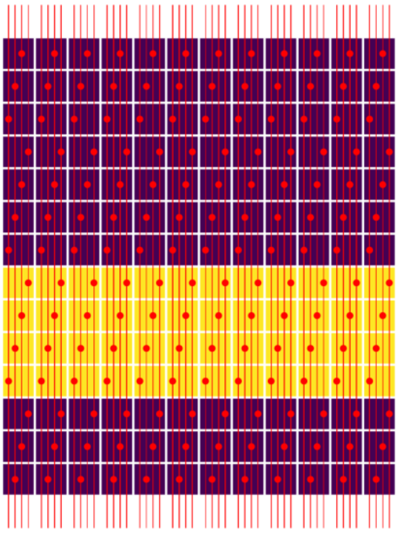

Figure 5-4: Segment of an EDET matrix. In physical view, a small matrix consists of 128 rows and 64 columns (electrical: 32 gate- and 256 drainlines). An active Switcher row/gate-line consists of 4 pixel rows (one electric row highlighted in yellow). Each pixel within an electric row needs its own drainline connection to avoid an accumulation of drain currents.

The procedure describes a variant of the rolling shutter mode: 4 pixel rows are switched on at once by a gate high pulse provided by the Switcher, as depicted in Figure 5-5.

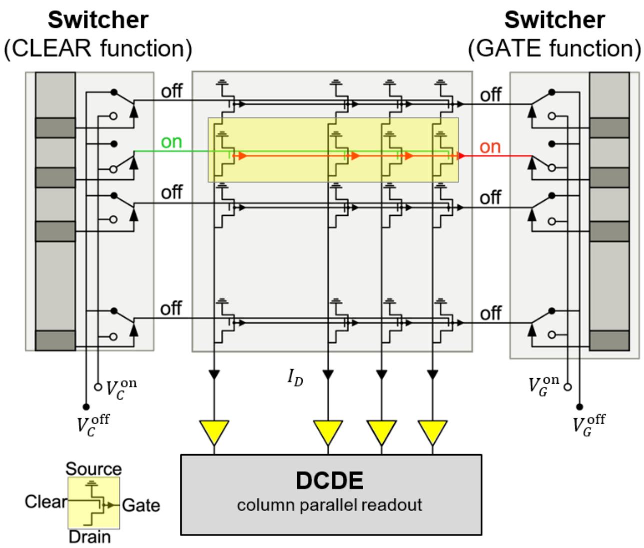

Figure 5-5: Schematics of a DEPFET sensor operated in the rolling shutter mode. The rows are activated sequentially by the Switcher chip. The drain currents are transmitted in parallel to the readout chip (DCDE) for further processing. Before switching to the next row (or set of rows) the clear pulse is applied (Note: gate and clear function are physically implemented into one chip).

All pixels of that row are read out in parallel, operating the collection-readout-clear cycle outlined above. Then, these four rows are switched off and the next four rows are turned on for readout until all rows of a matrix have been read out and the cycle starts again.

5.3.2 EDET Module & ASICS

A picture of a fully populated EDET All Silicon Module (ASM) dummy is shown in Figure 5-6.

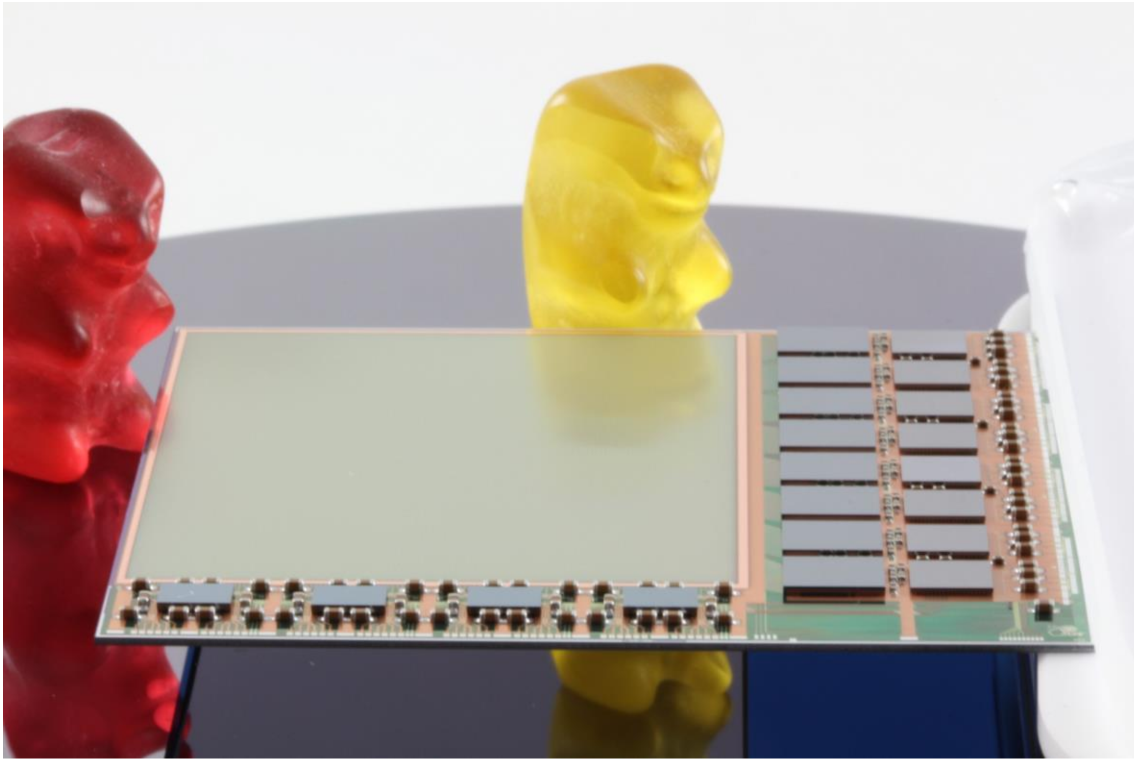

Figure 5-6: EDET ASM (external dimensions $48{,}865 \times 37{,}865\ \mu m^2$) with the smooth $3 \times 3\ cm^2$ sensor area and four Switcher chips mounted on the “balcony” of the module. At the so-called “end-of-stave” region, first a row of 8 DCDEs receives the drain currents, digitizes and transfers them to the 8 DMC/DHPs for the further readout. The gummi bears illustrate the actual size proportions.

The inner part of the module contains the sensitive pixel matrix surrounded by a thicker support frame, which grants mechanical stability to the module. The periphery is populated by 3 types of application-specific integrated circuits (ASICs):

5.3.2.1 Switcher

Four Switcher chips are placed on the balcony, the smaller insensitive region of the module and provide the row control (enabling of gates) and the clear mechanism [117, 118].

5.3.2.2 DCDE

8 Drain Current Digitizer chips for the EDET (DCDE) system receive the DEPFET transistor currents and digitize them by means of analog-to-digital-converters (ADC). Each

chip consists of 256 analog channels that are connected to the 256 matrix drainlines via bump bonding. The central component of each analog channel is the resistive current receiver depicted in Figure 5-7: a transimpedance amplifier converts the current input from the drainlines to a voltage, which is translated back into a current by the output resistor R_S for the following analog to digital conversion.

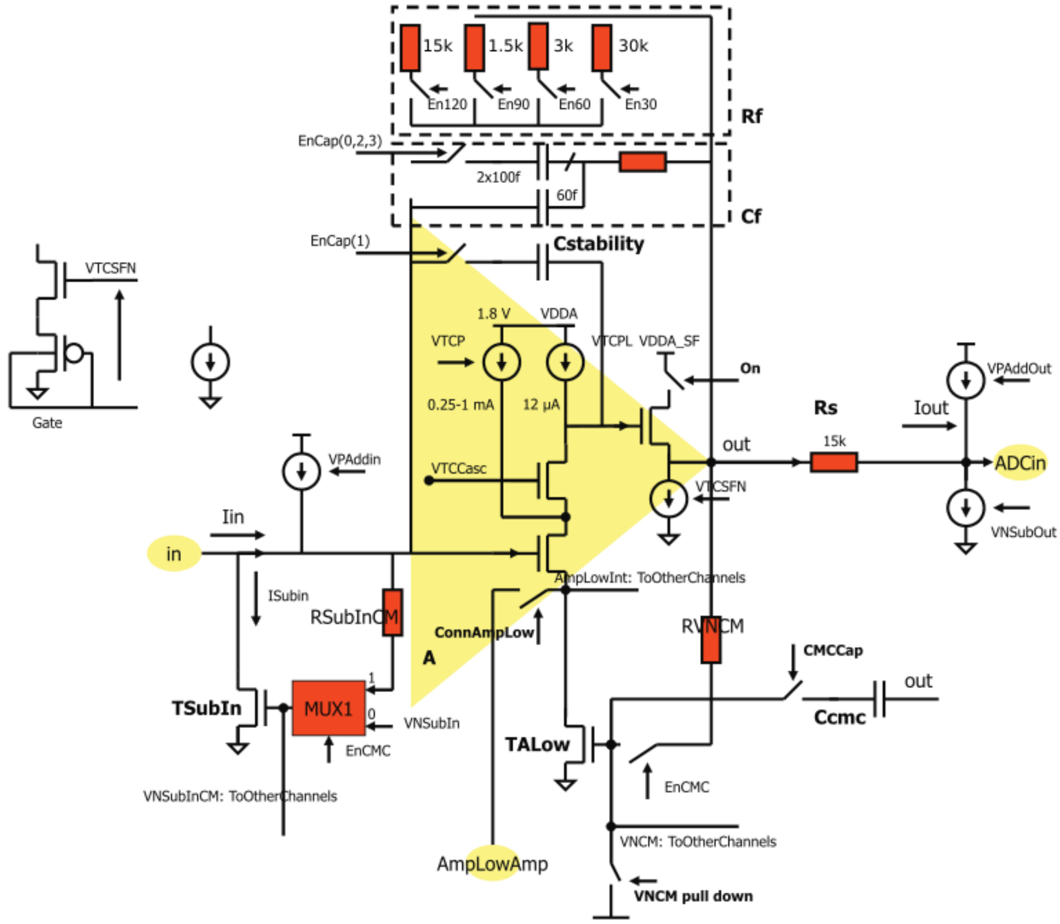

Figure 5-7: DCDE Receiver consisting of an input stage for the adjustment of the drain current (registers VpAddIn and VnSubIn) in order to align it with the DCDE’s dynamic range. The following transimpedance amplifier (TIA – yellow triangle) delivers a voltage which is converted into a current for digitization by the output resistor [119].

5.3.2.3 DHP/DMC

At maximum speed, the DCDE produces a data output of 2.56 GB/s. For the entire EDET system, consisting of 32 DCDE chips, the total data rate would add up to 81.9 GB/s, or 360 terabytes per hour of continuous acquisition. This poses a major challenge for the analysis and data storage. For an event based detector like BELLE’s PXD, a similar huge amount of data is met with another ASIC chip, the Data Handling Processor (DHP) [120] delivering some first order data reduction. The chip is able to filter out all pixels which do not experience a charge collection above a certain threshold. However, the EDET project primarily aims at the recording of scattering or shadow images, hence a full frame readout is necessary.[14] Additionally, it is not intended to operate the system on a continuing basis, but to record short biological processes of up to 1 ms with frame rates in the 80 KHz range.

Thus, it was clear from the beginning that BELLE`s DHP-T[15], which actually steers the readout process, could not be reused for the new requirements.[16] The planned Digital Movie Chip (DMC-T) is based on the DHP heritage and uses the same 65 nm technology. It should be able to capture and store up to 50 consecutive full frames in its buffer memory per burst, followed by a break for the transfer of the data to the peripheral electronics. The overall duty cycle (active time) is targeted to be at 10%.

The planned chip reuses a lot of features from its predecessor:

- Sequencing of the Switcher
- Controlling of the DCDE signals (DCDE clock, JTAG, synchronization, receiving the ADC data, sending the 2-bit DAC offset compression data)
- Providing a 1.6 Gbit interface for the data transfer to the DAQ backend

In addition, the DMC assumes a lot of new tasks:

- Controlling of the data storage process in the DMC memory
- Facilitation of various camera operation modes:
    - *Stop*: halting the readout in a specific row with the matrix current in the on-state
    - *Purge*: looping through the matrix without data acquisition in order to remove accumulated charge during the stop mode
    - *Idle/Run*: regular acquisition sequences (sampling – clear operation)
    - Variable burst lengths
    - *Masking*: skipping defective rows
    - *Windowing*: select arbitrary region of interest (ROI) sizes for speed up of the frame rates and reduction of the data volumes

5.3.3 Peripheral Components of the DAQ System

TEM detectors must be operated under vacuum conditions. Figure 5-8 shows a CAD view of the EDET camera composed of 4 modules, arranged in a cloverleaf-like geometry. To minimize backscattering of the TEM beam electrons, the module assembly is mounted on a polysilicon housing (“brick support” equipped with a water cooling) with slightly sloped walls, an extra vacuum cavity between the sensitive area and the detector backplane and an inside coating with a low atomic number material (e.g. Carbon) [121].

[14] Alternatively, the DHP can also deliver full data frames (“memdump”-mode) but at a much lower fps-rate.

[15] The „T“ denotes the TSMC 65 nm technology

[16] For lack of completion of the DMC, the DHP was used for all measurements in this thesis.

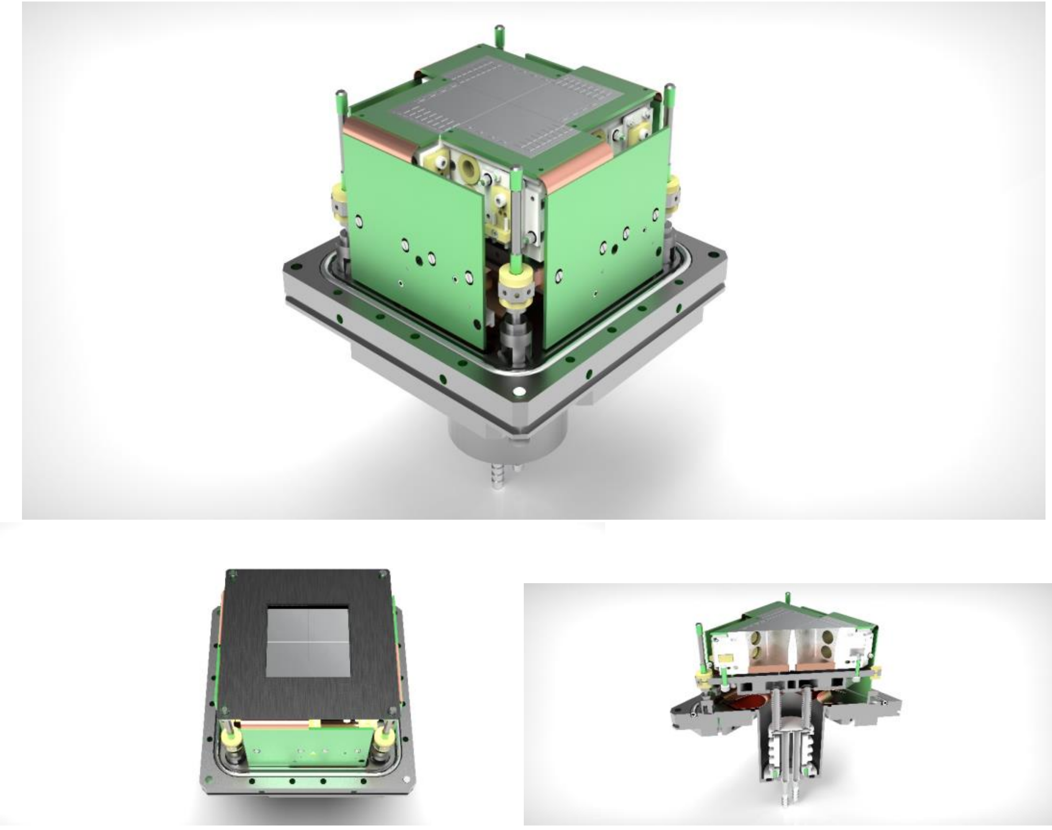

Figure 5-8: Top: CAD picture [122] of the EDET Detector with 4 ASMs (grey) on the top, connected to the Double-L Shaped Patch-Panels (green), all mounted on a silicon brick support. Bottom Left: Top view with a window-like 1 mm Titanium or Tantalum shield to protect the ASICs from radiation damage. The inner edges are inclined to minimize scattering effects and a 1 mm distance gap should avoid any mechanical damage. The shielding can be further improved by an additional low atomic layer (Aluminium) of 0.5 mm on top [121]. Bottom Right: Cross sectional view with slightly sloped walls.

Another component, which is commonly referred to as Double-L Shaped Patch-Panel (DLSP), delivers the supply voltages to the module and in turn receives the readout data. Both are routed via a vacuum signal- and voltage feedthrough (VIC – Vacuum InterConnect) to the outside power generating and data processing systems. A block schematic with the most relevant parts of an EDET module is presented in Figure 5-9.

The first piece of the outside detector system is the Module Interface Circuitry (MIC), compiled from the following three parts:

- MIC Power Module Stack (MPMS), consisting of the MIC Power Module (MPM) with the main service to generate the raw voltages for the DLSP from a single 12 V power input voltage and the MIC Housekeeping Module (MHM) which is realized as a so-called “piggy-back” (extra **PCB**). The latter assumes the functions of controlling and housekeeping.

- MIC Brain Module (MBM): the main tasks include the data reception, synchronization, buffering and transfer over an UDP framer. Furthermore, the **JTAG** configuration (see also APPENDIX A) master housekeeping and online monitoring functions are provided. It uses a Mercury+ XU1 FPGA board [123], which includes a high performance SoC device (XILINX ZYNQ).
- MIC Service Module (MSM): contains all interface connectors to the other modules (including VIC)

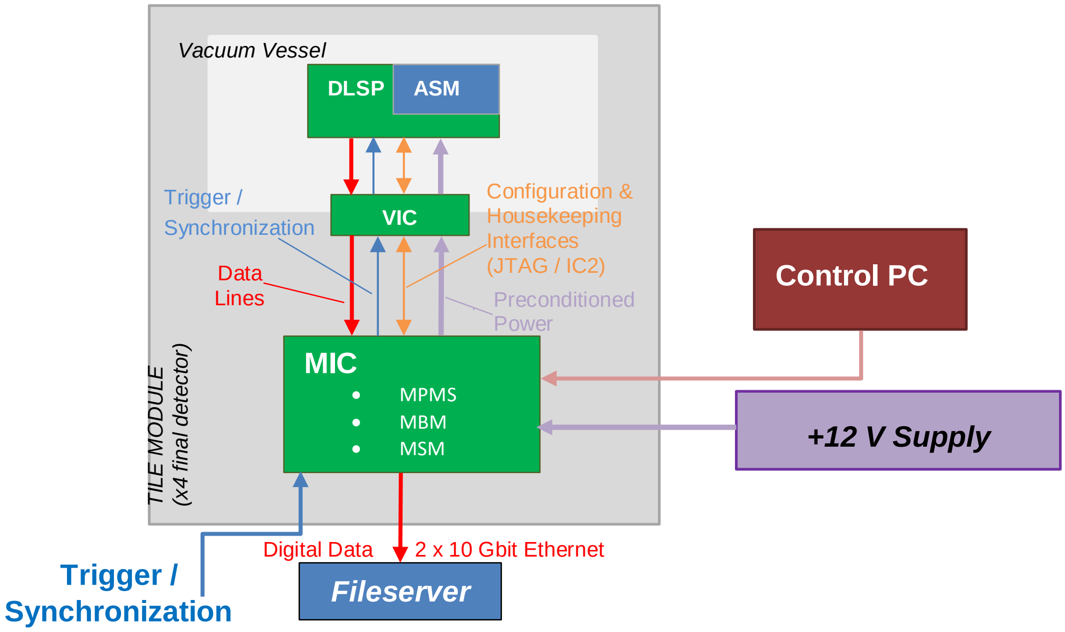

Figure 5-9: Block schematic of a complete EDET Module.

The UDP data stream from the MBM is transferred over 2 optical 10 GBit Ethernet connections to a dedicated fileserver for the data storage. The offline analysis compiles the data from the 4 fileservers and establishes the corresponding TEM movies.

6 EDET-Hybrid Board

6.1 Goal & Philosophy

For the development of an innovative, highly complex detector system a prudent strategy assumes a step-by-step approach rather than trying to launch a final design from close to scratch. As a starting point, a small EDET matrix was mounted on an existing Hybrid 5 test bench [124] from the BELLE II collaboration. Bit by bit, other components including the PCB itself, were replaced and tested until a functional prototype was accomplished.

By pursuing this stepwise approach, a lot of system design failures and debugging time were presumably saved. The small prototype setup, with all relevant building blocks of the final detector should guarantee enough flexibility for testing different scenarios and functionalities.

6.2 EDET Hybrid Board

The central part of the EDET test system is a PCB which houses a small sensor, all necessary ASICs, auxiliary parts (resistors, capacitors and inductors) and the needed power and data line connectors, as shown in Figure 6-1.

Figure 6-1: EDET Hybrid Board[1] (10 cm x 10 cm) with a small sensor of 128 x 64 pixels in the middle (flat grey surface 7.68 mm x 3.84 mm). North of it, one can find the Switcher chip, right to the matrix the DCDE and DHP. Various capacitors and resistors ensure stability for the different voltages. All supply voltages can be probed at the labeled access points. The board establishes its power connection by means of a 51 pole D-Sub-Micro-D Glenair connector at the left. The RJ45 connector provides the JTAG connectivity, whereas the ***Infiniband*** *connector at the bottom right is responsible for the data transfer.*

[1] Design by Christian Koffmane.

In contrast to the ASM, the ASICs are accessed indirectly by separate wirebond adapters onto which they are bump-bonded.

Apart from some necessary adjustments for a somewhat larger matrix, the new designed EDET Hybrid board entails two significant improvements compared to the original Hybrid 5 board: first, the $10 \times 10\ \mathrm{cm}^2$ quadratic structure provides more flexibility and better probing conditions. Second, different connectors (RJ45, Infiniband) allow the direct connection to the EDET system components, thereby eliminating an intermediary JTAG interface to the FPGA, which was hosted by another PCB.

6.3 Testing Procedures

To qualify the detector before operation, a comprehensive testing procedure was developed, which can be classified by three main areas:

- *Functional Tests*: in particular, powering and interconnect test checks. Some of the replaced components offer new functionalities which have to be investigated. The functional tests will be described in the next section.

- *Standard Optimization*: various optimization algorithms were developed to minimize interferences from the system components. These include, among other things, data transfer delay optimizations, DCDE settings optimization (ADC **transfer curves**) and the determination of the optimal sampling point. Some of the standard procedures are described in APPENDIX B.

- *System Optimization*: the interaction of several components determine the system response function. For an efficient detector, additional optimization routines are necessary, especially a single pixel calibration, the optimization of the charge collection function and the minimization of noise and other disturbing influences on the image recording. The implementation and outcome of these procedures as well as performance measures with respect to the image quality are the subject of the following two main chapters.

6.3.1 Functional Testing Procedures

6.3.1.1 Power Up Sequence

All EDET ASICs, especially the Switcher chips [125] are very sensitive to a correct biasing. For this reason, a strict power up sequence had to be implemented to prevent possible detector damages. Additionally, most voltages are sensed and protective current limits should avert any system breakdown. After powering, the currents and voltages should be observed within the right range, indicating the system is working correctly.

6.3.1.2 JTAG Chain

Once the different readout chips are fixed on the ASM via bump bonding, one might worry whether a physical pin correctly connects to another pin. While for a small matrix on a Hybrid board this “debugging” process can be performed (with some effort) by probing the pads of the wirebond adapters, for the ASM this approach is not feasible. Instead, the connectivity is checked via JTAG as described in APPENDIX A.

6.3.1.3 DCDE Gain Settings

The DCD[2] was originally designed for the BELLE II project. The BELLE II design specification foresaw a maximal **occupancy** of 1.5 % for the first layer of the pixel detector (PXD) [126]. This implies, that at maximum every 66th pixel of a readout frame gets a hit. For TEM images the situation is considerable different: the pixels situated within the projected specimen contours get less or no hits, while all other pixels expect the full intensity of up to 100 electrons per frame. Certainly, this induces a much higher drain current input to the DCD. As a consequence, the dynamic range of the DCD had to be increased significantly. This was achieved by both, a change of the dimensions and the number of feedback resistors R_f in the transimpedance amplifier (see Figure 5-7), as presented in Table 6-1.

	BELLE II	*EDET*
En30	26k	30k
En60	13k	3k
En90	19k	1.5k
En120		15k

Table 6-1: Comparison of the DCD feedback resistors for the BELLE II and the EDET project.

Each feedback resistor can be activated individually. The current gain is defined as $G \equiv R_f/R_s$. Since one can choose out of four different resistors, a total of 15 combinations is possible as listed in Table 6-2 (unchecking all resistors is not a reasonable option). The highest gain is always obtained by the exclusive activation of the highest feedback resistor, i.e. $30\text{k}/15\text{k} = 2.0$. To minimize the DCDE gain, all feedback resistors, which are arranged in parallel, must be switched on. The lowest gain can be calculated according to the parallel resistors equation as

$$\frac{1}{R_{f_{tot}}} = \frac{1}{30} + \frac{1}{3} + \frac{1}{1.5} + \frac{1}{15} = \frac{1}{1.1} \Rightarrow G = \frac{0.\overline{90}}{15} \approx 0.06$$

[2] DCDB/DCDE, the last letter refers to BELLE II or EDET respectively. DCD is used in a more general sense.

En30	En60	En90	En120	Gain	Gain Factor
1	1	1	1	0.06	1.00
0	1	1	1	0.06	1.03
1	1	1	0	0.06	1.06
0	1	1	0	0.07	1.10
1	0	1	1	0.09	1.43
0	0	1	1	0.09	1.50
1	0	1	0	0.10	1.57
0	0	1	0	0.10	1.65
1	1	0	1	0.15	2.54
0	1	0	1	0.17	2.75
1	1	0	0	0.18	3.00
0	1	0	0	0.20	3.30
1	0	0	1	0.67	11.00
0	0	0	1	1.00	16.50
1	0	0	0	2.00	33.00

Table 6-2: Calculated DCDE current gains from the possible DCDE feedback resistor combinations. The gain factor is determined by dividing the actual gain by the lowest gain. One notices a significant gap in the possible gain settings between gain 11.0 and gain 3.3.

In comparison, the lowest possible DCDB gain would be:

$$\frac{1}{R_{ftot}} = \frac{1}{26} + \frac{1}{13} + \frac{1}{19} = 0.168 \Rightarrow G_B = \frac{5.95}{15} \approx 0.4$$

corresponding to a gain factor of 6.55.

The next step investigated the actual dynamic ranges of the DCDE. The DCDE possesses, inter alia, a calibration circuit which can be configured to allow for a channel-wise injection of an external calibration current. The external current source was independently measured by an SMU and provides a total range of about 248.0 µA. It is gradual adjustable, by highly granular **DAC** steps ($1\,\mathrm{DAC}{\sim}3.82\,\mathrm{nA}$) up to a maximum of 65,000 steps. Both, the external source current and its digitized output show some volatility. Therefore, after choosing a specific DCDE channel, each injected current value was measured 256 times (arbitrarily chosen) and eventually the median value of this array was determined. Figure 6-2 shows a section of the external source input which was increased by intervals of five DAC steps and the corresponding histogramed ADU numbers. The red line indicates the median values.

Since the DCDE measures the drain currents with an 8-bit precision, the digitized ADU output would jump, when the input current approaches the edge of the next ADU value. As an example, with respect to the DCDE 3.3 gain setting one can infer an additional current injection of 0.67 µA per ADU from Table 6-3. This corresponds to about 175 input DAC steps. Since there are no intermediary values, the ADU output would show no change until the input current was increased high enough that the majority of the 256 measurements focuses around the next ADU step. This behavior is also called the quantization error. The resulting curve should ideally resemble an equal sized step function with monotonic increasing 255 steps. However, in reality a toggling of the median values was observed, especially at the edges. Furthermore, the step widths are occasionally irregular and sometimes it is even possible that some ADU values are simply omitted. The latter observation is also referred to as a missing code and will be treated together with other ADC errors like integral non-linearity (INL) and differential non-linearity (DNL) in APPENDIX B of this thesis.

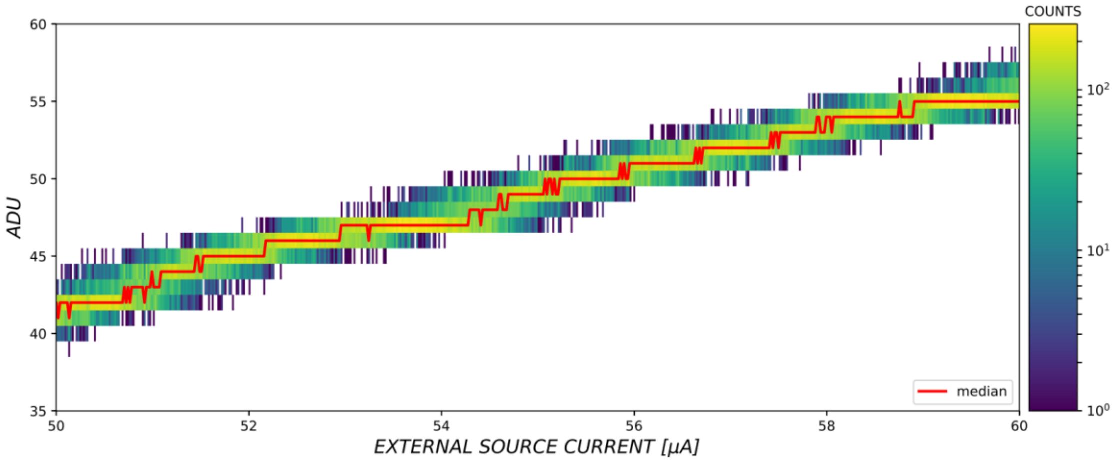

Figure 6-2: Selection of ADC raw values and their median.

Figure 6-3 depicts a selection of different ADC transfer curves for different gain settings. The curves are truncated at 30 and 230 ADU respectively in order to represent exact 200 ADU and to exclude non-linear effects at the start and at the end of the transfer curve.

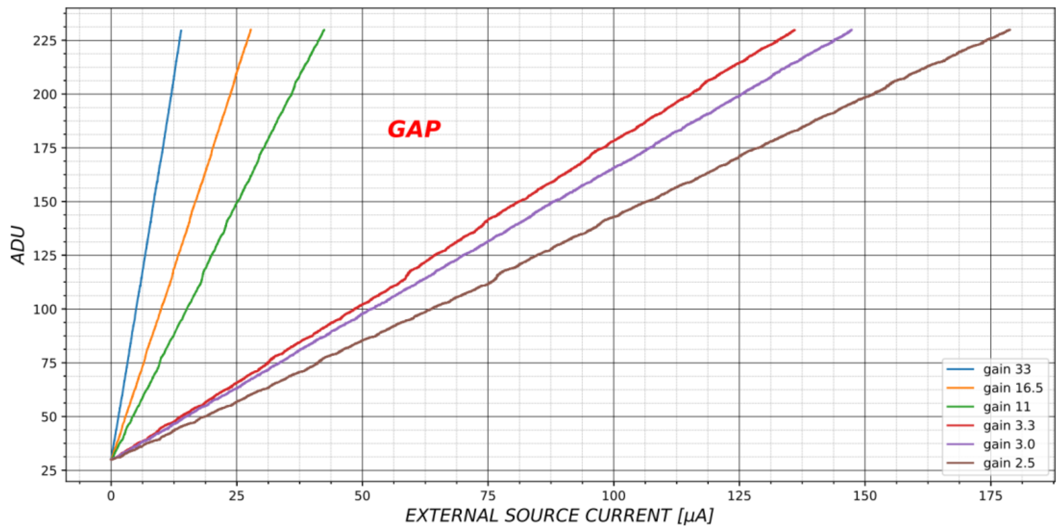

Figure 6-3: ADC Transfer Curves for different DCDE gain settings. Transfer curves for lower gain settings were not recorded, since the external current source was not strong enough (apart from that, these settings will be hardly needed, since they exceed even the dynamic range of an EDET pixel).

The subsequent Table 6-3 expresses the dynamic ranges in current units as well as the value of one ADU and its reciprocal value. Additionally, the calculated and measured gain values are compared. For the measured gain, the highest gain is used as the basic gain number and the others are simply determined by multiplying this number with the ratio of the highest gain range current and the specific range current.

Calculated Gain	***ADU/µA***	***µA/ADU***	***Dynamic Range 200 ADU [µA]***	***Measured Gain***
33.0	14.29	0.07	14.0	33.0
16.5	7.23	0.14	27.8	16.6
11.0	4.78	0.21	42.4	10.9
3.3	1.49	0.67	136.0	3.4
3.0	1.36	0.74	147.4	3.1
2.54	1.13	0.91	178.9	2.58

Table 6-3: Summary of different gain settings. The high gain setting reacts quite strongly on small signal variations and is able to detect very weak signals. Nonetheless, the more electrons hit a pixel at the same time, the signal output would quickly exceed the high gain dynamic range, so lower gain settings are necessary.

To better understand the problem associated with the gap, consider how the individual pixel currents are represented by the DCDE if there was no charge injection (pure drain current only). Figure 6-4 depicts the offset distributions for the DCDE gains 11.0 and 3.3 expressed in ADU. The origins for the distribution widths can be partly attributed to process variations during the manufacturing of the matrix and partly to DCDE contributions.

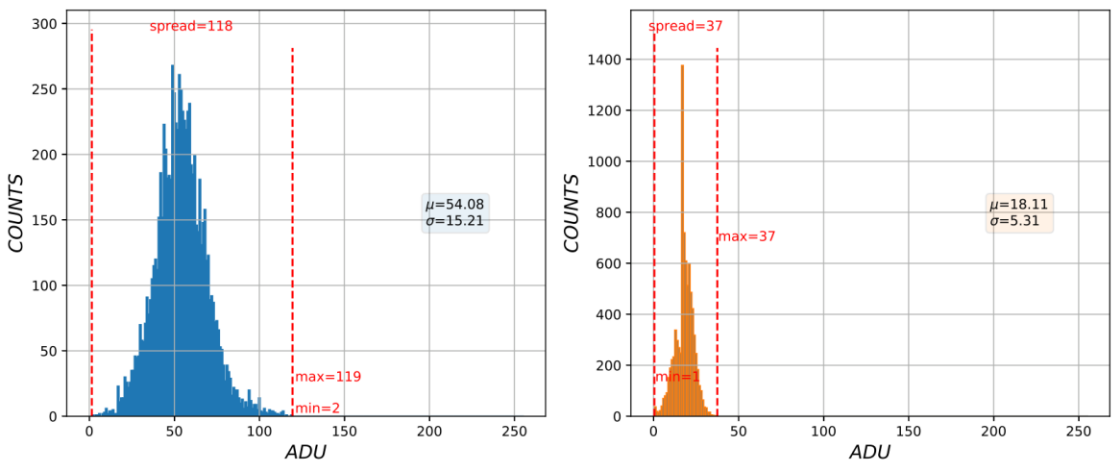

Figure 6-4: Offset variations for different DCDE gains 11.0 (left) and 3.3 (right). The spread of 118 ADU (37 ADU for the 3.3 DCDE gain setting) translates to a total current variation of about 25 µA.

From Equation 5-11 one notes that $I_D \sim W/L$ ($W \gg L$). The shorter the gate length, the larger the effect of length variations caused by over- and under-etchings. Internal investigations[3] reveal a gate length dispersion of about 4.4% (3 standard deviations) for the shortest gate length. Moreover, the drain current is also influenced by $V_G - V_T$, V_T itself dependent on the difference between the two deep n- and p-implants.[4] A variation of 0.5% for each implanter dose would cause an error of

$$\Delta Q/A = \sqrt{0.5^2 + 0.5^2} \times 10^{10} e^-/\mathrm{cm}^2$$

subject to nominal doses of about each $1 \times 10^{12} e^-/\mathrm{cm}^2$ (applying Gaussian error propagation). Using the equation for a parallel-plate capacitor ($C = \varepsilon_0 \varepsilon_r A/d$):

Equation 6-1
$$\Delta U = \frac{\Delta Q}{C} = \frac{\Delta Q \cdot d \cdot e^-}{\varepsilon_0 \varepsilon_r \cdot A}$$

where $e^- = 1.602 \times 10^{-19}$ C, $\varepsilon_0 \varepsilon_r \approx 3.453 \times 10^{-13}$ F/cm for silicon dioxide. Assuming a silicon dioxide thickness of $d \approx 10^{-5}$ cm (100 nm), the corresponding change in the threshold voltage can be calculated at about 0.033 V. Since only the relative changes are relevant, the quadratic term in Equation 5-11 can be simplified to

Equation 6-2
$$I_{D,sat} \sim \frac{\left[(V_{D,sat} + \Delta U)^2 - (V_{D,sat} - \Delta U)^2\right]}{V_{D,sat}} = 400 \times \Delta U\ \%$$

or 13.2%. Adjusting the gate voltage to provide a drain current of $I_{D,sat} = 100\ \mu\mathrm{A}$, the resulting basic drain current fluctuations would amount to about 13.2 µA.

Process variations also occur in the DCDE, hence the final offset distribution can be affected by the selected DCDE settings. A histogram of the transfer curve slopes (described in APPENDIX B.2), determined for each individual DCDE channel is shown in Figure 6-5.

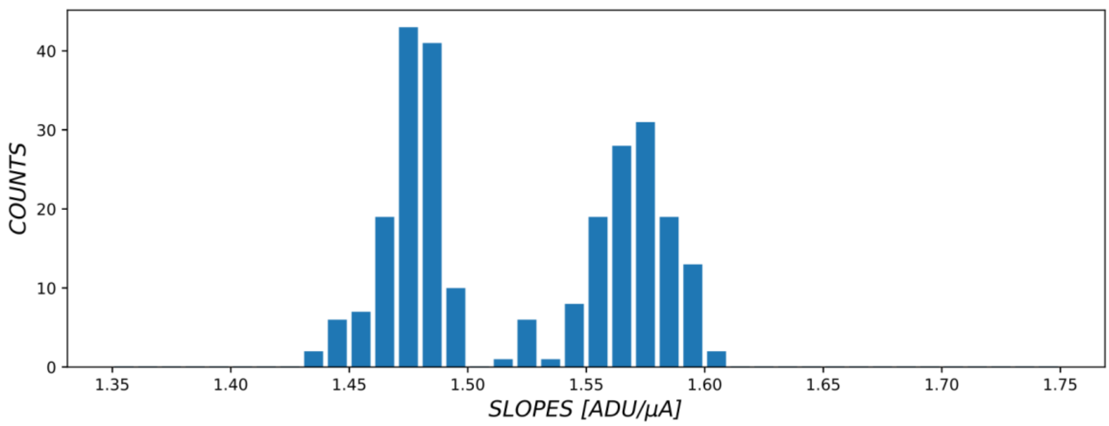

Figure 6-5: Distribution of the transfer curve slopes of all 256 channels of a specific DCDE setting. This distribution on its own would contribute about 10% to the offset variation.

[3] Conversation with Florian Schopper.

[4] From internal measurements the mean for V_T can be located at around -0.24 V.

As shown in Figure 6-4, the actual offset spread of a specific matrix was measured at 37 ADU using a gain of 3.3. On the other hand, for a gain of 11.0 the distribution expands to 118 ADU, so for the highest pixel currents there are only 137 ADU “left” for the signal charge $(255 - 118 = 137)$.

If one reverts back once more to Figure 5-1, the key problem can be clearly understood: 200,000 electrons in the internal gate would produce an extra signal current of over 30 µA. Since 137 ADU correspond to just 29 µA (using the numbers from Table 6-3) in relation to the 11.0 DCDE gain setting, for some pixels the true charge can no longer be mapped to a correct ADU value, rather these would exceed the dynamic range. By contrast, the same charge would only create an extra charge of 45 ADU for the 3.3 gain setting and the maximum raw signal value would amount to just 82 ADU.

Every additional injected charge would be collected in the OF-region with an amplification by a factor of 3 to 4 lower. 800,000 electrons more would produce an extra drain current of maximal 40 µA for the 3.3 gain setting, corresponding to another 60 ADU. While for the higher gain setting, the dynamic range limits for all pixels would have been long ago surpassed, the maximum raw ADU value in the lower gain setting would not exceed 150 ADU. Effectively, the full dynamic range would not be utilized and thus, some contrast information would not get fully exploited.

However, the DCDE includes also an offset compression mechanism which will be explained in APPENDIX B.4. This instrument accomplishes a narrower offset distribution by adding additional currents (0, 1, 2, 3 times a certain basis current and multiples of the basis current) to each pixel individually and by deducting a global current to bring all pixels back into the dynamic range. Unfortunately, the strength of the base current was designed comparably high in the DCDE, so the maximum achievable offset compression reaches only about half to two thirds of the original distribution (ideally, the width of the distribution would shrink to one quarter).

Alternatively, the original DCDB could be also tested since it offers at least one attractive setting in the gap region as one can extract from Table 6-4.

En30	*En60*	*En90*	*Gain*	*Gain Factor*
1	1	1	0.40	6.55
0	1	1	0.51	8.49
1	0	1	0.73	12.08
1	1	0	0.58	9.53
0	0	1	1.27	20.90
0	1	0	0.87	14.30
1	0	0	1.73	28.60

Table 6-4: Calculated DCDB current Gains from the possible DCDB feedback resistor combinations. Especially the gain factor 6.55 offers a potential alternative to the DCDE.

6.3.2 Standard Optimization Procedures

The standard optimization procedures are described in more detail in APPENDIX B:

- The transmitted bit-streams between DCDE and DHP experience some small delays which have to be corrected by suitable delay settings.
- To minimize noise inputs from the DCDE, the bias settings for the input and digitization stages are swept in order to get an optimized ADC transfer curve.
- The sampling point analysis determines the optimal sampling point, at least to avoid the sampling procedure during the clear operation.
- The 2-bit DAC offset compression decreases the width of the offset distribution.

7 Calibration

7.1 Overview

The basic goal of any detector calibration is scalability, i.e. making the output of each pixel comparable. Ideally, after interposing a specific calibration algorithm, each pixel reacts in an equal way, if exposed to an equal external stimulus.

Variations from the manufacturing process lead to variations of the pixel response functions. The pixel-to-pixel gain differences are typical for all detectors [127] and can be referred to as gain dispersion. For the EDET sensor, the intended signal compression (non-linearity of the response curve) introduces a further degree of complexity, since the pixel's internal gate region shows a much higher amplification than its overflow region. In the absence of this feature, the pixel gains could be much easier calibrated with monochromatic radiation (e.g. from a synchrotron or free electron laser). A further challenge is related to a quantitative issue: the full DH80k FPA comprises over 1 million pixels, which have to be calibrated individually. Various methods appear applicable, but as each of which has its advantages and disadvantages, a short brainstorming should be applied. There is no "silver bullet" rather a combination of methods fulfilling the objective.

Table 7-1 summarizes several options together with comments about their applicability:

INSTRUMENT/METHOD	***EXAMPLE***	***PROS***	***CONS***
X-ray (low energy): X-ray tubes or radioactive sources	^{109}Cd 22/25 keV	delivers exact, characteristic energy levels for an absolute calibration acceptable photon interaction probability capability to calibrate all pixels at once auxiliary tool for cross-calibration of other methods	radiation damage can only calibrate one point on the pixel's charge curve at a comparably low level complex spectra (could be mitigated by monochromators)
X-ray (high energy)	beyond 100 keV	scalable intensity device depending flat field	very low photoabsorption probability dominated by the Compton effect accessibility (synchrotron radiation sources)
β^--emitter	$Sr^{90}\ \beta^-_{avg} = 196\ keV$	similarity to a TEM beam no vacuum apparatus necessary	radiation damage continuous spectrum most of the electrons would leave the detector, so the escape energy has to be measured (scintillator)

α-emitter	Am^{241} 5.486 MeV (encapsulated also usable as 60keV γ-source usable) Gd^{148} 3.184 MeV		severe radiation damage energy level too high vacuum device and corresponding interconnection hardware necessary
SEM/TEM		gradual increase of both, intensity (in 10eV steps up to 300keV) and quantity (focusing/defocusing) → build complete charge curves	vacuum device and corresponding interconnection hardware necessary Poisson noise (shot noise) due to fluctuations of emitted TEM electrons → precise intensity measurements necessary
Laser		no radiation damage intensity controllable via applied voltage and/or time (pulse width & frequency) full control of individual pixels	total energy transfer unknown (quantum efficiency) only cell-by-cell calibration lack of absolute calibration
Light Emitting Diode (LED)		no radiation damage controllable intensity (by frequency or LED current) simultaneous calibration of all pixels possible	total energy transfer unknown (quantum efficiency) lack of absolute calibration
CLEAR backemission	uses variation of integration time	simultaneous calibration of all pixels	level of original backemission not known finding optimal operation point for all pixels (process variations)

Table 7-1: Sensor Calibration – Overview of some possible instruments

Since the main application area for the EDET sensor will be a TEM, one would naturally consider a collection of β^--emitters for the calibration process. Indeed, some vendors offer specific sets of nuclides, consisting of e.g. C^{14}, Tc^{99}, Cl^{36}, Pb^{210}, Pm^{147} and Sr^{90} covering an energy range from 156 to 2282 keV [128]. However, there are several problems associated with this approach: first of all, beta decays generate a continuous spectrum which complicates the identification of the correct peak level. Second, already at an energy level of 156 keV most electrons would traverse the 30 µm or 50 µm thick silicon sensor without depositing their total energy. Accordingly, one would have to measure the escape energy of the electrons leaving the detector in order to determine the absorbed energy. Finally, at an energy of about 2.1 MeV ($\beta\gamma \approx 4$), the ionization level reaches a minimum, which implies the creation of only a few thousand electrons.[1]

[1] Delta electrons with an energy deposition exceeding hundreds of keV are produced rarely.

α-sources on the other hand leave all their energy within the sensor but at a cost: the calibration operation can only be done under vacuum conditions, therefore a vacuum device and a corresponding interconnection hardware are indispensable. Furthermore, and much severe, the radiation damage produced by α-particles would severely affect the detector performance within a short time.[2]

An interesting idea focuses on a particular sensor feature for self-calibration: as described in chapter 8.4, a high voltage applied to the clear contact removes the electron charge from the internal gate and the overflow region. This is necessary to facilitate a continuous detector operation and to implement equal operating conditions at the beginning of each integration cycle. If the clear voltage is lowered below a certain level, the respective electron flow turns to the opposite direction. Depending on a variable integration time both, the internal gate and the overflow region would fill up successively. This appealing approach has two significant shortcomings: first, the level of the original backemission is not known quantitatively, so cross-calibration would be needed. Second, the operation window is very narrow and an optimal operation point for all pixels is hard to find, as due to process variations, all pixels exhibit slightly different backemission characteristics.

The BELLE II collaboration employed a ^{109}Cd source as the workhorse for an absolute pixel calibration. The characteristic energy lines are precisely known and the internal gate capacity of about 40,000 electrons well absorbed the generation of an average of 6,000 electrons per hit, sufficiently over the detector's noise threshold and substantially below the internal gate limit. However, for the larger internal gate capacity and the extended overflow region of the EDET sensor one needs at least 4 anchor points[3] to build up an approximate charge curve (see section 7.3.2). For the IG region one can use a variable X-ray source with exit windows [129], e.g. made of Rb^{37} ($K_\alpha = 13.4\ \mathrm{keV}$), Mo^{42} ($K_\alpha = 13.39\ \mathrm{keV}$), Cd^{48} ($K_\alpha = 23\ \mathrm{keV}$), Ba^{56} ($K_\alpha = 32.2\ \mathrm{keV}$) and Tb^{65} ($K_\alpha = 44.5\ \mathrm{keV}$).

At first glance, for the OF region X-ray sources with higher energies seem a quite logical alternative. However, several other practical problems appear: first, the relevant photoelectric absorption decreases substantially with higher energy. As an example, while for a 20 keV photon in silicon the photoelectric absorption coefficient is $4.089\ cm^2/g$ [130], the coefficient decreases to just $0.0068\ cm^2/g$ for 150 keV photons.[4] The reason for this sharp decline is two-fold: on the one hand, the total attenuation coefficient in general decreases until reaching a minimum level at around 2 MeV for silicon. Additionally, for photons above an energy level of 60 keV, the Compton effect starts to dominate the attenuation process.

---

[2] Alpha sources are exemplarily used for the calibration of solid state alpha spectrometers, for applications in environmental monitoring and research.

[3] Assuming no offset for the zero charge injection, the internal gate region would theoretically need just one fixed point. Nevertheless, in order to catch also potential slope changes two points are more accurate.

[4] With regards to X-rays or energetic electrons, this thesis uses the NIST XCOM or NIST ESTAR data base. Attenuation coefficients or stopping powers can be directly read off from the respective web page or linearly interpolated between two data points [87, 242].

As indicated above, the exponential attenuation law (Equation 4-1) relates the attenuation of photons to the properties of the substance the photons are penetrating. With respect to a 50 µm thick silicon sensor about 4.65% of all 20 keV photons would produce a signal. By contrast, for 80 keV photons the photoabsorption probability reduces significantly to just about 0.06%. In effect, this would rise the total integration time by a factor of 78 in order to collect the same pixel statistics (assuming a similar source intensity). Another (soft) issue of this method concerns the availability of suitable energy sources (synchrotron radiation sources).

Compared to the approaches presented so far a pulse controllable laser offers a lot of advantages: as will be shown later, provided convenient optics, spot diameters under 10 µm can be focused, well below the EDET pixel dimension of $60 \times 60\ \mu m$. The beam intensity is controllable via the applied amplitude and time (frequency and/or pulse width). By this means, it is possible to establish high granularity charge curves for every pixel, covering the whole dynamic range. The Titanium shield on the front side of the sensor forces to illuminate to the back side. Since the entrance window on the back side contains a 3 µm p-layer, one has to use longer laser wave lengths (red to infrared region). Otherwise, especially when using photons in the UV-region, most of the generated electron/hole-pairs recombine in the p-layer and almost no charge would be registered.[5]

On the negative side, two issues have to be addressed: first, the quantum efficiency of the laser pulses is unknown. Fortunately, this can be cross-calibrated in combination with a ^{109}Cd source: for this purpose, a single laser pulse is adjusted to the mean energy of the radioactive source. At the next step, the pulse frequency is increased by integer steps (keeping all other parameters of the laser pulse constant). This guarantees, that an integer multiple of the pulse charge is injected into the respective pixel.

The second deficiency of the laser approach is a more practical limitation: operational speed. Although, some techniques have been conceived to increase the efficiency of the laser calibration process, the proposed method, after all, remains a cell-by-cell calibration. The sheer size of the whole detector with over 1 million pixels requires extraordinary long measurement times, even if other issues like perfect alignment (i.e. the laser position is always moved to the center of the next pixel) are solved, which makes this approach impractical.

A potential solution to this dilemma could be the use of a laser in combination with a so-called “top-hat” lens, which aims at a homogeneous illumination of a larger area with more or less constant intensity, i.e. partial “flat-field” illumination.

Anyway, a much more efficient instrument with respect to large pixel arrays is the operation of a high power light emitting diode (LED). Under certain conditions, one generates a sufficiently diffuse light source approximating very closely a perfect flat-field.

[5] For a red photon with a wavelength of 635 nm and an energy of 1.95 eV, the required silicon layer to get a 99% absorption is about 13 µm. A green photon with 530 nm wavelength reaches just about 4.5 µm for the same criterion.

Nevertheless, the laser remains an invaluable tool for the analysis of the single pixel charge collection, whereas the LED serves as the method of choice for the calibration of large sensor areas.

Similarly to a LED, a TEM beam can be used for the detector calibration. However, several obstacles need to be overcome: as a prerequisite, the electron intensities must be adjustable, e.g. by changing the duty cycle with help of an electronic shutter. Since the beam operates in vacuum, a corresponding interconnection hardware has to be manufactured. Furthermore, the TEM beam needs to be sufficiently defocused to get a homogeneous radiation. A more practical issue concerns the non-availability of a TEM at HLL. Finally, one should be aware, that every electron irradiation leads to some radiation damage.

To sum up, TEM calibration is only possible, if the respective device is physically available. Lasers are very useful for in-pixel studies, but not for large area calibrations. The most promising approach for the large sensor uses the combination of a LED illumination and an X-ray source for the cross-calibration.

One general comment: the following measurements were carried out on different hybrid boards with different matrices. This had no impact on the observed characteristics and general validity of the results.

7.2 X-Ray Source

7.2.1 Source Characteristics

X-ray sources deliver discrete energy spectra, which allow to determine an absolute anchor point for the cross-calibration of other calibration instruments. The ^{109}Cd source turns out to be well suited for the basic calibration task of the EDET sensor. The amount of photon emissions per 100 decays is presented in Table 7-2:

Type/Shell ***(^{109}Ag)***	***Energy*** ***(keV)***	***Photons*** ***(per 100 decays)***
XL	2.634 – 3.748	10.37
XK_{α_2}	21.9906	
XK_{α_1}	22.16317	84.31
XK_{β_3}	24.9118	
XK_{β_1}	24.9427	
$XK_{\beta_5''}$	25.146	
XK_{β_2}	25.4567	
XK_{β_4}	25.512	17.9
$\gamma_{1,0}$	88.0336	3.66
SUM		**116.24**

Table 7-2: Photon Emissions induced by ^{109}Cd decay [131]. The dominating spectral line occurs at around 22 keV. Note, that the X-ray production is higher that the decay rate.

^{109}Cd decays by **electron capture** to the isomeric state (88 keV) of ^{109}Ag [131]. The de-excitation from this state predominantly happens through emission of gamma rays (3.66% @ 88.03 keV), conversion electrons, Auger electrons and X-rays.

At room temperature, the average energy to produce an electron-hole pair in silicon averages about 3.6 eV which is more than three times higher than the impact ionization (band gap of 1.12 eV). The difference can be allocated to acoustic and optical phonon emissions [132]. Thus, if the energy of an incident 22 keV photon is divided by the average electron-hole pair creation energy, about $6{,}111\ e^-$ are generated. The detector converts this analog signal (i.e. generated electrons) into digital detector units (ADU).

7.2.2 System Preparation

To avoid unnecessary radiation damage to the sensor, a qualitative assessment of the expected radiation was made: according to the terms of the "Nominal Source Certificate" provided by the vendor (Eckert & Ziegler, US-CA), the ^{109}Cd nuclide has a half-life of $462.6\ \pm 0.7$ days. The disk-shaped source with a diameter of 6.35 mm consists of a thin deposit of the active material, electroplated on a 0.127 mm silver substrate. This design reduces self-absorption significantly. The disk is embedded in a stainless steel capsule as depicted in Figure D - 1, with a tungsten plug to the top side. A 1 mm thick beryllium layer, sealed into the window opening, prevents conversion or Auger electrons from escape. The source's measured activity for the reference date (Oct 2019) was specified at 740 MBq or $7.4 \cdot 10^8$ decays. The ^{109}Cd capsule is enclosed in a massive tungsten cover hut, screwed together with a cover body and a collimator pipe opening. The distance between the source and the collimator opening was measured at 7.1 mm.

The intensity declines according to the inverse-square law $1/z^2$, where z denotes the distance to the source.[6] It can be shown, that the doses of a point and a disk source are within 1%, if the distance is at least three times[7] the largest source dimension [133].[8] The radiation intensity per pixel at a distance[9] of 10 mm can be calculated on the assumption, that the source activity is equally distributed on a sphere with a radius of 10 mm.[10] The area of the sphere can be set in relation to the area of an EDET pixel:

$$\frac{A_{sphere}}{A_{pixel}} = \frac{4 \cdot 10{,}000^2 \pi\ \mu m^2}{60 \cdot 60\ \mu m^2} \approx 349{,}000$$

6 Treating the source as a point source.

7 In this specific case, the diameter of the collimator of 4.3 mm defines the relevant disk diameter, so a total distance of 13 mm would be sufficient.

8 For the gain calibration it is not essential to obtain a point source (in contrast to the later modulation transfer function – MTF measurements, see chapter 8.2). The closer one can get to the sensor, the more hits are recorded, the shorter the sensor is exposed to radiation damage.

9 The PCB indentation was measured at 2 mm, the source–collimator distance is 7.1 mm, so the closest possible distance is around 10 mm.

10 Effectively, only X-rays passing the collimator pipe deliver a noteworthy contribution.

Furthermore, the photon absorption coefficient for a 22 keV photon in silicon is $3.05\ cm^2/g$ and the resulting interaction probability yields 3.49%. Including decay X-ray emissions from Table 7-2, one can expect for sensor pixels within the collimator area

$$7.4 \cdot 10^8 \cdot \frac{0.0349}{349{,}000} \cdot \frac{84.31}{100} \approx 62 \frac{hits}{pixel}/s$$

@ 22 keV photons.

The revolving frame time[11] at the (currently implemented) lowest possible DCDE readout frequency for a small EDET matrix device takes 4.096 µs, corresponding to 244,140 frames per second (fps). Accordingly, at the time of writing, the implemented readout speed of about 9,500 fps missed over 96% of all frames. Since only this small fraction of data can be extracted, the average waiting time increases to approximately 0.4 seconds until a pixel records a hit.[12] To get reasonable statistics beyond 1,000 hits per pixel the average recording time of 400 seconds should be no issue, but the low frame readout yield implies, that the detector has to be substantially longer exposed to radiation as intended.

There are some approaches to minimize radiation exposure: first, the still used DHPT offers an option to use the zero suppression mode[13], which only delivers hit data (sensor hit occupancy for continuous acquisition is constricted to 3% [134]). However, this mechanism is not foreseen for the final DMC and also not applicable for TEM scattering images. Alternatively, the actual frame read out rate can be increased to the full DHPT data transfer capacity which restricts the absolute readout speed for the large matrix to somewhat lower than 5,000 fps (or close to 20,000 for the small matrix).[14] Limitations in integration time due to the BELLE readout system[15] can be overcome by a nice trick: the DHPT, which among other things also steers the Switcher, does not know the size of the connected matrix. The memory space theoretically allows for the programming of a total of 8 daisy-chained Switchers. If the sequence is adapted for a maximum size sensor, the signal for a new frame (*SerIn*) will only be sent after all real and virtual electrical lines

[11] Continuous operation procedure: after the readout and clear operation for the last row, the Switcher immediately enables the first row for readout (rolling shutter mode).

[12] Charge sharing between pixels (clusters) were neglected.

[13] Zero suppression only delivers pure event data above a prefixed threshold. The information contains 4 values: the pixel address (row/column), the ADU value and the common mode correction. Anything else, especially data from empty pixels gets omitted.

[14] Theoretically, zero suppression allows for the recording of every consecutive frame (in case of a large module up to 80,000 frames), while for the full data readout a maximum of only 4,882 frames is achievable: the data transfer link provides a data rate of 1.6 Gbit/s, after the 8b/10b encoding an effective data rate of 1.28 Gbit/s (=160 Mbyte/s) can be achieved. The DHPT section of a large module contains 128 x 256 = 32,768 pixels (32,768 byte) → 204.8 µs per frame (a factor of 4 lower for the small matrix). The DHPT storage capacity is even more limited: the current DHPT memory depth consists of 16 SRAM blocks, 1024 address values with a depth of 128 bits (corresponding to 16 ADC pixel values). 512 address values are reserved for the raw data, equivalent to 512 Switcher gates on a hypothetical matrix with a dimension of 2048 x 64 pixels (512 gates, 256 drainlines). An EDET module contains 4 Switchers consisting of a total of 128 gates, so altogether just 4 consecutive EDET frames can be stored.

[15] At the time of writing, the new DMC chip was not available.

have been activated. Correspondingly, the total integration time can be increased by a factor of 8. As we know, there is no remedy without side effects: one electrical Switcher line (4 matrix rows) would be cleared before read out, so it does not deliver any signal.

7.2.3 EDET Sensor Energy Calibration

7.2.3.1 Dynamic Range Analysis

EDET pixels were intentionally constructed to store a lot of electrons in their internal gate and overflow region. Otherwise, a high contrast would not be achievable with shadow images. For the ^{109}Cd source calibration, only the highest DCDE gains (33.0, 16.5 and 11.0 times the lowest gain) can be considered. A 22 keV photon generates on average above 6,000 electrons which induce, dependent on the used matrix gate length, between 15 and 45 ADU in the high gain mode[16]. The lower DCDE gain at 3.3 would be useless, since it is by a factor of one tenth less sensitive, delivering highly imprecise results. In particular, the 22 keV and 25 keV peak would become indistinguishable from one another.

In order to get an unambiguous ^{109}Cd calibration peak, the highest DCDE gain should be selected, though one must be aware that in this case, not all pixels can be operated within the dynamic range of the DCDE. The total dynamic range for the DCDE high gain (see section 6.3.1.3) comprises about 18 µA.[17] On the other hand, the offset variation of all pixels at a drain current of $I_D = 100\ \mu A$ can reach 34 µA for a dark frame[18] at the DCDE 3.3 gain, as shown in Figure 7-1.[19]

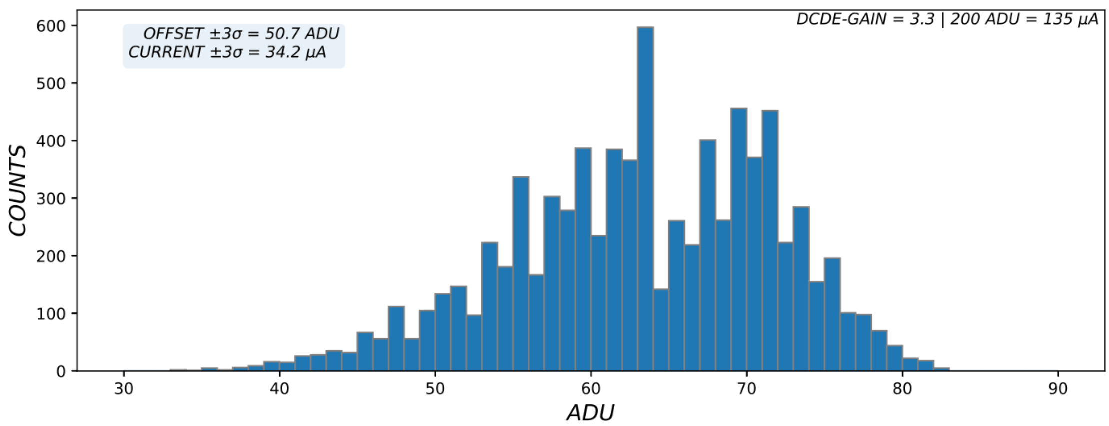

Figure 7-1: Pixel offset variation for a small EDET matrix in the 3.3 DCDE gain mode (one tenth lower than the highest DCDE gain). The distribution spans about 51 ADU which translates into a current range of 34 µA.

---

[16] For gains 16.5 and 11.0, halves or thirds of those, respectively.

[17] 14 µA for 200 ADU.

[18] Pure offset recording in a dark box, no external charge injection.

[19] The actual range of the offset distribution is highly influenced by the used nominal gate length (4, 5 or 6 µm).

Switching back to the high gain mode, the dispersion of the output currents is so large, that it exceeds the dynamic range of the front-end electronics, as can be seen in Figure 7-2 (blue histogram). It is self-evident, that for an appropriate calibration the pixel's offset distribution should lie within the operational window.

In reality, the dynamic range is restricted further, since the pixel's offset level must provide sufficient headroom for the digitized ADU response to the photon peak of the 22 keV line. Imagine, the pixel's average ADU response to a 22 keV photon would be at 40 ADU and the individual offset level was already registered at 220 ADU. Accordingly, the total value would theoretically surpass the 8-bit DCDE digitization maximum of 255 ADU. In effect, this peak will be not recorded and the algorithm would erroneously select another 'highest value', precisely the distance offset – dynamic range limit of the final hit distribution, as reference value for further calibration procedures. On the low side of the dynamic range, a photon hit would certainly move an out-of-range pixel back into the dynamic range, if the pixel's intrinsic offset value was not too far off the entry point.[20] Again, this pixel would not be eligible for further calibration purposes since the starting point was truncated by the shift distance between the actual "out-of-the-dynamic-range" level and the entry point into the dynamic range.

One solution for overcoming the dynamic range problem is provided by the 2-bit DAC adjustment in the DCDE (see APPENDIX B.4), presented in Figure 7-2.

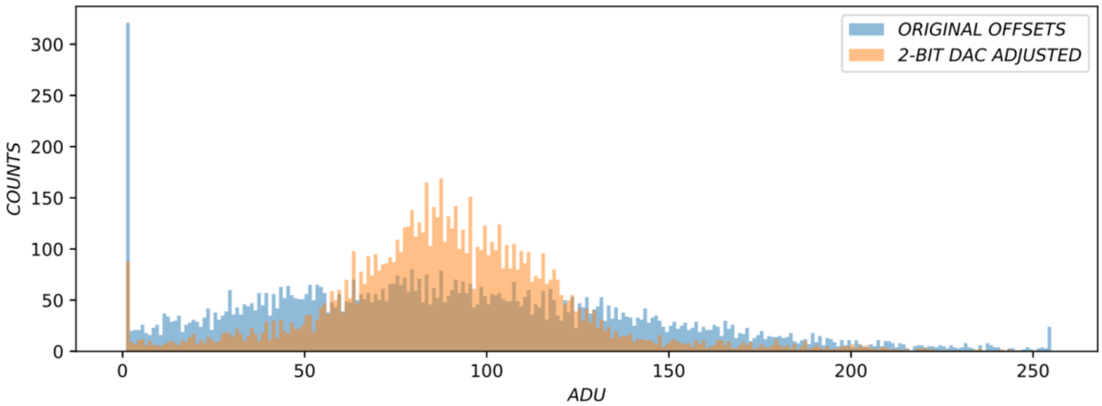

Figure 7-2: Offset comparison original data and 2-bit DAC adjusted data. With respect the original offsets, over 300 pixels missed the dynamic range at the bottom (indicated by the large blue bar on the left), while at the upper end significantly less.[21] As a result of the 2-bit DAC algorithm, the number of pixels out of the dynamic range were reduced from over 300 to under 100 and the distribution was substantially shifted and compressed to the left side, so only a few pixels show an offset value beyond 200 ADU.

[20] Besides, any very rare events from the 88 keV γ-rays occur. Although they make up about 3% of all ^{109}Cd photon emissions, the photoabsorption probability for a 50 µm thick sensor significantly reduces to just 0.04% compared to 3.05% for a 22 keV photon, so they are not visible in the final spectrum.

[21] To maximize the dynamic range, the main body of the distribution was shifted as far as possible to the left side. This can be realized quite well with the adjustment of two DCDE registers (*VnSubIn* and *IPAddIn*).

The 2-bit DAC adjustment considerably narrowed the offset distribution[22], although still about 90 pixels remained out of the dynamic range.

As mentioned, the DCDE offers an option to switch to a lower gain mode. This would also mitigate the problem with pixels outside the dynamic range or pixels too close to the dynamic range ceiling. Especially for the next, about 2 times lower DCDE gain level, there is a significant improved chance to get a reasonable operation point for all pixels, however one has to keep in mind that this goes at the expense of a better resolution.

7.2.3.2 Filtering

Two threshold limits were imposed for counting a signal as a hit. First, a noise threshold was set in order to mask out noisier pixels. Second, to make the analysis faster (specifically, the hit detection), a single hit threshold discarded low signal events. In case of charge sharing/clustering to neighboring pixels, the hit threshold created an undesired side effect: pixels below this limit were set to zero and a potential remaining single ADU in the neighboring pixel was counted as a single hit and allocated to a comparable low ADU level. Nonetheless, this method only increased the left tail of the final distribution somewhat.

7.2.3.3 Raw Data Adjustments

To reduce potential impacts from radiation damage, the data recording was done in several steps, each of which used updated offset values: after storing the first offset data,[23] the radioactive source was moved to the sensor in order to record about 50,000-100,000 frames. Thereafter, the source was moved away and the data was evaluated for the hit detection. In a first step, the raw data had to be **common mode** corrected[24] since this was not automatically provided by the DHPT (compared to the zero suppression readout mode). Then, a relative simple algorithm eliminated residual cluster data, i.e. data with charge splits to neighboring pixels. The identified single pixel hits, i.e. no entries to neighboring pixels, were subsequently assorted to the individual pixel charge histograms.

The same cycle repeated until a predefined total number of frames (or equivalently, sufficient statistics) was reached. One might object this circuitous method and question why not all frames were recorded with one offset data. [25] The main reason is related to a slight downshift of the offset levels by radiation damage effects. This could potentially widen the 22 keV peak or worse, even shift it to a lower level (1-2 ADU). In essence, by moving the source back and forth and record new offset data in between, a degradation shift of the hit data could be mostly avoided.

---

[22] Since the exact ADU value for out of the dynamic range pixel remains unknown, an exact standard deviation parameter does not make any sense.

[23] Usually, 1001 frames were taken for the offset data.

[24] The same algorithm as described in the DHPT manual [90] was used.

[25] Besides, there are some memory issues with the computer: $100{,}000\ (frames) \times 8{,}192\ (pixels) \times 8\ (bit\ data) = 819.2MB$.

As events with charge sharing were suppressed, the single hit threshold level has a big impact on the shape of the spectrum. Higher values increase subthreshold losses and increase the fraction of events below the peak energy. Additionally, the chosen single hit threshold of 10 ADU broadened the left tail of the distribution. If for example a 22 keV photon created 30 ADU in a specific pixel and this photon hit two pixels with a charge sharing of 21 ADU in the first pixel and 9 ADU in the second pixel, the charge in the second pixel would have been omitted for not passing the threshold. However, the charge in pixel 1 would have been counted as a low single hit of just 21 ADU.[26]

Figure 7-3 gives an impression of the shape of the histogramed data for a selection of 9 pixels. The dominating peak represents the 22 keV photons and a much smaller peak to the right represents the 25 keV photons. The hit counts to the left display noise effects and collection inefficiencies, e.g. split charges to neighboring pixels not reaching the minimum hit threshold (10 ADU).

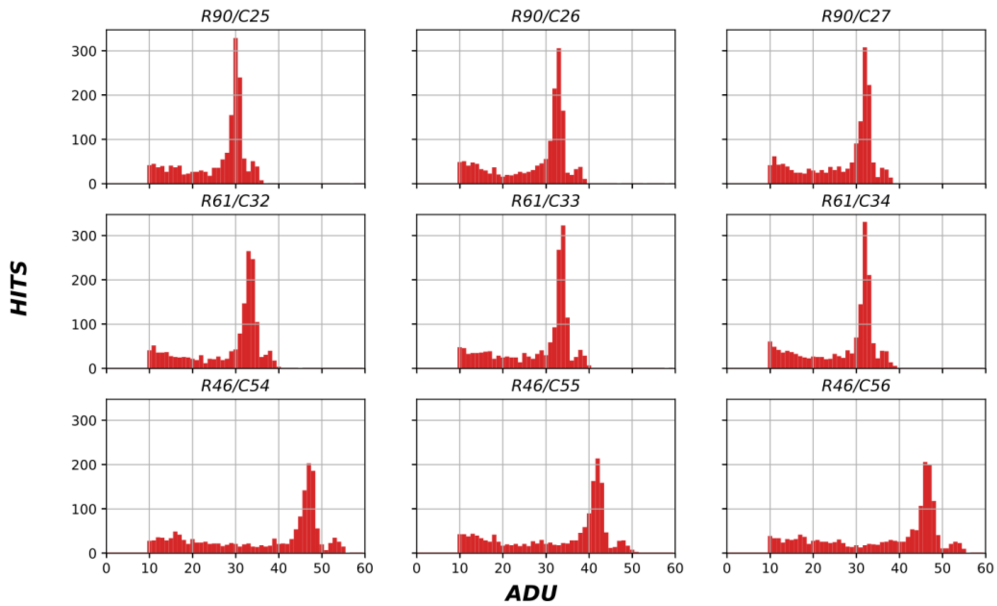

Figure 7-3: ^{109}Cd spectrum on a selection of EDET sensor pixels with different pixel responses: low gains in the top row, average gains in the middle row and high gains in the bottom row. In all of these pixels, the much smaller 25 keV photon peak is also clearly visible.

If all hits were summed up pixel-wise, one can create a hit count map (single hits per pixel) as depicted in Figure 7-4.

[26] The selected single hit approach is computationally much easier to implement than a clustering hit algorithm.

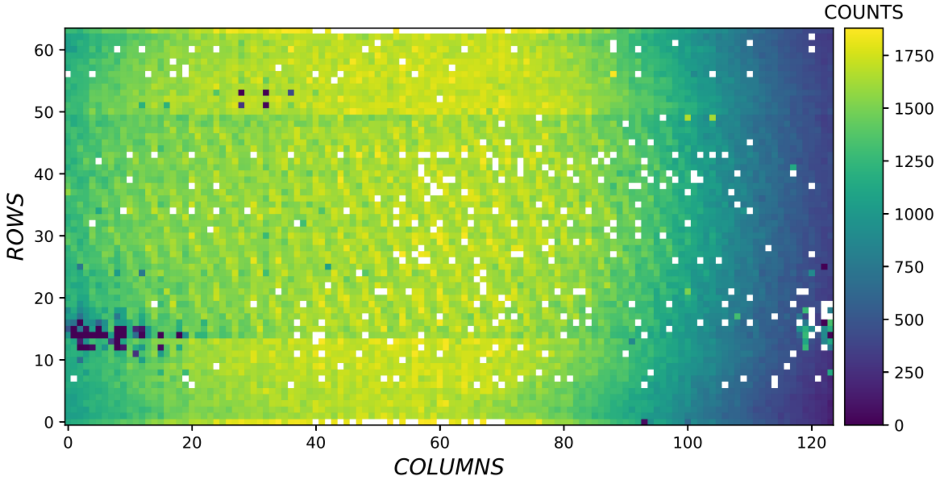

Figure 7-4: ^{109}Cd hit count map of a 124 x 64 pixels EDET sensor (the permanently cleared first electrical row is not depicted). The central spot within the collimator tube encompasses about 70-80 pixels corresponding to 4.2 to 4.8 mm, pretty much in line with the collimator's diameter of 4.3 mm. White spots represent masked pixels either exceeding the noise or single hit threshold limit.

From all of the single hit distributions, the individual pixel gain can be extracted as reference value for the cross-calibration of other methods (laser, LED). To this end, the peak value is determined individually for each pixel and finally stored in an array. Figure 7-5 visualizes this operation for the whole matrix.

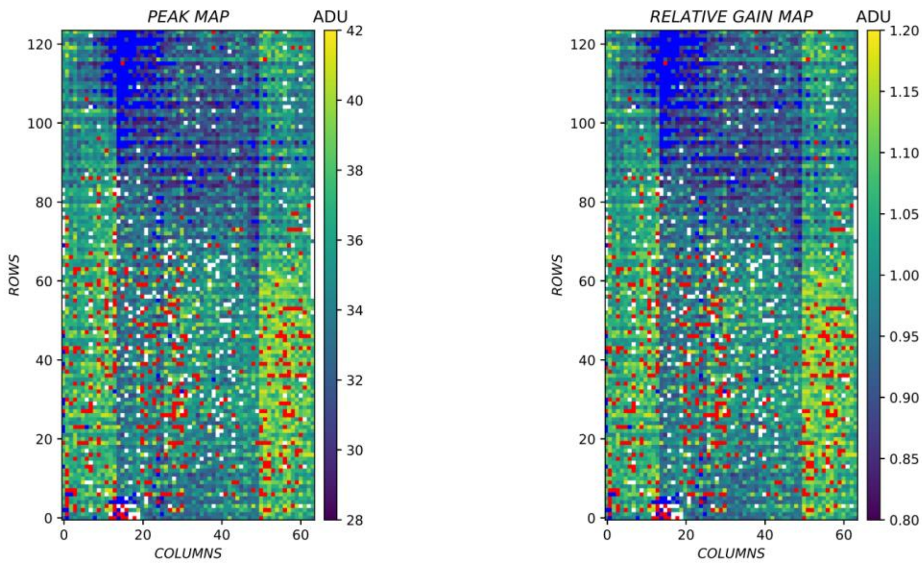

Figure 7-5: Left: Distribution of the peak value for every single pixel, i.e. the peak of each single distribution. Blue pixels indicate values below 28 ADU, the red color is reserved for pixels over 42 ADU and white spaces represent masked pixels from the noise threshold and single hit threshold. Right: Relative Gain Map, simply dividing every single pixel's peak value by a global peak value, which was determined as the median peak value for the whole matrix. Noticeable is the lower gain for most pixels in the sharply delineated, broad middle stripe of the sensor, a possible indication, that other components (DCDE, wirebond adapter) outside the matrix may exert an influence on the pixel gain.

Note, the blue and red colored pixels remained unconsidered for the analysis because of a too large deviation from the median value of 35 ADU (a fixed range of $\pm 20\%$ was assumed for including all process related variations).[27] The division of the peak value by the overall mean value constitutes the relative gain map to the right.

It would be tempting to aggregate all pixels into a common histogram without further data calibration as shown in Figure 7-6 below. Additionally, one could attach a Gaussian fit with a standard deviation and use that as a proxy for the detector's resolution. In doing so, important information from the individual pixel histograms would be unexploited and the real detector capabilities would be underrated.

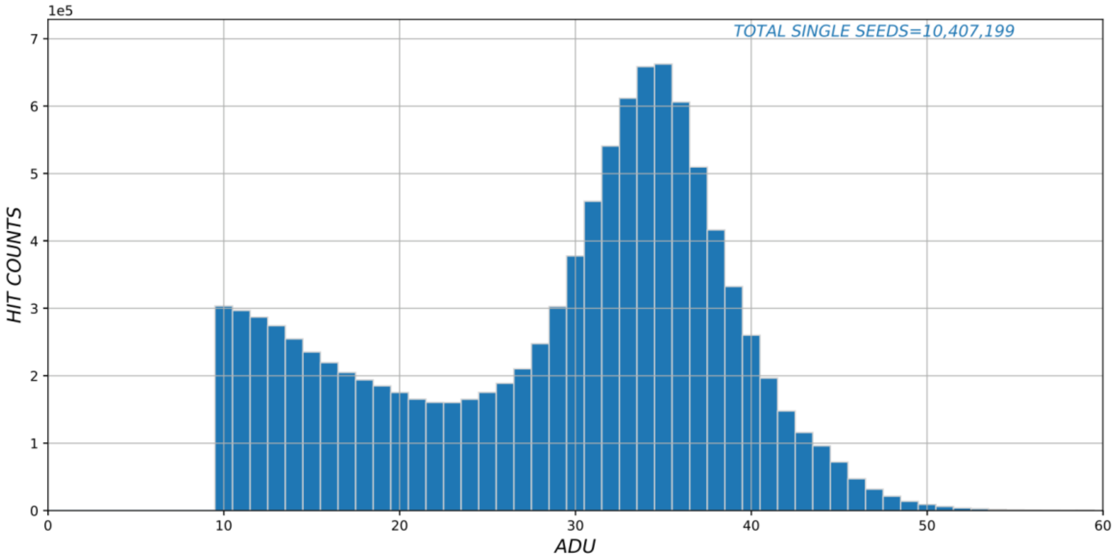

Figure 7-6: Aggregation of all pixels to one single histogram showing a peak at around 35 ADU.

A more accurate approach uses of the available information from the single pixel histograms to reconstruct the actual shape of the distribution. Algorithmically, this was implemented by a stretching/compression-mechanism as depicted in Figure 7-7. In a first step, all distribution peaks of each pixel were shifted to a value of 22 keV, representative for the most active characteristic line of the Cadmium source spectrum. In a second step, two cases were distinguished: if the recorded peak was higher than the Cadmium peak (with respect to the measurement above, this was the case for all eligible[28] pixels) the distribution had to be compressed, in the reverse case the distribution was stretched. For the re-binning of the shifted ADU values the interval widths were adjusted to the relation between original peak and Cadmium peak. A specific routine assigned the original ADU value to the correct keV bin.

[27] By this measure, out-of-the dynamic range effects were by and large excluded.

[28] Pixels within the $\pm 20\%$ range to the median value of all pixels.

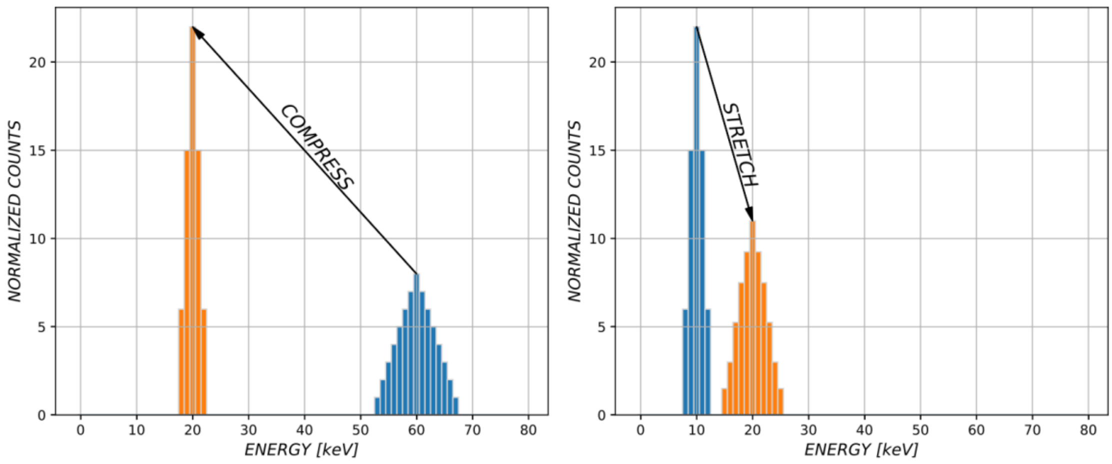

Figure 7-7: Compression and stretching of individual pixel histogram data.

The developed algorithm was not perfect but delivered acceptable results. Figure 7-8 applied the compression algorithm to a single pixel.

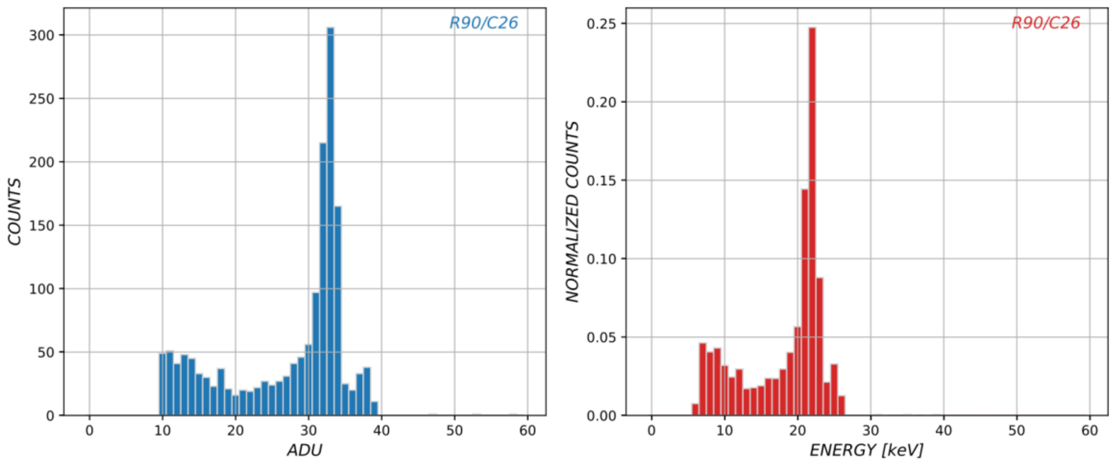

Figure 7-8: Conversion of Pixel R90/C26 data by compression to a standard energy spectrum. Note, that the pixel's shape remains conserved and the 25 keV peak is still visible.

Now, by adding up all eligible pixels and performing a normalization by division of the total counts, a sensor energy spectrum can be established, as depicted in Figure 7-9.

A comparison of the 22/25 keV peak heights reveals a relation of 7.3. When going back to Table 7-2, one would notice that the peak height ratio between all K_α and K_β lines amounts to just $84.31/17.9 \approx 4.7$, much smaller than the observed value. The difference can be explained by the following parameters: from the aggregated sensor peak value one can infer a peak ratio of $35/22 \approx 1.6$. While both K_α lines are situated close together at around 22 keV, a sub-branch of the K_β lines already deviates by about 0.5 keV. If the detector response was linear, this translates to an additional synthetical ADU value of $0.5\ \mathrm{keV} \times 1.6\ \mathrm{ADU/keV} = 0.8\ \mathrm{ADU}$, in other words on average about $0.8 \times 2.65 = 2.12$ of the higher photon values ($2.65\ K_{\beta 4}$ photons per 100 ^{109}Cd decays) would already be recorded by a higher pixel ADU value.

In effect, the denominator is not 17.9 but $17.9 - 2.12 = 15.78 \rightarrow 84.31/15.78 = 5.34$. Incorporating also the different photon absorption probabilities of 3.49% for 22 keV photons and 2.36% for 25 keV photons this results in $5.34 \times 3.49\%/2.36\% \approx 7.9$, very close to the observed relation.[29]

The second peak is now clearly visible although the left tail shows substantial higher values, which can be mainly attributed to the above described hit threshold limit and some noise effects.[30] In a nutshell, the EDET detector is behaving as expected and it is able to resolve small energy differences of 3 keV. This might be important for other applications. Because of some process variations, individual pixels show individual gains which have to be calibrated to make the sensor an accurate instrument for the envisioned recording of stroboscopic images. The ^{109}Cd source calibration delivers the reference points for the following laser and LED calibrations.

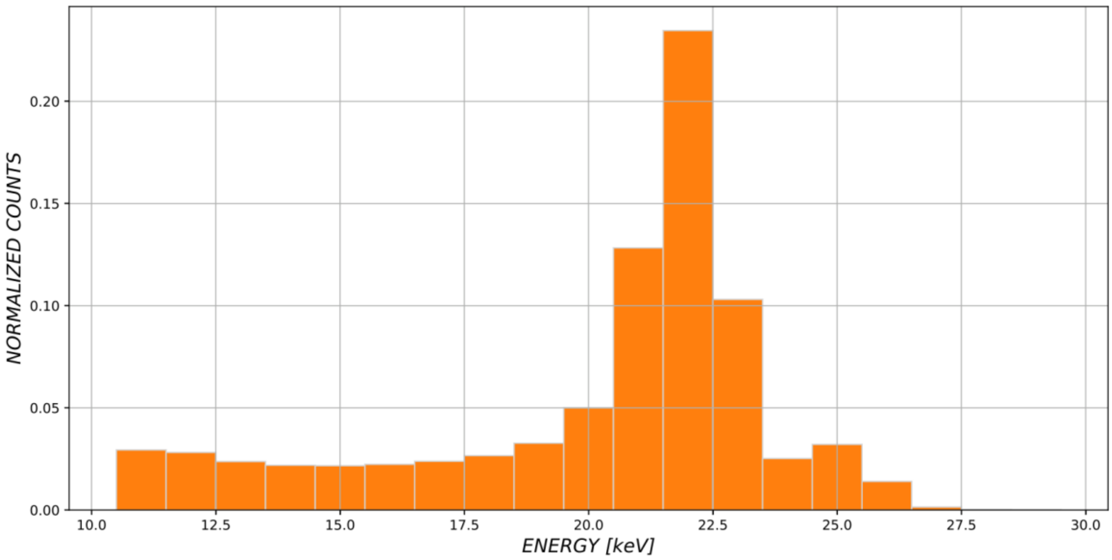

Figure 7-9: Calibrated ^{109}Cd energy spectrum for all pixels within a predefined minimum and maximum MPV. The total area is normalized to 1. The 25 keV peak is clearly visible.

[29] The final deviation can be explained with the discretization of the energy steps within the detector.

[30] At the time of writing a delay optimization for the 2-bit DAC values was not incorporated. Therefore a lot of pixels had to be masked.

7.3 Laser Pixel Calibration

7.3.1 Laser Parameter Characterization

7.3.1.1 Selection of the Laser Wavelength

For the calibration of EDET pixels by a laser or a LED device, the selection of an adequate wavelength is of major importance: since the top of an EDET pixel is highly structured (among other things, with a dense grid of aluminium lines) and additionally covered with a thin Titanium/Tungsten layer, all laser and LED illuminations were performed to the backside of the EDET sensor.

As mentioned, some of the generated electron/hole pairs get lost due to recombination in the about 3 µm thick p-layer. To calculate the penetration depth of a specific wavelength λ in silicon, one has to know the absorption coefficient α. It can be derived from the following equation:

Equation 7-1

$$\alpha = \frac{4\pi \cdot k}{\lambda}$$

where k denotes the extinction coefficient. Extinction coefficients can be looked up in tables from spectroscopic ellipsometric measurements, as in [135]. Since these were tabulated along the corresponding energy levels, the used wavelength had to be converted to eV according to the well-known Equation 4-2.

A 635 nm red laser photon implies an energy of 1.9525 eV. Only energy levels in 0.10 eV steps were quoted, so the respective k value had to be interpolated. The extinction coefficients for 1.900 and 2.000 were tabulated at 0.016 and 0.022 respectively. Linear interpolation determined the value for $k = 0.019$. Inserted into Equation 7-1 finally delivered an absorption coefficient of about $3790\ cm^{-1}$.[31] In order to determine the photon range for a 99% absorption, one simply has to multiply

Equation 7-2

$$-\ln(0.01) \cdot \alpha^{-1} \approx 12\ \mu m$$

α^{-1} is also called the absorption depth or the attenuation length. On the other hand, if one uses a green light laser at 530 nm wavelength, the 99% absorption depth significantly reduces to just about 4 µm and a lot of the generated charge would have had already recombined. Moreover, since the p-layer is not equally dense and equally thick,[32] this would raise another complication for an efficient detector calibration. From the above assessment, it is advisable to use a red to infrared light for the EDET sensor calibration.

[31] An absorption coefficient of $3790\ cm^{-1}$ would mean that the radiation would be reduced by a factor of e (Euler's number) after passing a distance of $1/3790\ cm \approx 2.64\ \mu m$.

[32] Small fluctuations from the implantation and etching processes.

Apart from that, two conditions must be met to make the laser a reliable tool for the pixel calibration:

(1) It has to be ensured that the laser spot can be sufficiently focused within the pixel area, that no neighboring pixel gets any charge.
(2) The injected charge can be increased in equal steps or at least in a foreseeable way.

7.3.1.2 Determine Laser Focus Position

The first task can be quickly checked by using a multispectral imager like Sony IMX219. The pixels[33] are equipped with on chip color pigment filters, covering groups consisting of 4 pixels in a tessellated arrangement of one red, one blue and two green filters [136]. Notwithstanding that lasers are monochromatic light sources, the spectral sensitivity is high enough at least for one pixel in the quad.

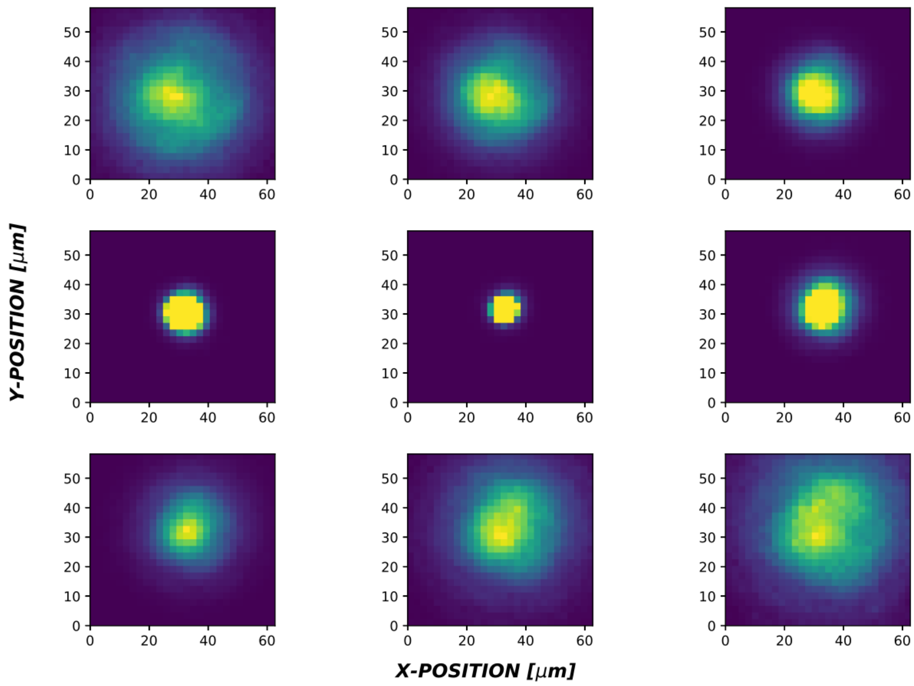

Figure 7-10: Determination of the focused laser position by varying the vertical distances between laser lens and a Sony IMX219 sensor. Only red filtered pixel values are represented by an artificial increased pixel size (factor of 4). The recorded picture sequence above shows the most interesting slides of the vertical displacement (total range of 1mm with hundred 10 µm steps). The surrounding laser spot area was adjusted to represent the typical dimensions of an EDET pixel. The most focused position in the central diagram proves that the spot dimension can be focused to a diameter of about 10 µm, well within one pixel's area.

[33] Unit cell size of 1.12 µm x 1.12 µm.

Embedded in a Raspberry Pi single-board system and equipped with a Python library (Picamera), this device can be easily used for “plug & play”.[34] The only thing the operator needs to do is to position the laser spot to the camera’s lens and move the laser in small steps in vertical direction, while recording frames. The latter requirement is performed by a linear XYZ-stage, where the relevant Z-stage offers a total range of 25 mm and a smallest step width of 0.1 µm. By gradually moving in and moving out the focus position, the one with the thinnest **waist** can be quickly found. A section of the recorded beam diameters is presented in Figure 7-10.

A more sophisticated method for determining the spot size of the focused laser position provided the so-called edge scan. To this end, a small PCB populated with a Hamamatsu S4584-06 diode was designed [137]. The laser had to be kept at constant intensity and the starting point for the recording was chosen to be close to the edge of the diode’s sensitive area. The edge served as a “knife”, since when moving out of the sensor in horizontal direction more and more parts of the beam spot hit the insensitive region. The generated photocurrents were measured with a Keithley 2612B source meter. The measurement suite started by first moving the laser in vertical direction by one step, followed by a prespecified range move in horizontal direction (the recorded intensity dropped from “full-in” to zero). The transformed photocurrents generated a bunch of sigmoid curves. The curve with the steepest gradient corresponds to the focal point of the laser beam.

The measured data was fit by a Gaussian distribution. The probability density function for a gaussian profile is:

Equation 7-3

$$f(x) = \frac{A}{\sigma \cdot \sqrt{2\pi}} e^{-\frac{1}{2}\left(\frac{x-\mu}{\sigma}\right)^2} + d$$

A : amplitude

μ : mean

σ: standard deviation

d: offset parameter

The cumulative distribution function of a gaussian distribution is:

Equation 7-4

$$F(x) = \frac{A}{2}\left[1 + \mathrm{erf}\left(\frac{x-\mu}{\sigma\sqrt{2}}\right)\right]$$

with the error function erf , which as is known can only be determined numerically. Figure 7-11 depicts the knife-edge scanning points in focused position together with a shaded error area and a gaussian fit.

[34] The scientific applicability has been well documented in [100].

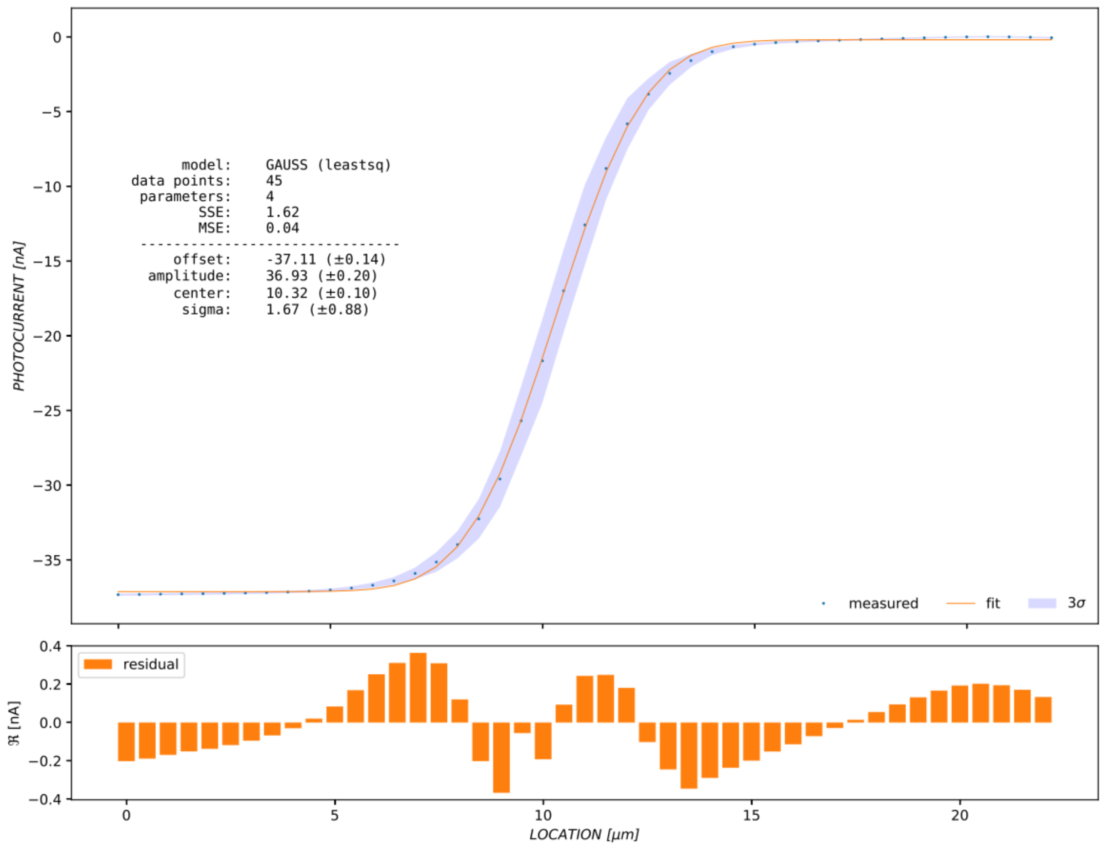

Figure 7-11: Knife-edge scan on a Hamamatsu S4584-06 photodiode. The blue shaded area in the top diagram covers 3 standard deviations. The red Gaussian fitting line reveals a good approximation with the given data points (blue), also visible in the low residuals depicted in the bottom diagram. Additionally, some statistical figures like error sum squares (SSE – sum squared differences between each observation and the mean) and mean squared error (MSE – average of SSE) are given.

Up to now, the implicit assumption was made, that the Gaussian beam exhibits a circular shape, but it is also imaginable that the beam bears an elliptical cross-section because of some lens aberration or other distorting factors. To investigate this further, one can either turn the lens by 90 degrees or move the laser to the other edge of the photodiode perpendicular to the original direction.

Thereafter, the discrete derivative for the collected data points in X- and in Y-direction were calculated. The differences themselves should resemble a Gaussian normal distribution. Accordingly, another curve fit was made as shown in the two diagrams of the right side in Figure 7-12.

The beam radius $w(z)$ (half of the beam diameter ϕ_{1/e^2}) defines the distance to the beam axis where the intensity drops to $1/e^2 \approx 13.5\%$. For distances of 1.5 $w(z)$ and 2.0 $w(z)$ the intensity decreases further to 1.1% and 0.03% respectively [138], see APPENDIX C.

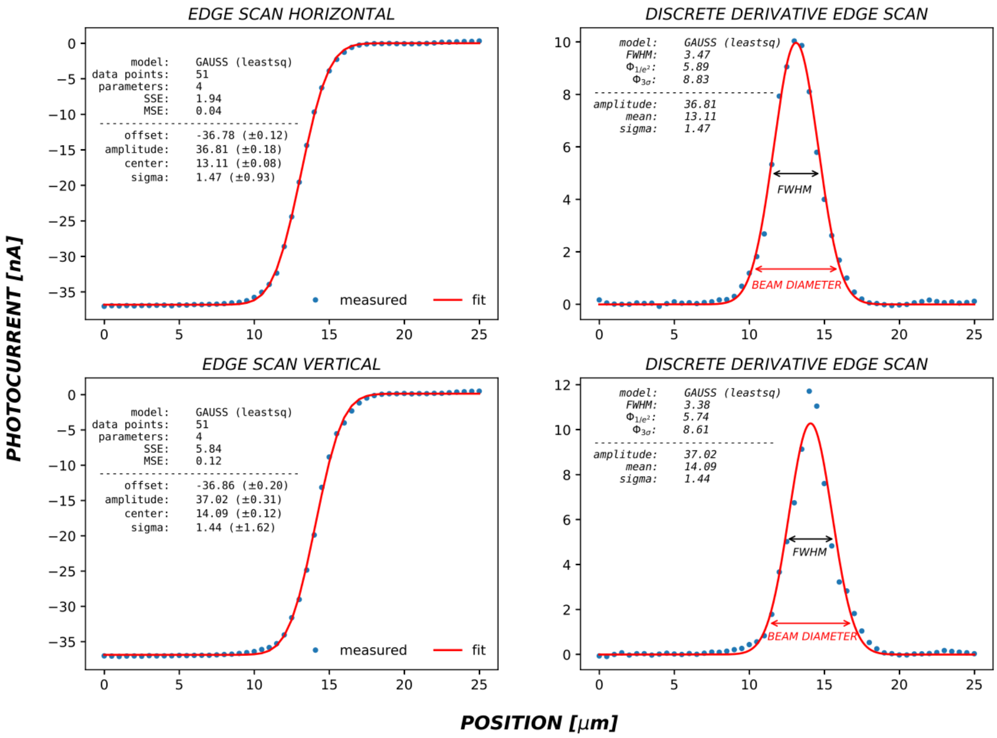

Figure 7-12: Local laser scan on a Hamamatsu s4584-06 diode. Left: knife-edge scan in horizontal and vertical direction fitted to a Gaussian cumulative distribution function. The motorstage position was moved by 51 half-µm steps. Right: discrete derivative of the knife-edge data with a fitting Gaussian density function. From the relation $\phi_{1/e^2} = FWHM \cdot \sqrt{2/ln(2)}$ [139] the beam diameter should be about 1.7 times the depicted full width half maximum (FWHM) of the intensity profile. The beam spot exhibits an almost perfect symmetrical shape.

The approach with a Gaussian fit offers a lot of advantages. First, it is easy to reconstruct the beam spot with a two dimensional Gaussian distribution of the two vectors X and Y:

Equation 7-5

$$f(x,y) = \frac{1}{2\pi\sigma_X\sigma_Y\sqrt{1-\rho^2}} e^{-\frac{1}{2(1-\rho_{xy}^2)}\left[\left(\frac{x-\mu_X}{\sigma_X}\right)^2 - 2\rho_{xy}\left(\frac{x-\mu_X}{\sigma_X}\right)\left(\frac{x-\mu_Y}{\sigma_Y}\right) + \left(\frac{y-\mu_Y}{\sigma_Y}\right)^2\right]}$$

Since both measurements were determined independently, the correlation coefficient ρ_{xy} can be assumed at 0 and the bivariate probability density function reduces to:

Equation 7-6

$$f(x,y) = \frac{1}{2\pi\sigma_X\sigma_Y} e^{-\frac{1}{2}\left[\left(\frac{x-\mu_X}{\sigma_X}\right)^2 + \left(\frac{y-\mu_Y}{\sigma_Y}\right)^2\right]}$$

With the given parameters a synthetic beam spot can be reconstructed as depicted in Figure 7-13:

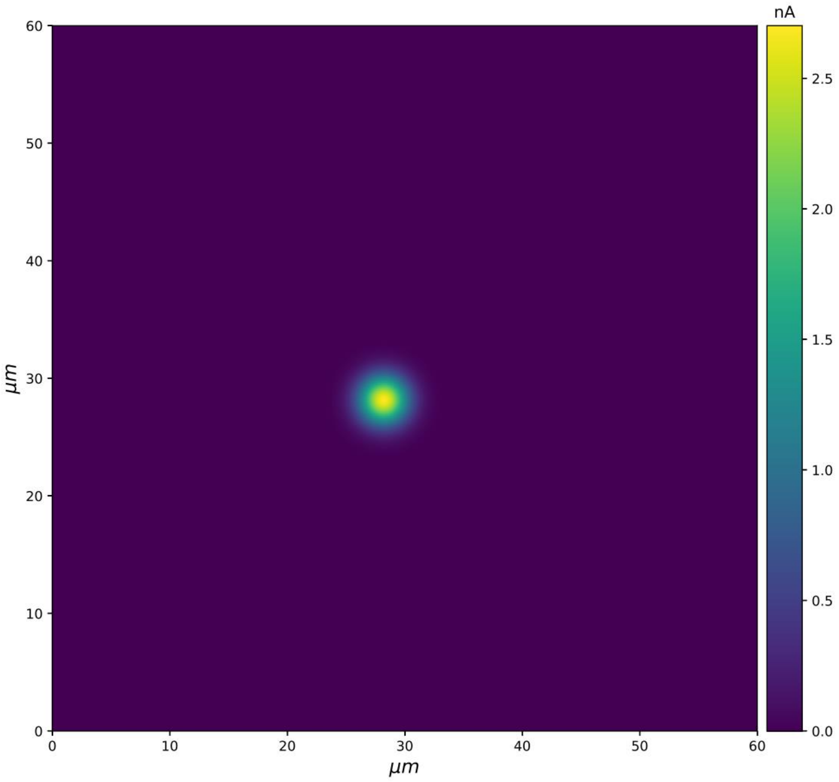

Figure 7-13: Reconstructed Laser beam spot from knife-edge measurements. The diagram outlines the dimension of an EDET sensor pixel. If focused, the laser beam charge can be easily placed into one pixel.

As one can see, the laser spot diameter can be made sufficiently small to guarantee that no neighboring pixel gets any charge.[35] A close to focus positon does not only facilitate the single pixel calibration but is also useful for other measurements like single pixel analysis, the establishment of charge collection functions or single pixel voltage sweeps as described in section 8.4.2. Unfortunately, EDET pixels are comparably small and therefore, a similar focus optimization by a knife-edge measurement could evolve into a cumbersome effort. Especially, if the beam was originally (unintentionally) positioned to a corner region where the intensity splits up to four pixels. To the rescue, one can take advantage of the Gaussian beam properties described in APPENDIX C.

An ideal Gaussian beam would provide a beam propagation factor of $M^2 = 1$ (see Equation C - 7) which can be roughly met with high-quality Helium-Neon lasers. For the actual deployed TEM_{00} diode laser a value of $M^2 \approx 1.1\ to\ 1.7$ should be achievable [140]. To verify this assumption, the focused position was moved out in both directions and by regression analysis $M^2 = 1.318$ was determined as depicted in Figure 7-14. The beam waist at focused position was measured at $w_0 = 2.95\ \mu m$, the Rayleigh length z_0 was calculated at $\sim 31\ \mu m$ (factoring in M^2).

[35] One caveat: the diameter is also dependent on the actual beam intensity.

From Equation C - 8 the divergence half angle could be determined at

$$\theta_0 = \frac{\lambda \cdot M^2}{\pi w_0} = \frac{0.66 \cdot 1.318}{\pi \cdot 2.95} = 93.9\ mrad$$

Assuming a maximal acceptable diameter of $40\ \mu m$ for a $60\ \mu m$ square pixel, the margin of error for the z-position could reach approximately (rearranging of Equation C - 3):

Equation 7-7

$$z = \sqrt{\left(\frac{z_0 w_z}{w_0}\right)^2 - 1} = \sqrt{\left(\frac{31 \cdot 20}{2.95}\right)^2 - 1} \approx 210\ \mu m$$

This implies, that the ideal focus position can be missed by about $\pm 210\ \mu m$ and the selected pixel would be still exclusively illuminated (provided a correct alignment in x- and y-direction).

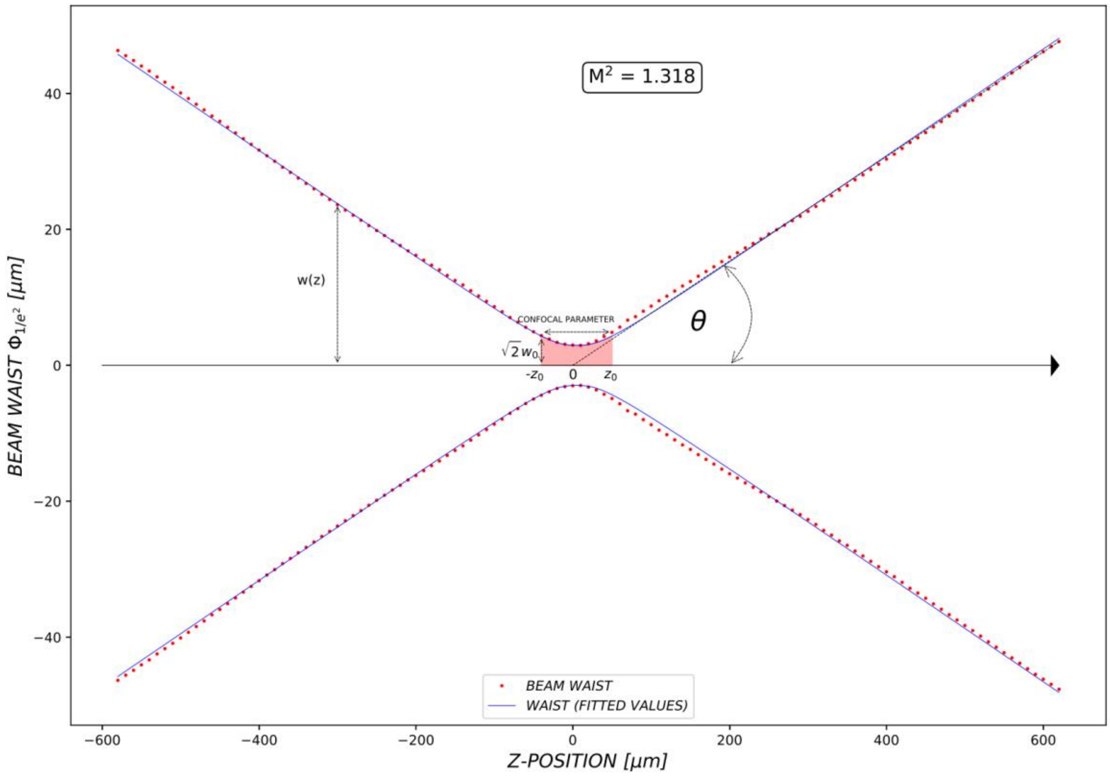

Figure 7-14: Beam waist w_0, Rayleigh length z_0 , confcocal parameter, divergence half angle θ_0 and beam Propagation Ratio M^2(least-square fitting on measured data points).

7.3.1.3 Laser Stability Analysis

The second necessary criterion for an efficient pixel calibration requires the injected charge to be increasable by equal steps or at least in a predictable way. Once more, the verification of this condition can be accommodated by the photodiode. Instead of the vertical laser position variation, now the frequency[36] is increased by constant steps. Ideally, the resulting photocurrent curve output from the diode should exhibit a constant

[36] In principle, the same goal is achievable by a variation of the pulse length while keeping the frequency constant.

slope as shown in Figure 7-15. The outcome shows a good agreement with the expectation of a straight line.

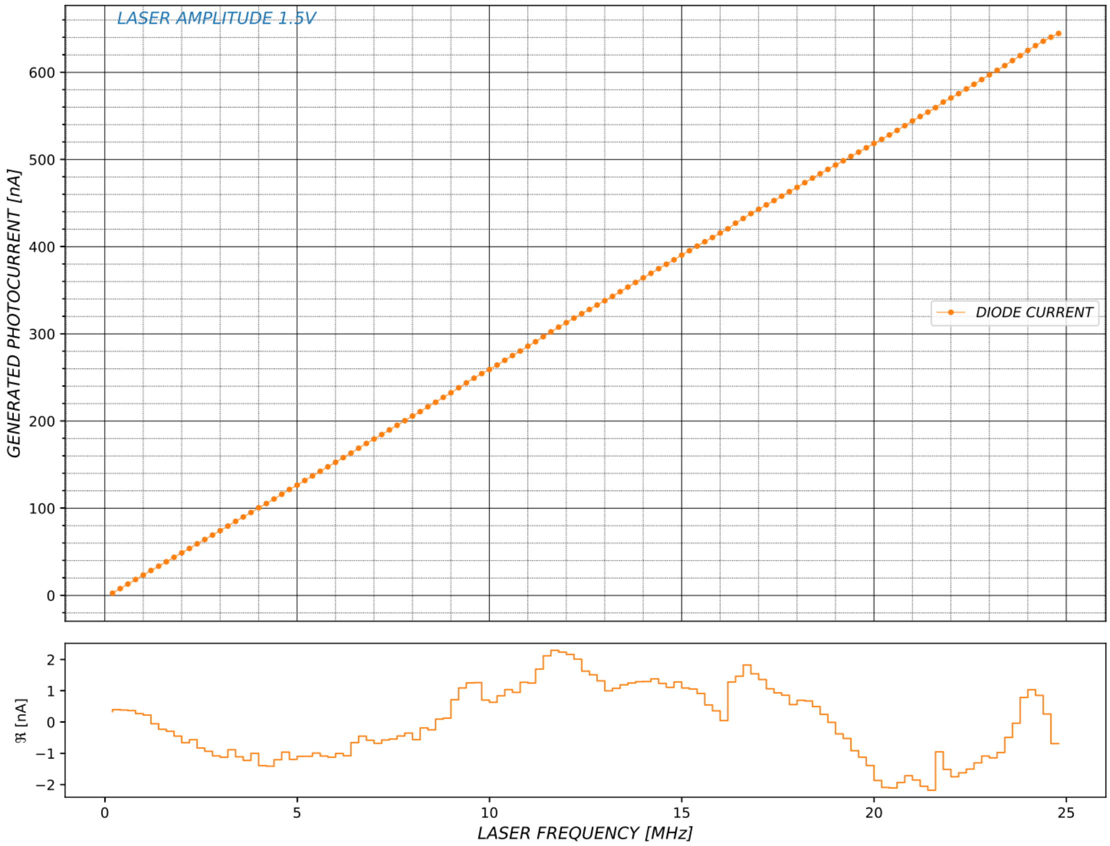

Figure 7-15: Generated photocurrent on a Hamamatsu S4584-06 PSD (photo sensitive detector). The laser frequency was increased by 125 steps of 200 kHz. The bottom diagram shows the residuals from a straight line fit.

7.3.2 Laser Scans

Having proven that a laser beam is an eligible tool for the calibration of the EDET sensor, a lot of specific measurements can be realized. As a first step, the intra-pixel charge sensitivity can be visualized by moving the laser spot gradually by $1\ \mu m$ steps in x-y-direction as depicted in Figure 7-16. For simplicity, only the highest scan value of all surrounding pixels was considered for a specific scanning point (effectively, this procedure produces the charge collection function of a single pixel).

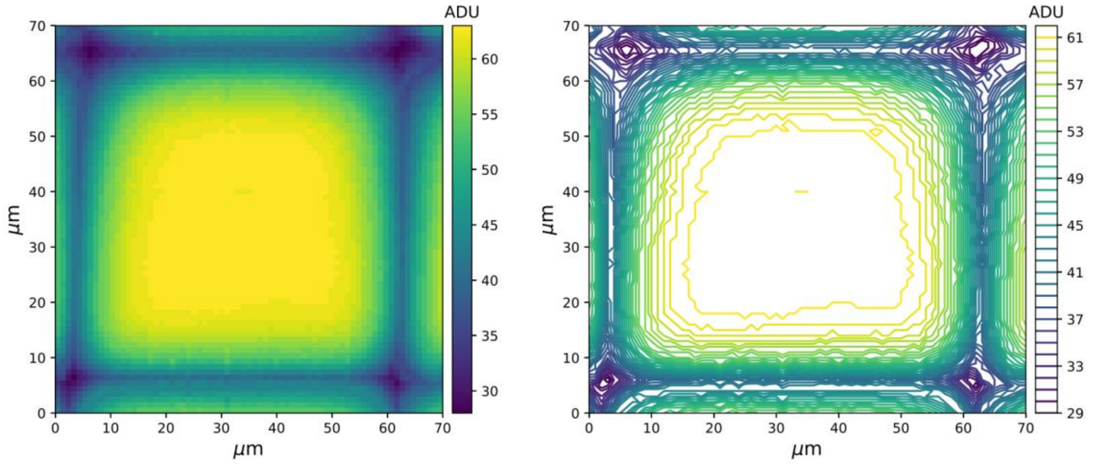

Figure 7-16: Left: Single EDET pixel (R51/C27) recorded by means of a focused laser spot. For the visualization, only the highest pixel charge was accepted (no neighboring pixel charges). The boundaries to the neighboring pixels are clearly discernible. The larger dark fields, visible in the top pixel areas indicate the position of one of the sensor's drift lines. In addition, a closer inspection reveals, that the matrix was not perfectly aligned to the laser stage but slightly tilted. Right: same data in a contour representation. From the brightest area in the center of the pixel one can infer, that the beam was not perfectly focused. Otherwise, this region would reach out closer to the pixel's borders (if one counts the $1\ \mu m$ step intervals from the brightest edges to the darkest pixel border lines one gets about $13\ \mu m$ instead of ideally below $10\ \mu m$ laser beam diameter).

Similar to a single pixel, one can also scan a larger pixel area[37] as shown in Figure 7-17.

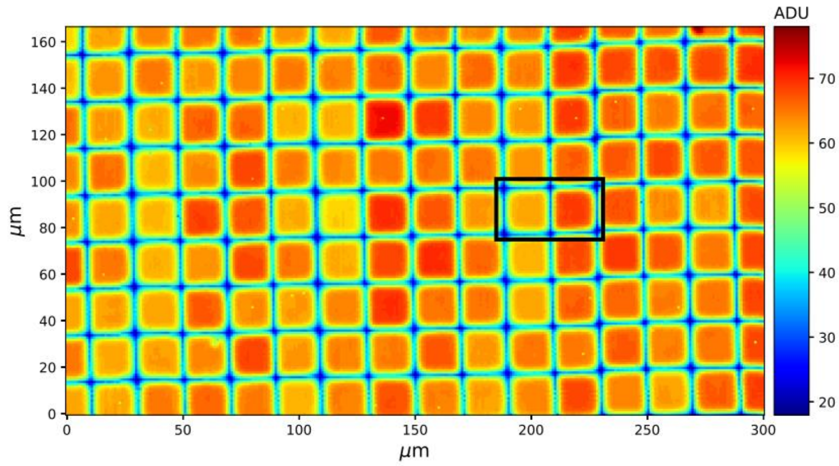

Figure 7-17: Laser scan on a 9×16 pixel array. The matrix orientation was tilted by 90° (DCDE on the left side). The focused laser spot was moved in $3\ \mu m$ steps. The double pixel structure (exemplarily marked by a black rectangle) is faintly visible by the more concise edges on the facing sides. Every second pixel row (now oriented in vertical direction) is pervaded by a drift line rounding down the collected charge at the pixel corners (thicker blue area). A small tilt to the motorstage position is also clearly visible.

[37] However, it is advisable to increase the $1\ \mu m$ step size, otherwise this will take a very long time.

For this multiple pixel scan a low DCDE gain of 3.3 was selected and the recorded ADU value of 70 indicates, that a charge of about 400,000 electrons per scanning point was injected (compare to Figure 7-21). One thing immediately catches the observer's eye: the pixels react quite differently to the same illumination with a variation from 59 ADU to 72 ADU in the most extreme cases – a clear sign for the need of pixel calibration, but this discloses just one part of the story. To reconstruct the total deposited charge, one has to sum up the generated ADU values from all neighboring pixels, especially for the scanning points at the side edges and even more importantly, at the pixel corners.

7.3.3 The Calibration Challenge

The pixel's nonlinear response involves an additional calibration challenge, which will be discussed in the following. In order to present things clear and simple, the calibration approach was limited to a 3×3 pixel array (including about half of the surrounding pixels to consider edge and corner effects, hence a total of 25 pixels). As before, the diagram of Figure 7-18 on the left side depicts the highest recorded value. One recognizes substantial in-pixel charge variations as well as substantial charge decreases, in case the laser was moved to the edges and even more when moved to the corners. Turning the attention to the right diagram, the picture totally reverses its appearance, since now the sum of all generated charge (in all neighboring pixels) with respect to the specific scanning point was included (mind especially the different scaling).

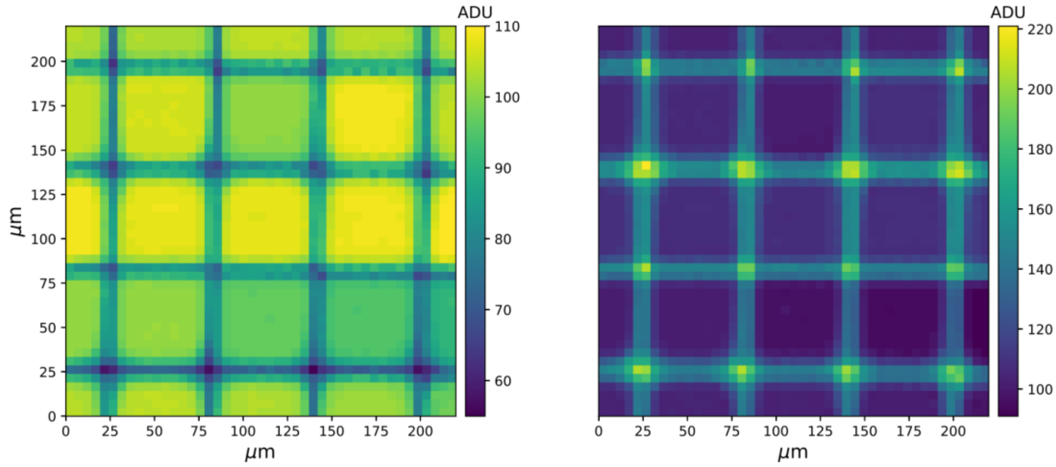

Figure 7-18: Laser scan in $5\ \mu m$ steps on a small pixel array. Left: only the highest value of all considered pixels (i.e. all neighboring pixels) for the respective scanning point was recorded. Right: all pixel values (including neighboring pixels) to the specific scanning point were added together. The light/dark zones completely reverse and the differences between the center of a pixel and the corners reach out to over 100 ADU, mainly caused by different gain regions of the neighboring pixels.

Since the laser spot size could not be made infinitesimal small and diffusion and repulsion processes induced a certain degree of spatial charge dispersion, the charge was split between two or even 4 pixels at the edges and at the corners respectively. On the assumption of a constant charge collection (i.e. no charge was lost), the shallow intensity regions should have disappeared, after summing up all pixel values to the specific scanning point. In the end, one would expect a mosaic structure, deviating only by different pixel gains and no visible border structures. On the contrary, the variation has become even more distinct and one notices a huge difference between the center points of a pixel and their corners, now with opposite sign.

This observation might appear strange at first glance. For a better understanding, one should remember the non-linear response of an EDET pixel as described in chapter

5.1. If the laser spot was moved out from the central pixel region towards another pixel, at a certain distance more and more photons of the laser spot area hit the neighboring pixel. As the latter has not generated any charge so far, first the internal gate region fills up. Because of the substantially higher gain, the additional ADU value obtained is much higher than the corresponding ADU reduction in the original pixel, which still absorbs most of the laser illumination and thus remains in the overflow region.

This can be ongoing to an extreme at the corners where 4 pixels assemble together as shown in Figure 7-19.

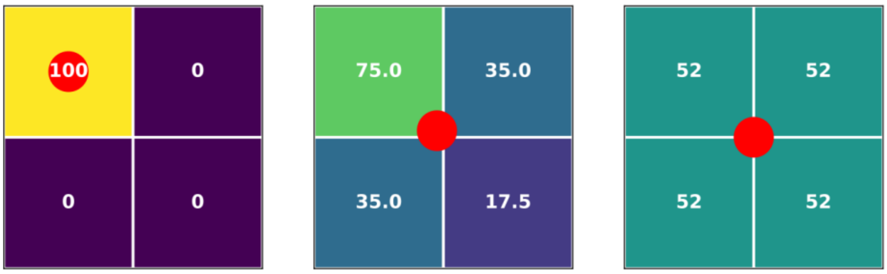

Figure 7-19: Non-linear response of 4 synthetic, identical EDET pixels while moving the laser spot (red) from the center of one pixel to the corner of four pixels.

The hypothetical example above bases on the following assumptions: 4 adjacent, homogeneous pixels, an internal gate gain 3.5 times higher than the overflow gain, an identical capacity of the internal gate of 50 ADU and an external charge injection of 100 ADU. If the laser spot is moved exactly to the corner of 4 pixels, the total charge would equally split up to these 4 pixels. Since the gain relation was assumed at $1{:}3.5$, a charge of 10 ADU lost from the considered pixel in the overflow regime to a neighboring pixel's internal region would create there an additional charge of 35 ADU. To calculate the new pixel values, in a first step part of the total charge is used to fill up the internal gate regions of the other 3 corner pixels, totaling $50/3.5 \times 3 \approx 43\ ADU$. In other words, a reduction of 43 ADU in the overflow region of the start pixel corresponds to a total increase of 150 ADU in the neighboring pixels (due to the higher amplification of their internal gate regions). The remainder of 7 ADU is equally allocated to all four pixels. As a result, instead of an initial value of 100 ADU the new measured charge would now amount to $4 \times 52 = 208$ ADU, a difference of 108 ADU.

In summary, sensor calibration is a necessary task for all pixel detectors. For the EDET sensor, an additional complexity arises, because of the above described non-linear response functions. The next section describes how this can be accomplished.

7.3.4 Laser Calibration Approach

7.3.4.1 The Synchronization Problem

To figure out the individual pixel response function, a (fine grained) charge curve for every pixel must be established. This can be achieved by means of a focused laser beam to the center of each pixel, while increasing the laser pulse frequency (or pulse width) by equal steps.

Beforehand, one precondition concerning the appropriateness of a pulsed laser for the pixel calibration has to be met: it must be possible to time the laser frequency with the sensor's readout frequency in such a way, that the selected pixel gets exactly an integer increase of the additional laser bunches.[38]

Although the laser cannot deliver triggered bursts, the recording of charge curves can be accomplished by carefully choosing the laser frequency with respect to the readout frequency, as shown in Figure 7-20.[39]

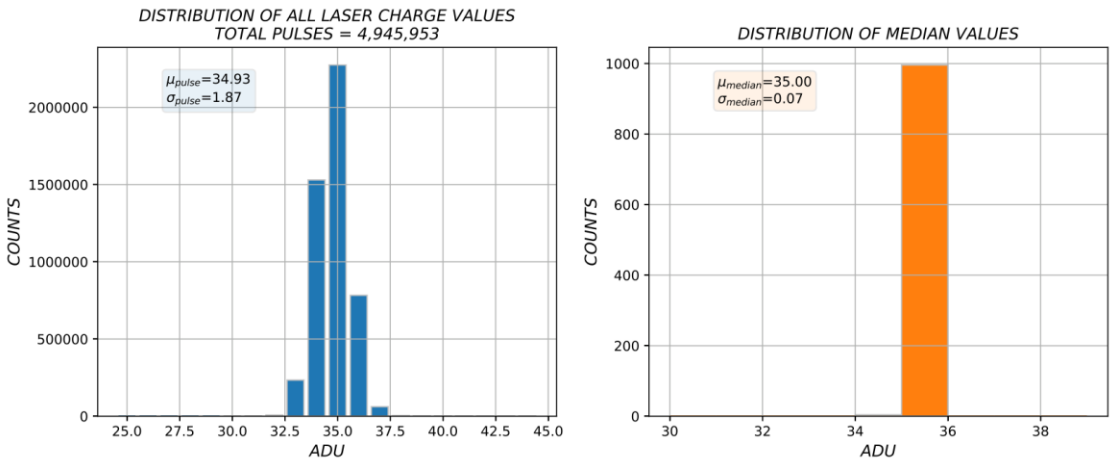

Figure 7-20: Generated pixel charge distribution from a constant laser pulse on 5 million frames (Pixel R109/C38) with a DCDE gain of 33.0. Left: Histogramed data for all measurements exhibiting just a small variation from the peak value at 35 ADU. No double charge was registered and the amount of zero charge was slightly above 1%. Right: Piling up only the median values of 5,000 frames portions. The yield can is almost perfect.[40]

[38] For similar measurements conducted on behalf of the BELLE II modules [155], a NIM-TTL-converter was used for the synchronization.

[39] For the following measurements a different board with a gate length of 5 µm was taken.

[40] This analysis was repeatedly done with different pixels and also with different laser amplitudes and different laser pulse widths. Sometimes the median charge splits up to 2 neighboring ADU values but this is more a confirmation rather than violation of this approach, since the chosen total pulse energy could by chance lie between two ADU values.

7.3.4.2 Establishment of a Laser Charge Curve

After this preparatory work, it is now possible to record charge curves for single pixels. In order to determine the generated electrons per injected laser pulse (absolute calibration), it is not necessary to have an energy calibration for all sensor pixels. In theory, one calibrated pixel would be sufficient, provided that the DCDE was switched into the same DCDE gain setting the ^{109}Cd source data was recorded. The following injection of a single laser pulse (@245 kHz) per frame should be close to the ^{109}Cd source peak-ADU value[41], or to be less restrictive, the laser pulse charge must be at least within the dynamic range of the particular DCDE gain. In the latter case, the energy calibrated laser pulse p_{e^-} can be easily determined by the simple rule of three:

$$p_{e^-} = \frac{ADU_{pulse}}{ADU_{Cd^{109}}} \cdot 6{,}111$$

In reality, one should not rely on just one single data point, but rather inspect a few more pixels, optionally combined with a small string of measurements by increasing the frequency in integer steps and taking the differences. The average $\overline{ADU}_{pulse}$ should give a better proxy for the injected pulse charge. With the knowledge of the calibrated pulse charge and the laser kept in focused position on one selected pixel, a first charge curve can be recorded as depicted in Figure 7-21. This curve can be parameterized by, for instance, a polynomial of degree 6.[42]

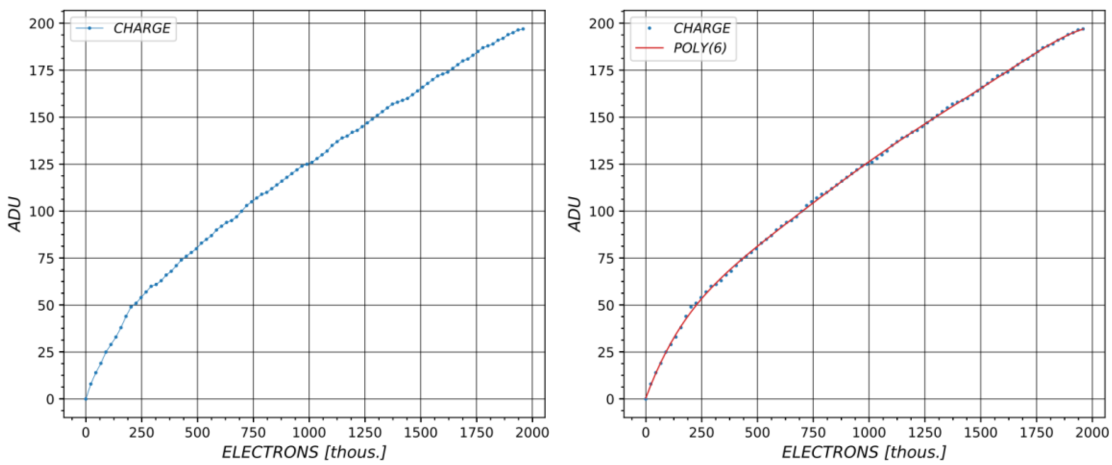

Figure 7-21: Left: Charge Curve of Pixel R53/C27 with a pulsed laser. The pulse frequency was increased by 95 steps à 245 kHz. Each data point represents the median value of 5,000 frames. The DCDE gain was selected at 3.3 times the lowest possible gain. The two-tier behavior of the pixel (signal compression) is clearly visible with a steep rise related to the internal gate region up to a kink, followed by a significantly lower gain in the overflow region. Right: Parameterization of the same pixel charge curve by a polynomial of 6th degree.

[41] Adjustment of the laser amplitude and/or laser pulse width accordingly.

[42] A compromise between an accurate reproduction of the curve and avoidance of overfitting problems.

One can do this parametrization readily for all 9 pixels of Figure 7-18 and store the respective polynomial terms (7 including the constant term) in an individual array for each pixel. The diagrams of the recorded charge curves and the corresponding polynomial fits are displayed in Figure 7-22.

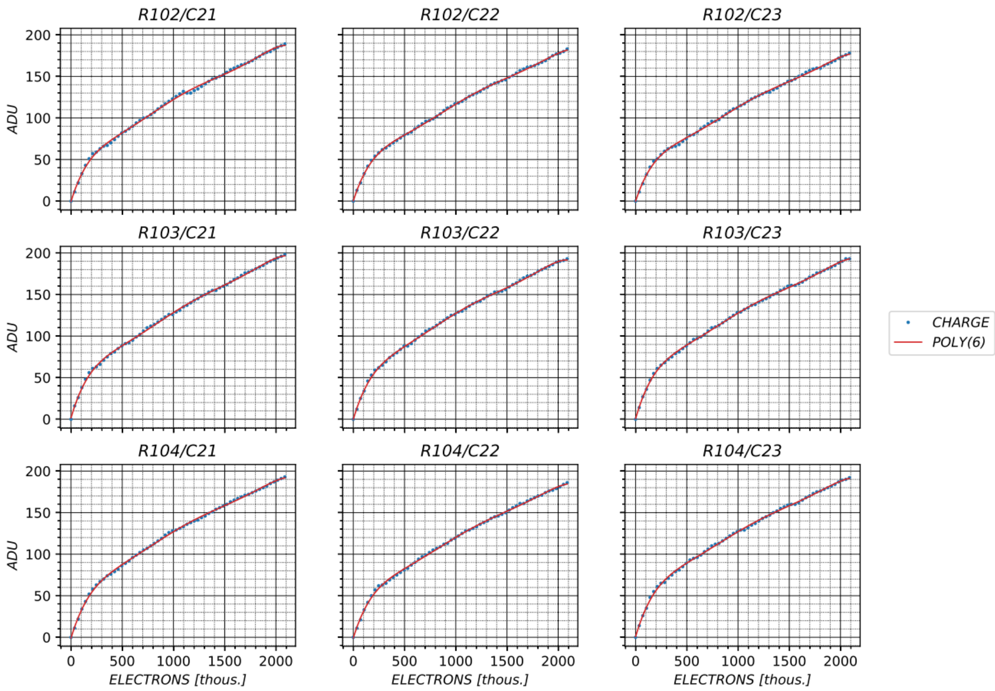

Figure 7-22: Selection of charge curves for a 3×3 pixel array and their respective 6th degree polynomial fit.

Although it is theoretically possible to hit every ADU value of a pixel (despite its non-linearity) with equal frequency steps, this is impractical and not necessary. As one can see from Figure 7-22, all charge curves show a similar shape and can be – in the broadest sense – understood as a combination of two straight curves. They deviate just in the steepness of the internal gate region along with their internal gate capacities (determining the position of the kink) and by their overflow slopes. As an example, whereas pixel R103/C21 reacts with an ADU value of over 190 on 2 million stored electrons, pixel R102/C23 just produces 170 ADU for the same charge injection.

7.3.4.3 Polynomial Calibration Procedure

All further recorded ADU values could now be brought to a common scaling by linking them to the registered charge curve. In other words, for a given ADU value of a specific pixel, the respective charge level from the memorized charge curve had to be looked up. Mathematically, this can be expressed as the search for the root:

Equation 7-8 $$f(x) - y = 0$$

With the polynomial parameters at hand, it is possible to reverse the cause-effect relationship: given a specific output value, which input value can be inferred? Computationally, this can be implemented with a Newtonian solver algorithm. However, in order to speed up[43] the calibration process, it was more efficient to generate a 1-D array of a lot more electron data points[44] and to compute the y/ADU-values in question with the pixel specific polynomial. Then, a simple lookup algorithm detected the closest electron value for the actual measured ADU score. In a last step, the determined electron number was reconverted to ADU by applying the reference pixel's polynomial.[45]

Switching back to the 4-pixel "corner" example above, the outcome is completely different: as one can see in Figure 7-23, 100 ADU of the respective pixel corresponded originally to about 720,000 electrons. At the corner, this charge split up to 180,000 electrons for each pixel. If the sensor recorded an ADU value of 51 for each of the 4 corner pixels, one now directly inferred about 180,000 electrons from the individual charge curves.[46] This time, the 4 ADU values were not added together but their respective electrons. From the assembled electron amount of 720,000 then the correct ADU value of 100 was restored. In summary, the program delivers the correct input value to a given output value, regardless of signal compression, i.e. different internal gate capacities and/or different amplifications.

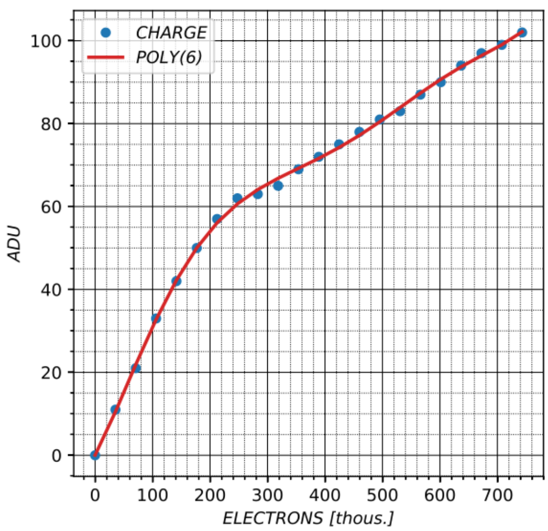

Figure 7-23: Charge curve pixel R104/C21 (zoomed in). The relation between internal gate and overflow region gain slope was measured at about 3.56.

[43] In total, 45×46 scanning points, for each of them a 5×5 pixel array was recorded. Most of these arrays consisted of zeros and one single pixel value, but also up to four values at the corner points.

[44] From the respective polynomial parameters.

[45] In this particular case, the central pixel was taken. In general, a synthetic pixel with the median ADU value should be selected.

[46] In this hypothetic example, the corner pixel response functions were assumed to be identical.

The outcome of this algorithm applied to all scanning points of Figure 7-18 is presented in Figure 7-24. Only a few spots stick out (visible in the zoomed-in diagram), but by and large a homogeneous sensor profile was achieved.

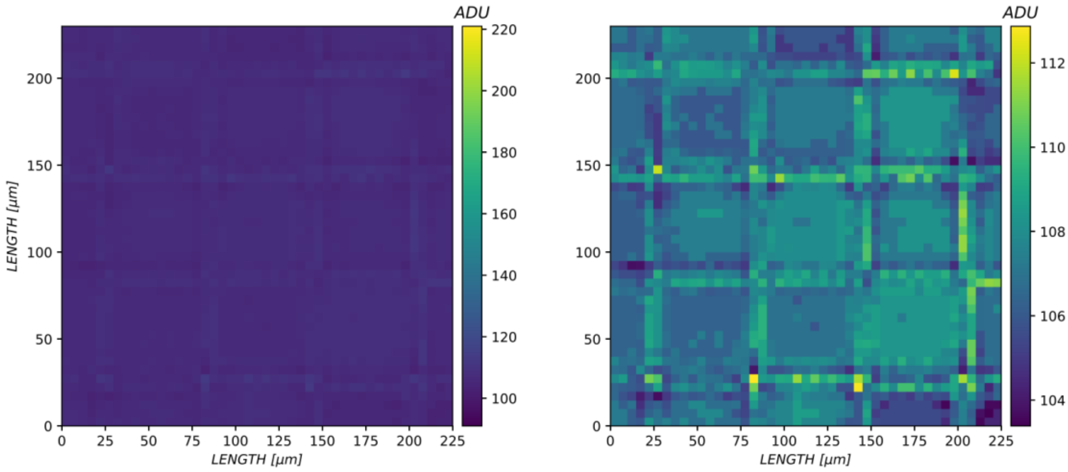

Figure 7-24: Left: Calibration of a 5×5 pixel area, illuminated with a constant laser beam using the same scale as in Figure 7-18. Right: Zooming-in of the same area. The divergence was substantially reduced with the exception of a few outlier points. The center of each pixel varies just between 106 to 108 ADU (originally between 95 and 109 ADU).

7.3.4.4 Straight Line Calibration Approach

There is one important consideration, which has not been discussed yet: time, required to calibrate all pixels of a DH80k FPA with 4 modules à $512 \times 512 = 262{,}144$ pixels. With the proposed approach and the original equipment this cannot be reasonably implemented. A typical charge curve recording for the prototype sensor consisted of the following steps:

- set a frequency step for the pulse generator by the computer: 0.1 s
- record 5,000 frames and store the median value: 0.5 s
- set the next frequency step …

The above described charge curves were recorded with 71 frequency steps, so one single charge curve alone took almost 43 seconds.

Worse, in order to guarantee that the focused laser is positioned to the central area of the beam (the central area covers about $30 \times 30\ \mu m$ see Figure 7-16) the motorstage should not exceed a step width of 15 µm and the curve with the highest ADU values for the relevant pixel should be selected.[47] Anyway, this approach is highly inefficient, since it increases the total measurement time by another factor of 16. Therefore, a much smarter proposal was needed.

As a first step, the angle between the motorstage and the sensor can be relative exactly determined from a small scanning section as for example from Figure 7-17. With the

[47] The move of the motorstage itself consumes little time: the highest achievable speed in the data sheet is 1.5 mm per second or about 0.01 seconds per 20 µm move.

knowledge of the correct angle, one can position the laser spot in the center of a start pixel and adjust the motorstage movements in such a way, that it is possible to move ahead in 60 µm steps.[48] Additionally, some better external equipment could be acquired, which would reduce the intermediate switching and repositioning operations almost to zero.[49] Since the detector consists of 4 independent modules, it would be also advisable to perform the calibration process in parallel. Anyway, the real bottleneck remains the data recording: the final detector is able to produce about 8,000 fps (duty cycle of 10%). 5,000 frames would require 0.625 seconds, in total one charge curve of 71 frequency steps would require about 44 seconds. Applied to 262,144 pixels (just one module, if a parallel process is assumed) this would take over 134 days. Sure, one could reduce the recorded frame number for the averaging, but this would still mean a long time of permanent operation.

When analyzing this problem carefully, one might wonder whether it is really necessary to record a charge curve with 71 data points. Contemplating the characteristic shape of the charge curves it appears, that the same curve can be approximated with a combination of just two straight lines intersected by a kink, which effectively marks the extension of the internal gate capacity. The only necessity are two charge points in the internal gate region and two charge points in the overflow region (with reasonable distances each). In essence, this approach reduces the required calibration time by a factor of almost 18, still a few days of continuous recording, but definitively manageable. The calculation of the slope parameters as well as the intersection points is an easy algebraic task, the resulting straight lines are presented in Figure 7-25.

[48] The specs from the used motorstage data sheet indicate a high precision of 2,5 µm on a length of 25 mm.

[49] With 60 µm moves, the motorstage itself needs about 0.04 s at its fastest pace. Anyhow, for 1 million pixels this small delay alone amounts to a total duration of over 11 hours. More elevated systems are faster by a factor of 1,000 and even more. Another optimization concerns pulse generators with the possibility of uploading the frequency array into the memory, so only a start trigger from the computer would be necessary, which reduces switching times significantly.

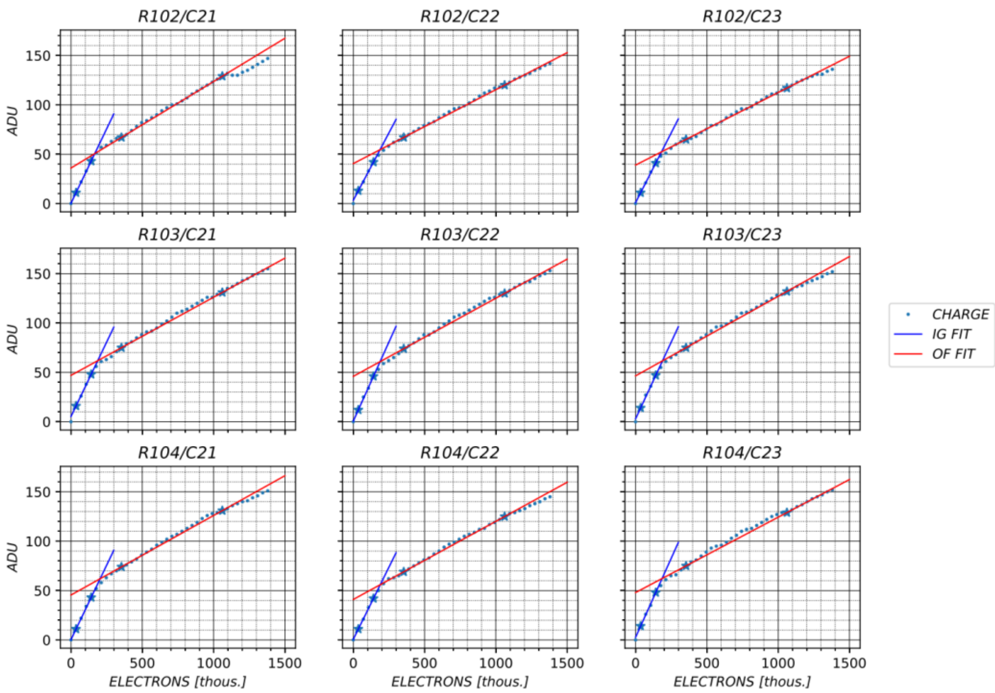

Figure 7-25: Reconstruction of 9 pixel charge curves with two straight lines using just two data points (marked with a star) for each line. Compared to Figure 7-22, the dynamic range was reduced to about 150 ADU.

Admittedly, this approach overestimated the size of the internal gate region (depending also on the chosen data points) and sometimes deviated significantly from the real data, especially for higher charge injections (> 1 million electrons), as noticed e.g. for pixel R102/C21.[50] On the other hand, this method delivers some rewarding insights into the specific characteristics and variances of the considered pixels. Armed with the new generated characteristic parameters, one can now visualize the distribution of the different pixel gains, resulting from the division of the individual pixel slope by the average pixel slope for both regions. One might extract additional information by relating the internal gain vs the gain of the overflow region or the variations of the kinks as a proxy for the internal gate capacity. An overview of all these parameters with respect to the selected scan area is provided in Figure 7-26.

[50] As one can observe from Figure 7-22, there is a slight curvature at higher ADU values. Nevertheless, one should not put too much emphasis on that region, since in the standard scenario a maximum injection of about 100 electrons per pixel and per frame is expected and this would create just about 778,000 electron-hole pairs [192].

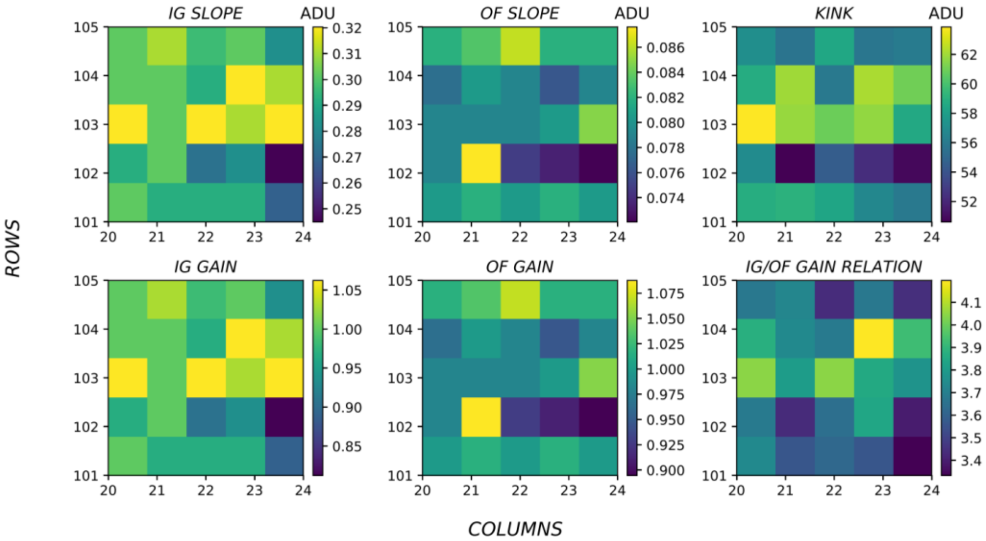

Figure 7-26: Distribution of different slope parameters on the matrix section presented in Figure 7-18. The IG and OF gains are expressed in units of the central pixel's (R103/C22) gain. The IG/OF gain relation compares the amplifications between internal gate and overflow region and ranges between 3.4 and 4.1. Even for this small area, the kink as a proxy for the internal gate capacity shows a relative high variability (between 52 and 62 ADU).

The calibration goes along the method described before: the only complication is an additional intersection point (Ix_{ij}, Iy_{ij}), which acts as a demarcation between the internal gate and the overflow region. Mathematically, the respective electron amount els_{ij} for a given ADU value ADU_{ij} can be calculated with the slope parameters $k_{ij}^{IG}, d_{ij}^{IG}, k_{ij}^{OF}, d_{ij}^{OF}$ by reversing the straight line equation:

Equation 7-9

$$els_{ij} = \begin{cases} \dfrac{ADU_{ij} - d_{ij}^{IG}}{k_{ij}^{IG}} if\ ADU_{ij} < Iy_{ij} \\ \dfrac{ADU_{ij} - d_{ij}^{OF}}{k_{ij}^{OF}} if\ ADU_{ij} \geq Iy_{ij} \end{cases}$$

where ij denotes the index of the respective pixel. Again, a reference pixel had to be chosen in order to convert the electron amount back to an ADU scaling. The algorithm uses two trivial straight line equations for the center pixel with the intersection point Ix_{ij}^{c}. A comparison with the polynomial method is shown in Figure 7-27.

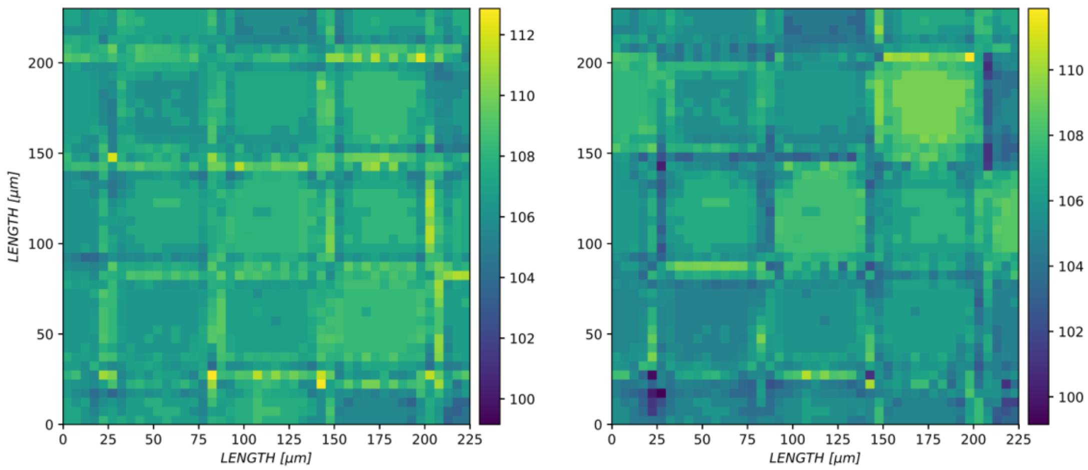

Figure 7-27: Left: Calibration of an EDET sensor pixel section by the polynomial fitting method. Right: Calibration of the same area derived from two straight lines (the slopes represent the gains of the internal gate and overflow region together with an intersection point, which serves as a proxy for the internal gate capacity). Both methods significantly reduce pixel divergences, however the second approach is superior in terms of calibration speed.

7.3.4.5 Top Hat – Towards a Flat Field Calibration

To speed up the sensor calibration once more, a last adjustment screw, which has not been touched yet, must be turned: the simultaneous calibration of a larger pixel area. However, this suggestion needs one specific requirement: the creation of a uniform or also called “flat-field” illumination. [51] Only under this condition the sensitivity variations between the different EDET pixels can be reliably measured. It is mandatory, that each pixel within the homogenous illumination zone gets the same charge (within some predefined tolerance level), otherwise the calibration would be useless. Simply using a defocused Gaussian beam would fail, since the characteristic shape is conserved: the pixels directly hit by the central beam get the peak charge, while outside pixels receive radial decreasing intensities along a Gaussian curve.

If continuing with a laser illumination, at least one additional refractive optical component must be introduced in order to reshape a Gaussian laser beam (TEM_{00}) into a uniform flat-field (also called “flat-top” or “top-hat”) profile. As an example, the GTH-4-2.2 [141] beam shaper lens converts an infrared Gaussian beam into a square top-hat profile. For the experimental setup, some additional calculations and work must be done. First, the lens specifications foresee an input beam with a diameter of $\emptyset = 4mm \pm 0.15mm$ $(@\,1/e^2)$. Rearranging Equation C - 3 for the 660 nm wavelength, this corresponds to a relative short distance of

$$z = z_0 \cdot \sqrt{\left(\frac{w_z}{w_0}\right)^2 - 1} \approx 21\,mm$$

[51] Needless to mention, that this will bring down the total calibration time by the amount of homogeneous illuminated pixels. Additionally, a cumbersome correct positioning of the initial laser pulse and an investigation of the correct angle between motorstage and sensor can be omitted.

from the laser focus position to the top-hat shaping lens.[52] If needed, an additional beam expander can adjust the effective beam diameter to the design input parameter. In contrast to the usual experimental setup, the alignment has to be carried out in lateral direction with the beam shaping lens mounted in a ring holder. An additional focusing lens is required to Fourier-transform the top-hat image into the focal plane. The free aperture has to be at least 2.2 times bigger than the beam diameter and the focal length[53] (f) of the focusing optic can be calculated as follows:

Equation 7-10
$$\text{top hat width} = \frac{2.2}{1000} \cdot \text{f}$$

In order to get a $1 \times 1\, mm^2$ sensor area illuminated (comprising $16 \times 16 = 256$ pixels) a focusing distance of about 45 cm must be reserved.[54] The homogeneity is stated at $\pm 5\%$ relative to the average intensity within the top-hat profile, this means, high-low differentials of up to 10% are possible as outlined in Figure 7-28.

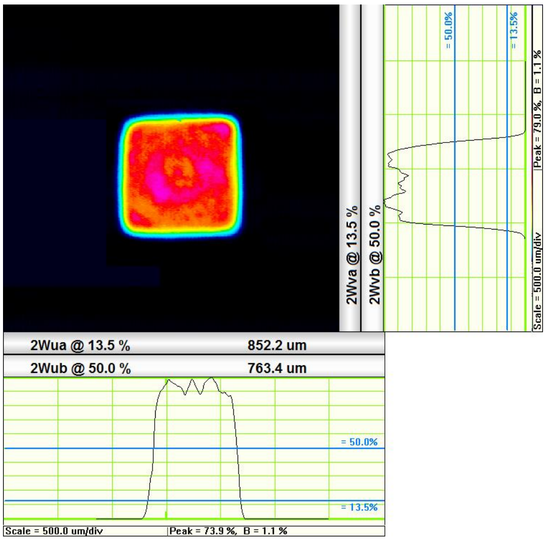

Figure 7-28: TopHat GTH-4-2.2 intensity profile (courtesy of TOPAG Lasertechnik GmbH).

7.4 LED Pixel Calibration

7.4.1 General Considerations

Alert readers might reason, if it is possible to calibrate large pixel arrays in parallel, one could even think about a whole sensor calibration in a single sweep. Essentially, this concerns the search for a more efficient calibration source, even though the basic two requirements remain the same: first, it must be ensured that every pixel sees the same intensity. Second, the illumination intensity must be adjustable in order to generate individual charge curves for each EDET pixel.

[52] The beam propagation ratio M^2 has to be 1.4 or better.

[53] Working distance.

[54] For this particular lens, top-hat edge lengths of up to 2 mm can be realized.

The characteristics of a light emitting diode (LED) also seem to perfectly fit both requirements from above. However, the initial conditions for the sensor calibration get turned upside down: the single pixel calibration approach requires a collimated beam with little divergence, focusable to a tiny spot. By contrast, the whole sensor illumination preferably investigates a diffuse light source. The photons should impinge on the sensor as evenly distributed as possible to create a homogeneous flat-field. Unlike lasers, LEDs emit incoherent light and the further one vertically moves away from the sensor, the more uniform distributed the light becomes for a given area. The degree of diffusion can be additionally increased by artificial means.[55]

7.4.2 LED Description

For the test setup, a high power infrared emitter from Osram (SFH 4235 Platinum DRAGON [142]) with a centroid wavelength at $\lambda = 850\ nm$ was used. It features relative short rise and fall times at 7 ns and 14 ns respectively.

First and foremost, LEDs are current driven devices, even though they can be also operated in a pulsed mode, like a laser. Initially, a high-speed LED driver circuit for ns-pulse switching[56] [143] was used for the calibration. However, this board seemed to be usable to a limited extent, since at higher frequencies (9 MHz) the output became unstable.

In the following, a brief overview/recap touching the construction and principles of operation of LEDs should be given. As the name suggests, LEDs belong to a special type of semiconductor diodes that emit light when electrically biased. They are closely related to standard diodes with a typical p-n junction, which has to be biased in forward direction. If the positive electric voltage to the p-type material (anode) exceeds some threshold voltage (2.5 V for the SFH 4235), it will force free charge into the **depletion zone** where electrons recombine with holes and release energy by emitting electrical radiation (electroluminescence).

LED producers prefer semiconductors with a direct band gap[57], since most of the energy should be released in the form of light after an electron in the conduction band recombines with a hole in the valence band. In the other case of an indirect band gap, a much higher amount of energy gets dissipated in form of heat. As the photon flux from the junction radiates uniformly in all directions, the industry is investing many efforts to increase the extraction efficiency [140]: for instance, some LEDs consist of a metal base with a concave area, serving as a reflector. Also the geometric design can facilitate the escape of a greater light fraction. In addition, it has become common practice to roughen the planar surface of the LED layers or to provide it with a texture. To further improve the

[55] E.g. sand-blasted aluminium plates or integrating spheres (also known as Ulbricht Kugel), which contain reflective walls where the incoming beam undergoes multiple diffuse reflections.

[56] The optical rise and fall times could be reduced further down to 2.6 ns.

[57] Infrared LEDs are usually made of Indium Gallium Arsenide.

radiant yield, especially high power LEDs use several stapled layers, with a more reflective level beneath the emission layer (e.g. a distributed Bragg reflector) compared to the one above (resonant cavity LEDs).[58]

For the selection of a suitable LED, the necessary information is provided by the datasheet: the term “forward current” indicates, how much current flows across the LED's leads, from anode to cathode (e.g. max. 1,000 mA for the SFH 4235). An increase of the forward current proportionally increases the light output (conditional, that the maximum rating will not be exceeded) but also raises the heat dissipation. Therefore, a great emphasis should be placed on the cooling of the LED. For this purpose, an extra copper holder was designed, as depicted in Figure 7-29 with a mounting stick and a ripped cooling block to efficiently transport away the LED generated heat.[59]

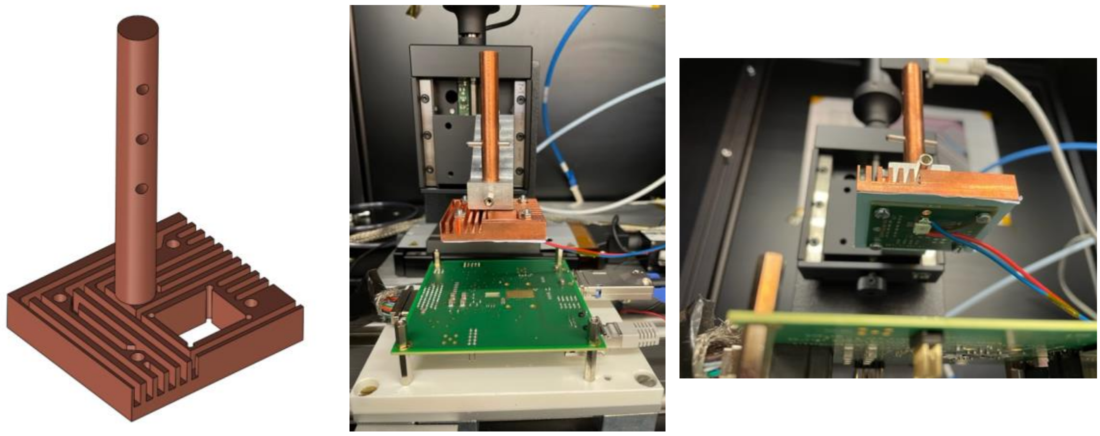

Figure 7-29: Left: LED copper holder with a ripped cooling block, designed to dissipate as much heat as possible.[60] Middle: LED illumination to the backside of the EDET Hybrid Board. Right: The LED was glued on a small PCB and screwed to the bottom of the holder with a thermal pad in between.

The “threshold forward voltage”[61] determines how much voltage the power source at minimum has to supply in order to induce the LED to emit light. The SFH 4245 datasheet suggests a typical forward voltage of 3 V.

The “total radiant flux” expresses the output power by recording the light intensity from all directions (measured by an integrating sphere or a goniophotometer).

A special feature of LEDs is related to the wavelength shift due to higher forward currents. For the SFH 4245, the mean wavelength shifts slightly to higher values and the corridor of possible wavelengths narrows considerably (from originally 125 nm to just 30 nm) at half of the maximum forward current level.

[58] For more about LEDs consult [108].

[59] A first approach with a 3D printed holder was not usable because it was deformed like wax during operation.

[60] Design by Martin Soyer.

[61] Below the threshold forward voltage nothing happens. Once the threshold is exceeded, the forward current exponentially increases with an increasing forward voltage.

To compare different LED designs, the "angle of view" parameter specifies the change of the maximum brightness of the LED when moving in horizontal and vertical direction. This is a very important criterion, since it graphs the intensity decline for different viewing angles and therefore particularly assists the suitability assessment of a flat field illumination.

In our application, the LED was simply soldered on a small PCB and connected by two wires to a power supply at the prescribed typical forward voltage of 3 V. The PCB itself was glued with a thermal conductive pad to the copper holder and mounted on a XYZ-motorstage. As stated, in contrast to the Laser frequency measurements the LED was operated in current mode. The LED powering current can be simply increased by constant forward current steps and hence, one no longer has to care about switching transistor losses, voltage drops on long wires or long wire inductances.[62]

7.4.3 LED Characterization

Ahead of any charge curve generation with a LED, four eligibility criteria have to be examined:

(1) *Linearity*: does an equal increase of the LED input current lead to an equal rise of the LED intensity?
(2) *Stability*: does the LED intensity remain stable over a certain period?
(3) *Reproducibility*: does the LED output deliver the same result if repeated with the same settings?
(4) *Homogeneity*: is the LED light emission equally distributed across a certain area or equivalently, does it resemble to a flat-field?

Once again, the first three criteria can be tested with the well-tried photodiode. Prior to this, the vertical distance between the LED and the photodiode should be fixed, since there is a trade-off between light homogeneity and light intensity. A larger distance between the LED source and the sensor certainly benefits the desired flat field. On the other hand, the intensity decreases by the inverse square law and, at some critical distance, the illumination might be insufficient to produce full-range charge curves for the sensor pixels.[63]

Anyway, for a comparison of quantum efficiencies, the LED source distances between the reference photodiode and the EDET sensor must be exactly measured. Given a distance of about 6 cm, a small difference of just 3 mm already leads to an intensity deviation of 10% $(6^2/6.3^2 \approx 0.9)$.

[62] Pulsed LEDs pull charges from the nearby capacitor and then try to pull power from the PSU. Since wires exhibit inductance and currents cannot change instantly, this in turn could potentially cause the voltage and herewith the LED brightness to drop.

[63] The intensity reasoning is subordinated. Instead, one can use stronger or multiple LEDs.

7.4.3.1 LED Linearity

Figure 7-30 depicts the photocurrent generated by an increase of the LED forward current in 410 single 1 mA steps. The measurement procedure[64] consisted of 10 seconds recording time, the determination of the median output value, an increase to the next forward current level, another recording interval of 10 seconds and so on. At a cursory glance, the photodiode response curve in the left diagram resembles a straight line. However, a closer look at the differences of consecutive current steps exhibit substantial variations, mainly caused by a LED heat-up. To better control this variable, a lot of adaptions to the timing procedure were investigated. The following sequence delivered acceptable results: turn on the LED, wait 1 second, record data for another second, turn off the LED, wait 2 to 30 seconds[65] before the next forward current rise. The outcome of the optimized operational procedure is presented in Figure 7-32.

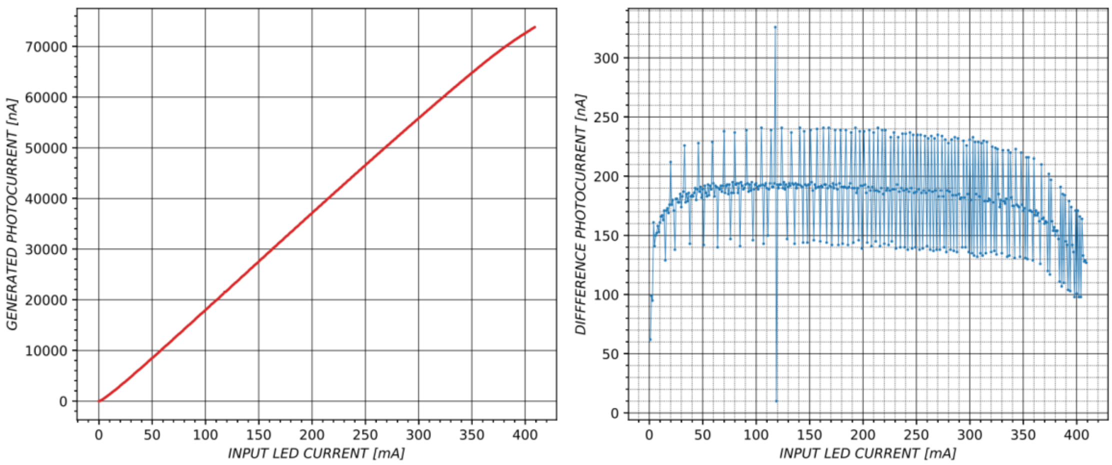

Figure 7-30: Left: Measured Photocurrent from a Hamamatsu S-4584-06 photodiode. The LED input current was increased 410 times by 1 mA steps. Right: Differences of generated photocurrents for consecutive increases of the LED intensity.

The light intensity seems to increase directly proportional to the forward current, at least over a wide range. However, the charge differences at the curve's low intensity end, depicted in the right diagram of Figure 7-32, follow rather a logarithmic growth path up to a forward current of around 50 mA. After fading out to a more or less constant level until a forward current of 300 mA, the charge differentials experience a pronounced decrease.

The observed curvature at the front end was not pleasant, but could be corrected along the method introduced for the laser calibration: the measured photocurrent level PC_{50mA} at the LED input of 50 mA set the reference point. The next step fitted a straight line to the linear region, i.e. the data points between PC_{50mA} and PC_{300mA}. From the straight line's slope, the required forward current FC_{adj} to produce the same photocurrent as for

[64] Measured by a Keithley 2612B source meter.

[65] Depending on the forward current level to provide enough time for a cool down.

PC_{50mA} was inferred. Since the adjusted value was apparently lower than for the initial PC_{50mA}, all forward current data points above 50 mA had to be corrected by a constant factor of $(50\ mA - FC_{adj})$. Accordingly, the front end was replaced by the proportionate, adjusted range.

Similar to above, a polynomial was fitted to the original photocurrent values up to PC_{50mA}. The adjusted forward current level, given a certain photocurrent, was determined by a horizontal comparison of the polynomial value and the straight fitting line, corrected by the constant factor and extending into the new front end.[66] Essentially, the equal forward current steps were replaced by narrower steps at the front side, as can be exemplarily seen in Figure 7-31.

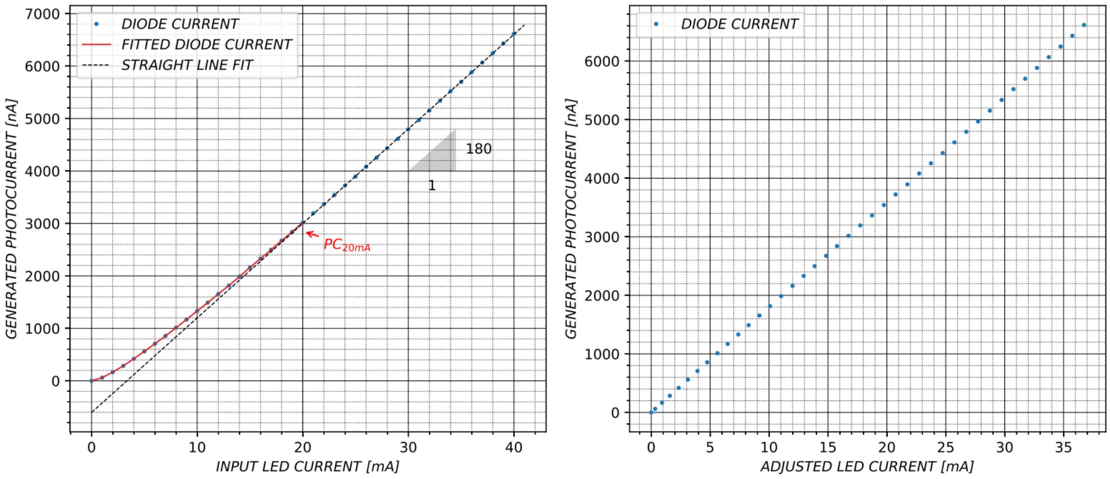

Figure 7-31: Left: Section of the LED current measured with a photodiode (for illustrative purposes the LED input current stops at 40 mA and the pivotal point between curved and straight line area is located at 20 mA). The curvature at the low intensity end significantly deviates from a straight line fit, sketched in by a slope triangle. Right: Linearization of the curvature by adjusting the selected step width, which leads to much narrower step sizes at the curve's front end.

Another method for the front end linearization of the LED output curve adopts the exact opposite way: how much forward current would be needed to increase the photocurrent level uniformly as for a hypothetical linear curve. Now, the input forward current steps at the beginning were stretched before converging to equal sizes above the level of 50 mA. The new input current steps were derived from the extrapolated straight line fit and entered into the inversion of the polynomial. The second method offers the advantage that the injected charge[67] steps remain constant and can be directly tuned to the calibration points from a radioactive source, while for the first method the forward current curve can

[66] In theory, a polynomial would not be needed. The photocurrent points have to be only horizontally matched with the points from the fitting line and the corresponding adjusted forward current levels. Nonetheless, the polynomial approach smoothes out some outliers and other aberrations.

[67] Instead of the forward current steps.

only be used as an operand and must be calibrated by the respective electron charge injection.

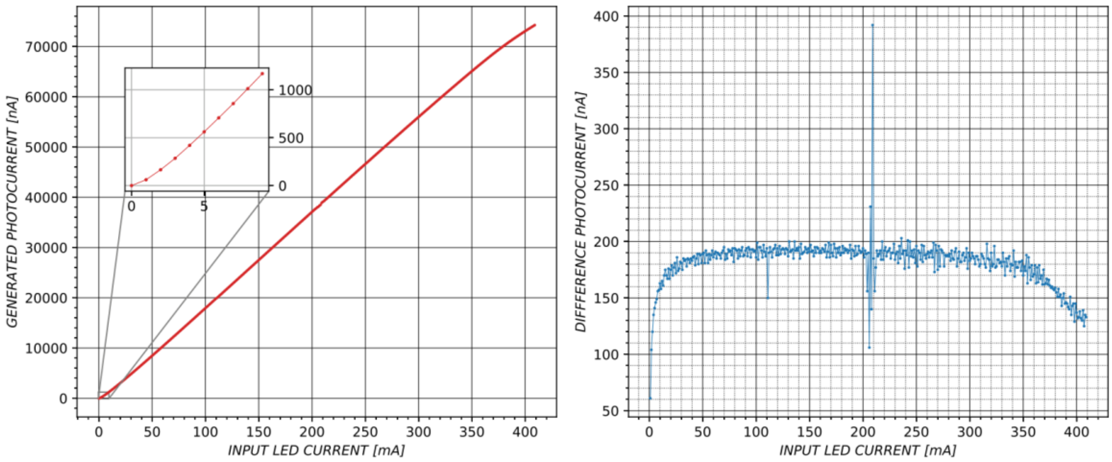

Figure 7-32: Left: Same structure as in Figure 7-30, except for a different recording procedure: this time the measurement cycle started with turning on the LED, followed by a waiting time of one second, data recording for a further second (over 20 raw data points), calculation of the median value, then turning off the LED and waiting for 2 to 30 seconds in the idle state (dependent on the forward current level). The inset depicts the front end of the curve, exhibiting still some curvature. Right: Differences of subsequent photocurrent data points. From 50 mA to 300 mA the subsequent photocurrent increases now oscillate within a comparable narrow range with the exception of an extraordinary spike in the middle, which arose recurrently. This spike was not further investigated, since the polynomial fitting applied to the sensor charge curves will flatten away such outliers. The observed decline at the back end sets the operational limit for the LED illumination.[68]

A closer inspection of the LED output curve in Figure 7-32 reveals, that the net increases of successive photocurrents can deviate up to 30 nA. Since 1 Ampere amounts to $6.24 \times 10^{18}\ e^-/s$, 30 nA correspond to a quite decent sum of electrons: $18.7 \times 10^{10}\ e^-/s$. However, to ensure comparability with the EDET sensor, several corrections have to be made: first, the area of an EDET pixel comprises $60 \times 60\ \mu m^2$, which is by a factor of 972 lower (photodiode $1 \times 3.5\ mm^2$). Second, an Ampere unit references an interval of 1 second, while the target read out frequency of the EDET sensor provides 80,000 frames per second (the small sensor of the test setup delivers almost 298,000 frames). If both factors were taken into consideration, the amount of comparable electrons for an EDET pixel reduces to just

$$\frac{18.7 \cdot 10^{10}}{972 \cdot 80{,}000} = 2404\ [e^-/\text{pixel}/\text{frame}]$$

for the large module and for the small matrix to just 645 electrons/pixel/frame, under the assumption of the same quantum efficiency as for the photodiode.

[68] Higher forward current values should be manageable with a better cooling device.

7.4.3.2 LED Stability

Concerning the second criterion (2), the investigation focused on the measured photocurrents from the LED, which should remain stable within a certain period.[69] The used source meter was able to register over 20 measurements within one second. As shown in Figure 7-33, the measured photocurrent variations are within a single or low double digit range for LED forward currents up to 200 mA. At 225 mA and higher, a downward degradation of about 80 nA occurred within 1 second measurement time, although this must be set in relation to the total level of 41,700 nA and 55,800 nA respectively. For the charge curve measurements this degradation will be mitigated, since the recorded median value catches just about half of the downward shift.

If the duration of the data taking was increased to 2 seconds, the picture was pretty much the same with the exception for the highest LED input current at 300 mA, where the total decline now amounted to over 150 nA. If the LED was maintained in the on-state for significant longer periods (up to 10 seconds), a stable output could only be realized up to a forward current of 50 mA. Beyond, the generated photocurrent decreased considerably by 340 nA for the highest LED intensity.

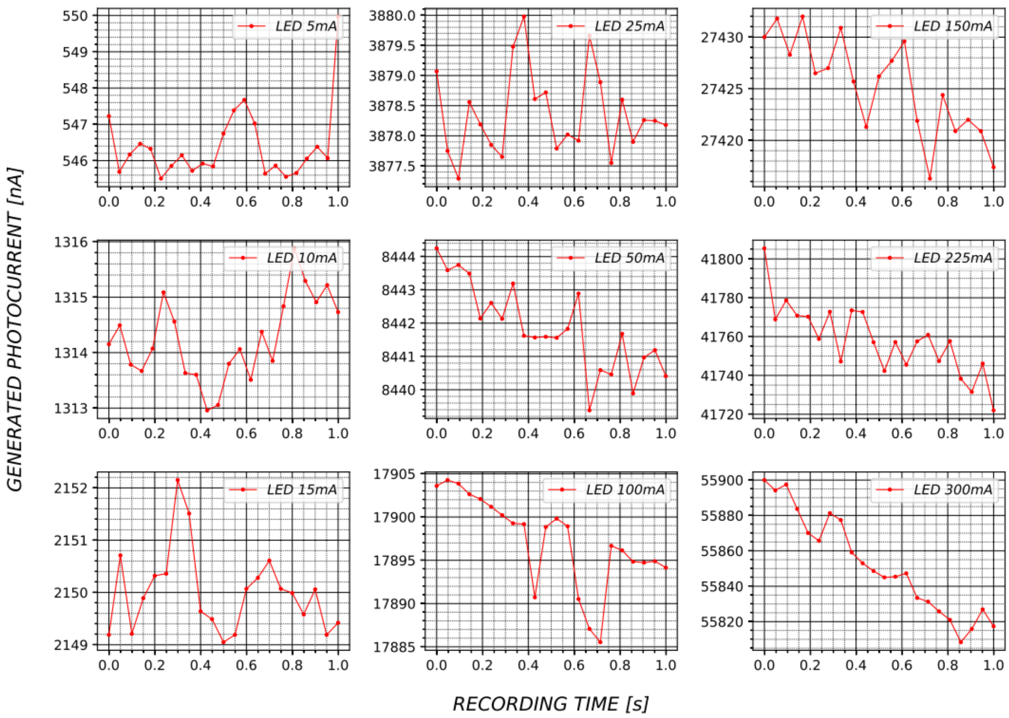

Figure 7-33: LED stability analysis. The following measurement procedure was implemented: turn on the LED – wait 1 second – measure over 20 photocurrent levels during the prescribed recording time (1 second in this case) – wait 30 seconds – switch to the next current level.

[69] On a less stringent requirement, the basic scenario of data collection within a time period of 1 second should show only low fluctuations.

7.4.3.3 LED Reproducibility

With respect to criterion (3), the intention was to check, if the same experimental settings deliver the same results if repeated. A recorded charge curve would be useless for calibration if a repeated measurement under identical conditions would deliver different results. For this purpose, the measurements were repeated one hundred times according to the measurement suite for criterion (1). As presented in Figure 7-34, the deviations are again very small even for higher currents.

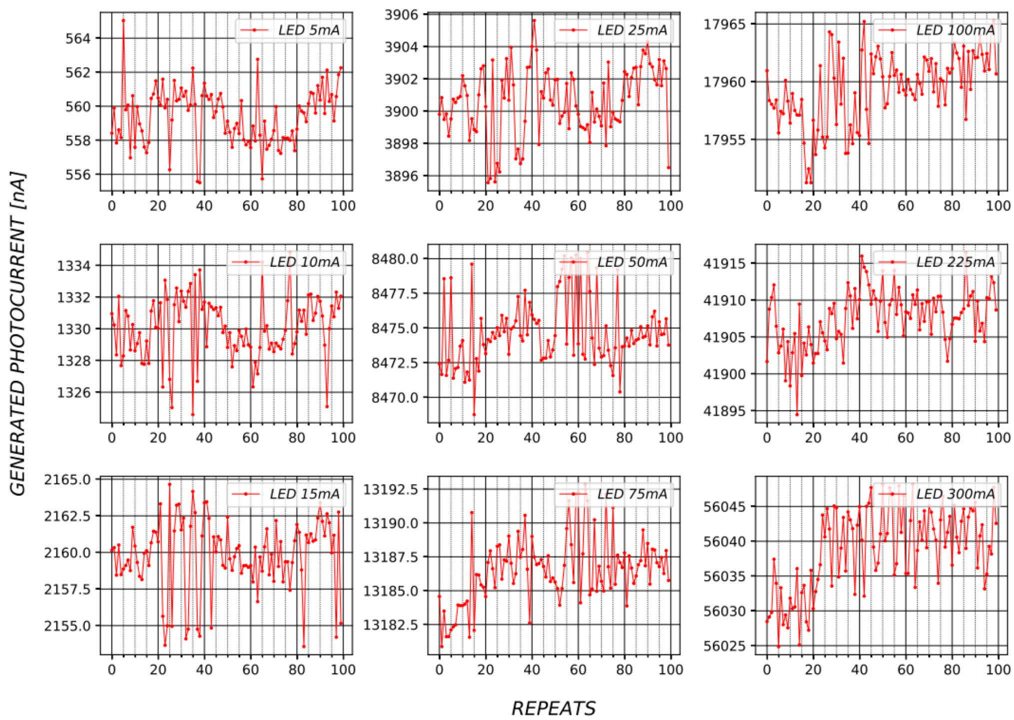

Figure 7-34: Repeating one hundred times the standard measurement procedure described for criterion (1).

7.4.3.4 LED Homogeneity

After the evaluation of the first three criteria, it was time to turn to the EDET sensor for an assessment of the LED homogeneity. Beforehand, a few theoretical considerations should be made. According to Lambert's cosine law, the intensity observed from a perfect diffuse radiation source depends on the cosine of the angle between the direction of the incident light and the normal to the surface [144]:

Equation 7-11 $$I_R = I_{R0} cos\theta$$

where I_R is the radiant intensity, I_{R0} the perpendicular radiance and θ_R the angle between the viewing direction and the normal to the surface. On the assumption, that the light source was positioned exactly over the center of a small rectangular matrix with 7.68 mm length[70], the intensity differences to the edges should diminish with increased source – sensor distance. Table 7-3 lists different source – sensor distances and the calculated intensity decreases. For as little as 3 cm, the radiant intensity difference already decreases to less than 1%. To be on the safe side, a distance of 6 cm was chosen for all performed LED measurements. According to [145], the intensity profile of a LED will tend towards a Lambertian emitter, if the system randomizes the angular distribution of light, which is definitely the case for the used LED.[71] Another evidence for the LED as a Lambertian radiator can be inferred from the angle of view parameter in the LED data sheet, where the off-axis illuminance declines very close to the cosine of the angle.

Distance Source-Sensor	*Sensor mid-edge extension*	θ_R	*Norm-Intensity*	*Edge-Intensity*
1	0,368	0,353	1	0,938
2	0,368	0,183	1	0,983
3	0,368	0,122	1	0,993
4	0,368	0,092	1	0,996
5	0,368	0,073	1	0,997
6	0,368	0,061	1	0,998
7	0,368	0,053	1	0,999
8	0,368	0,046	1	0,999
9	0,368	0,041	1	0,999
10	0,368	0,037	1	0,999

Table 7-3: Comparison of small EDET matrix central and edge intensities dependent on the distance between radiation source and sensor.

To verify the assumed homogeneity of the LED light, the source was moved in both horizontal and vertical directions. For better clarity, 9 representative matrix pixels were selected as shown in Figure 7-35.

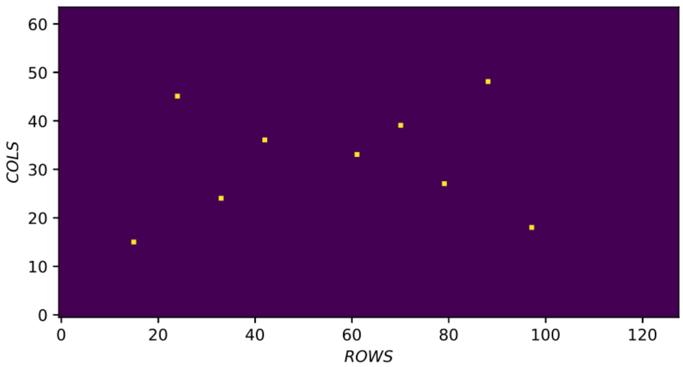

Figure 7-35: Selection of representative pixels for testing the homogeneity of the LED light source. Pixels at the edges were omitted on purpose, because if the LED was moved too far away, the PCB's indentation casted a shadow on the edge pixels.

[70] Corresponding to the longer dimension of a small EDET matrix.

[71] Besides, the usual surface texturing and a lot of back and forth bounces occurring between the top and the bottom surfaces of a high power LED favor a Lambertian propagation significantly.

Figure 7-36 depicts the generated ADU values in the EDET sensor from a constant LED illumination. The LED source was moved in $0.1\ mm$ steps covering an area of $1\ mm^2$ in the horizontal plane. 4 pixels do not show any deviation, while the other pixels show some small variation. For all of these variations there is no clear trend visible, so the deviations can be also attributed to some noise or digitization effects. Anyway, it is fair to assume at least for an array of 16×16 pixels the LED provides excellent flat field conditions.

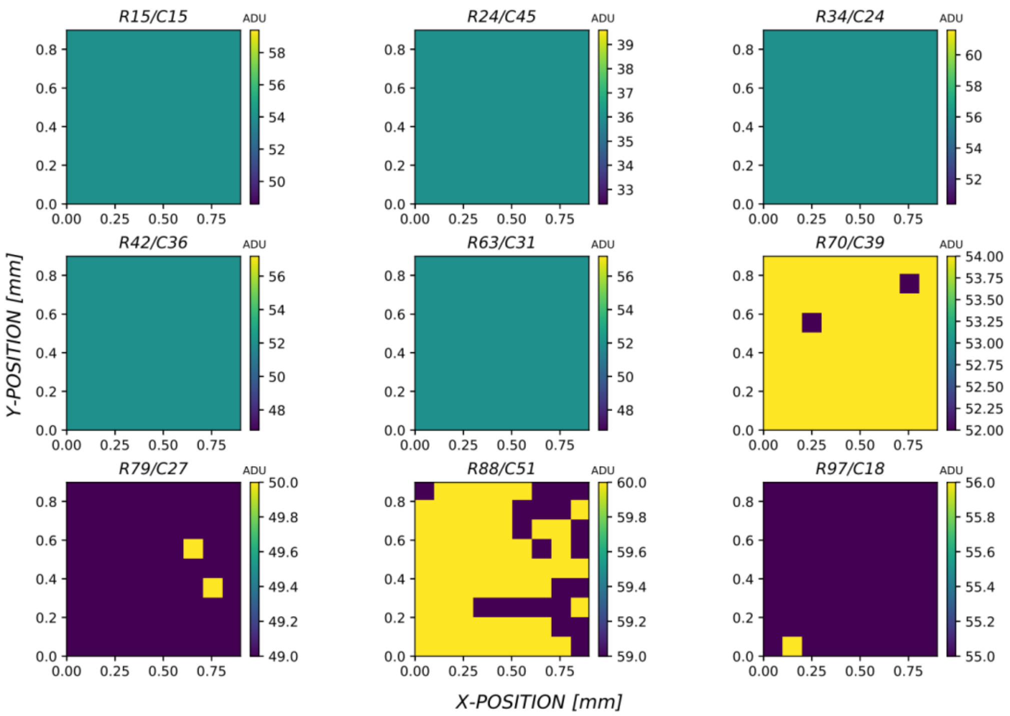

Figure 7-36: Selection of 9 EDET matrix pixels illuminated with a constant LED. The light source was moved by $0.1\ mm$ steps in both x- and y-direction.

Even if the LED was moved over a significant larger array of $5 \times 5\ mm$, as one can see in Figure 7-37, the flat field assumption was largely confirmed.[72] Again, four pixels did not show any deviation, while the ADU level deviated by a maximum of just about 6% for two pixels.

[72] The width of a small matrix is just 3.84 mm.

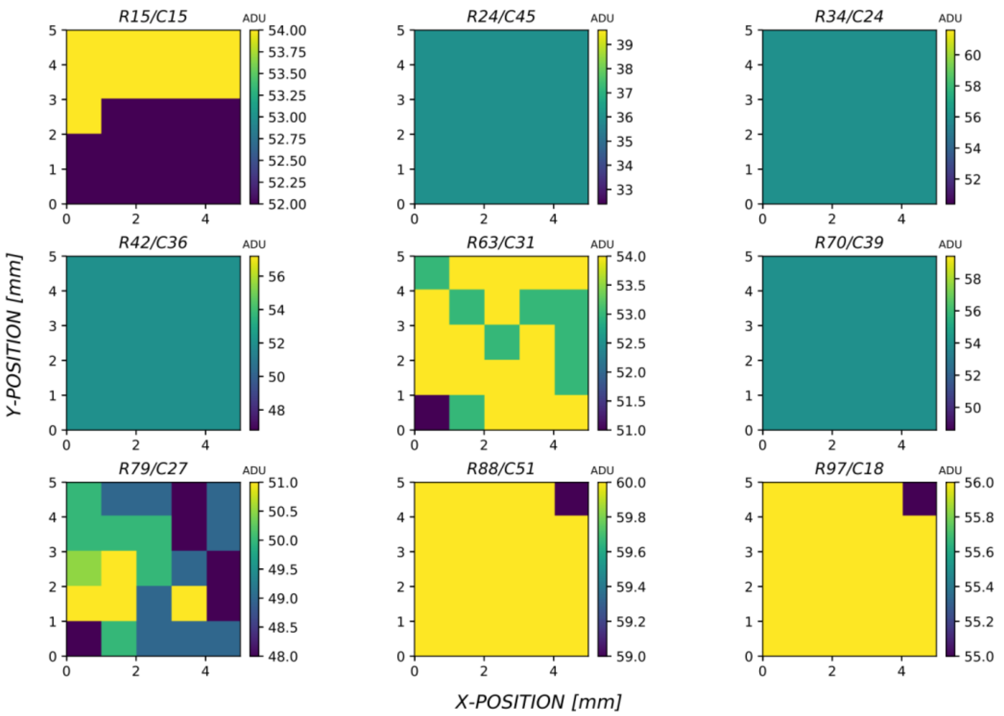

Figure 7-37: Selection of 9 EDET matrix pixels illuminated with a constant LED, moved by 1 mm steps in both x- and y-directions, exposing an area of $25\ mm^2$.

7.4.4 Derivation of an EDET Matrix IR Photon Flux Quantum Efficiency

The quantum efficiency QE of a photodiode relates the number of electron-hole pairs obtainable as a photocurrent to the number of incident photons [146]:

Equation 7-12
$$QE = \frac{S \times 1240}{\lambda} \times 100\ [\%]$$

with $S\ [A/W]$ the photosensitivity and $\lambda[nm]$ the wavelength. The datasheet of the photodiode includes a spectral response diagram, where one derives a photosensitivity of 0.52 for the used LED wavelength at 850 nm. Inserted in Equation 7-12 yields a quantum efficiency of about 76% for the photodiode, so the effective number of incident photons per frame on a hypothetical EDET pixel (under ceteris paribus assumptions) must be upwards corrected to $2404/0.76 = 3{,}153$ photons (849 photons for the small matrix).

To estimate the LED quantum efficiency for the EDET sensor, the following approach was applied: as illustrated in Figure 7-38, the peak of the ^{109}Cd source hit histogram marks the characteristic 22 keV energy line of the selected pixel. The respective conversion response at 32 ADU equals about $22{,}000 \div 3.6 = 6{,}111$ electrons. The ADU level serves as the common base, allowing to infer the corresponding LED forward current value (3.08 mA) from the pixel's individual (unadjusted) LED charge curve.

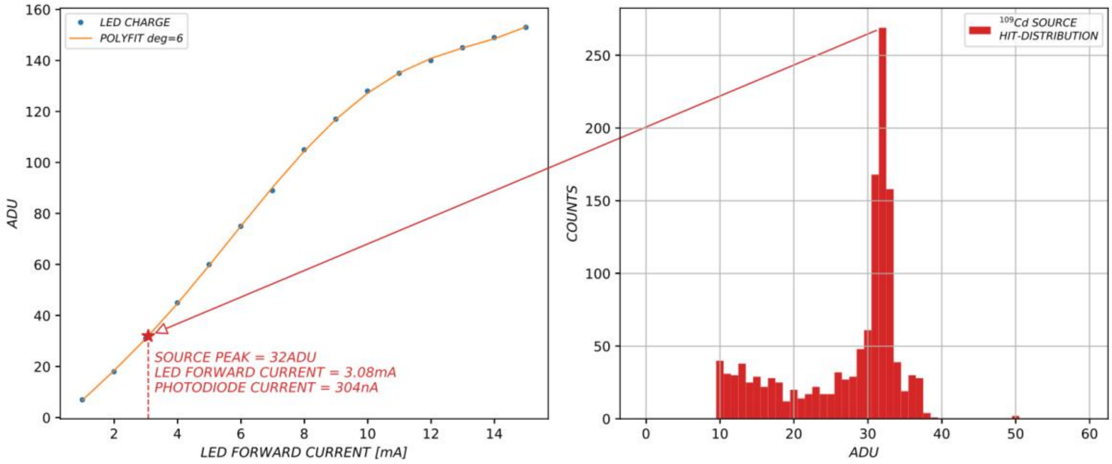

Figure 7-38: Left: Fitted LED charge data of a single EDET pixel. Determination of the equivalent LED forward current (unadjusted) from the ^{109}Cd source peak (32 ADU) by the method described in 7.3.4.3. Right: Corresponding hit distribution from a ^{109}Cd source.

The respective photodiode current for the unadjusted LED forward current of 3.08 mA can be derived by linear interpolation at about 304 nA. With this information at hand, it is possible to calculate the LED quantum efficiency for a single EDET pixel: according to the preceding calculations, 304 nA correspond to $645/0.76 \times 304/30 = 8{,}600$ incident photons. Hence, the QE of this particular pixel can be determined at:

$$QE = \frac{\#\,\text{generated electrons Cd}^{109}\text{source}}{\#\,\text{incident photons}} \times 100 = \frac{6{,}111}{8{,}600} \times 100 = 71\%$$

Reverting back to the observed 30 nA deviation of subsequent LED charge increases, in electron terms this amounts to just one tenth or about 603 electrons for the small matrix. By comparison, a LED forward current level of 300 mA induces about 1.14 Mio electrons within a single pixel for this particular matrix.

7.4.5 Absolute LED Calibration

In theory, the position of the ^{109}Cd source peak should go hand in hand with the pixel gain. To match a given ^{109}Cd source peak, the required LED input ideally remains constant. In other words, there should be no difference if a certain amount of electrons was generated by one high energy photon or by multiple low energy photons. The same number of stored electrons should induce the same drain current and finally convert to the same ADU output level. In order to verify this assumption, the front end of an EDET sensor’s LED charge curve was not fitted with a polynomial as depicted in Figure 7-38 but with a linear regression line. The extracted slopes of all pixel regression lines served as a proxy for the different pixel gains in the internal gate region.

In order to resolve the adjoined peaks (22 keV vs 25 keV) of the ^{109}Cd source, the highest DCDE gain mode was employed. On the downside, a lot of pixels had to be masked (particularly out of dynamic range pixels, but also noisy pixels and drainlines with partially disconnected pixels). Nevertheless, 6,598 out of 8,192 pixels were usable for the analysis. The right diagram of Figure 7-39 depicts the pixel slope distribution ranging from 15 to 35 ADU, a mean value at 22 ADU and a skew to the right.[73] As said, the variability is mainly attributable to process variations, amplified by the shortest of all used gate lengths. The left diagram depicts the distribution of the derived LED input currents (using the slope and y-intercept parameters from the linear regression) which are necessary to match the different ^{109}Cd source peaks.[74]

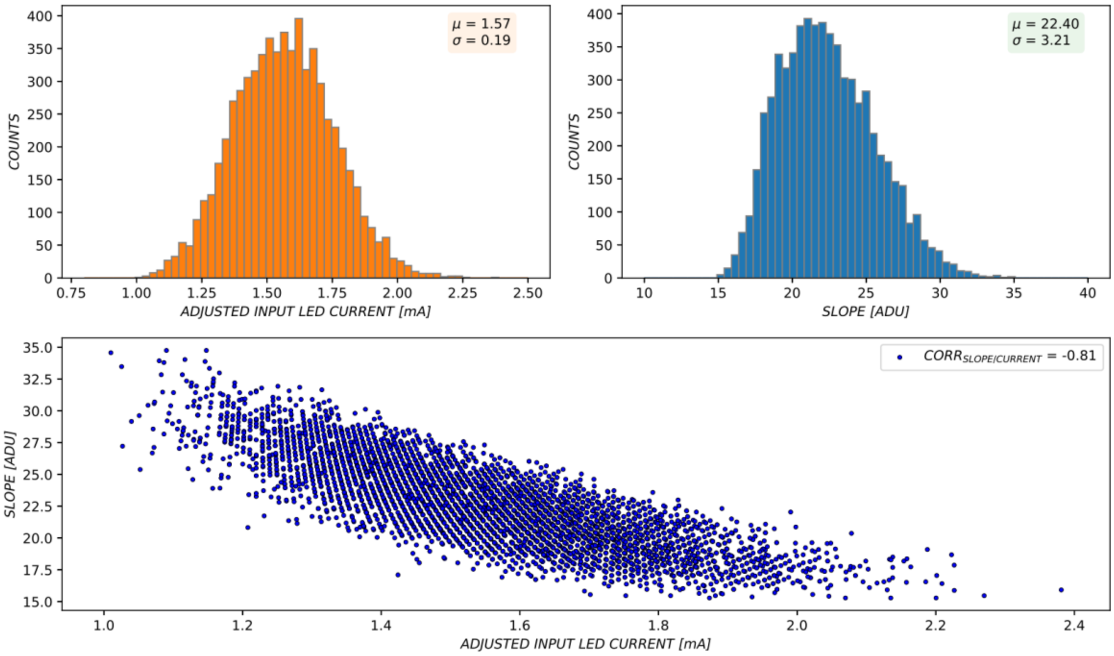

Figure 7-39: Top Left: Distribution of the derived input LED currents to match the corresponding ^{109}Cd source peak ADU values. Top Right: Distribution of the individual pixel slopes (as a proxy for the individual pixel gains in the internal gate region) inferred from a regression line to the first four LED curve data points. Bottom: Correlation between the adjusted input LED current and the resulting pixel slopes.

In case the correlation would have been perfect, the outcome of the derived input LED currents in the bottom diagram of Figure 7-39 would establish a single downward sloping line: the higher the adjusted input LED current, the lower the pixel gain (approximated by the slope of the LED curve) and vice versa. Anyway, the pixel gain slopes and the corresponding input LED currents show a strong, but not perfect negative correlation of -0.81.

[73] Digitization allows only for integer steps.

[74] It would be impractical und extremely time consuming to determine the needed LED current to match the source peak for each pixel individually.

Actually, the adjusted[75] LED current was determined at 1.57 mA equaling a photocurrent[76] of 300 nA. For two standard deviations at 1.19 mA and 1.95 mA, the respective photodiode current levels can be derived at 227 nA and 372 nA. This variation of roughly 70 nA corresponds to about ±1,400 electrons.

Possible reasons for this deviation are:

- Usage of different calibration sources.
- The outcome from the ^{109}Cd source measurement was a single gain number per pixel, while the linearization of the input charge points delivered a slope as a proxy for the internal gate gain.
- Tiny dust particles, randomly distributed on the sensor surface cover small areas and prevent some of the low energy photons from entering the silicon bulk.
- DCDE effects: in contrast to the ^{109}Cd source measurements, the LED illuminated all pixels at once, potentially provoking unwelcome side effects, like for example cross talks within the DCDE (see also chapter 8.3).

To get a best estimate for the absolute charge generation, the mean LED value should be used as the basis. However, for the general calibration task it is more relevant, that the LED approach has been proven as stable, repeatable, homogeneous and to a wide extent linear. The deviations of consecutive intensity increases were small and especially in the case of large charge storages negligible.

7.4.6 LED Matrix Calibration

7.4.6.1 Establishment of LED Charge Curves

With this preparatory work done, the LED system is now ready for establishing full LED charge curves with respect to the EDET sensor pixels.

Unlike a focused laser, the LED illuminates the whole sensor with equal intensity. Meanwhile, the DAQ samples full frame raw data, composed of the pixel charge, the common mode and the offset level. The offset level[77] has to be in any case deducted to get the net signal. By contrast, a common mode correction is not necessary, since the statistical process of data collection (i.e. taking the median value of 3,000 frames) also flattens out common mode variations (see Figure 8-31).

For the following measurement, a total of 80 increasing photon intensity steps (by whole numbers in terms of the absolute calibrated basic intensity) were injected, starting with small steps at the beginning (in order to replicate more precisely the internal gate and kink region) and a five times larger step width thereafter. By this means, all pixel values were set on a common ground, since the input charge injections should be (almost) iden-

[75] Beforehand, the LED induced charge data has to be linearized along the procedure described above. Otherwise, a linear regression fit would not make sense.

[76] The deviation is a consequence of the linearization.

[77] Sometimes also called dark frame.

tical to all pixels. To determine the corresponding electron value for a given ADU measurement, one can simply store all recorded charge injection points per pixel and interpolate. One can as well try to fit two straight lines for every pixel as shown in 7.3.4.4 and readily calculate the inversion or one applies a polynomial fitting method. In any case, a reference electron input charge valid for all pixels was established. To facilitate the comparison between calibrated to uncalibrated data, the referenced electron values inferred from the single pixel signals, were converted back to common ADU values using a benchmark curve, in this case the median curve (see Figure 7-40).[78]

Compared to the laser charge curves (Figure 7-22) the transition zone (kink) between internal gate and overflow region appears at a much lower ADU level and the shape in the overflow region differs slightly more from a straight line approximation. Additionally, the amount of generated electrons needed to reach the same ADU level is significantly lower.

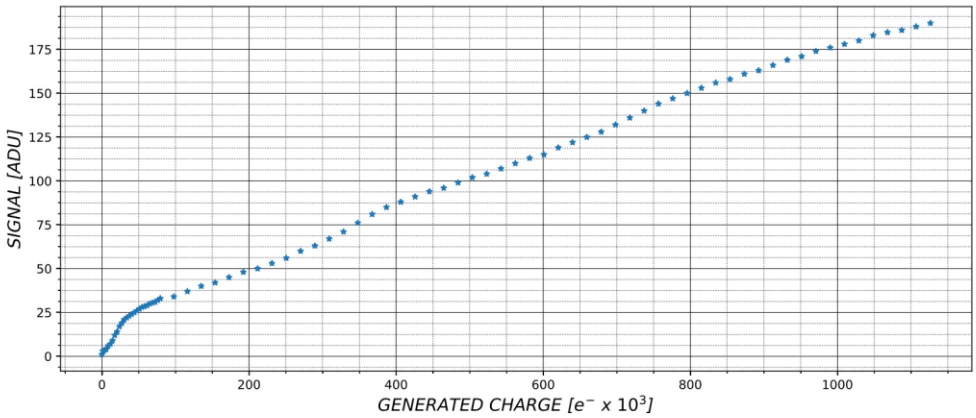

Figure 7-40: EDET sensor charge curve constructed from median values of all pixels.

The last observation can be easily resolved: while for the laser measurements the longest available gate length at 6 µm was used, for the LED measurements the shortest design at 4 µm was deployed. The gate length relation of Equation 5-14 implies a factor of $\sqrt[3/2]{6/4} = 1.84$ higher amplification for the shorter gate length. Accordingly, a lower amount of electrons was required to produce the same ADU value.

Similar considerations on the kink position would rather expect a higher value. However, the shorter gate length was outbalanced by the linear reduction of the gate capacity as well as by the larger impact of the parasitic correction factor f from Equation 4-9.

For the uneven curve shape[79] in the overflow region, a higher polynomial fit of 8th degree was necessary to get acceptable results, as can be seen on the left diagram of Figure 7-41. Moreover, another attempt was made to linearly regress both regions, as can be observed in the right diagram of Figure 7-41. One notes relative high residuals, especially at the back end of the charge curve.

[78] For the laser measurement, the central pixel was taken for convenience.

[79] An outcome of the later described “ghost charge effect”, see chapter 8.3.

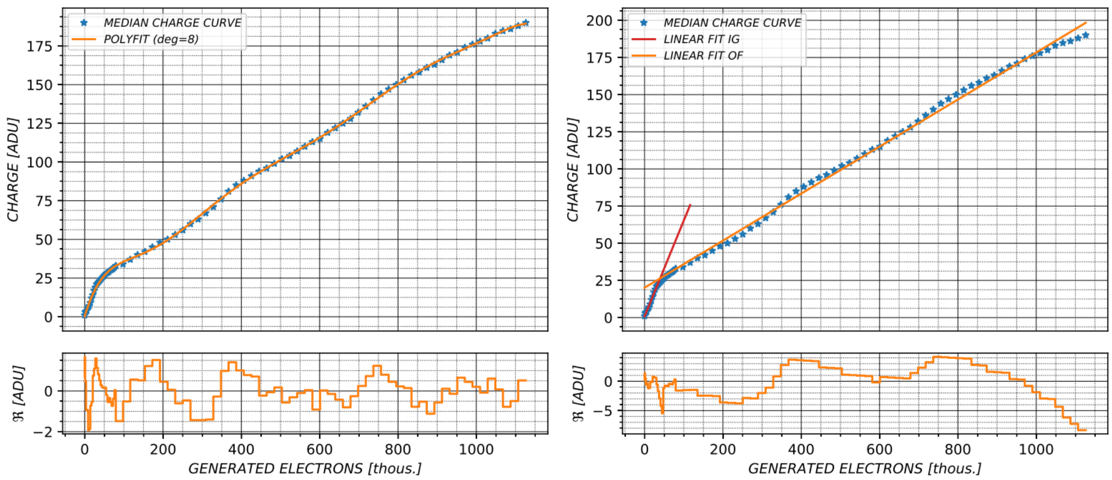

Figure 7-41: Left: Median charge curve of all 8,192 pixels for a small EDET matrix. The individual charge points were fitted by a polynomial of 8^{th} degree. The residuals are depicted on the bottom part of the diagram. Right: The internal gate and overflow regions were fitted by two linear regression lines.

7.4.6.2 LED Matrix Calibration

With the availability of a common charge curve for every single pixel, it is now possible to calibrate the whole matrix. The left diagram of Figure 7-42 shows an uncalibrated flat field illumination with offset correction. Additionally, a distinct band structure is visible with a (on average) lower amplification in the broad middle stripe and a higher amplification in the two outer stripes. The regular pattern in the middle band indicates some influence from the matrix drainlines and/or from the DCDE channels. Due to different pixel responses, the measured charge values range from 90 to over 140 ADU.

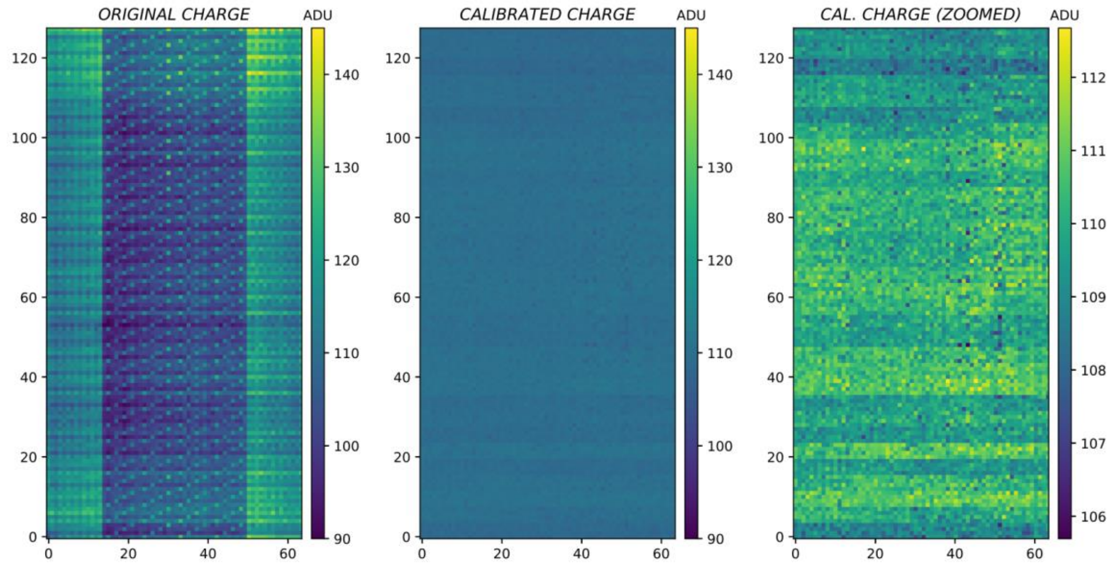

Figure 7-42: Left: EDET small matrix sensor pixel charges generated from a homogeneous LED flat field (applying a LED forward current, which was not used for the charge curve generation). Middle: Calibration of all pixels by the same algorithm developed in section 7.3.4. Right: Zooming in the calibrated final ADU range, diminishing to just 6 ADU.

For the originally registered ADU values, the same calibration procedure as with the laser was applied.[80] In order to establish an equal scaling, the determined electron values were finally inserted into the polynomial of the reference curve. The result is depicted in the middle and in the right (zoomed-in) diagram of Figure 7-42.

7.4.6.3 Pixel Gain Statistics

The linearization of the two different pixel gain regions was not fitting quite as well as with the laser.[81] Nevertheless, the illumination of the whole matrix provided much larger statistics, since the slopes for all pixels could be computed and consolidated to a histogram as presented in Figure 7-43.

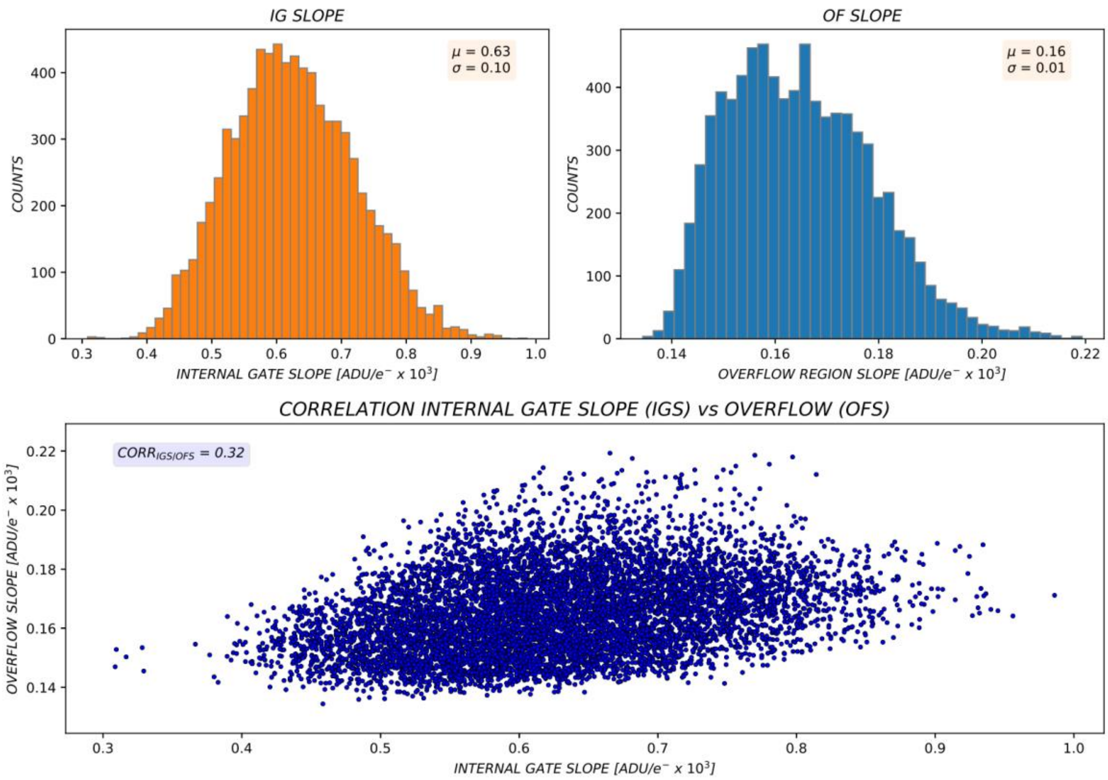

Figure 7-43: Top: Distribution of the internal gate and overflow region slopes for an EDET matrix with a 4 µm gate length. Compared to Figure 7-39 the mean internal gate slope is about 10.56 times lower, in good accordance with the about 10 times lower DCDE gain. Especially the OF slope distribution exhibits a distinct tail to the right side. Bottom: Correlation between internal gate and overflow slope.

The average amplification in the internal gate region was by a factor of about 4 higher than in the overflow region. The slope variations were substantially higher in the IG region, amounting to $\pm 16\%$ (versus $\pm 6\%$ in the OF region applying a twofold standard deviation).

[80] I.e. artificial creation of intermediary data points and look-up of the nearest value.

[81] An impact from the ghost charge effect, which will be explained in section 8.3.

On the assumption, that gate length variations dominate the pixel gain, one would expect a rather high correlation between IG and OF slopes.[82] However, the relative low correlation coefficient of 0.32 suggests, that there are, apart from the gate length, additional factors exerting an influence on the individual pixel gains.[83]

As a first candidate, the general offset level was considered. In theory, a higher offset level is caused by a higher drain current. According to Equation 4-14, the internal gate pixel gain $g_{q_{corr}}$ is proportionally related to the square root of the drain current. Contradictory to this consideration, both the IG- and the OF-region gain exhibit negative correlation coefficients of –0.24 and –0.65 to the pixel offset values, derived from the correlation matrix in Figure 7-45: the higher the offset level, the lower the gain.

A comparison of the higher offset levels in the middle stripe, shown in Figure 7-44, with the corresponding charge levels in Figure 7-42 seem to confirm this observation. Apparently, there are other factors leading to an inversion of the originally presumed relationship.

The offset levels can be further separated into a contribution from the DCDE channels and one intrinsic part. The DCDE channel impact was determined by averaging the offset values for every DCDE channel[84] and then, repeating the result 32 times for every electrical line. The deduction from the original offsets delivered the adjusted offsets as shown on the right side in Figure 7-44.

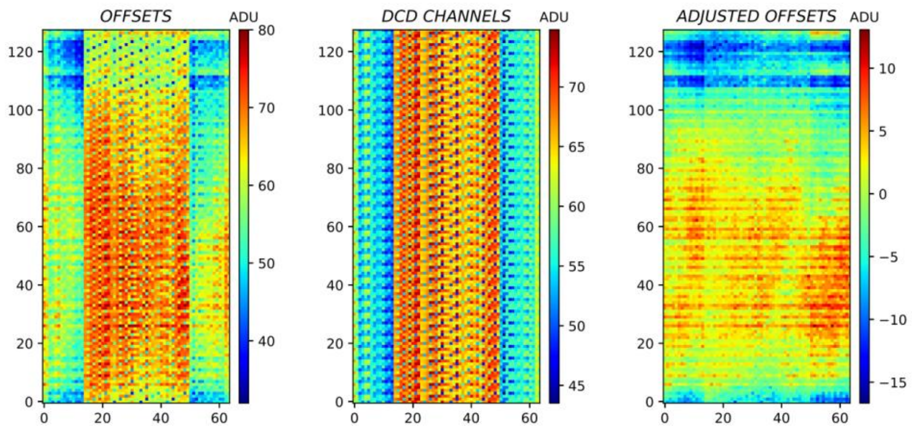

Figure 7-44: EDET small matrix offset distribution, average of DCD channels and adjusted offset levels.

The relative high negative correlations of the DCDE channels with the IG slope (–0.52) and the OF slope (–0.59) suggest, that there are superimposed processes within the DCDE, which significantly affect the recorded pixel gains, while the adjusted offsets are almost uncorrelated (positive at 0.29 vs IG-slope, negative –0.29 vs OF-slope).

[82] Unlike Figure 7-26, the slopes were not normalized by the average slope.

[83] The term gain is synonymously used for the slopes in the internal gate and overflow regions.

[84] 32 pixel values, each from one electrical line.

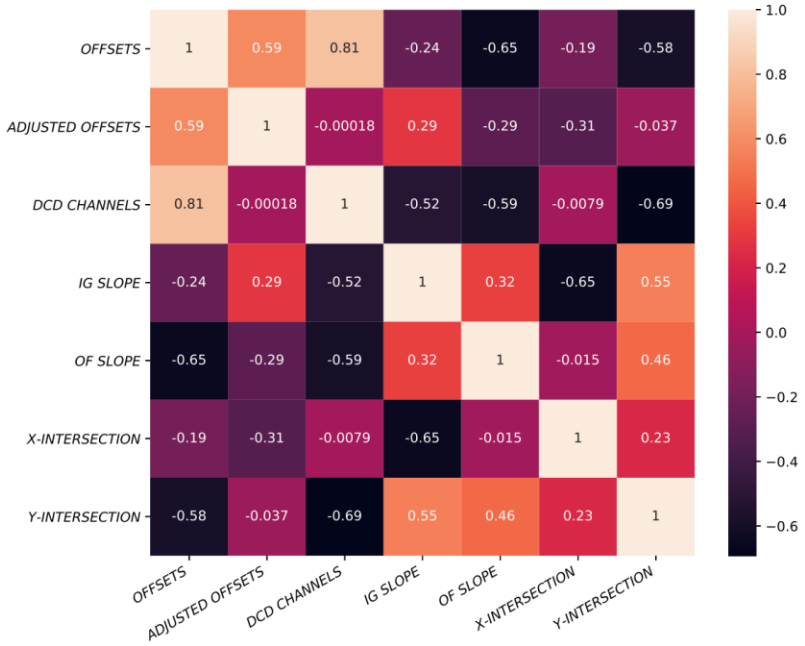

Figure 7-45: Correlation matrix for different EDET matrix parameters.

8 Sensor Characteristics

8.1 Measures of Image Quality

The most basic performance parameters used to evaluate electron detectors are [147]:

- *(spatial) resolution*: defined by the smallest spacing between two objects that can be clearly imaged, in other words, the smallest distance between separated objects that a device can record
- *contrast*: the ratio of the signal difference to the average signal level
- *noise*: the uncertainty (random variations) a signal was recorded

More advanced measures incorporate pairs of these basic gauges like Signal-to-Noise Ratio (SNR – contrast & noise), the Modulation Transfer Function (MTF – contrast & resolution) and the Wiener Spectrum (noise & resolution) or even all of them, in particular the Rose Model and the system Detective Quantum Efficiency $DQE(f)$. The latter describes the strength of the detected signal relative to noise and varies similar to the MTF with the spatial frequency (inverse of the periodicity with which the Fourier decomposed image intensity values change) of the signal.

By means of these image quality criteria, a comparison of different detectors is feasible either within one modality[1] (e.g. X-ray source, photons, electrons) or across different imaging modalities. Two fundamental characteristics have to be kept in mind [148]:

- no image can exactly represent the original object
- no two images will be identical, even if acquired with the same detector on the same region of interest

The variability is a stochastic property and can be generally referred to as noise.

In linear systems theory, a given $m \times n$ input matrix $\boldsymbol{f}$ is linearly[2] and shift invariantly[3] modulated by the detector to a specific digital output image $\dot{\boldsymbol{g}}$:[4]

Equation 8-1 $$\dot{\boldsymbol{g}} = \boldsymbol{H}\boldsymbol{f} + \dot{\boldsymbol{n}}$$

where $\boldsymbol{H}$ is usually called the system response or transfer function, represented by a $(m \times n)^2$ matrix and $\dot{\boldsymbol{n}}$ a single realization of the noise. With respect to scattering images, the Poisson noise introduced by the TEM beam electrons outweighs by far the noise contribution from the EDET system (charge diffusion, charge transfer inefficiencies & electronic noise from the backend).

[1] In healthcare physics the illumination source is sometimes also referred to as „imaging modality“, categorized by the method in which images are generated.

[2] A system is considered to be linear, if its output can be expressed as a weighted sum of the input constituents. If input f_1 results in output $g_1(x,y) = H\{f_1(x,y)\}$ and input f_2 results in $g_2(x,y) = H\{f_2(x,y)\}$, then

$$H\{af_1(x,y) + bf_2(x,y)\} = H\{af_1(x,y)\} + H\{bf_2(x,y)\} = ag_1(x,y) + bg_2(x,y)$$

[3] A system is considered to be shift invariant, if the response function, H, does not change as a function of position in the image.

[4] Each element in $\boldsymbol{f}$ is called a ‘del’ or detector element, while each element in $\boldsymbol{g}$ is called a ‘pixel’.

There is a fundamental difference between scattering or shadow imaging with high contrast resolution and electron counting used for low dose applications [148]: in general, a high contrast resolution suffers from the intrinsic blurring[5] of the imaging system. Specifically, the resolution between two objects can be significantly affected by the lateral spreading of the signal. On the other hand, at low contrast the noise sometimes outweighs the signal, that even large objects might not be discernible.

Consequently, for scattering image applications it is desirable to get the MTF as high as possible. Whenever the detector is used as a counter, in applications such as Cryo-TEM, where the total dose is strictly limited by radiation damage, the $DQE(f)$[6] must be maximized [149, 52, 63].

In the following, the MTF is used as the main criterion for the evaluation of the system performance.

8.2 Modulation Transfer Function (MTF)

8.2.1 Introduction

The Modulation Transfer Function is a widely used measure of imaging quality, especially for components (sensor, lens, mirror or the complete camera system) in the optical industry.[7] In a more illustrative way, it describes the EDET detector's "sharpness" or resolution, that is the ability to transfer various levels of detail from an object to an image [150]. An important influencing parameter on a sensor's MTF is the pixel size. As a (very) coarse assessment, the following rule applies: the smaller the pixel size the better the MTF [151]. Given a certain spatial frequency, the MTF conveys the reduction in intensity modulation, the contrast measured in line pairs per distance (per mm or per pixel) relative to low frequencies. Low frequencies correspond to the coarse details of the original picture or input signal. The better the system response at high frequencies, the higher the contrast of the system [152].

Equation 8-2

$$\%\text{Contrast} = \left[\frac{I_{max} - I_{min}}{I_{max} + I_{min}}\right] \times 100$$

In analogy to audio signals, when transferred from the time domain into the frequency domain by Fourier Transformation, the MTF represents the Fourier transformed spatial frequency response (SFR) of an image's contrast. Strictly speaking, the expressions MTF and SFR are not completely identical since SFR represents the generic term associated with the complete system response, while MTF describes individual effects of a

[5] Correlation between pixels.

[6] The $DQE(f)$ is defined by $DQE(f) = \left(\frac{SNR_{out}}{SNR_{in}}\right)^2$. A perfect device would maintain the signal-to-noise ratio of all signals presented to it and accordingly, would have a $DQE(f) = 1$.

[7] The system MTF represents the product of the MTF for the individual components.

particular component [153]. Nevertheless, both SFR and MTF are usually used interchangeably.

Several approaches can be applied to determine the MTF of a silicon pixel detector system [154]: the imaging of periodic patterns, the “slit-image” and the “knife-edge”-method, the latter commonly also referred to as the “slanted-edge”-method. As an example for a periodic pattern, the harmonic Siemens-star projects a test chart, which variates sinusoidal between dark and light parts resembling a wheel with 72 “spokes” on the sensor as shown in Figure 8-1 [155].

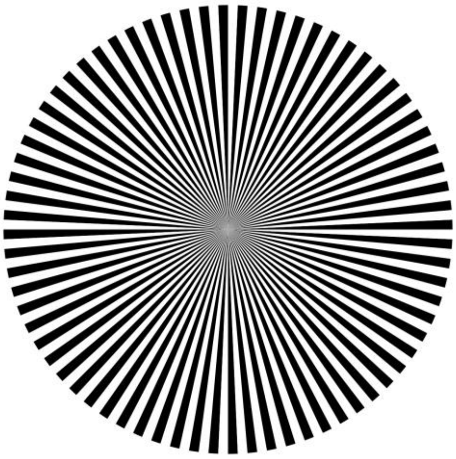

Figure 8-1: Siemens Star Test Chart.

The distance between the different black and white wedges (the combination of one black and white line pair is also called a “cycle”)[8] gets smaller while moving closer to the center of the Siemens-star. Although this method reacts relative insensitive to noise and provides directional MTF information, it has also some limitations [156]: it is slower and requires more space.

The slit-method uses a narrow slit milled into the shielding material, which requires a very precise fabrication of the slit. On top of that, the slit must be narrower than the pixel size. A major problem might arise because of the high radiation exposure needed to transmit sufficient exposure through the slit to the sensor [157].

By comparison, the slanted-edge-technique images the projection of a slightly tilted straight edge onto the rows or columns of the EDET sensor. The tilt angle should lie between 2° and 10°.[9] As a result, the exact edge position (marking the transition from

[8] Cycle relates more to the alteration of sine waves whereas for square waves the term line pair is preferred. However, in this thesis both expressions are interchangeably used.

[9] Results from vertical, horizontal or 45° edges are phase-sensitive and should be avoided. Although the ISO 12233 standard recommends angles of either 5° or 5.71° this instruction can be neglected since the MTF does not strongly depend on the chosen tilt angle.

low- to high-intensity) varies from pixel row to pixel row delivering different edge responses, which are finally composed to an Edge Spread Function (ESF, see Figure 7-11 and Figure 8-14 right diagram).

A single pixel row would be insufficient for the MTF analysis, since aliasing[10] due to undersampling in the detector will cause fluctuating results [158, 159]. However, a superposition of several rows significantly improves the quality of the resulting ESF. For that purpose, two-dimensional data from a region of interest (ROI) along the edge is projected to a one-dimensional array of equally spaced bins. This synthetic ESF is then differentiated to obtain the Line Spread Function (LSF). The normalized magnitude of the Fourier transformation performed on the LSF finally yields the MTF.

The maximum MTF of an imaging system can be also characterized by a *sinc* function and should conform with the ideal MTF [160].

Equation 8-3

$$MTF_{\upsilon_{pix}} = \mathrm{sinc}(d\nu\pi) = \frac{\sin(d\nu\pi)}{d\nu\pi}$$

where ν is the spatial frequency (reaching the first minimum at $\nu = 16.\dot{6}$ and $d = 0.06\ mm$ the size of an EDET pixel).

Some typical SFR-metrics have become common practice: the distance, covering the rise from 10% to 90% expresses the width of the edge response, while the width of the LSF is usually conveyed by the Full-Width-at-Half-Maximum (FWHM). The MTF10 leads to an SFR of 10% and describes the absolute maximum of details one can find in an image. By contrast, the MTF50 is preferred when trying to agree sharpness with the subjective perception of the human visual system.

In summary, using an edge response offers a lot of advantages [161]:

- measurement simplicity
- the blurring of an image is best discerned at the edges
- all common edge responses have a similar shape even though they may originate from different light sources
- the Line Spread Function (LSF) is easily to derive by applying the discrete derivative and the MTF can be directly determined by the one-dimensional Discrete Fourier Transform (DFT) of the LSF
- similar edge responses have similar MTF curves

8.2.2 Influences on the Modulation Transfer Function

The selection of the illumination source can already affect the MTF curve of a specific detector system. An MTF established under TEM conditions will certainly deviate from an MTF with a LED and this in turn would certainly diverge from an MTF with an X-ray source. With respect to a TEM, electron scattering effects are unavoidable. For an infra-

[10] ISO 12233 terms image artefacts occurring in a sampled imaging system due to insufficient sampling as aliasing. It can lead to a jagged stair-stepping at the edge transitions.

red LED, diffraction and reflection issues can occur, whereas for the ^{109}Cd source, geometric considerations as well as fluorescence effects from the source collimator have to be analyzed.

Since various measurements incorporate X-rays or electrons, the comprehension and optimization of the full process is essential to both, the avoidance of unnecessary detector damage and possible time savings. As a consequence, the individual MTF determination is preceded by an analysis of the main influencing variables.

Apart from the whole geometry (especially the distances between knife edge – sensor and knife edge – source respectively) several other factors must be considered for their potential impact on the sensor's MTF: diffraction, fluorescence (e.g. in the tungsten collimator of the ^{109}Cd source) as well as reflections and electron scattering in the silicon detector. Additionally, a simulation of the ^{109}Cd source MTF was performed.

8.2.2.1 Geometrical Considerations (low diffraction sources)

The ^{109}Cd source geometry is described in APPENDIX D. As one can see in Figure 8-2, a 0.1 mm thick tungsten sheet is placed directly on the EDET Hybrid Board PCB, covering about half of the pixel sensor. If the radioactive disk source is positioned very close to the detector, the source can no longer be treated as a point source. X-rays from the outer radius reach significant parts of the covered region and degrade the sharpness of the knife edge. The intercept theorem applies: if the source is moved further away, the penumbra region reduces correspondingly approaching the ideal case (at the expense of a much lower intensity).

The edge of the tungsten sheet should be vertically aligned to the center of the source disk. If the collimator opening of the tungsten holder is positioned just 2.9 mm away from the tungsten sheet, the total vertical distance from the tungsten edge to the radioactive disk center would be 10 mm according to the inherent source geometry (source – opening distance of 7.1 mm). Since the inner radius of the collimator pipe is 2.15 mm and the distance from the source to the inner edge of the collimator pipe is 1.8 mm, the maximal source disk radius (total disk radius of 3.175 mm) which can contribute to the penumbra region is:

$$\frac{8.2}{10} = \frac{2.15}{x} \rightarrow x = 2.62\ mm$$

Looking at Figure 8-2, one notices, that the source geometry does not allow to exploit the full potential of the embedded radioactive material, since the inner collimator edge shields radiation from the outer disk areas. Furthermore, by means of another application of the intercept theorem and a total distance of the tungsten sheet to the sensor of 2 mm, the half-shaded region eventually would extend to about 0.52 mm:

$$\frac{10}{2.62} = \frac{2}{y} \rightarrow y \approx 0.52\ mm$$

or almost 9 EDET pixels à 60 µm.

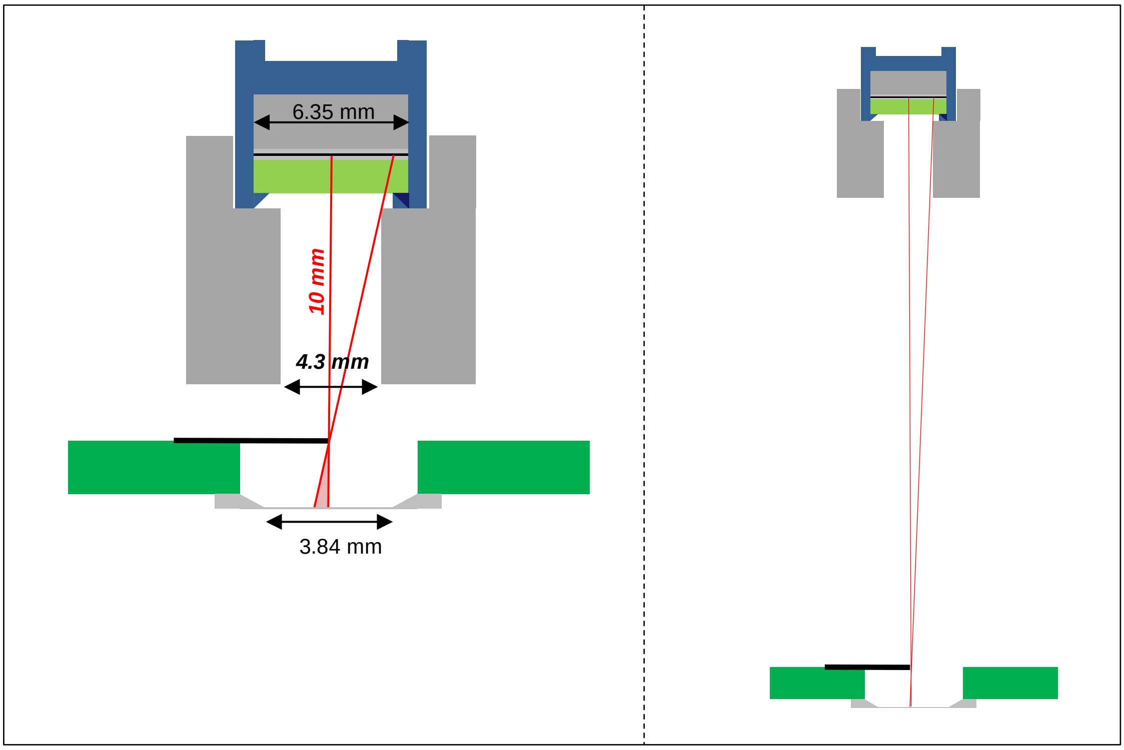

Figure 8-2: Right: Schematics of the ^{109}Cd capsule embedded into the tungsten holder (tungsten hut not shown) placed directly over the EDET Hybrid Board's (dark green) small backside indentation. A 0.1 mm tungsten sheet (black) covers about half of the attached small EDET matrix. At this very close distance, X-rays emitted from the outer radius of the extended radioactive disk source significantly contribute to the illumination in the sheltered area of the sensor. Left: Moving the radioactive source further away transforms the disk more and more to a point source, thereby significantly reducing the impact from the disk geometry. Dimensions are not to scale.

If the source – sensor distance is enlarged to 45 mm, the active disk area shrinks to 2.24 mm whereas the penumbra area reduces significantly to just about 0.1 mm or 1.66 pixel lengths. The source distance can be enlarged further to 100 mm and the half shaded area would shrink to just about 44 µm and so forth. Anyway, the benefit of increased sharpness will be counterbalanced by a significant increase of the integration time since the intensity of the radioactive source reduces by the square distance law.

Until now, it was only considered to increase the knife edge – source distance but there is a potentially more efficient lever. Instead, the knife edge can be brought closer to the sensor. Admittedly, a direct placement onto the sensor would be optimal but not recommendable, since this would certainly lead to mechanical and electrical damage. However, with a special internally designed jig (see CAD-picture in Figure 8-3) the knife edge could be positioned just a few hundred µm away from the sensor.

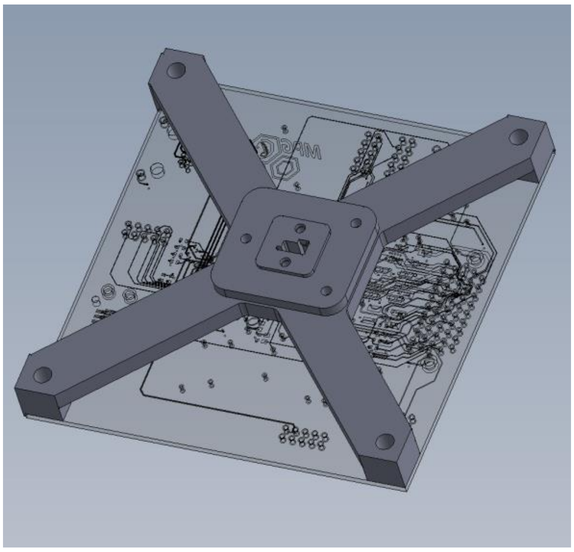

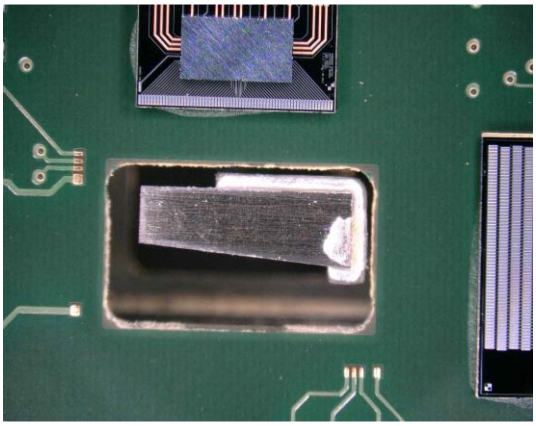

Figure 8-3: Left: Jig, mounted on the backside of an EDET Hybrid Board with an indenter (central part), holding the knife edge. The distance is controlled by spacer rings.[11] Right: Topview section of an EDET Hybrid Board without sensor but populated with a Switcher (north) and a DCDE (east). The Tungsten knife edge glued on the indenter is intended to be moved as close as possible to the sensor's backside.

As an example, this measure would shrink the penumbra region to about 111 µm on the assumption of a sensor – edge distance of 0.5 mm for the original envisaged source position.

8.2.2.2 Diffraction

Influences from diffraction on the knife edge measurements mainly depend on the used wavelength. A related approximation can be found in APPENDIX E.

According to Planck's equation

Equation 8-4
$$E = \frac{h \cdot c}{\lambda}$$

the wavelength λ for a 22 keV and 25 keV photon is $\lambda_{22keV} = 5.63 \cdot 10^{-11} m$ and $\lambda_{25keV} = 4.96 \cdot 10^{-11} m$ respectively. If the knife edge is put directly over the indentation of the EDET hybrid board, the distance to the sensor is $d_2 = 2 \cdot 10^{-3} m$. At a source – knife edge distance of $d_1 = 45 \cdot 10^{-3} m$, Equation E - 7 can be used. At $\nu = 2.4$ the intensity already diminishes to lower than 10% ($> 20dB$, see Equation E - 6) and the corresponding penumbra region of the sensor would reach just

$$h = 2.4 \cdot \sqrt{\frac{5.63 \cdot 10^{-11} \cdot 2 \cdot 10^{-3}}{2}} = 0.569\ \mu m$$

[11] Design by Johannes Treis.

Therefore, diffraction effects from ^{109}Cd source photons, are – as expected – negligible. By contrast, if the MTF analysis would be executed by a LED source with 850 nm wavelength, diffraction effects would increase the half shade region substantially to 70 µm, which would already blur the image by more than one pixel dimension.

8.2.2.3 Fluorescence

When electromagnetic radiation impinges on matter, their component atoms may become ionized. As already described in section 4.3.5, fluorescence occurs when the excited electron relaxes back (typical time for the excited state in the nanoseconds range) to a lower energy state. The required energy $h\nu_{ex}$ to stimulate fluorescence must be higher than its ionization potential and a photon of an energy $h\nu_{em}$ is emitted.[12] In case of X-rays, the expelled electrons originate from the inner shells of the atom. The lower energy state may not be the original ground state. The electron may also lose its remaining energy through further fluorescent emission or non-radiative relaxation dissipated as heat (enhancement of lattice oscillations via the generation of phonons) [162]. As mentioned, the fluorescence quantum yield ω highly depends on the atomic number. A steep rise for high energetic K-shell photons can be observed, attaining over 0.9 for Z-materials beyond 56 (Barium). For the L-shell, significant lower quantum yields were detected [163].

With regards to the ^{109}Cd source, fluorescence effects from the tungsten collimator's inside walls could potentially spoil the MTF. The walls enclose a relative large area (larger than the radioactive disk) and notwithstanding that fluorescence is isotropic, the collimator acts at least for part of the absorbed X-rays as a new radiation source to the sensor. As depicted in Figure 8-4, X-rays emitted from the radioactive source cannot directly strike the whole sensor area, since part of it is shielded by the tungsten sheet. However, by inciting fluorescence to the inner walls of the tungsten holder, also obstructed regions of the sensor could potentially register photon hits.

[12] Lower than needed to prime excitation (**Stokes shift**).

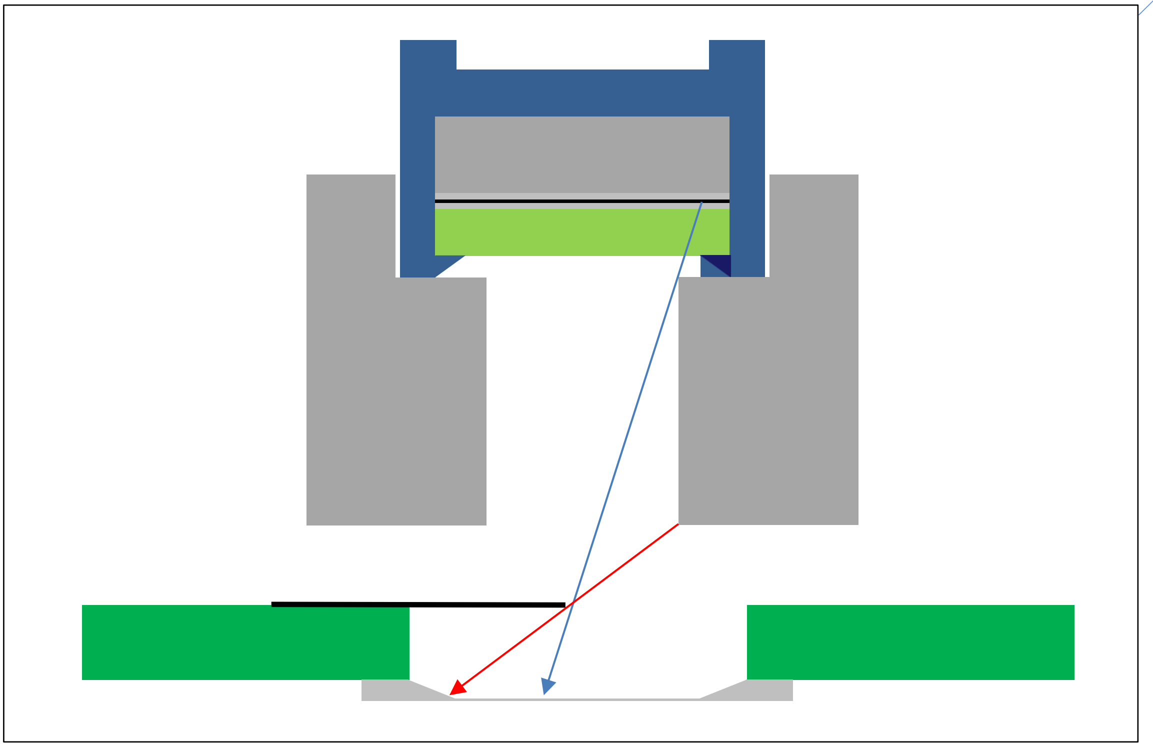

Figure 8-4: A Tungsten sheet (black) was placed on the EDET Hybrid Board's (dark green) backside indentation with the attached small EDET matrix. Above that, the schematics of the ^{109}Cd capsule were drawn, put into a tungsten holder with the collimator pipe. If the source is positioned very close to the matrix, fluorescence photons from the inside walls of the collimator could potentially reach the whole sensor area. Dimensions are not to scale.

The K-shell emission lines of tungsten range between 59 to 67 keV, the L-shell spectra are limited to about 8 to 11 keV [164]. Although the fluorescence quantum yield ω_K for the K-shell goes almost to 1 ($\omega_K = 0.956$ for tungsten [165]), its contribution can be a priori neglected for two reasons: a low absorption coefficient because of its high energy and the small portion of 88 keV photons from the ^{109}Cd source. For the L_1, L_2 shells the effective fluorescence quantum yields are $\nu_1 = 0.271, \nu_2 = 0.304$ respectively [163].

In other words, almost 30% of the 22/25 keV photons hitting the Tungsten collimator get reemitted as lower energy X-rays between 8 and 11 keV. This could potentially generate another spectral peak in the sensor. Nevertheless, for the overall contribution some significant adjustments have to be made. To begin with, the $1/e$ absorption length[13] for a 25 keV photon in tungsten is about 15 µm, while for an 8 keV photon the respective distance reaches just 3 µm. As a consequence, a significant part of the evoked fluorescence would be self-absorbed within the tungsten material. Additionally, since the detour via collimator pipe increases the average path length, some further attenuation by the distance square law has to be taken into account. One might object the large area of the collimator pipe as a strong fluorescence source, but this would only partly counteract the isotropic nature of radiation: compared to an EDET pixel at a distance of 10 mm, an equal sized imaginary pixel within the collimator area 5 mm away (to both, source and

[13] The distance traveled, where the original intensity drops to $1/e$.

sensor) would initially get in fact 4 times as much irradiation.[14] However, putting fluorescence yield and self-absorption aside, the back radiation does not take place in one direction but isotropically. Performing a back-of-the-envelope calculation, the final destined EDET pixel only gets a tiny fraction of

$$\frac{4 \times 100\pi}{4 \times 25\pi} \cdot \frac{A_{pixel}}{A_{sphere}} = \frac{0.06 \times 0.06}{4 \times 25\pi} \approx 4.58 \times 10^{-5}$$

the direct source intensity. Certainly, two significant adjustments have to be made: first, as said a significant part of the comparable large pipe area[15] has to be taken into consideration, which counterbalances the calculation by a factor in the order of 10^4. Second, the lower energy photons experience a much higher absorption (coefficient is 8 to 20 times higher).

All corrections included, the overall fluorescence contribution from the collimator material can be estimated less than 10% compared to the 22/25 keV peak. For the ESF compilation, it can be easily excluded by simply rising the accepted charge threshold limit.

8.2.2.4 Reflection

For the MTF measurements with the ^{109}Cd source, reflections could occur at the inner wall of the tungsten collimator. External total reflection takes place at an angle below the critical angle θ_c which is typically less than a degree for X-ray energies [166]:

Equation 8-5

$$\theta_c(\deg) = \frac{1.65}{E_{keV}}\sqrt{\frac{Z\rho}{A}}$$

for tungsten $Z = 74$ is the atomic number, $\rho = 19.3$ the density in g/cm^2 and $A = 183.85$ the atomic weight. The critical angle can be increased by higher densities and lower energies. For 22/25 keV X-rays, the corresponding angles are calculated at only 0.209° and 0.184° respectively, so for the MTF simulation reflection effects can be ignored.

For the same reasoning, X-ray reflections on the silicon sensor surface are only of immaterial significance. However, for LED measurements, reflection effects can be considerable, since the reflectivity of silicon is over 30% for infrared photons [167].[16] Consecutive back-reflections from underneath the edge sheet could extend much further into the covered sensor area compared to pure diffraction effects.

8.2.2.5 Electron Beam Scattering

As already explained in Section 4.2.4, the volume of the electron beam scattering in a thin silicon sensor can be substantial and as a result, heavily affect its spatial resolution. Ideally, the excitation volume would maintain a cylindrical shape with a diameter corresponding to that of the incident beam [168]. However, dependent on the incident energy,

---

[14] Treating the source as a point source.

[15] The whole pipe area is even larger than the total source disk area.

[16] A reflectivity peak of 73% occurs at 270 nm wavelength.

elastic and inelastic scattering events cause electrons to deviate significantly from their original trajectories. For the scattering of low energy electrons, comparable in energy to ^{109}Cd X-ray photons, the simulation can be easily performed by the free downloadable software CASINO, described in [169, 170, 171]. As one can see in Figure 8-5, the trajectories for low energy particles are confined to a very narrow region of a few µm.

Any low energy electron should not create an electron cloud larger than this, hence the effect on the sensor sharpness expressed via MTF should be minor. To be sure, one should keep in mind that electrons can impinge on different places of the pixel surface, however the overall extension of the cloud itself is limited to a few µm, so charge sharing should constitute only a rare event.

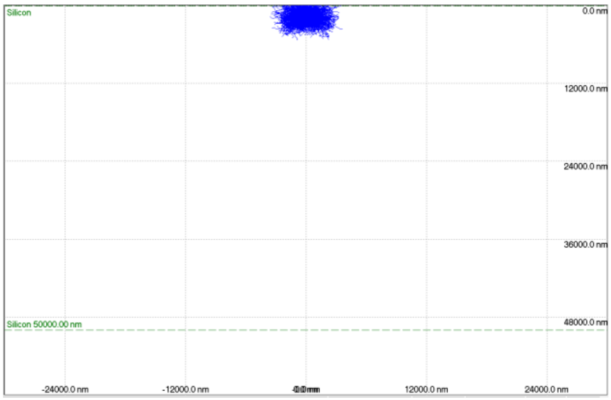

Figure 8-5: Monte Carlo Simulation of a 22 keV electron hitting a silicon layer with the same dimension as an EDET pixel. The blue heap on top symbolizes the different electron trajectories. The analysis was performed with 1,000 trajectories. Coordinates are in x and z direction and dimensions are given in nanometers.

For TEM electrons, a lot of additional processes become significant, such as backscattering, secondary electrons and X-ray generation. To consider all these effects with respect to the beam spreading, several Geant4 simulations were carried out.[17] Figure 8-6 depicts the simulated trajectories of 1,000 electrons onto the EDET sensor. Evidently, the impact of electron scattering within the silicon sensor can be considerable.

[17] All Geant4 simulations were performed by Ibrahym Dourki.

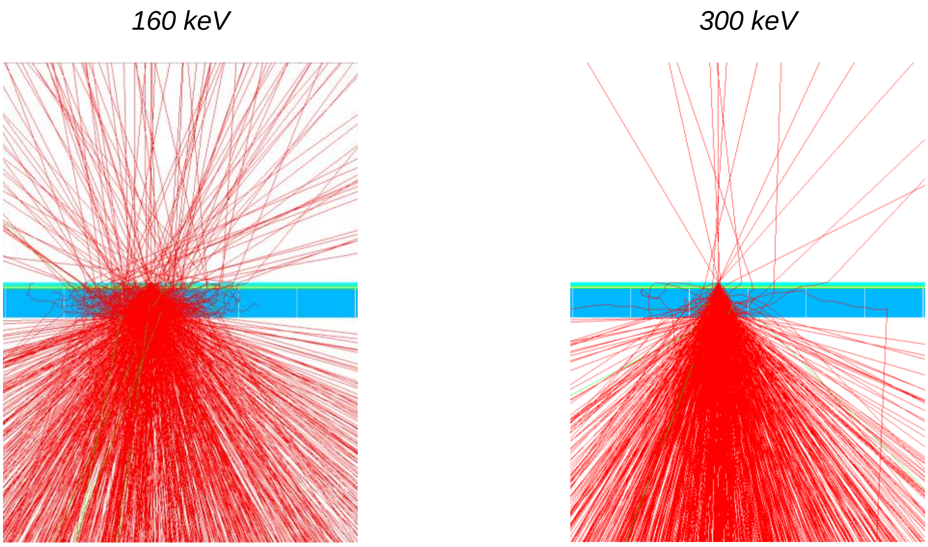

Figure 8-6: Left: Geant4 simulation of a 160 keV TEM-beam impinging on an EDET sensor (with entrance layers). The figure depicts 6 EDET pixels, separated by white lines. The electron trajectories (red) undergo significant backscattering, the in-pixel scattering cone reaches out to over two pixel lengths. Right: 300 keV beam with a significantly reduced in-pixel scattering.

A cross section of different TEM beam energies for 30 µm and 50 µm thick sensors is presented in Figure 8-7 and Figure 8-8 respectively. As a general observation, the thinner the sensor and the higher the energy, the lower the electron straggling (and therefore, the better the resolution).

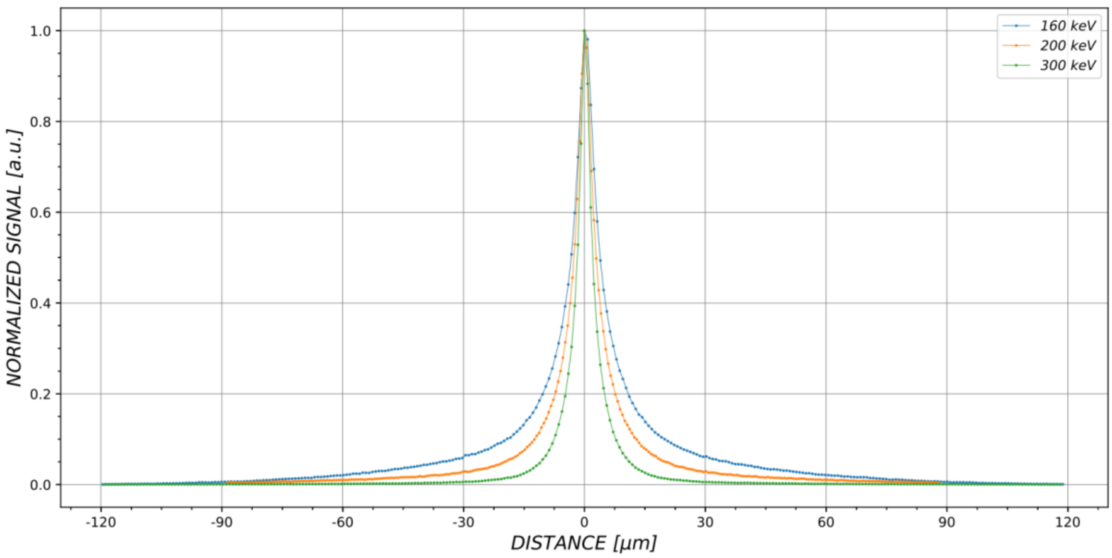

Figure 8-7: In-pixel scattering width of different TEM-energies on EDET pixels of 30 µm thickness. The data points represent the binning of the respective energy deposition from a total of 200,000 Geant4-simulated electrons. According to this simulation 200 keV electrons would blur approximately a full EDET pixel pitch (60 µm).

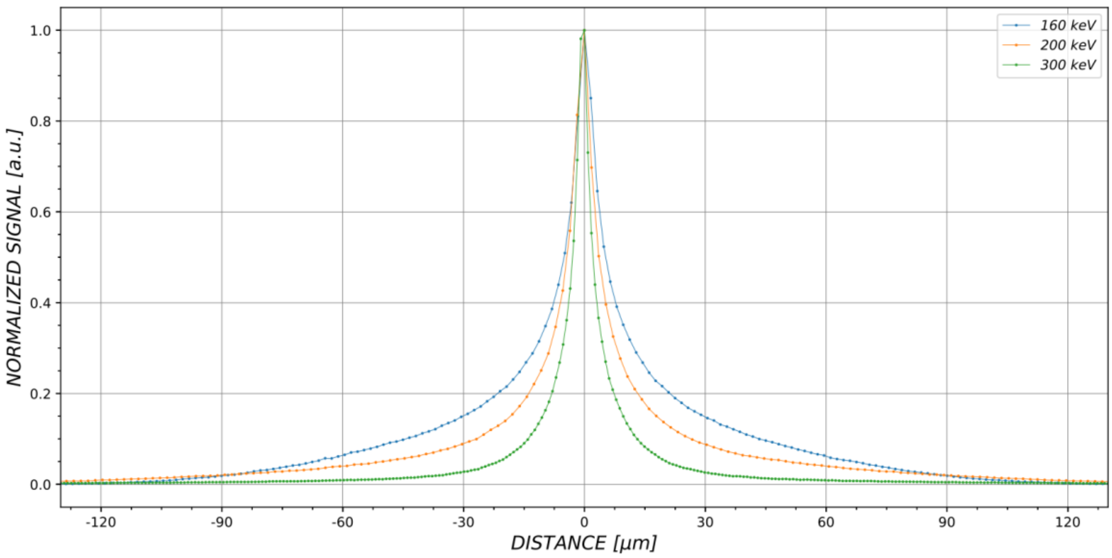

Figure 8-8: In-pixel scattering width of different TEM-energies on EDET pixels of 50 µm thickness. The data points represent the binning of the respective energy deposition from a total of 200,000 Geant4-simulated electrons. The scattering volume is significantly higher compared to the 30 µm thick sensor.

8.2.2.6 Artificial Edge Construction

In order to get reference values for the ideal case, a simulation of the MTF measurement with the ^{109}Cd source was implemented.

The simulation of an artificial edge was performed in almost the same manner as the synthetical spot described in APPENDIX D. The only complication is related to the positioning of the knife edge over the PCB indentation. The position of the knife edge was assumed to be directly under the center of the source. The vertical distance source to knife-edge was measured at 46.4 mm (for the real measurement), the knife-edge sensor distance was determined at 2 mm (by a laser scan). The intensity for the numerical integration was calculated for each 5 µm step moving along a single line. This line on its own contains the characteristics of a typical edge spread function. As shown in Figure 8-9, the line is repeated 128 times in vertical direction to reproduce the row dimension of a small matrix. The next step implements the tilting of the edge: starting with a loop, where the initial line values are shifted by one step to the right, followed by adding up each of 12 step values to one single pixel value ($12 \times 5\mu m = 60\mu m$). Within the edge transition area the pixel values gradually change by 1/12$^{\text{th}}$ or $0.08\dot{3}$. Accordingly, the simulated slanted angle will be about

$$\theta = \tan^{-1}(0.08\dot{3}) \approx 4.76°$$

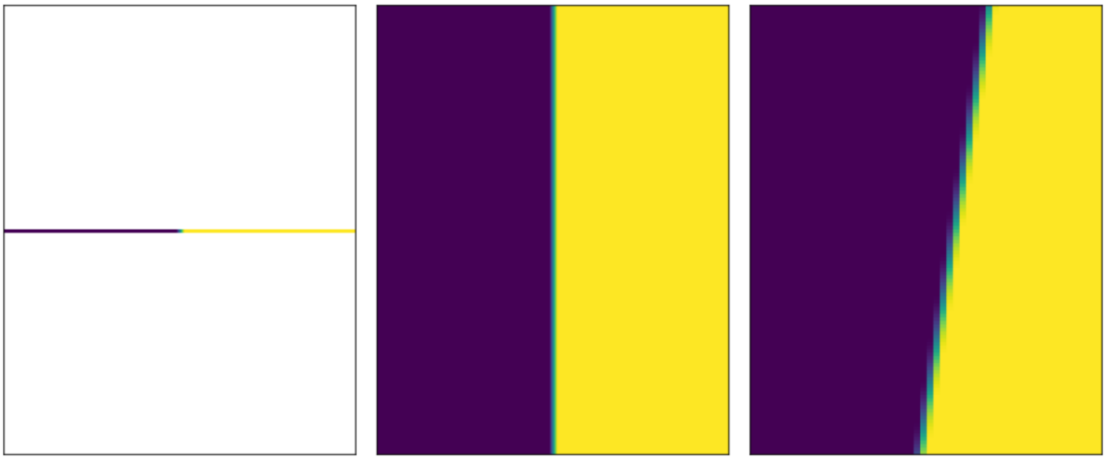

Figure 8-9: Simulated radioactive source on an EDET sensor with a slanted edge. Left: single line as outcome of the simulation process. Middle: repeat of the simulated line 128 times to reproduce the rows of an EDET small matrix. Right: tilt the edge transition region to an angle of 4.76°.

8.2.3 The Slanted-Edge Method

A lot of open source programs [172, 173, 174] provide the necessary tools to evaluate the slanted-edge spatial frequency response of a specific image. The objective for writing an own algorithm was the full integration of measurement and analysis. The International Organization for Standardization (ISO)[18] published the Standard ISO 12233:2017 "Photography – Electronic still picture imaging – Resolution and spatial frequency responses" with clear guidelines and procedures for an edge based spatial frequency response (e-SFR).

The method was originally developed for photographic devices which by default should record the reflected light of a homogeneously illuminated test chart. For the EDET matrix, the relevant steps of the e-SFR algorithm had to be adapted as enlisted below. In order to get a benchmark MTF, an ideal synthetical slanted-edge image was created as presented in Figure 8-10.

8.2.3.1 Selection of the edge region of interest (ROI)

The purpose of the EDET detector is not to produce nice black & white photographic pictures (although in principle feasible), but to record high energetic electrons and photons in the tens to hundreds keV range. In absence of a standardized test pattern, the knife edge (0.1mm tungsten sheet) has to be put as close as possible over the sensor and tilted between 2°-10° to the (vertical or horizontal) pixel orientation.[19] If illuminated with a radiation source, the result should give a two dimensional matrix with a bright and a dark light intensity area and a transition region in between.

[18] Field: Image Technology/Photography/Photographic Equipment. Projectors

[19] MTF is not strongly dependent on the edge angle, at least between 2° and 10° it appears to be nearly the same [110]. The ISO 12233:2000 Annex I test chart uses an tilting angle of approximate 5°.

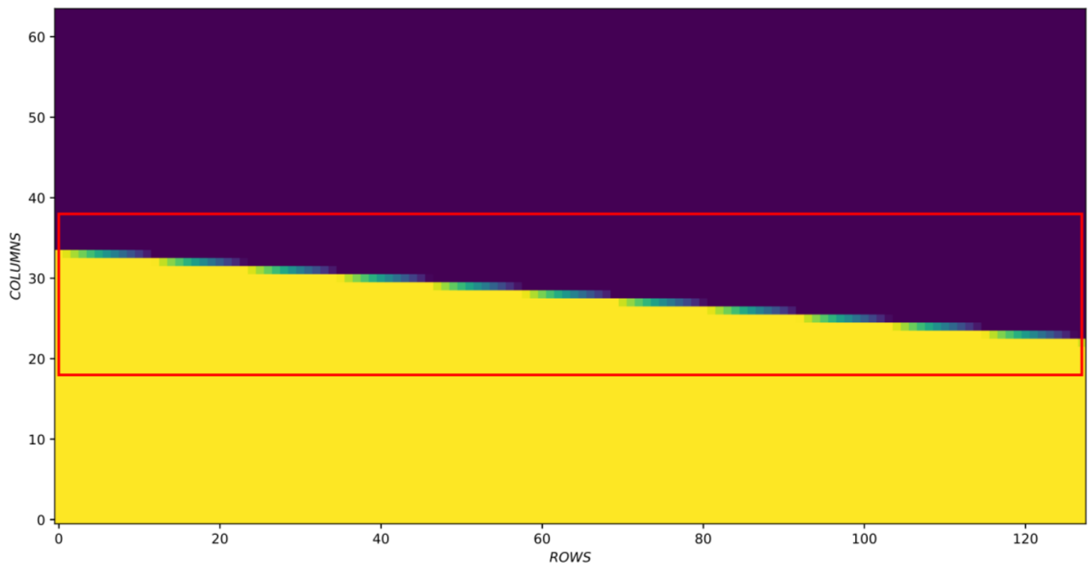

Figure 8-10: Synthetically generated ideal knife-edge of a small matrix EDET sensor with an angle of 5°. The red rectangle selects the region of interest (ROI) containing the edge position, the sector over which the calculations are done.

A careful selection of the input data can already improve the measured e-SFR [175]. Since the data outside the edge region for real systems merely contribute to noise fluctuations, it is recommended to limit the region of interest (ROI) close to the edge feature.[20]

8.2.3.2 Estimation of the edge location and slope

The finally obtained MTF is very sensitive to the correct determination of the edge angle. To figure out the slope and the angle of the slanted edge, each pixel row perpendicular to the edge (in Figure 8-10 vertically orientated) is convolved[21] with a finite impulse response (FIR) filter

$$\begin{cases} h = [+1/2\,, -1/2] \ldots \text{when moving from "dark into the bright"} \\ h = [-1/2, +1/2] \ldots \text{when moving from "bright into the dark"} \end{cases}$$

meaning that the derivative value for a pixel x is equal to $-1/2$ times the value of the pixel immediately to the left, plus $1/2$ times the value of the pixel to the right

The coordinates of the centroid (maximum) value for each line serve as the input for the slope determination applying the least square method. From the slope, the corresponding angle θ in degrees can be easily calculated:

Equation 8-6
$$\theta^{\circ} = \frac{180}{\pi} \cdot \tan^{-1}(k)$$

[20] As a rule of thumb, the ROI size can be determined by $N = 1/\tan\theta$ where N is the number of rows/columns and θ the slanted edge angle [196].

[21] Convolution is a very important technique in digital signal processing since it relates three signals of interest: the input and output signal and the impulse response.

The identification of the correct angle is of utmost importance, since for larger errors (more than $\pm0.04°$) the zero of the MTF curve occurs at a lower frequency [154].[22] As shown in Figure 8-11, the recalculation of the original angle of 5° shows a deviation of just 0.018° which can be considered as sufficient.[23]

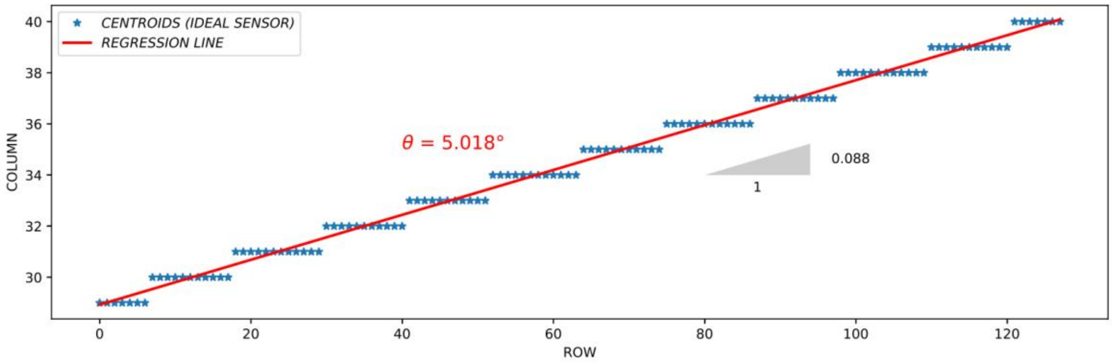

Figure 8-11: Centroid points for each pixel row expressed by their column number. Although the "ideal" sensor was originally constructed with an angle of 5°, the determined angle from the convolution approach deviates slightly by 0.018°.

The real data was similarly recorded as the absolute pixel calibration with the radioactive source, described in chapter 7.2. The only two adjustments made were

- first, the placement of a tungsten sheet directly over the indentation on the backside of the PCB to constitute a slanted edge and
- second, in order to better accomplish the ideal of a point source, the ^{109}Cd apparatus was moved to the widest distance the motorstage could provide on the vertical axis.

At first sight, this approach might seem a little bit odd in relation to the standard procedure for determining an edge spread function. Sure, every digital camera must be exposed a certain time duration to collect enough energy to discern distinct objects. However, in the specific case with a radioactive source the optical aperture is open for several hours and it is not discriminated by ADU converted energy levels but by different (threshold dependent) levels of hit counts, in other words, the EDET sensor is operated as a counter. For the edge region one can expect, that the more area of a pixel is covered by the knife edge, the less intensity it would register. About 1,500 hits for the uncovered pixels should be sufficient to get acceptable statistics. Like before, noisy pixels and hot pixels were masked. Additionally, pixels outside of the core spot region were excluded. As a consequence, the region of interest had to be confined to an area of 70 pixel rows and 20 pixel columns as depicted on the left side of Figure 8-12. Pixels masked during the measurement were linearly interpolated along the sensor column.

[22] After the initial estimate, the edge angle can be changed by small increments around the initial value. The angle corresponding to the maximal MTF integral represents the best estimation for the edge angle.

[23] More sophisticated approaches use a double Hough transformation followed by an iterative MTF maximization algorithm [191] or a modified slanted-edge method that estimates the edge angle by fitting a two-dimensional function to the ROI data [180].

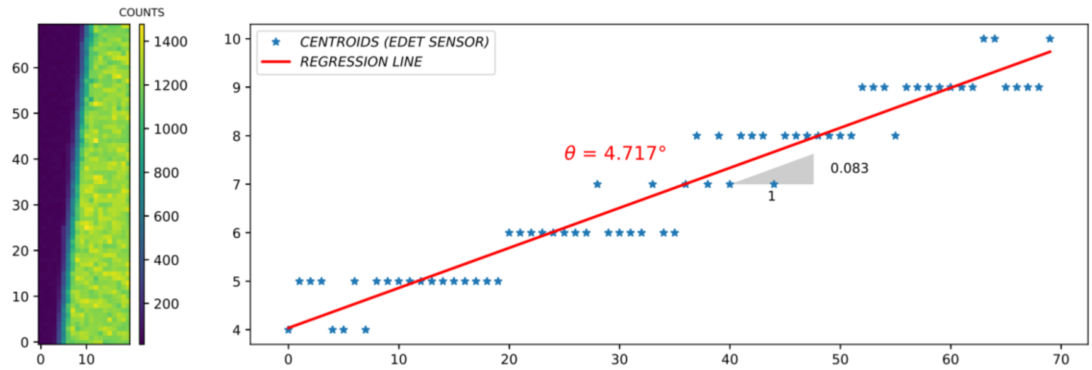

Figure 8-12: Left: Knife-edge ROI of the EDET small matrix illuminated with a ^{109}Cd source. The tilt angle $\theta = 4.717°$ is very close to the angle of the simulated edge ($\theta = 4.76°$). Compared to the result from the ideal sensor in Figure 8-11, one can clearly observe that the centroid points are no longer regularly distributed, an unmistakable sign of some sharpness deterioration.

8.2.3.3 Formation of a super-sampled line spread function array

To build the edge spread function, the pixel coordinates of the ROI are projected onto the unit vector $\vec{n}$ perpendicular to the edge gradient with slope k:

Equation 8-7
$$\vec{n} = \frac{\binom{1}{k}}{\sqrt{1+k^2}}$$

As shown in Figure 8-14, in each row the location of the edge shifts a little bit. The distance parameter z which denotes the shortest distance from a pixel at coordinates $\vec{P}_{r,c}$ (r, c indexing the row and column numbers) to the slanted edge vector $\vec{E}_{x,y}$ can be calculated by [176]:

Equation 8-8
$$z_{r,c} = \vec{n} \cdot (\vec{P}_{r,c} - \vec{E}_{x,y})$$

where (x, y) are the coordinates of an arbitrary point on the edge. Since the final one-dimensional array of sub-pixel elements can be easily shifted by a constant amount, one can take also the left bottom edge pixel of the ROI with coordinates $(0,0)$ as the reference edge point and Equation 8-8 simplifies to

Equation 8-9
$$z_{r,c} = \vec{n} \cdot \vec{P}_{r,c}$$

By multiplying the individual pixel vector $\vec{P}_{r,c}$ with the orthogonal edge unit vector $\vec{n}$, the positional information is projected onto a one dimensional line along the orthogonal knife-edge gradient $\vec{n}$. Apart from the spatial information, the corresponding pixel intensity values $v_{r,c}$ must be stored to finally yield a set of tuples

$$\vec{S} = \binom{z_{r,c}}{v_{r,c}} \text{ for all } (r, c) \in \text{ROI matrix address}$$

The combined projection onto a line orthogonal to the edge gradient generates a superposition of the registered row scans and will contain more edge response samples with different phase shifts than any single scan. This over- or super-sampling procedure effectively increases the sampling resolution and reduces aliasing or adverse phase effects.

Aliasing occurs when the bandwidth[24] of the input signal exceeds the Nyquist rate. The Nyquist sampling theorem states, that if a signal is sampled at the Nyquist frequency f_N, defined as a half cycle per pixel or half of the sensor resolution (expressed in pixels per mm), the original signal can be perfectly reconstructed. For the EDET sensor with 60 µm spacing, the sensor resolution would be $1000/60 = 16.\dot{6}$ pixels/mm and $\mathrm{f}_N = 8.\dot{3}$ line pairs per mm.[25] Signal energies above the Nyquist frequency are aliased leading to artificial low frequency signals in repetitive patterns (as shown in Figure 8-13) or as jagged diagonal lines in non-repetitive patterns [177].

Example of Aliasing

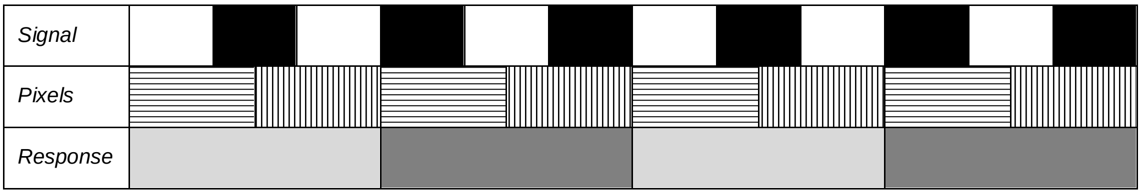

Figure 8-13: Line pair gauge: sensor pixels are shown in an alternating stripe pattern. The signal arrives at 3 cycles (one cycle corresponds to one black and white line pair) per 4 pixels = 3/2 f_N, whereas the sensor response is aliased, recording just half the Nyquist frequency or just one cycle (light-gray and dark-gray) in 4 pixels.

The projected values are not uniformly spaced, making them unusable for the Fast Fourier Transform (FFT), which produces a substantial reduction in computational complexity. By denoting the dimension of the first pixel row as N and forming a sampling grid of $N + 1$ main grid points, the projected data (see Figure 8-14) from the other rows can be binned into four equally spaced sampling intervals between each of the grid points. Then, the pixel data is averaged within each bin.

Although the interval sections are by a factor of 4 smaller than the original pixel size, a weighted average is preferred over a simple value average. Define $\delta(\vec{S}_z)$ as a counting function, collecting all appropriate values of the $\vec{z}$ array into a specified bin:

Equation 8-10
$$\delta(\vec{S}_z) = \begin{cases} 1 & j \cdot 1/4 \leq [\vec{S}_z] < (j+1) \cdot 1/4 \qquad j = 0, \cdots, 4N \\ 0 & \text{otherwise} \end{cases}$$

The value for the edge spread function $\overrightarrow{ESF}\,(j)$ equates:

Equation 8-11
$$\overrightarrow{ESF_j} = \sum_{j}^{4N} \frac{\sum \vec{S}_v \cdot \vec{S}_z \cdot \delta(\vec{S}_z)}{\sum \vec{S}_z \cdot \delta(\vec{S}_z)}$$

[24] Difference between upper and lower spatial frequencies.

[25] MTF results for other direct detectors can be found in [195].

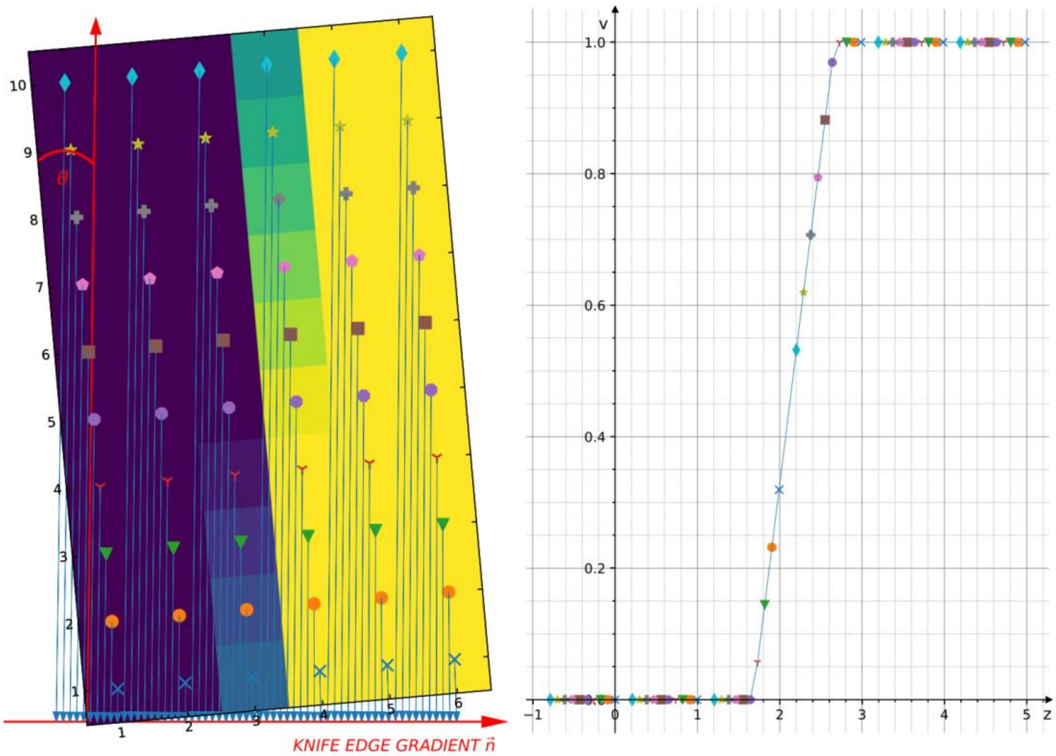

Figure 8-14: Left: Section of the ROI depicting the projection of each pixel on the knife edge gradient $\vec{n}$. Right: Construction of a super-sampled ESF from the projected 2-D image intensity values onto a 1-D representation.

Effectively, this creates a synthetical, over-sampled ESF exhibiting 4 times as many points along the line as a row of the original image data.

Any measurement typically introduces a certain amount of random variation in the signal. The measured ESF data can be optimized by several smoothing steps [178]. This procedure is commonly known as filtering. Nonetheless, it is crucial to balance very carefully a reduced noise against the integrity of the data, which must not be compromised in the process. A variety of smoothing methods can be implemented as for example outlined in [178, 179].

The ESF-data first had to be normalized to range between 0 and 1. This was achieved by a baseline subtraction, determined from the average of the left tail of the ESF array before the first inflection point (FIP). All values before the FIP were subsequently set to the floor level of 0. The adjusted array elements were then divided by their maximum value. The filtering was applied at very small dosages by a simple moving average with a small window of just 3 data points[26] in order to retain the original signal as much as possible. The first peak after the second inflection point (SIP) provided the reference for

[26] The smaller the window, the higher the residual noise on the one hand but the more signal features are preserved on the other hand.

the ceiling at 1. All following data points comprise the upper tail and were commonly set to 1. The outcome of different edge spread functions is presented in Figure 8-15.[27]

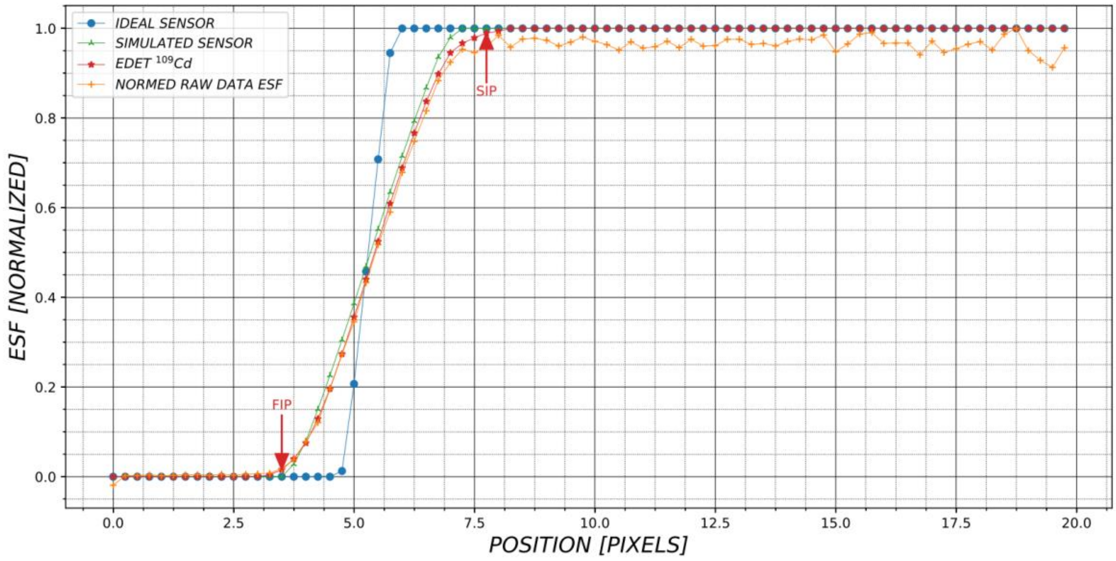

Figure 8-15: Different edge spread functions (ESF) for an ideal sensor, an EDET sensor radiated with a ^{109}Cd source and an associated simulated sensor.

The line spread function (LSF) is derived by computing the discrete derivative of an evenly spaced ESF array:

Equation 8-12
$$LSF_j = \frac{ESF_{j+1} - ESF_{j-1}}{2}$$

At the boundaries, the first difference is calculated meaning that at each end of the ESF array the discrete derivative is simply the difference between the two end values:[28]

Equation 8-13
$$LSF_{0/N} = ESF_{1/N} - ESF_{0/N-1}$$

so the LSF array has the same size as the ESF array. The shape of the LSF curve resembles that of a Gaussian pulse, as depicted in Figure 8-15. The LSF peak should be shifted to the center point of the array by “circular rotation”, that means elements beyond the last position are reintroduced at the first and vice versa. In order to reduce noise effects[29] from pixels positioned further away from the edge location, the line spread function shall be multiplied by a centered Hamming window:

Equation 8-14
$$W_j = 0.54 + 0.46 \cdot \cos[2\pi(j - 2X)/4X]$$

[27] [112] suggest to smooth the ESF array by a fourth-order, Gaussian-weighted, moving polynomial fit. In general, a more rigorous smoothing of the ESF produces a less noisy MTF but at the expense of dampening the high frequency response.

[28] Differing from ISO 12233 which just repeats the first and last value of the computed LSF.

[29] Pixels at the extremes of the window might have response due to noise but little response due to the image edge located at the center of the window.

with X related to the pixel sum of one row and 4 the super sampling factor.[30] In digital signal processing a Hamming window is frequently used for pulse shaping. As in general with window functions, it is zero valued outside a chosen interval and bell-shaped around the middle of the interval.

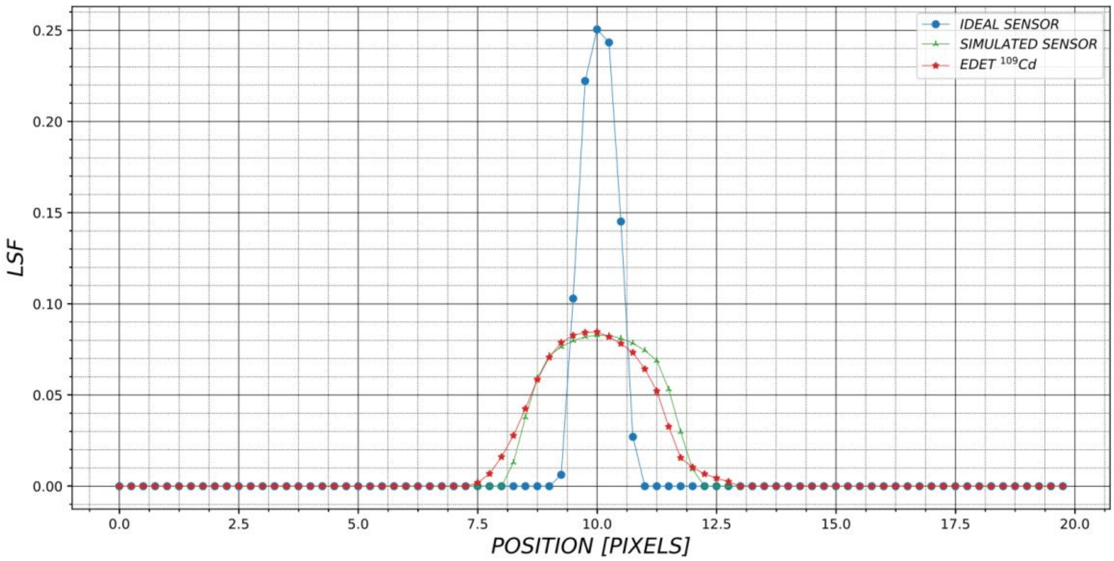

Figure 8-16: Line spread functions (LSF) for an ideal, EDET ^{109}Cd radiated and a simulated sensor. A Hamming window especially smoothes noise contributions at the tails of a LSF.

8.2.3.4 Computation of the MTF

The final modulation transfer function (MTF) uses the normalized amplitude of the discrete Fourier transform (DFT) of the windowed[31] LSF^W, corrected by a factor D_k for an MTF loss introduced by the discrete derivative used to derive the point spread function from the ESF. The ISO 12233:2014 and 2017 deliver two differing equations with respect to D_k and one quickly realizes, that both must be wrong[32] when trying to put them into code. The correct equation can be found here [180]:

Equation 8-15
$$D_k = \min\left[\frac{\pi k/N}{\sin(\pi k/N)}, 10\right]$$

with N the size of the LSF array and $k = 0, 1, 2, \cdots, N/2 \;\; or \;\; (N+1)/2$ if N is odd.

If $k = 0$ L'Hôspital's rule provides:

$$\lim_{x\to a}\frac{f(x)}{g(x)} = \lim_{x\to a}\frac{f'(x)}{g'(x)} \to \lim_{k\to 0}\frac{\pi k/N}{\sin(\pi k/N)} = \lim_{k\to 0}\frac{\pi/N}{\pi/N\cdot\cos(0)} = \frac{1}{1} = 1.$$

[30] This is equivalent to the customary definition of a Hamming window with $W_j = 0.54 - 0.46 \cdot \cos(2\pi j/N)$, $N = 4X$.

[31] Hamming window.

[32] Although in the main section it is correctly described as the „reciprocal of a *sinc* function".

The LSF correction factor primarily affects very high spatial frequencies, for the MTF50 it amounts to an increase of about 1.5% after all. The discrete Fourier Transform (DFT) decomposes the LSF into Fourier series of frequencies:

$$e - SFR_k = D_k \cdot \left| \frac{\sum_{j=1}^{N} LSF_j^W \cdot e^{-2\pi i \frac{jk}{N}}}{\sum_{j=1}^{N} LSF_j^W} \right|$$

Equation 8-16

$$k = 0, \cdots, \frac{N}{2} \; or \; \frac{N+1}{2} \; if \; N \; is \; odd$$

A basic property for the discrete Fourier Transform of a real-valued signal is its complex conjugate symmetry: with respect to the amplitude spectrum, negative frequencies are mirror-inverted to the corresponding positive frequencies. In other words, the frequencies increase up to $k = N/2$ (N the number of LSF sample points) and decrease thereafter laterally reversed. As a result, the sample has to be cut at the first half (representing the positive frequencies) and normalized by the zero frequency component[33] which is just the sum of the LSF^W array and finally corrected by D_k.

Since the e-SFR/MTF is defined as the magnitude or modulus of the Fourier Transform, the absolute of the complex Fourier numbers must be taken. The first zero of the e-SFR marks the resolution of one cycle per pixel.

To switch the frequency from line pairs or cycles/mm (remember a line pair or cycle is defined by a white and a black bar of equal width) to cycles/pixel one simply has to multiply the line pairs by the pixel pitch divided by 1 mm. As one can see from the comparison of Figure 8-16 to Figure 8-17: the smaller the LSF width, the broader the MTF in the frequency domain. As a general property of the Fourier Transform, compression of a signal in one domain results in a signal expansion in the other domain, and vice versa.

The MTFs for the real and the simulated EDET matrix are far away from an ideal sensor, but pretty much in line as shown in Figure 8-17. This points to some good detector properties, since the dominant influence on the MTF obviously originated from the applied geometry of the test setup. Detector inefficiencies (e.g. electronic noise from the readout circuitry) played a minor role.

With the own-built simulation tool at hand, the system sharpness can be expressed by a more descriptive figure, the blur Λ, constituting a length. Technically, it measures the width of the transition zone from the average dark to the bright region level (in other words, the width of the sloped area of the ESF). In the ideal case, this length approaches the pixel pitch, below no further resolution improvement can be achieved. For the ^{109}Cd source measurement, a comparable simulation with identical geometries shows $\Lambda = 210\ \mu\text{m}$ or 3.5 pixel dimensions.

[33] Yielding a value of 1,0 at a spatial frequency of 0.

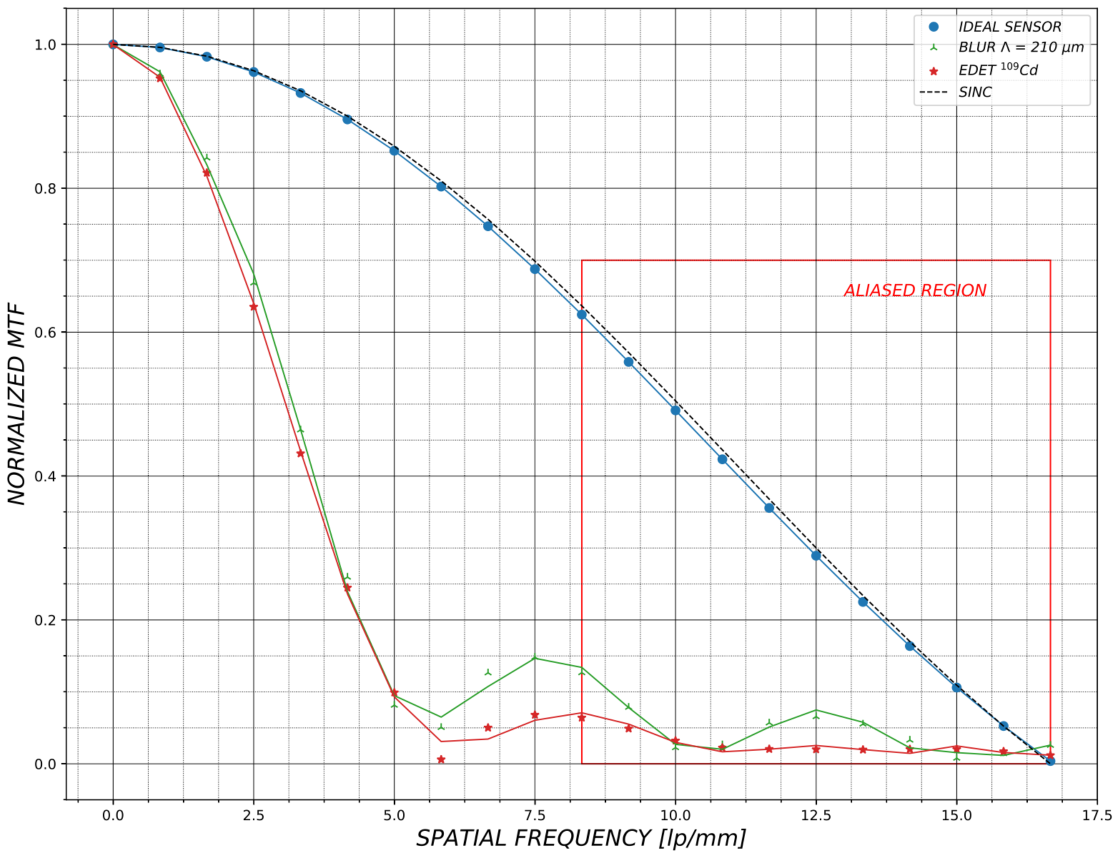

Figure 8-17: Spatial frequency response of a knife-edge measurement: an ideal EDET sensor would closely follow the MTF of a sinc function and reach the maximum of the spatial frequency at $16.\dot{6}$ lp/mm. However, values above $8.\dot{3}$ lp/mm belong to the aliased region (Nyquist frequency f_N). The MTFs from the simulated source and the real source measurements are in good accordance and only deviate for higher spatial frequencies.

8.3 Ghost Charge

8.3.1 General Observations

As indicated above, different imaging modalities will produce different spatial frequency responses for the EDET detector. Using adequate geometries (minimizing the edge position to the sensor and maximizing the edge–source distance), the procedure described with the ^{109}Cd source is best suited to get as close as possible to an ideal MTF for the EDET sensor. However, for the final operation in a TEM, the unavoidable impact from electron scattering in the silicon sensor as well as backscattered electrons must be accepted. Additionally, another complication arises: in contrast to the single hit counting approach used for the radioactive source[34], the pixels need to be calibrated in order to sort out the effect of different pixel gains on the edge response.

[34] Counting all hits above a certain threshold.

The latter is also true, when trying to get the edge response from a LED. Anyway, the spatial frequency is expected to decrease somehow due to diffraction issues as described in section 8.2.2.2. On the positive side, the LED application provides a flat field illumination to the entire sensor and the MTF measurement can be realized much faster. As depicted in Figure 8-18, the edge transition is clearly visible and, at a cursory glance, appears even less blurred than the first attempt with the radioactive source.

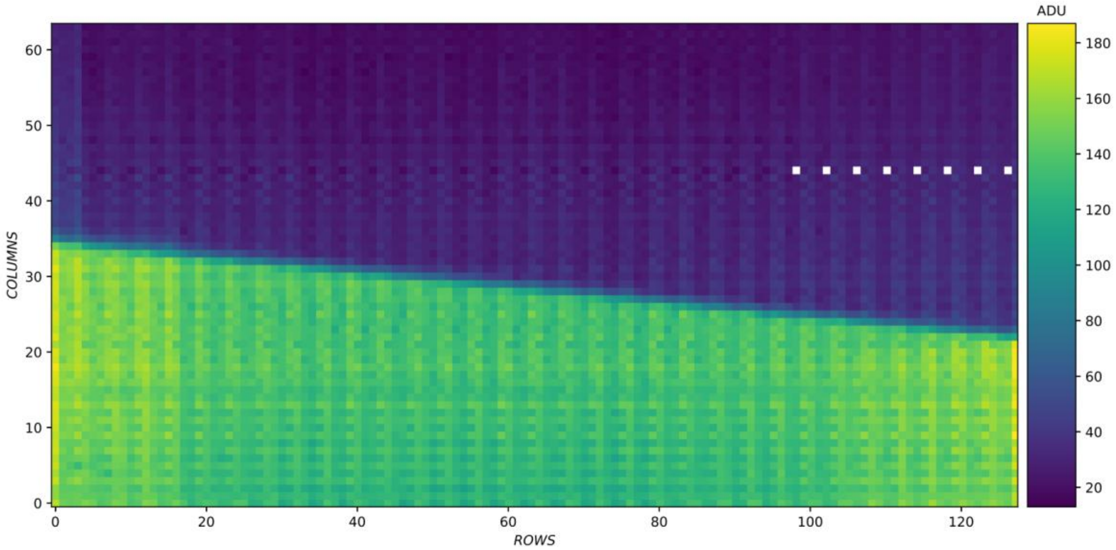

Figure 8-18: Knife edge measurement with a LED as illumination source. The tungsten sheet was again placed directly over the indentation of the PCB in 2 mm distance to a different EDET sensor (this time just 30 µm thick and featuring a gate length of 6 µm). The white pixel squares in the dark area indicate a drainline with partial disconnects.

Nonetheless, a closer look reveals some unexpected observations:

- While not getting any external stimulation, the pixels in the covered or “dark” zone delivered additional current signals, ranging from 13 to 53 ADU. This observation was totally unexpected, for there is no physical explanation. Neither diffraction effects, nor some misalignment of the light source from a central position could induce such a strange phenomenon.
- As with the bright area, the electrical rows in the shadow zone reveal a distinct pattern of alternating brightness, correlating with two pairs of a physical pixel row.

As mentioned, in order to exclude the effect from different pixel gains for the MTF evaluation, a calibration procedure was applied as described in chapter 7. The result is presented in Figure 8-19.

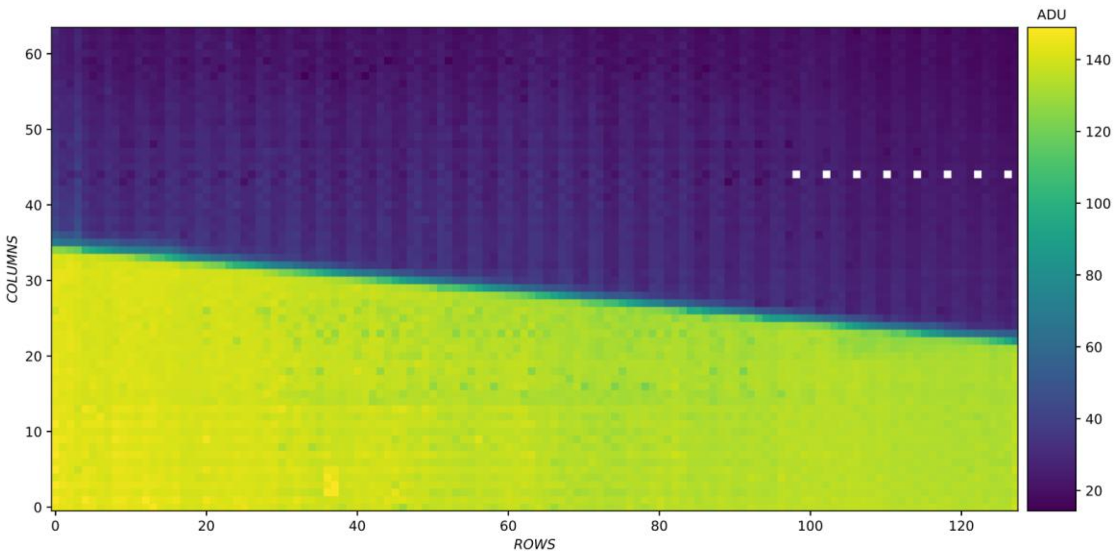

Figure 8-19: Slanted edge image after pixel calibration.

In the uncalibrated sensor, a repeating pattern along the drain lines (every fourth pixel in horizontal direction) was visible, which now got significantly reduced. The pixel variations in the illuminated zone were more than halved to a range of 120 to 150 ADU, albeit this disparity is still considerable and turns out to be substantially higher compared to all other calibration examples analyzed so far.

Beforehand, pixels in the bright region at both ends of the sensor showed a significant higher charge than the pixels in the middle region (this was especially true for the border pixels). Now, a distinct ADU gradient can be identified from the extreme left pixel row to the utmost right one.

Apart from that, a less pronounced gradient can be also observed for the dark zone. In addition, the characteristic stripe pattern along the electrical rows of the EDET sensor survived the calibration effort. While the spread in the shadow region narrowed (15 vs 43 ADU), this effect was obviously not removable during calibration.

In the following, this phenomenon of an additional measured pixel current without any external charge injection should be referred to as the “ghost charge”. On a pure visual inspection, one can notice, that the more pixels of an electrical row got illuminated (unobstructed area), the higher the overall charge level of these pixels rises and accordingly, the higher the ghost charge level for the corresponding pixels in the shadow region shows up. This is especially true for the first electrical row on the left side of Figure 8-19.

8.3.2 Measurement of a LED-MTF

Before devoting more research to the ghost charge aberration, the MTF for the LED illuminated sensor should be determined. As with the radioactive source, a careful selection of the region of interest is of prime importance. For the radioactive source, a homogeneous field was a priori constrained by the circle area related to the collimator aperture. The LED case provides a wider range, since all of the uncovered area got uniformly illuminated. Figure 8-20 includes also the knife edge measurement in horizontal direction, in accordance with ISO 12233. Unlike the vertical knife edge measurement and except for the knife edge region, both the dark and bright regions look quite homogeneous after the calibration. However, if an electrical row was partly covered and registered some charge, the whole row exhibits additional ghost charge, superimposed like a haze over all other pixels of the same row. This can be considered as another indication, that the ghost charge phenomenon is strongly related to the charge carrying electrical lines.

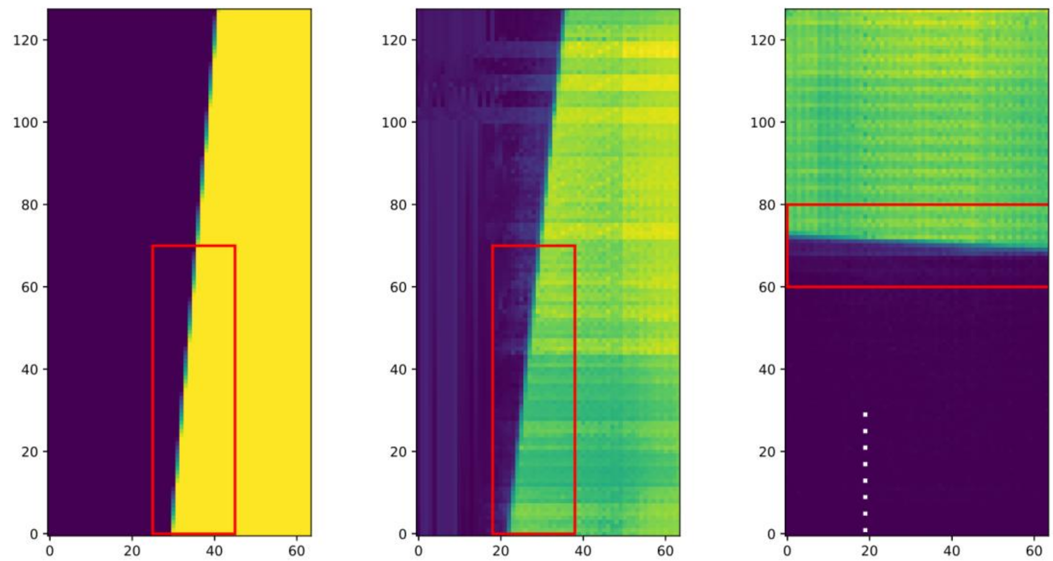

Figure 8-20: From left to right: knife edge recording for a synthetical ideal sensor, illumination by a LED source in vertical direction and in horizontal sensor direction. The angles were calculated at $\theta_V = 5.687°$ in vertical direction and $\theta_H = 3.175°$ in horizontal direction.

A zoomed comparison of the different ROIs together with an ideal sensor is presented in Figure 8-21.

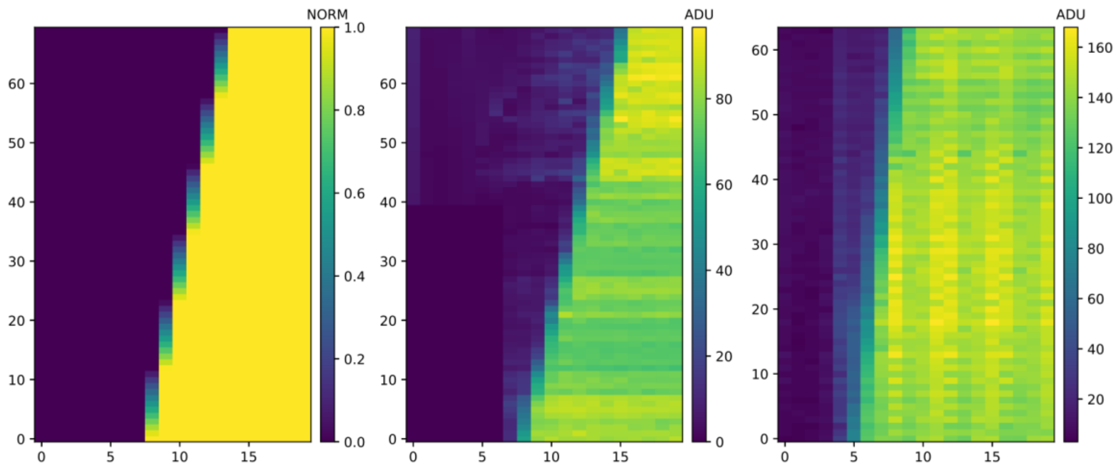

Figure 8-21: From the left to the right: ROIs of an ideal EDET sensor and a real sensor illuminated with a LED (calibrated pixel charges) in both vertical and horizontal directions (to ensure a better comparability, the ROI in horizontal direction was flipped by 90 degrees). Pixels in the shadow zone of the vertical knife-edge illuminated sensor feature ghost charge in form of a characteristic stripe pattern. If the covering sheet was placed in the horizontal pixel direction, the ghost charge effect is only visible in the knife edge region. The observed opacity in the edge region (in pictorial terms showing up like a "haze") is mainly responsible for the expanded blur length of the horizontal MTF at $\Lambda = 300\mu m$ (see Figure 8-23). For fully covered pixel rows, no ghost charge was detected.

The left diagram in Figure 8-22 shows the resulting ESF after projection and binning. The difference between the measured curves and the ideal curves is obvious – partially due to the resolution limitations of the sensor, partially due to diffraction effects. In addition, the ESF in horizontal sensor direction exhibits a much slower increase compared to the vertical measurement. Consequently, when looking to the right diagram, the line spread function of the vertical edge measurement shows a higher peak and a narrower width.

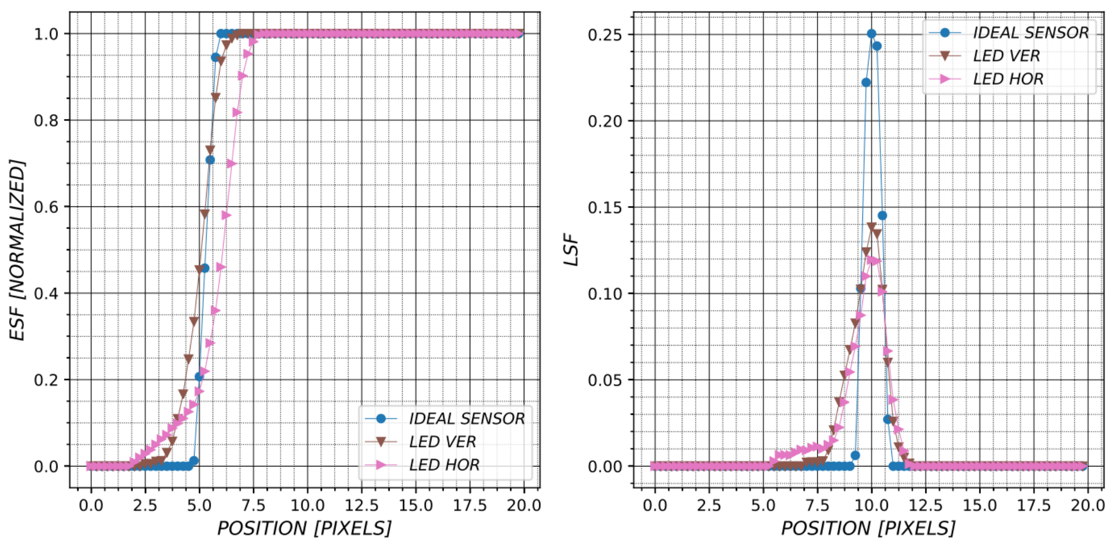

Figure 8-22: ESF (left) and LSF (right) functions for LED knife edge scans oriented in vertical (brown) and horizontal (pink) pixel direction. For a better classification, the ESF and LSF of an ideal sensor (blue) were also plotted.

As said, more compression in real space should translate to more expansion in Fourier space as shown in Figure 8-23. From the diffraction analysis in 8.2.2.2, a blur-length of $\Lambda \approx 80\ \mu\text{m}$[35] was expected, however the fitted simulation showed $\Lambda = 180\ \mu\text{m}$ for the MTF in vertical direction. The difference can be attributed to the ghost charge effect and possible reflections from the silicon surface.[36] As anticipated, the MTF in horizontal direction was slightly worse because of a stronger influence from the ghost effect (the edge proceeded along the pixel rows). However, compared to Figure 8-17, the spatial frequency for the vertical LED data was still above the MTF10 before reaching the aliased region, while for the radioactive source with the chosen distance the maximum resolution was just around 5 lp/mm.

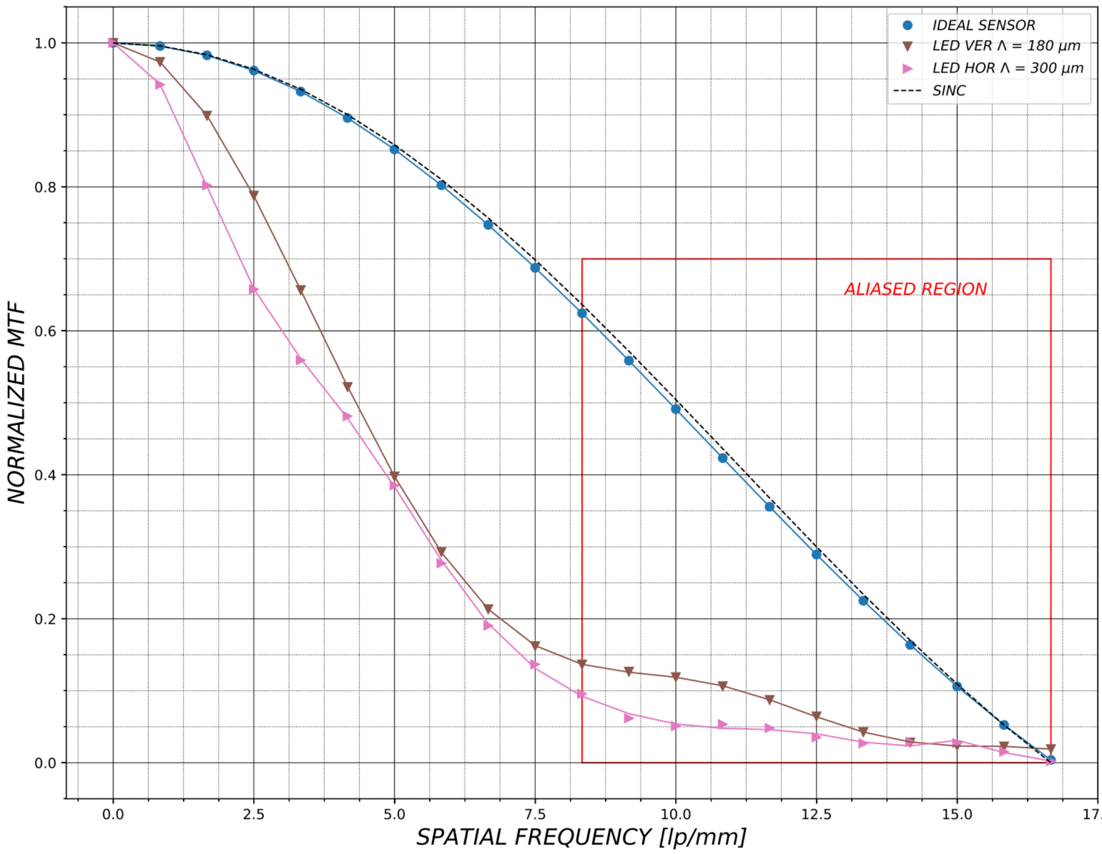

Figure 8-23: MTF for an ideal sensor and the corresponding sinc function. The measured spatial frequencies for the LED knife-edge scans, both in horizontal and vertical direction were significantly lower. Some of the degradation can be attributed to diffraction effects, which could be reduced by moving the knife edge position closer to the sensor. However, the adverse impact stemming from the ghost charge effect can be judged as severe.

[35] To be more precise, the number was calculated at $\Lambda = 70\mu m$ for a residual intensity of 10%. For simplicity reasons, this number was then just multiplied by 1.1 and rounded up.

[36] The reflectivity of silicon can go beyond 70% for wavelengths around 280 nm, while for 850 nm the reflectivity goes down to around 32%.

8.3.3 The Nature of the Ghost Charge Effect

This section explores the ghost charge effect in more detail and investigates raw (=uncalibrated) data to not miss any specific aspect of the ghost charge effect. Additionally, the raw data was not common mode corrected, since this would make no sense for scattering or shadow images. To suppress noise signals, a charge threshold (3 ADU) was set, i.e. any pixel value below remained unconsidered. In general, signal levels under the threshold were associated with no ghost charge signal.

It was already noted, that the ghost charge behaves differently for pixels of the same electrical row compared to pixels in drainline direction. To further investigate on this, Figure 8-24 depicts images of a high intense LED flat field illumination with the top and the bottom side of an EDET matrix alternately covered. It includes also two representative charge curves, one each from the illuminated and non-illuminated region. These curves are then compared to the standard LED charge scan, labeled as "*MASTER CURVE*" (charge curve). This scan was applied to the same sensor with the same system settings, but recorded without any obstruction or mask.

Although both curves, due to their rippled shape deviate from an ideal one, the curve in the bright zone almost identically reproduced the corresponding master curve from the master scan. By contrast, some curves in the dark zone display a tiny slope, instead of an expected horizontal straight line at the bottom.

If values above 10 ADU were excluded, as shown on the adjacent 2-D images with the restricted scale, one obtains a more detailed insight into the fine structure of the dark zones. Despite these pixels got no external charge injection, an additional signal of up to 10 ADU compared to a dark frame was measured.[37] Reversing sides for the mask position did not change the key message, though the average ADU level was slightly lower with exception of the higher ghost charge for the last electrical line.

This analysis is not intended to put too much effort on side effects, but the brighter flashing up of the top electrical row (4th diagram top row) might be a consequence of the rolling shutter read out: the rows are read out consecutively, without interruption[38] in an endless loop, while the DCDE itself does not know which row is currently active. So after the dark row 31, the charge bearing row 0 directly connects and the higher charge bearing potential might influence also the level of the preceding row 31.

[37] A dark frame corresponds to the median pixel values of 1001 frames without any illumination. 10 ADU translate to almost 7 µA for the particular DCDE 3.3 gain setting.

[38] Until the DCDE is powered off.

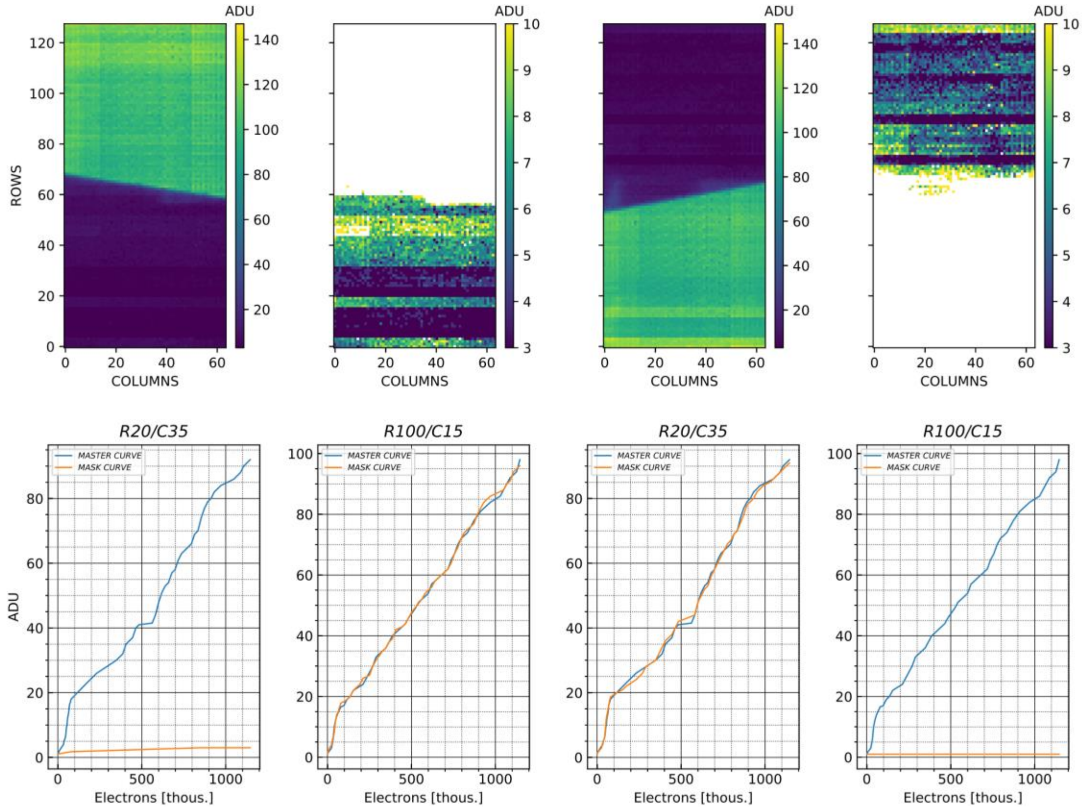

Figure 8-24: LED illuminated small EDET sensor, covered by a tilted tungsten mask, separating the matrix into two halves in horizontal (row) direction. The DCDE resided always on the bottom side. Apart from the transition zone, both regions look quite homogeneous and the charge curves in the bright area (two diagrams in the middle of the bottom row) almost reproduced the master curve's shape, including non-idealities. This behavior was observed, regardless from the position (top or bottom) of the shadowed region on the matrix. The lower scale images focus on the dark zones, where one notes substantial ghost charge signals for a lot of pixels. In general, the single pixel ghost charge level seems to correlate with the respective electrical row.

As already noticed, a positioning of the mask in parallel the drain line (column) direction altered the characteristics and extent of the observed effect. In particular, the registered amplitudes of pixels from the unobstructed region were measured significantly lower (compare the maxima of the colorbar scales between Figure 8-25 and Figure 8-24 (top left diagram), although both measurements were recorded with the same LED intensity).

At the bottom of the diagram, two representative charge curves from the bright zone were selected and again compared to the master scan: the same pixels from the masked scan now show a significantly lower amplification with a widening gap to the mastercurve, irrespective of same row pixels on the opposing dark side contained low ghost charge (Row 20: maximum 10 ADU) or high ghost charge signal (Row 118: maximum 28 ADU). Once more, the obstructed region exhibits a pattern of darker and brighter rows.

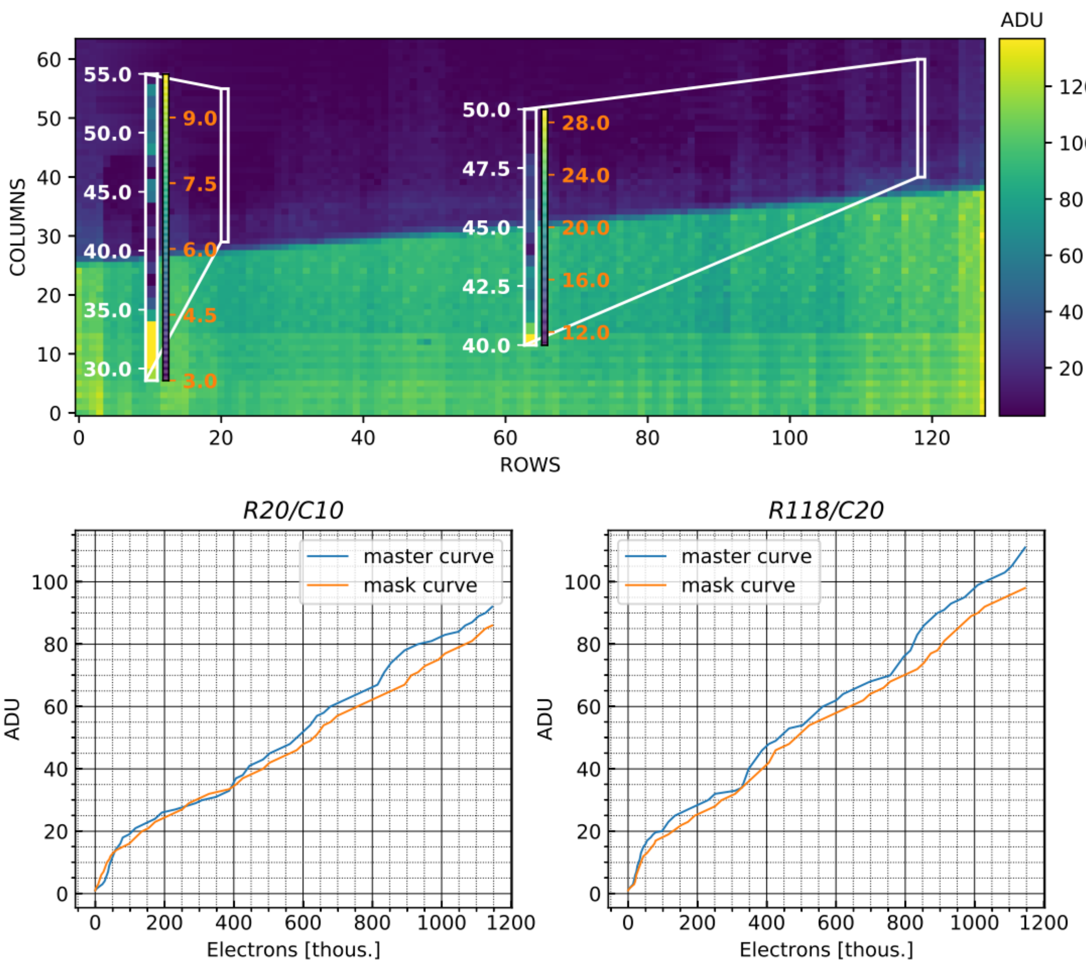

Figure 8-25: LED illumination small EDET sensor: the tungsten mask position was in the drain/column direction. The DCDE resided on the left side. Two insets magnify parts of the non-illuminated section of rows 20 and 118 respectively.

From the facts listed so far, one could conclude that especially the fraction of illuminated pixels within one electrical row dominantly contributes to the observed anomaly. To verify this assumption, two other masks[39] were produced, the first one covering everything with the exception of approximate one electrical row, as depicted in Figure 8-26. The slit was made smaller than the physical dimension (one electrical row $4 \times 60\mu m = 240\mu m$), since diffraction effects had to be taken into account. No ghost charge signal was observed for pixels outside the illuminated region as exemplified on the bottom right diagram for pixel R90/C34. However, the shape of the charge curve from a selected pixel of the illuminated slit region significantly differed from the master curve, not so much by its level but by its shape.

[39] All mask cuts were carried out by a laser into a 0.1 mm tungsten foil with a rectangular dimension of 6 x 12 mm.

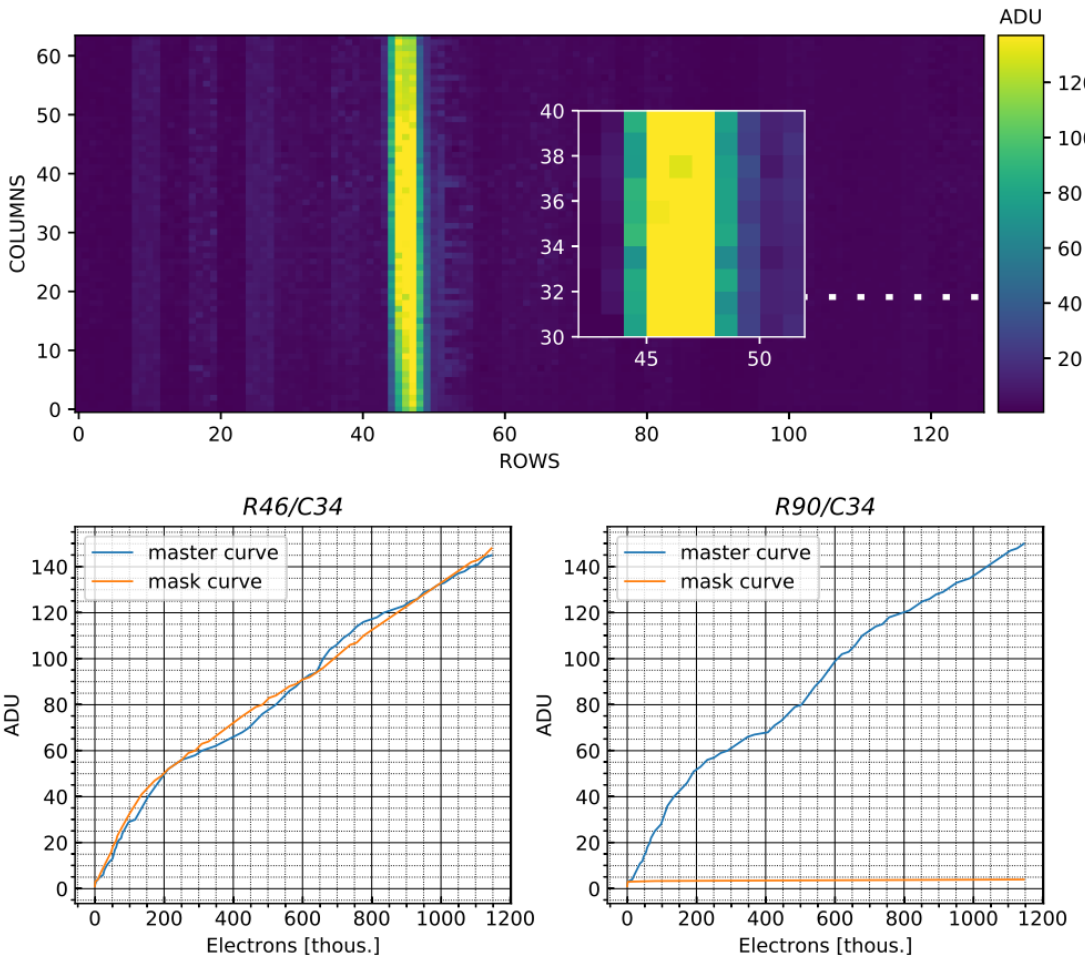

Figure 8-26: Mask with a small slit of 215 µm width (about 3.3 EDET pixel dimensions) used to illuminate the sensor pixels connected to one electrical row: rows 44 to 47 depicted in the inset of the top diagram represent one electrical row. As one can see, eventually 6 pixel rows were showing a significant LED induced signal, covering a width of 360 µm. This larger illumination region is due to diffraction effects at the mask edge, which has been calculated at about 70 µm using Equation E - 7, if a LED wavelength of 850 nm and an edge sensor distance of 2 mm were used. Applied on both sides $215 + 2 \times 70 = 355\ \mu m$ *confirms fairly well the validity of this equation. The charge curve of a representative pixel from the illuminated slit region on the bottom left diagram shows a much smoother shape that its corresponding curve from the master scan. Pixels outside the slit region do not show any ghost charge effect, as exemplarily shown by the horizontal flat line of pixel R90/C34.*

Figure 8-27 shows 9 further charge curves from the slit region, all approaching a close-to-ideal[40] charge curve shape, compared to their counterparts from the master scan: an initial steep rise, mirroring the stronger gain from the internal gate region, followed by a shallower but still straight slope characteristic for the overflow region. By contrast, the corresponding master curves display a rather sigmoidal shape around the OF straight lines, with deviations of up to 10 ADU.

[40] "Ideal" in that context means in accordance with previous simulations.

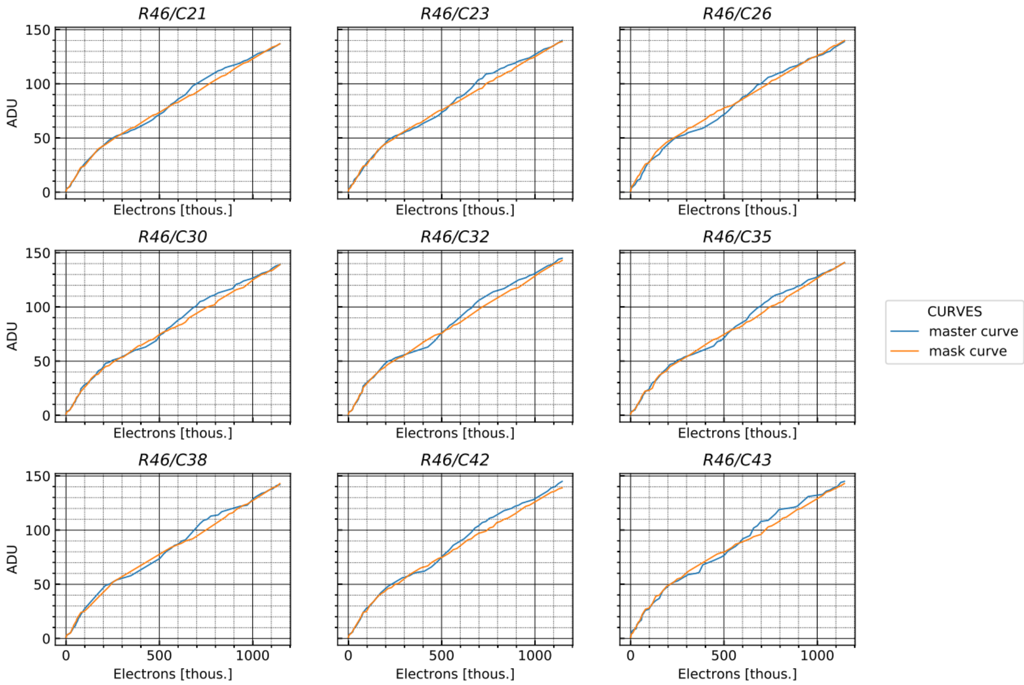

Figure 8-27: Selection of charge curves (orange) of a single pixel row, illuminated by a LED through a mask with a small slit. Compared to the master curves with the same LED on the uncovered sensor (blue), the single row illuminated charge curves show a close-to-ideal shape.

Another mask contained small drilled holes in drain line direction, as shown in Figure 8-28. The shadow picture diagram below excluded pixel values above 15 ADU. The charged pixels reacted in a mixed way: a significant lower amplitude, which was already observed for the mask in column direction, combined with a smoother shape, trending to an ideal curve.

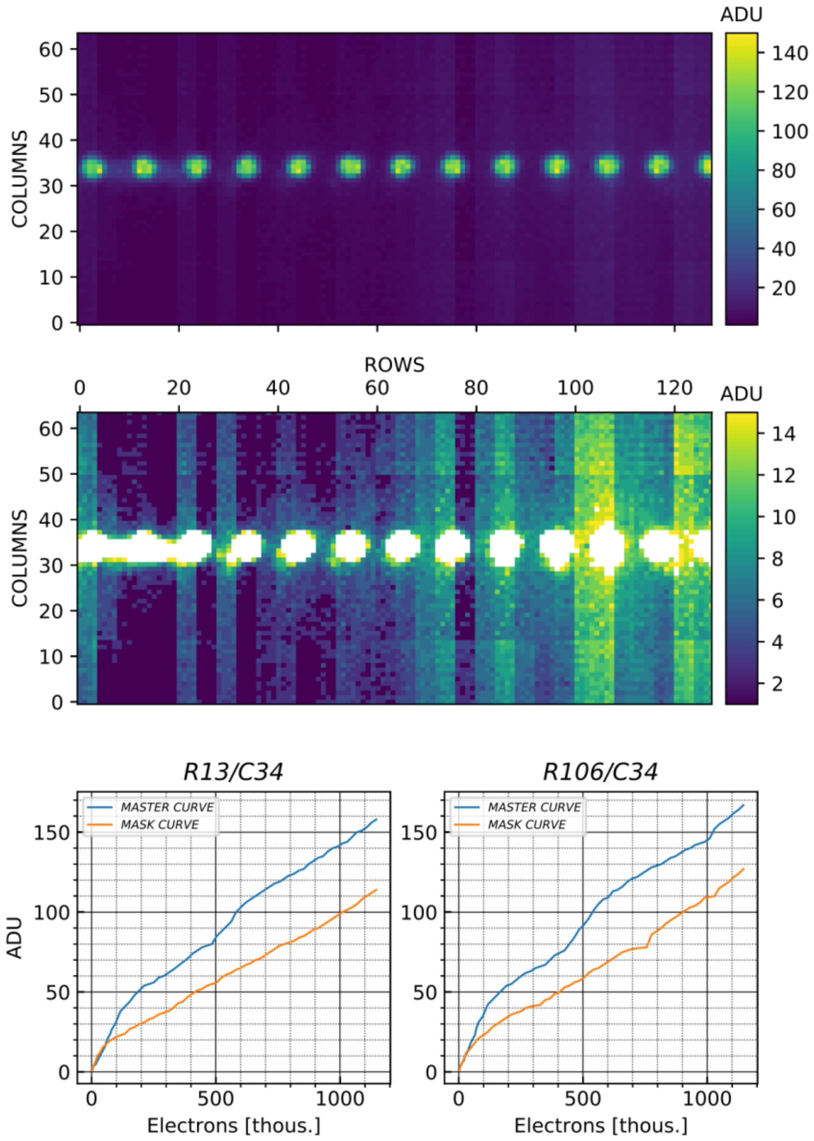

Figure 8-28: Small hole grid mask placed along the sensor's length direction. Despite the drilled holes had a similar size and were positioned at equal spacing, some pixel rows in the covered region display only very low ghost charge (e.g. rows 15-19), while other rows (e.g. 100-109) appear strongly elevated. Compared to their corresponding charge curves the amplitude of the pixels in the illuminated hole region was significantly lower (bottom two diagrams).

For further investigation, a mask with an evenly distributed hole grid was placed over the sensor, as shown in Figure 8-29. Any electrical row, comprising some external charge injection, experienced some additional ghost charge signal by increasing the offset over the whole pixel row. A closer look reveals an elevated ADU level, even for the non-illuminated pixels of a row with external charge injection and much less ghost charge for the rows in between.

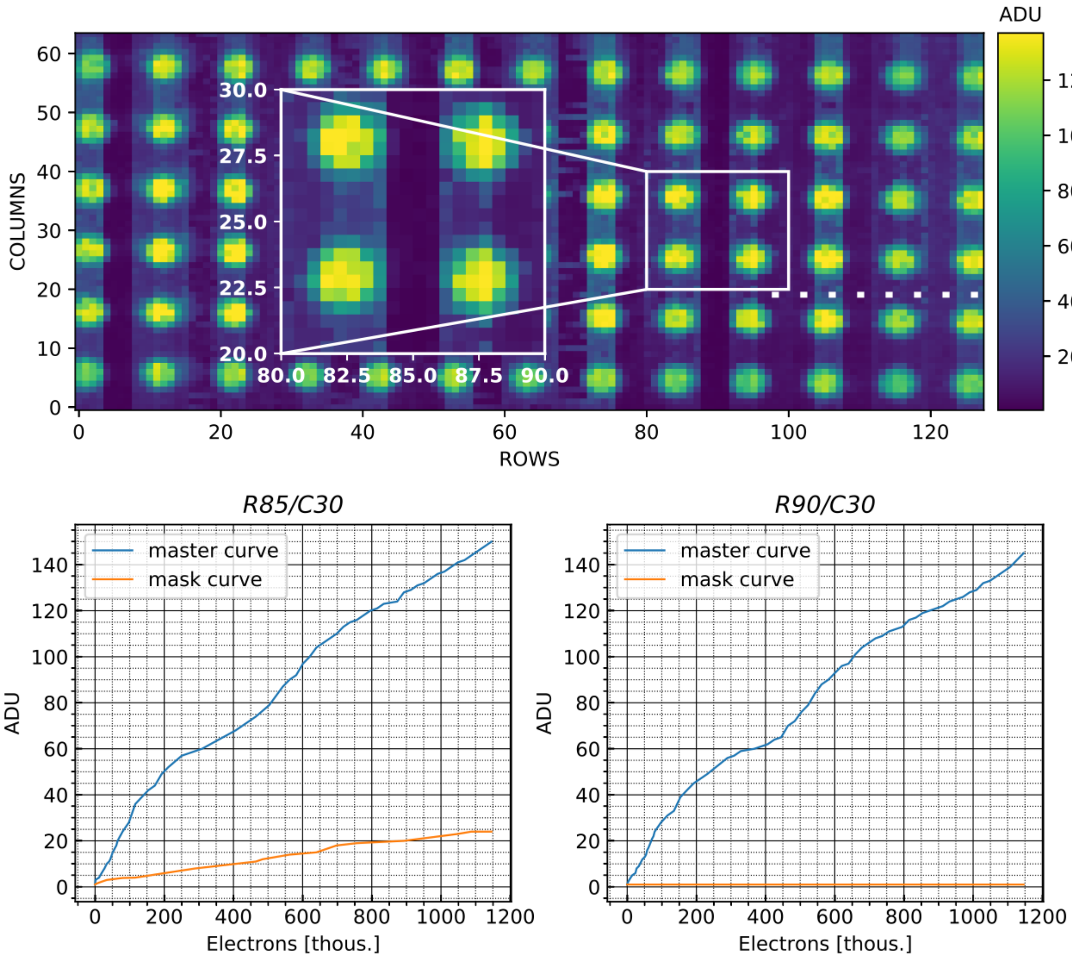

Figure 8-29: Tungsten mask with a regular pattern of tiny holes. The inset position of the upper diagram clearly shows, that electrical rows without any external charge contained zero or only small ghost charge signal. By contrast, if a certain row experienced some charge injection in some of its pixels, all other pixels of the same electrical row were affected by the observation of an additional ghost charge. The two selected pixel charge curves at the bottom of this diagram confirm that relationship (pixel R85/C30 was extracted from a row with charge injection, the row of pixel R90/C30 got no external illumination).

One of the most important applications for the EDET detector is related to the recording of weak-contrast, real-space scattering or shadow images. Figure 8-30 depicts two simple structures, a cross and a circle. Even though all the described phenomena occur in the vicinity of these structures, the specific shapes can be clearly discerned.

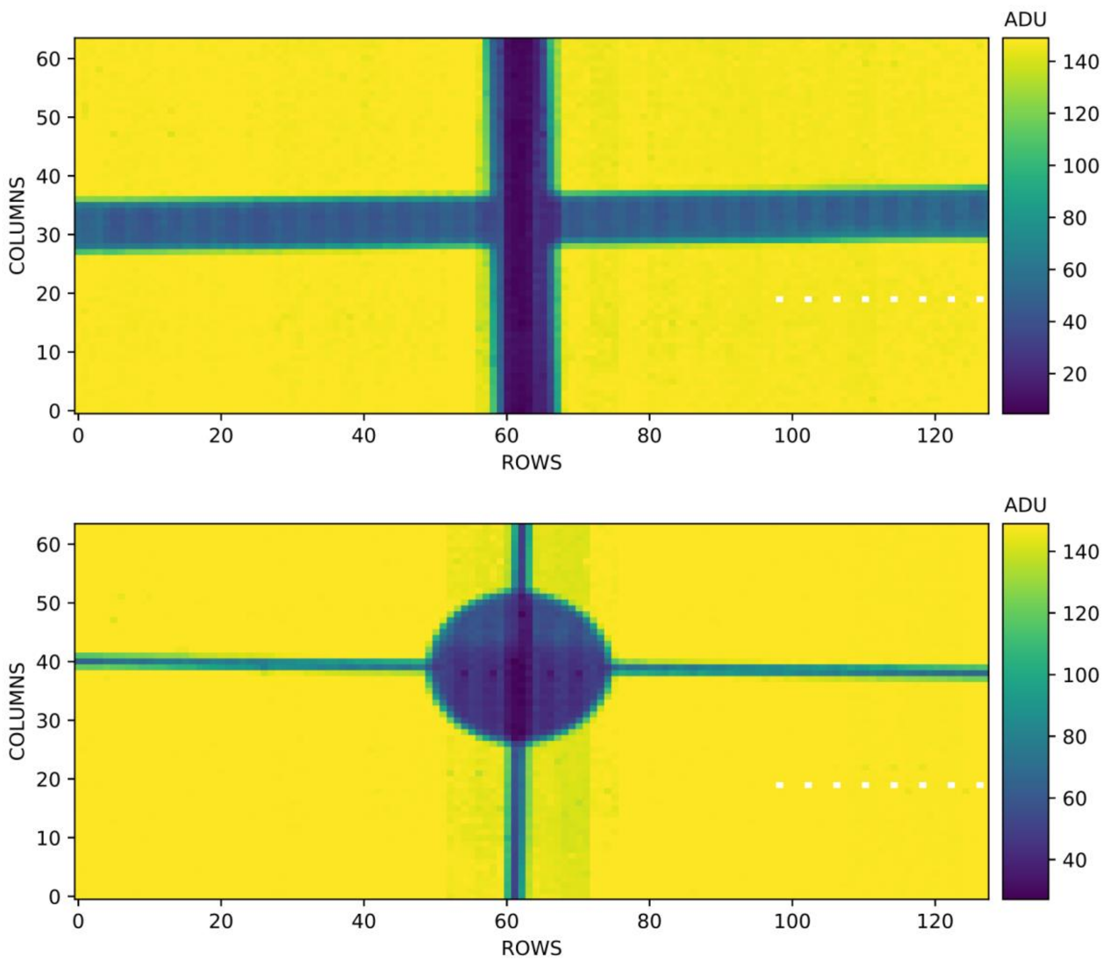

Figure 8-30: Shadow pictures of a cross and a circle in 2 mm distance to the EDET sensor, illuminated by a LED. The dark beam of the cross in row direction (rows 60-63 in vertical direction) corresponds to an electrical line, hence only very small ghost charge was observed. In contrast, the beam in drain line direction runs across the electrical lines and noticed a lot of additional ghost charge. On the bottom chart with the circle, the general charge level was reduced for the sensor rows containing the circle.

To sum up, the measured charge level itself depends on both, the overall illumination intensity but also on the fraction of illuminated pixels within an electrical row. The shape of the charge curve seems to be influenced by the charge level of the preceding rows.

8.3.4 EDET Detector Settings influencing Ghost Charge

Up to now, the analysis was confined to the description of the symptoms, i.e. the visible consequences of the ghost charge effect. The following investigation addresses the root causes and potential mitigation measures to reduce them. All three suspects, exerting an influence on the ghost charge level, are worth considering: the DCDE, the Switcher and of course the EDET matrix.

By varying several parameters of the different detector components, the impact on the ghost charge was evaluated. This in turn should allow to draw conclusions about the origin or nature of the ghost charge effect.

One might intuitively blame the lack of common mode correction for the stripe pattern, especially observed for the half covered sensor in column direction. However, a special investigation on 3 Mio dark frames revealed, that for the DCDE gain 3.3 the common mode variates basically within a relative very narrow range[41] of $\pm 3\ ADU$ as shown in Figure 8-31.[42]

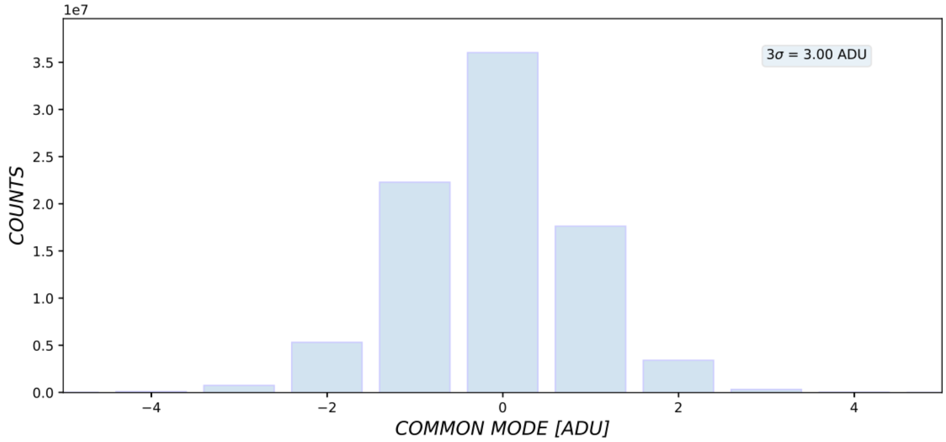

Figure 8-31: Common mode deviations for 3 Mio frames (DCDE gain 3.3) recorded on the basis of pure offset data, while keeping all detector settings constant. The shortest gate length was used. Similar measurements for longer gate lengths showed a significant lower variation.

To accentuate the ghost charge effect, the signal charge of a slanted edge measurement can be split into three areas as outlined in Figure 8-32: a bright zone, a dark zone and a transition zone. In the bright as well as in the dark zone, the largest charge variations were noticed between the electrical rows. Additionally, some correlation was observed: the higher the charge level and number of pixels in the illuminated region of a row, the higher the ghost charge signal in the respective shadow row. This points to some self-enforcement mechanism, acting upon all pixels of the respective electrical row. The transition zone was broadly defined, to exclude any diffraction effects in the covered area. Nevertheless, some pixels in the shadow zone show a ghost charge of up to 25 ADU, corresponding to a fictive drain current of 17 µA for the 3.3 DCDE gain.

[41] The results are strongly dependent on the selected gate length (4 µm for the above measurement). For the longer, nominal 6 µm (before etching) gate length the distribution is much narrower.

[42] Besides, common mode variations should be independent from signal.

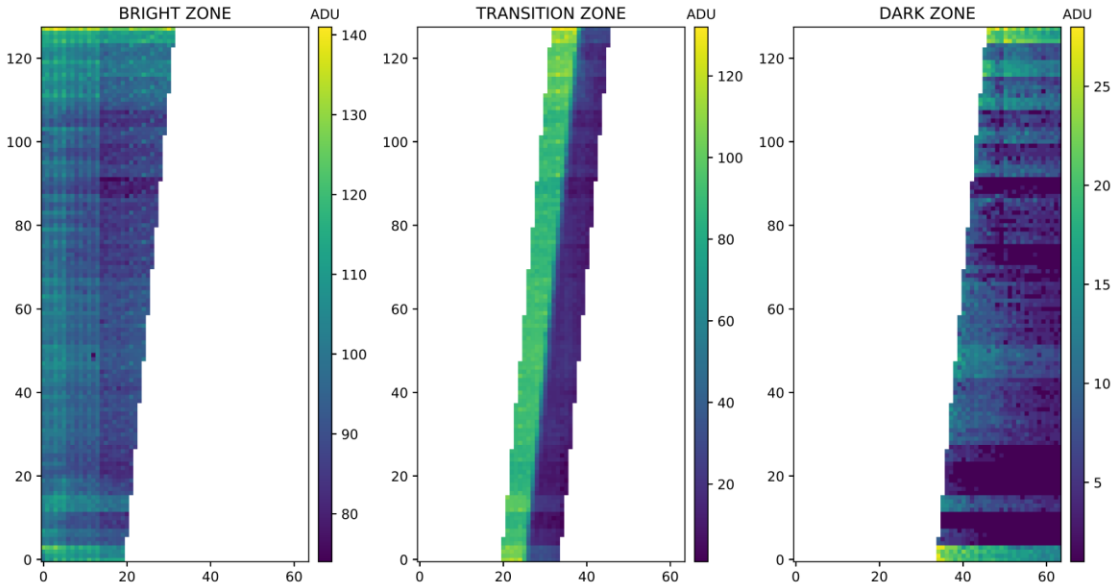

Figure 8-32: Separation of the obstructed sensor illumination in three special regions: bright zone, transition zone and dark zone.

To investigate the assumed correlation between ghost charge and electrical row more closely, all pixel values of an electrical row (4 physical rows) were added together, section by section for the bright (columns 1-18) and the dark zone (columns 45-62) and divided by their number (256 pixels). As shown in Figure 8-33, the selection confirms the basic statement, that a higher injected charge in the uncovered area correlates with a higher additional current in the shielded pixel area.

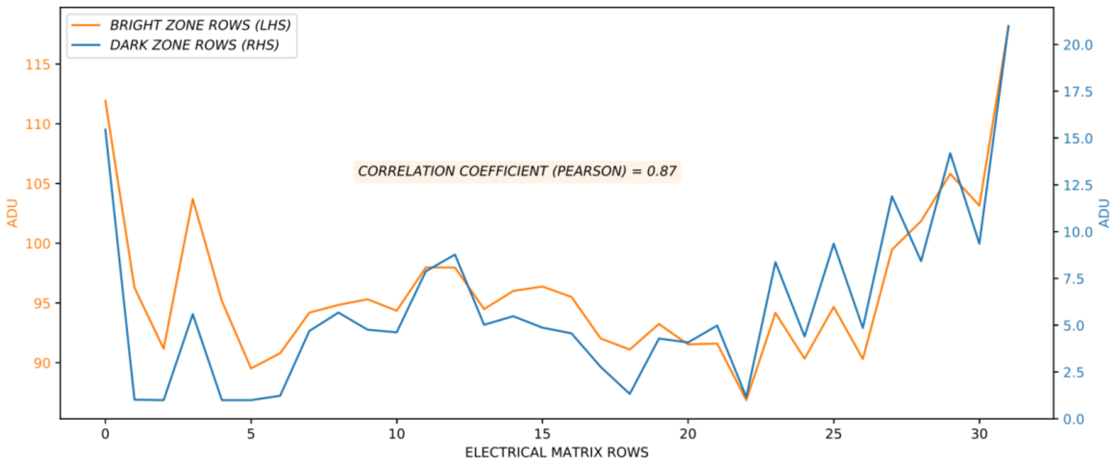

Figure 8-33: Row-wise (electrical) correlation of the ghost charge level in the obstructed region with the level of measured charge in the uncovered area.

The following search for optimized parameters intentionally used a different hybrid board to minimize the ghost charge problem. The best settings were then applied to the board just presented above. This approach should ensure, that the optimization results are reliable and of general validity.

Figure 8-34 depicts 9 representative pixel rows along their respective matrix columns, together with the corresponding drain currents expressed in ADU. All pixels were kept uncalibrated and 4 distinct charge levels were singled out. The observed ghost charge levels did not remain constant, but experienced a slight decrease towards the sensor edge in the dark zone. While the ghost charge effect behaved relatively benign for charge injections of up to 230,000 electrons per pixel, stronger illumination intensities induced a significant rise of the ADU level, also in the obstructed area where an external, physical influence could be excluded.

An interesting detail might have been hidden at first inspection: studying the charge levels under more scrutiny, one notices that the space between no charge injection and the lowest charge level is sometimes barely higher than between other step increases. This comes to a surprise since one would expect a much stronger increase for lower charges, because of the much stronger internal gate amplification. Take for example row 110: the charge levels for column 20 are at about 36 ADU, 58 ADU, 90 ADU and 108 ADU, so the difference between the second and third charge injection is relatively close to the difference between no charge injection and the first level (36 vs 32 ADU).

After the steep edge declines, the levels do not move immediately down to 0 but hover at 6, 13, 25 and 27 ADU respectively (average values of columns 40-60). Correcting the real charge data for the elevated ghost charge levels in the obstructed region, the new charge levels would now settle at 30, 45, 65 and 81 ADU. Admittedly, the situation is considerably more complex: as has been shown in Figure 8-27, the charge curves feature a rather sigmoid shape in the overflow region. This peculiarity could also explain the higher gap between the second and the third charge injection, resulting from the ghost level adjustment (the differences are now at 30, 15, 20 and 16 ADU). Additionally, this approach does not factor in a gradient towards the edge pixels (indicated by the downward sloping curves in the obstructed region), which can be observed especially for the rows 5 and 95.

Nevertheless, as a main message one can conclude that a level shift in the dark zone caused by the ghost charge effect is counterbalanced to some degree by a corresponding correlated level shift in the bright zone. This is positive news, as far as shadow imaging is involved, since ultimately only relative differences form the contours of a 2-D image. However, for the smaller contrast differences associated with scattering images, there is a risk that these get blurred by the ghost charge effect. Furthermore, the analysis so far dealt with fixed targets, hence the ghost phenomenon could be corrected offline to a certain extent. As far as moving objects are involved, the specific impact of ghost charge signals remains to be investigated.

At the end, it is indispensable to look out for measures to mitigate or even eliminate this annoying ghost charge effect.

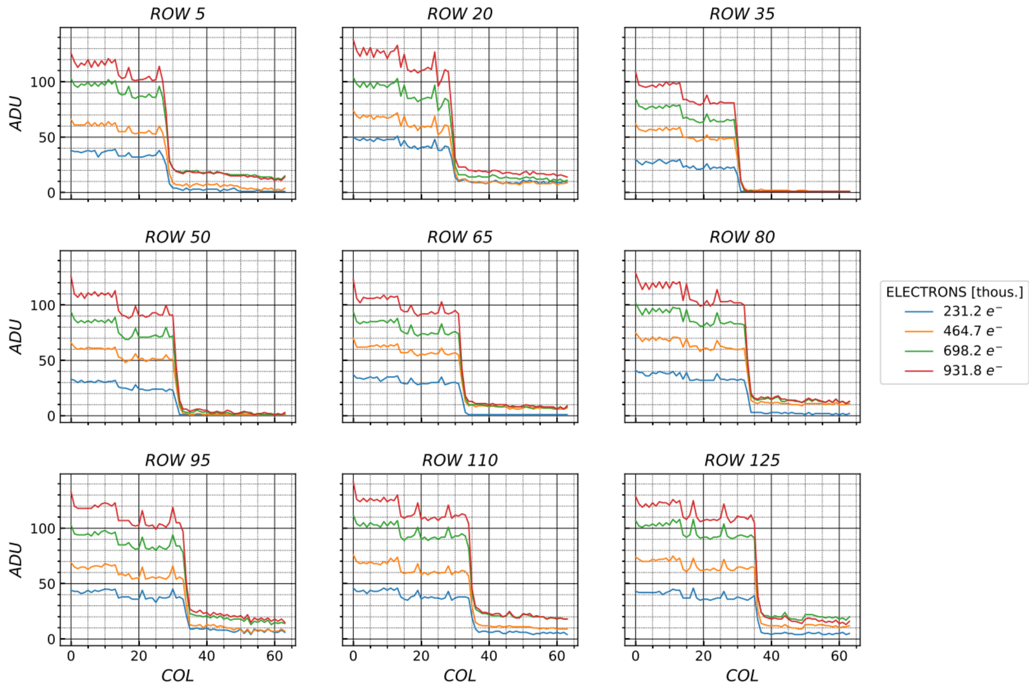

Figure 8-34: Selection of 9 pixel rows and the measured drain current in ADU, corresponding to 4 different illumination intensities (expressed in generated electrons per pixel).

The following analysis tried to get to the bottom of the problem by variating several system parameters. In the course of this investigation more and more evidence indicated, that the current arriving at the **transimpedance amplifier** (TIA) of the DCDE exerted a major influence on the ghost charge level. This current can be steered by all of the three aforementioned components of the detector.

8.3.4.1 Variation of Switcher Parameters to influence the Ghost Charge Level

The observations above suggest some conjunction of the ghost charge effect with the electrical rows, which are first and foremost steered by the Switcher. So, at first instance it was a natural approach, to investigate if a causal relationship exists by variating the most important Switcher parameters. A general malfunction can be excluded, otherwise this would not explain why the ghost charge effect does not occur in large areas of fully covered matrix rows as exemplarily shown with the slit mask. Nevertheless, it is possible that the clearing process turns out to be inefficient and a remaining charge in the IG- (or even in the OF-)region would contribute to a ghost charge signal.

To fully exclude influences from the clearing process, the first measure was to rise the clear spread[43] from 15 V to the maximum permissible voltage difference at 20 V [125]. For the sake of clarity, only 3 rows with the highest ghost charge effect were selected

[43] Difference between clear high and clear low amplitudes.

(65, 80, 125). The outcome presented in Figure 8-35 shows almost no influence from the higher clear spread on the ghost charge level.

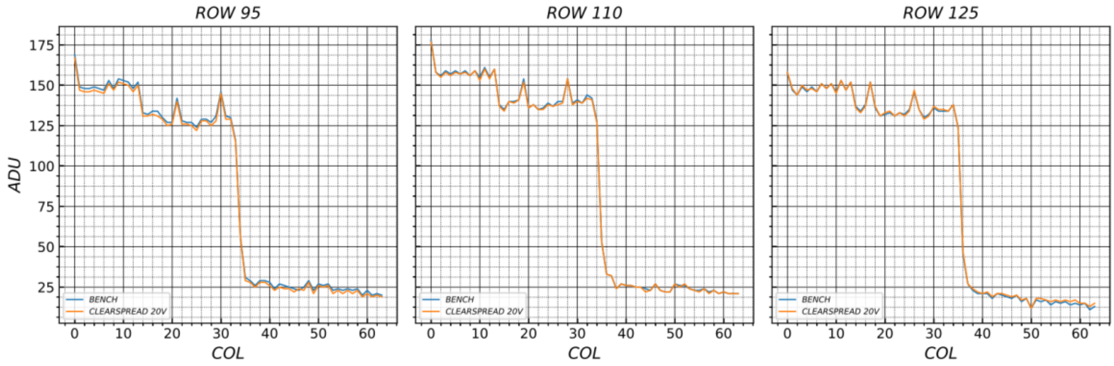

Figure 8-35: Influence on the ghost charge by increasing the clear spread from 15 V to 20 V. "BENCH"-mark refers to the standard settings measurement.

As a next step, the duration of the clear pulse was doubled from 4 clock cycles (one electrical line readout period consists of 32 clock cycles)[44] to 8 clock cycles:

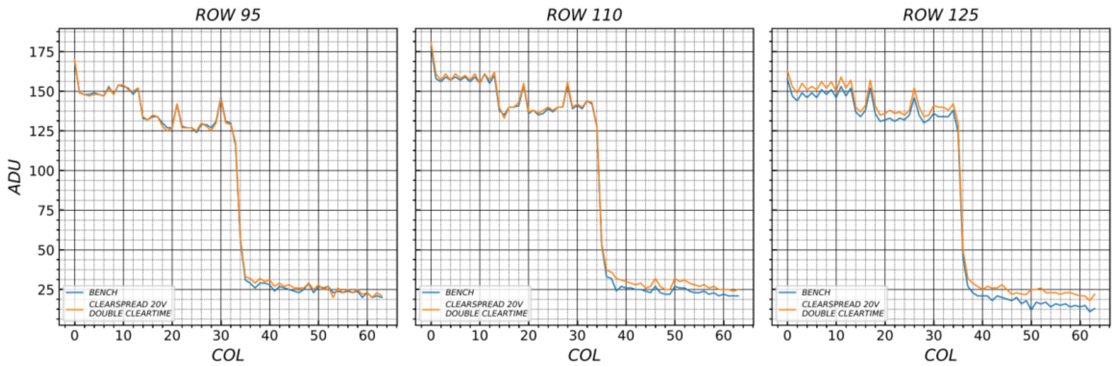

Figure 8-36: Influence on the ghost charge by increasing the clear spread to 20 V and additionally, doubling the duration of the clear pulse.

Again, a close congruence for both settings in the bright zone was obtained, even some negative impact with respect to the ghost charge (rows 110 and 125) could be registered. Though the finding is not unexpected, one cannot underestimate its importance: if an already strong clear pulse would have not been able to clear the used small matrix, it is even more unimaginable to erase electrical rows of an 8-fold length.

The last adjustable Switcher parameter being scrutinized concerned the selection of the sampling point. As one can see from Figure B - 12, the timing of the clear pulse and gate on voltage also influenced the general level of the drain current. However, a lower drain current must be compensated by a lower *VnSubIn* DAC to guarantee a similar offset starting position. As one can see in Figure 8-37, the single rows react with mixed results:

[44] As a reminder, a typical electrical line read-out cycle consists of the following steps: activation of the gate, fixed sampling period of 8 clock cycles, clearing operation and setting the gate back into an off state.

a positive influence on example rows 95 and 110 and an adverse impact on rows 20 and 125.[45]

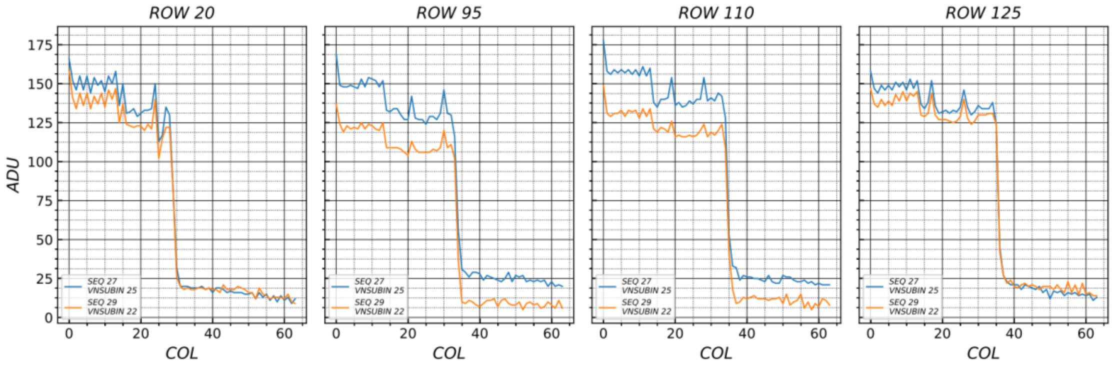

Figure 8-37: Influence of the chosen Switcher sequence (see APPENDIX B.3) on the ghost charge effect. Out of 32 possible sequences, two at sampling points 27 and 29 were selected for the comparison. Assuming that the clear pulse was set to 4 clock cycles, at least 4 out of 32 sequence shifts are not usable, since the charge sampling period (1 clock cycle) would overlap the clear operation. Additionally, the clear rise and fall times increase with the connected capacity (matrix) [125], so for the small matrix the number of unusable sequence shifts rather amounts to 8 (see Figure B - 12).

8.3.4.2 Variation of the Matrix parameters to influence the Ghost Charge Level

The matrix is operated by 7 voltages (bulk, gate, clear, cleargate, drift, guard, depletion and source voltage). From a logical viewpoint, only the gate–source voltage difference should have some reasonable impact, since this regulates the basis level of the drain current.[46] As more charge induces a higher drain current, a similar reaction can be also achieved by adjusting the gate-on voltage. However, a lowering of the drain current also makes an adjustment of *VnSubIn* necessary to shift all pixel offsets back into the dynamic range. Accordingly, one should not expect a significant effect within the DCDE as is confirmed by three selected charge curve comparisons in Figure 8-38. The situation even worsened, since the ghost charge level in the dark region increased, while the corresponding level in the bright zone decreased, thereby losing on the contrast, the total difference between bright and dark zone.

[45] The measurements depict only the pure signal, i.e. the black level was deducted from the gross charge.

[46] About 100 µA per drain channel if not stated differently.

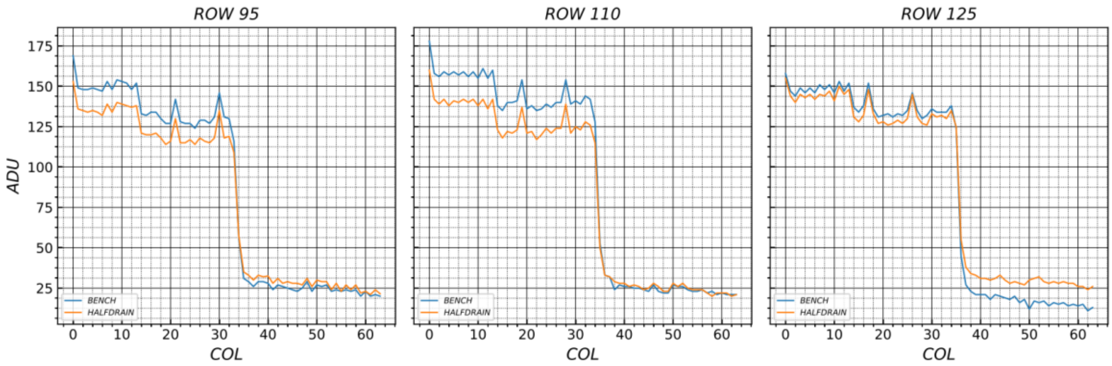

Figure 8-38: Influence on the ghost charge level from a decrease of the gate–source voltage, leading to a bisection of the drain current.

8.3.4.3 Variation of the DCDE parameters to influence the Ghost Charge Level

A schematic of the transimpedance amplifier, embedded in a resistive current receiver, was already presented in Figure 4-7. It converts the current obtained from a matrix drain-line into a voltage. A lot of current sources and current sinks were designed to fine tune the final output, particularly noteworthy are *VnSubIn, VnSubOut, VTCSFN, VPAddIn, VPAddOut, VTCP/VTCPL.*

The registers *VnSubIn* and *VPAddIn* determine the level of the drain current flowing into the transimpedance amplifier. *VnSubIn* acts as a current sink: the higher its 7-bit DAC level, the more current will be redirected into the sink. Usually, its main purpose is to adjust for the different gain settings as well as to get the offset currents from the 2-bit DAC compression back into the dynamic range. *VPAddIn*, an associated current source and by a factor of about 4 weaker than *VnSubIn*, serves for the fine tuning.

At this point, an important reminder must be set: before starting any measurement, all EDET pixels should be moved into the dynamic range of the DCDE. If this was not done correctly, as e.g. shown in the right diagram of Figure 8-39, the offset distribution narrows substantially, but a lot of pixels reside out of the dynamic range. Worse, the pixel offset levels do not react homogeneously by an equivalent shift to the left, but by a compression to a different distribution. This makes it impossible to predict the exact output on a given charge input (otherwise this base shift could be relatively simple corrected for).

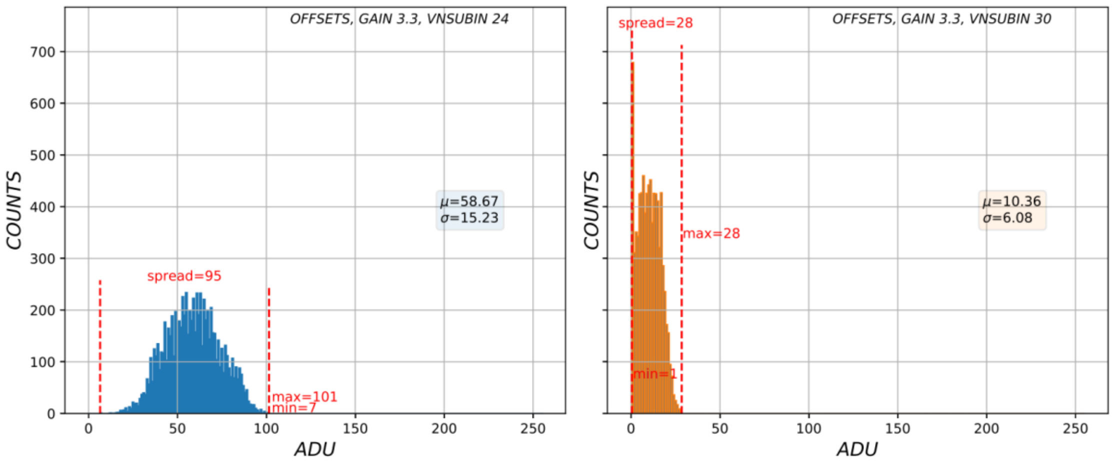

Figure 8-39: Left: Offset distribution for gain 3.3 and VnSubIn = 24, getting all pixels of the matrix into the dynamic range of the DCDE. Right: if VnSubIn was chosen too high, a lot of pixels exit the dynamic range of the DCDE.

Indeed, concerning the ghost charge effect this out-of-the-dynamic-range-approach would eliminate a lot of the ghost charge signal, as one can see in Figure 8-40. Effectively, this proposal would just sweep the problem under the carpet. Additionally, this comes at a cost: some smaller real charge signals remain unrecorded leading to a loss of information.

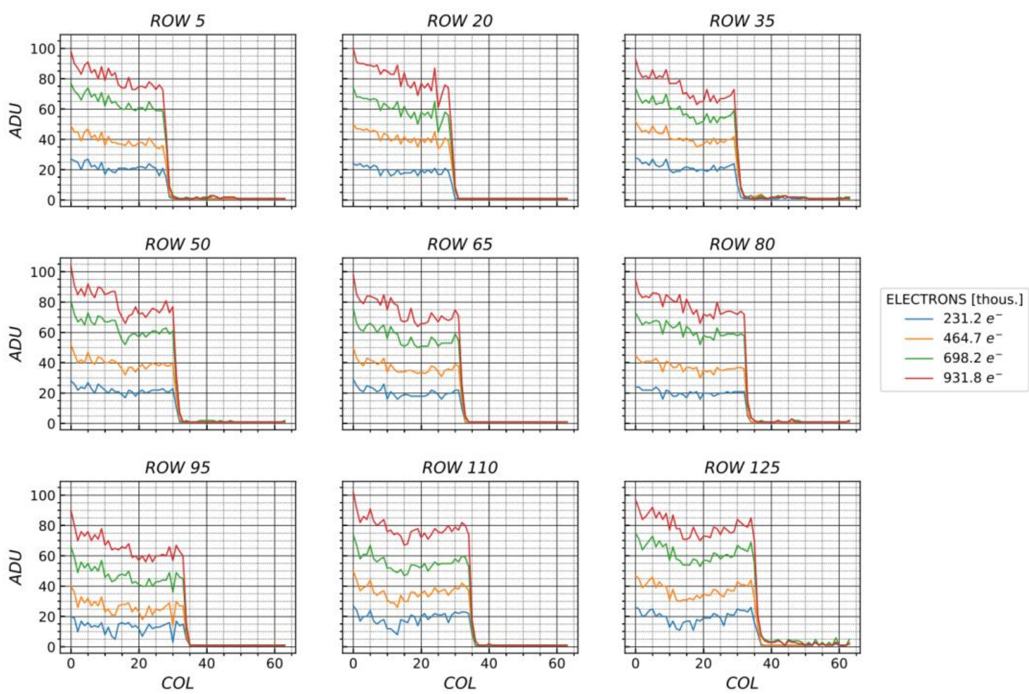

Figure 8-40: Ghost charge when VnSubIn was chosen too high, putting a lot of pixels out of the dynamic range.

The next contemplated current source *AmpLow* acts as a ground node for the TIA's input stage, implemented as a **cascode** *[181]*. Unlike *VnSubIn* and *VPAddIn* which control the current inflow to the TIA, *AmpLow* is an integral part of the TIA. An isolated increase of *AmpLow* from 350 mV to 500 mV delivers the following results, depicted in Figure 8-41:

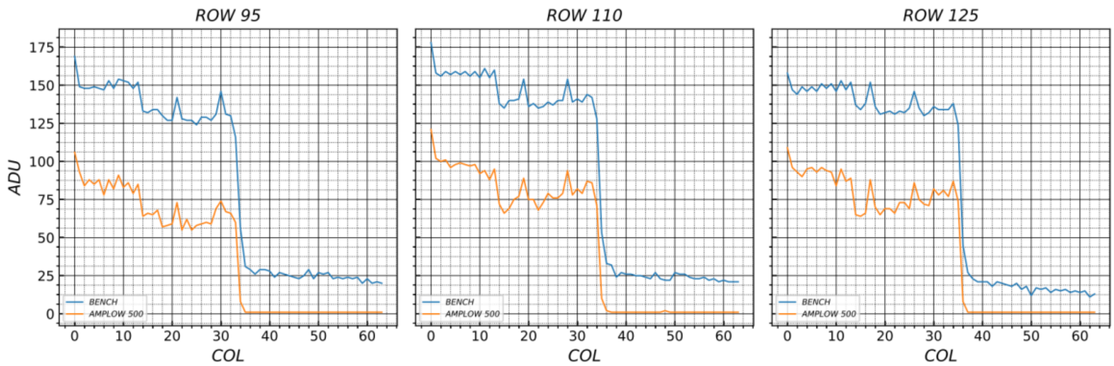

Figure 8-41: Influence on the ghost charge level by an increase of the AmpLow voltage level from 350 mV to 500 mV.

Though the ghost charge level in the shadow zone was reduced significantly, the charge level in the bright zone was even more reduced. As an unwelcome side effect, the inter-pixel variations have also risen. Moreover, significant increases with respect to *AmpLow* tend to shrink the dynamic range of the DCDE and to add some curvature at the start and at the end of the dynamic range as presented in Figure 8-42 (see also APPENDIX B.2.2).

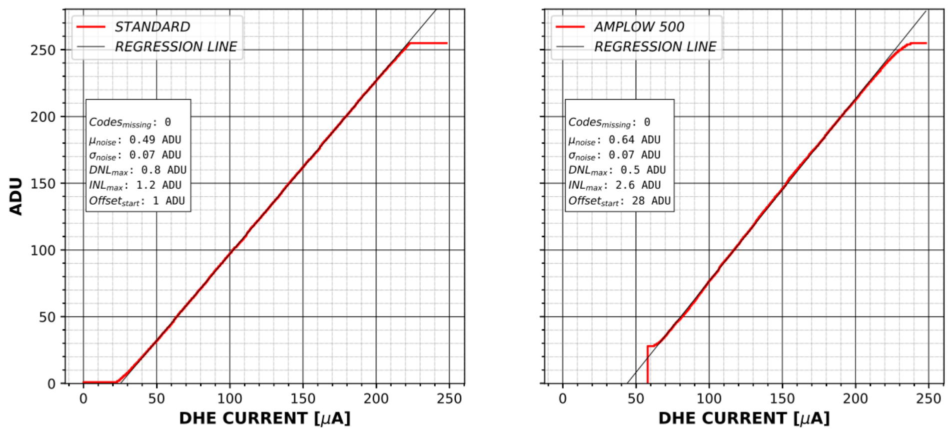

Figure 8-42: Analog digital transfer curves from an external current source. Standard settings of AmpLow at 350 mV (left) and AmpLow at 500 mV (right).

Considering all DCDE channels, this configuration would not only implement a significant restriction to the dynamic range between 25 and 40 ADU, but would also be accompanied with a significant higher missing codes issue (see APPENDIX B.2.1), as shown in Figure 8-43.

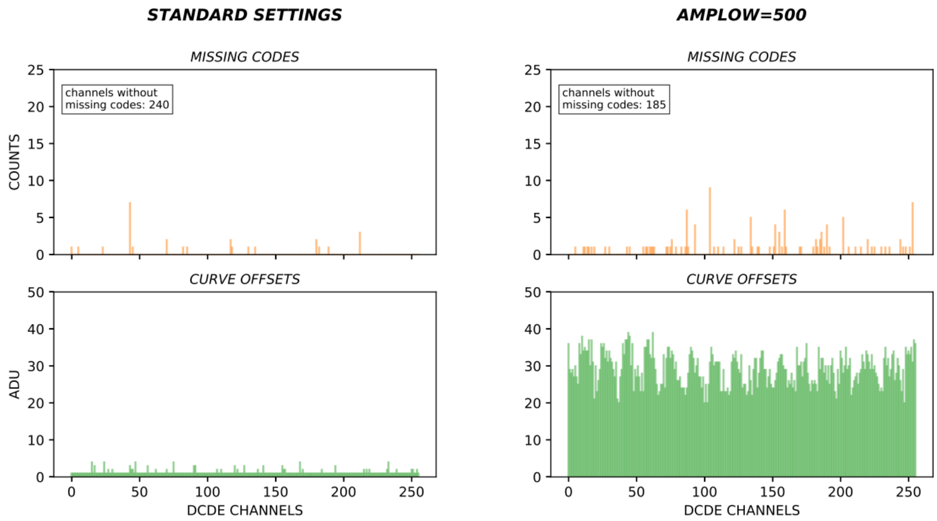

Figure 8-43: Overview of missing codes and curve offsets for different AmpLow settings (350 mV as the standard case versus 500 mV).

The current sink *VTCSFN* at the TIA's output stage conducts the current to earth. If the strength of this source was set too low, the input potential could be adversely affected, if high currents are routed through the transimpedance amplifier.[47] In Figure 8-44 the register for *VTCSFN* was adjusted from 60 to the maximum setting of 127. Depending on the row, some significant reduction of the ghost charge effect can be observed.

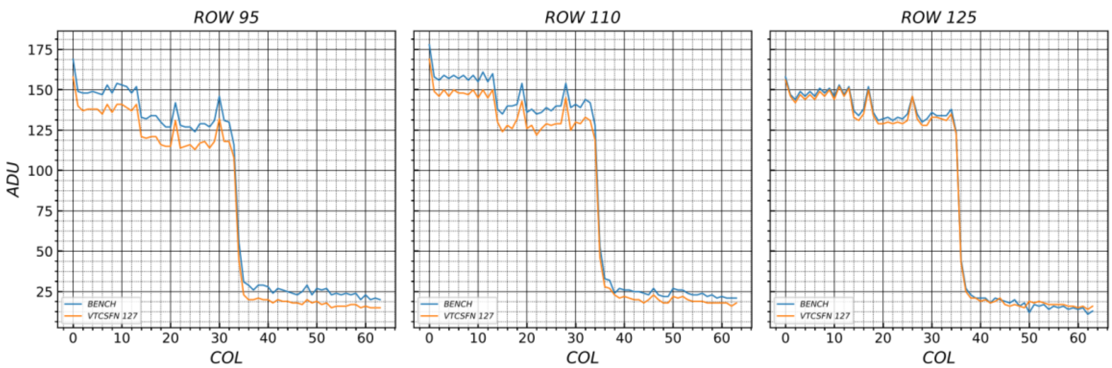

Figure 8-44: Influence on the ghost charge level by setting VTCSFN to 60 (bench-curve blue) and to 127 (orange).

Further improvements were obtainable by changing some parameters simultaneously, as presented in Figure 8-45. In addition to *VTCSFN,* the bias potential for the TIA's input stage *VTCCASC* was set to 120. To absorb the much higher expected drain currents from the DCDE (compared to the BELLE DCD), a new register *boost SubIn* was created as a supplement to *VnSubIn*. Technically, a check of this parameter must be met with a significant reduction of the *VnSubIn* DAC value, in order to bring the offsets back into the

[47] Conversation with the DCDE designer Prof. Ivan Peric.

dynamic range. For obvious reasons this measure also contributed to a reduction of the ghost charge.

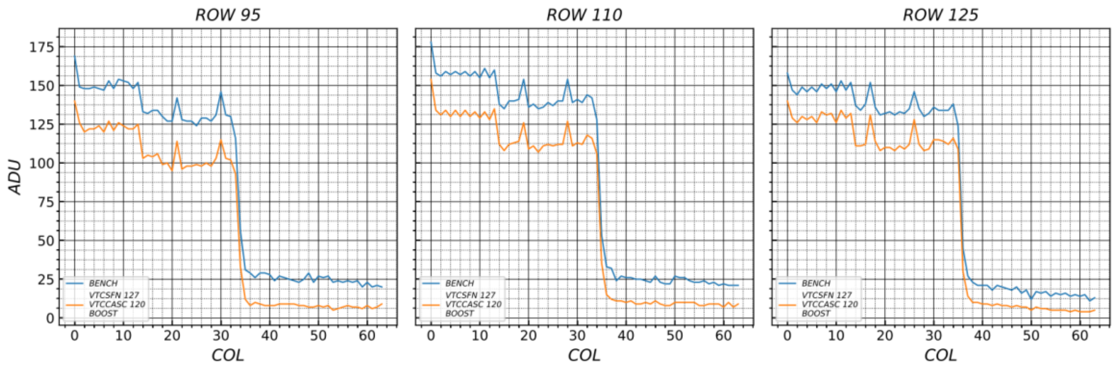

Figure 8-45: Influence on the ghost charge by variating multiple parameters of the DCDE receiver.

As stated at the begin of this section, the improved settings were then applied to the hybrid board presented in Figure 8-32, allowing a direct comparison in Figure 8-46. Apart from two electrical rows and some pixels in the broader vicinity to the edge, most pixels in the covered area did not bear any or only a very small ghost charge signal.

Various other combinations, as well as additional parameters like the current sources *VTCP/VTCPL*[48] at the TIA input stage were investigated with limited success.

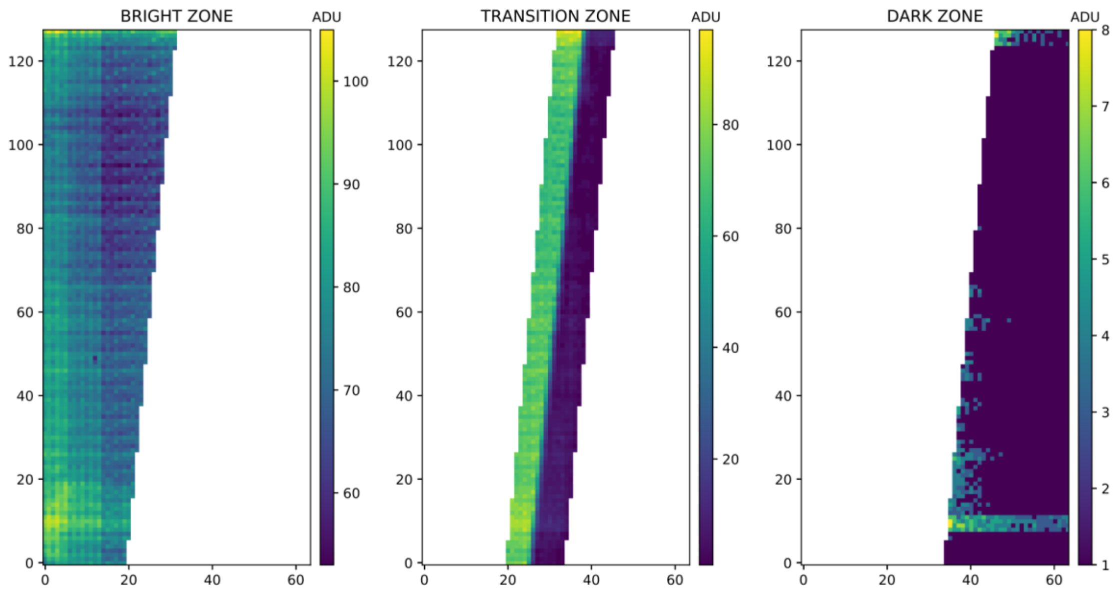

Figure 8-46: Separation of the obstructed sensor illumination in three special regions: as one can see, alternative DCDE settings significantly reduce the ghost charge effect.

The MTF measurements were also repeated with the improved settings. As a result, the new MTF, presented in Figure 8-47, looks optically better, however the blur length was only slightly reduced to $\Lambda = 165\ \mu m$. This can be mainly attributed to the edge pixels,

[48] *VTCP* decreases the ADU value if increased whereas *VTCPL* speeds up the amplifier.

immediately adjacent to the shadow region, where the ghost charge could not be fully eliminated.

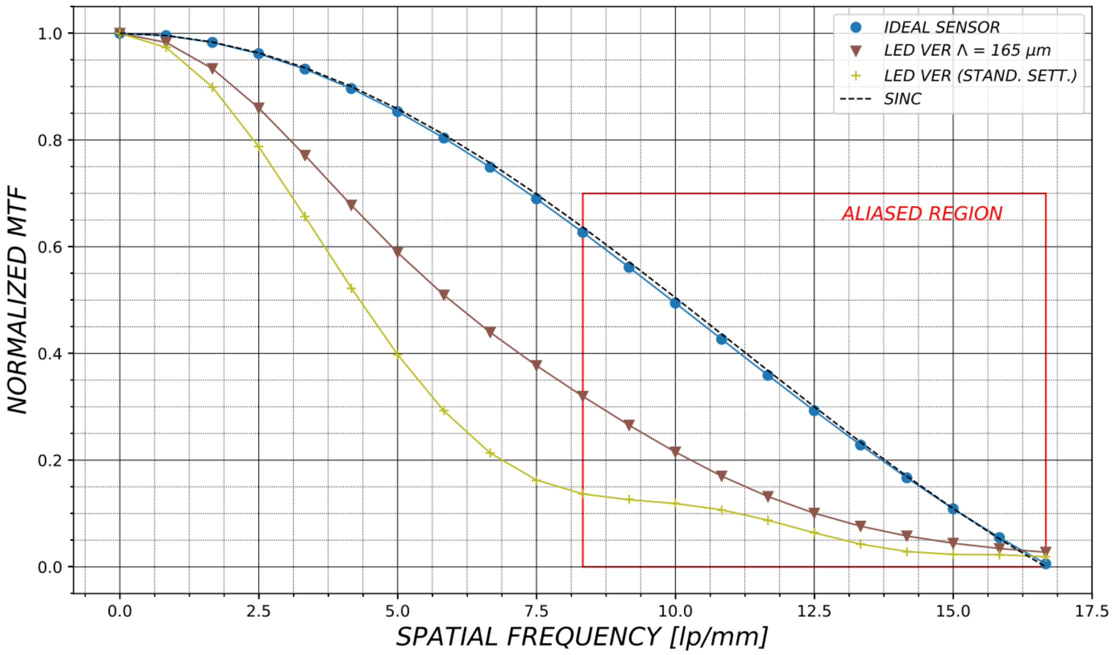

Figure 8-47: LED MTF on a calibrated EDET sensor with standard settings and with improved settings, aimed at reducing the ghost charge effect.

In summary, if improved settings for various DCDE parameters were selected, the ghost charge effect could be mitigated. The impact of this phenomenon is highly correlated with the illuminated pixels of the same electrical row. To some extent, such correlative moves could be calibrated away. However, this effect does not disappear completely and degrades the sharpness of the detector. The various findings of this analysis could provide some guidance for a future upgrade of the DCDE.

8.4 Voltage Sweeps

8.4.1 Operating Voltages for a DEPFET Pixel

All DEPFET voltages were referenced to the common source voltage (V_S) of the transistor, which was fixed at +7 V for the measurements of this thesis:

V_D: the DEPFET sensor is generally operated in the saturation region, therefore the gate and drain voltages have to comply with the p-channel MOSFET saturation condition:

Equation 8-17 $$V_G > V_T \text{ and } V_D < V_G - V_T$$

V_D is determined indirectly by the analog potential of the DCDE, which was set at +1.8 V compared to ground, so $V_D = -5.2\,\mathrm{V}$. In order to regulate a drain current of about 100 µA per channel, the operational gate voltages for the sensor (without radiation damage) were fixed between -1.6 V to -2.2 V, dependent on the used gate length. As already mentioned, V_T resides around -0.2 V, so the above condition was easily fulfilled.

$V_G^{\mathrm{on/off}}$: the gate on voltage puts the respective electrical row into an active state and induces a drain current. Care should be taken, that the gate off voltage is never set below the threshold voltage, since this would switch on all transistor channels simultaneously, causing a high current flow. As a consequence, this could potentially ruin the detector, either by damaging the readout chip or, in an extreme case, even cause the matrix drain lines to melt. The gate off voltage was typically set to +5 V.

$V_C^{\mathrm{on/off}}$: the clear on voltage has to be chosen high enough that a complete erasure of the stored charge is guaranteed. The clear off voltage is range limited: on the one hand, it should not be set too high to become attractive during the charge collection. On the other hand, it must not be set too low, since electrons could potentially flow back from the clear electrode to the internal gate (backemission) as one can see in Figure 8-50. Besides, the Switcher specifications foresee a minimum voltage difference between clear high and clear low of +5 V and a maximum of +20 V [118, 125]. An additional negative space charge (deep p-implant) prevents the electrons from drifting directly to the clear contact.

Four pixels share the same clear implant respectively. A common aluminium line connects them to the corresponding Switcher contact. For an efficient clear process, the difference or delta between the clear on/off voltages has to be selected sufficiently high. To verify the clear efficiency, a simple sweep was performed by +0.5 V steps for V_C^{on}, increasing the clear deltas from +5 V to +20 V ($V_C^{\mathrm{off}} = 1\mathrm{V}$) as shown in Figure 8-48.

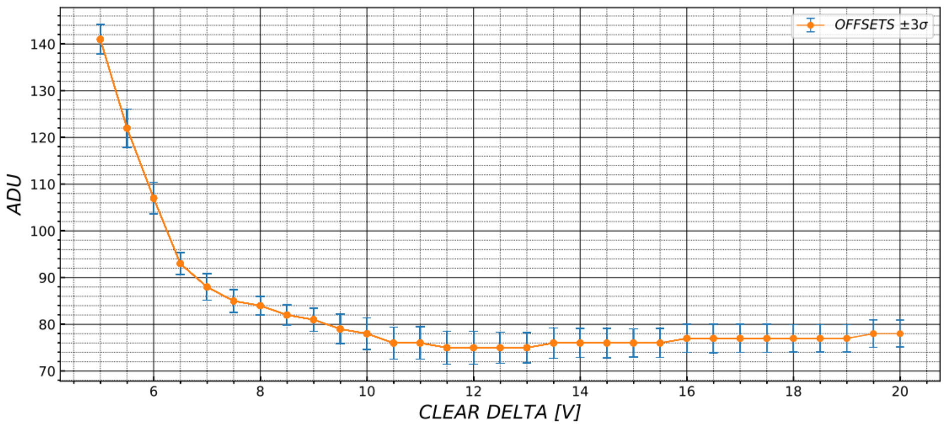

Figure 8-48: Increase of the clear delta, starting from +5 V (the clear off voltage was kept at +1 V) in 500 mV steps up to +20 V. The recorded median offset values of Pixel R64/C31 (each 5,000 frames) show a decreased clearing efficiency for clear spreads below +10 V. The deviations of $\pm 3\ ADU$, equivalent to three standard deviations can be mainly attributed to common mode fluctuations (see Figure 8-31).

If the clearing process turns out to be inefficient, leakage electrons should collect in the IG or OF regions and contribute to a higher drain current. As one can see, a complete clear can already be noticed for a clear delta of +10 V. Below this level, the clearing process does not work efficiently. For most measurements of this thesis the clear delta was fixed at +15 V.

V_{CG}: the cleargate (CG) voltage is common to all matrix pixels and must be optimized together with the clear voltage in order to find an optimal working point for an efficient clear process. In general, the cleargate voltage is set below the clear off voltage to form a potential barrier to the charge storing regions (IG, OF) as illustrated in Figure 8-49. If the cleargate voltage was set too close to the clear off voltage, two unfavorable scenarios are possible:

- In case the clear off voltage was set too high, the IG(OF)-region loses signal or even gets permanently cleared.
- In case the clear off voltage was set below the internal gate potential (or even below the overflow region potential), an electron backemission from the clear to the charge storing areas could be induced.

By contrast, a too negative cleargate voltage could establish an inversion layer below the cleargate, which opens up a parasitic current channel between source and drain.

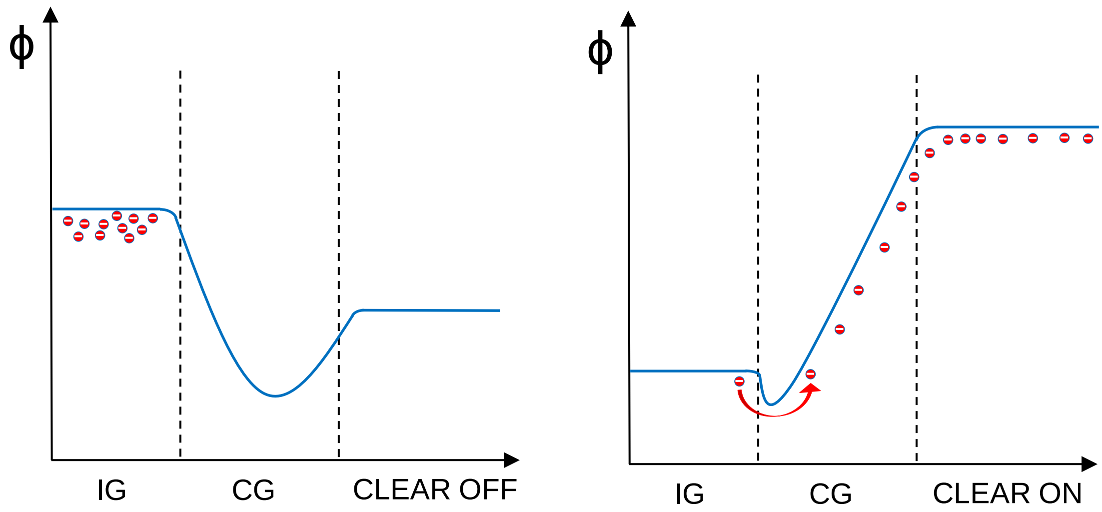

Figure 8-49: Clear and cleargate together regulate the potential barrier between the charge collecting regions and the clear contact. Left: Charge collection mode of an EDET pixel. While the clear is in off position, the electrons move to the higher potentials of the internal gate or overflow region. The cleargate potential prevents the electrons to move from the internal gate/overflow region and the clear potential in either direction. Right: The clear high voltage lifts also the cleargate barrier potential via capacitive coupling and empties the charge regions completely.

V_{PT}: silicon bulks were originally depleted from the top and the bottom side (“sidewards”) [182]. This can be realized by an additional wire bond together with an electrical link between the module's back side (with a stacked p-implantation) and its front side. Alternatively, a single-side or also called punch-through[49] biasing scheme is implemented for the EDET set-up. A punch-through occurs "when the voltage difference across two p-type electrodes, separated by the depleted n-bulk of the detector, is high enough to assist a large hole current between the electrodes" [183].

To understand the punch-through process one should imagine an undepleted bulk.[50] In an equilibrium state, a small built-in depletion region develops between the floating p-implantation on the back side and the silicon bulk. If now a slightly negative voltage is applied to the punch through electrode[51], a small region underneath starts to deplete. The positive bulk contact (n-implant which is biased about +10 V versus source) acts as a counter-electrode. Further voltage reductions cause an expansion of the depletion region until it reaches the space charge region close to the back implantation. At this stage, the region between these two electrodes becomes over-depleted and a hole current[52] evolves from the back electrode through the fully depleted region to the punch-through contact (punch-through current). A further decrease of the punch through voltage causes a decrease of the back potential until finally the entire bulk region becomes depleted.

The biasing scales with the squared bulk thickness and requires about two times of a conventional sidewards depletion. To learn more about this effect, specifically for DEPFET detectors consult [184, 185].

V_B: the bulk contact serves as a counter-electrode to the punch-through electrode. Additionally, it drains leakage electrons from the non-pixelated areas and establishes a natural border between the edge pixels and the frame area. The bulk ring (n-implant) surrounds the whole sensitive area and is positively biased at around +10 V.

V_{DT}: the large drift areas (p-implants) surrounding the transistor have to be negatively biased in order to route the electrons to the internal gate and the overflow region.

V_{GU}: the guard ring (p-implant) acts as a separator between the sensor and the world outside: the guard voltage influences the charge allocation between the positive bulk and the edge pixels. Electrons from outside the sensitive area are repulsed. Without guard, the bulk potential would directly connect to drift. If, for whatever reason, drift was chosen highly negative, an avalanche risk between drift and bulk can be attenuated by setting the guard voltage somewhat higher than the drift voltage.

[49] This should not be confused with the **punch-through** in a MOSFET where this is an unwelcome effect: a reverse bias applied to the drain contact causes an intersection of the depletion regions of drain and source with each other, resulting in a flow of leakage current and ultimately a breakdown of the MOSFET.

[50] Initially, a zero voltage is applied to the punch through contact at the front side of the detector.

[51] Internally, this is also referred to as the "high-voltage" contact.

[52] Holes are mainly created in the silicon bulk either thermally or from external irradiation, but also originate from leakage currents at the surface. They first move to the p-backside-layer, then along to the region perpendicular to the punch-through contact. From this point, they have to overcome a small potential barrier while crossing the bulk, before getting absorbed to the punch-through contact.

8.4.2 EDET Sensor Voltage Sweeps

The following measurement performed a variation of two voltages: the cleargate voltage (from -3.5 V to +5 V in 100 mV steps) and the clear off voltage (from 0 V to +15 V in 250 mV steps), while keeping the clear delta constant at +15 V. Using a DCDE gain of 3.3, a medium charge of about 90 ADU was injected from a LED source, equivalent to about 450,000 electrons (for the base setting of $V_{CG} = 0\ \mathrm{V}$ and $V_C^{\mathrm{off}} = 1\ \mathrm{V}$). After every voltage step, the net charge (=subtraction of the offset or dark frame values from the gross charge) was determined. Thereafter, the mean of all pixel values was entered into a 2D diagram, depicted on the left side in Figure 8-50.

The region for usable voltage combinations is primarily constrained by the backemission and inversion area, characterized by limiting[53] offset values as shown on the right diagram. As one can see, despite a DCDE low gain setting, the transition zones are rather small to put the DCDE into saturation. Since the used power supply did not provide negative clear off voltages, it could not be shown that the operation window of convenient voltage combinations forms out to a triangle (see [113], including a more profound discussion of voltage sweeps with respect to individual EDET pixels).

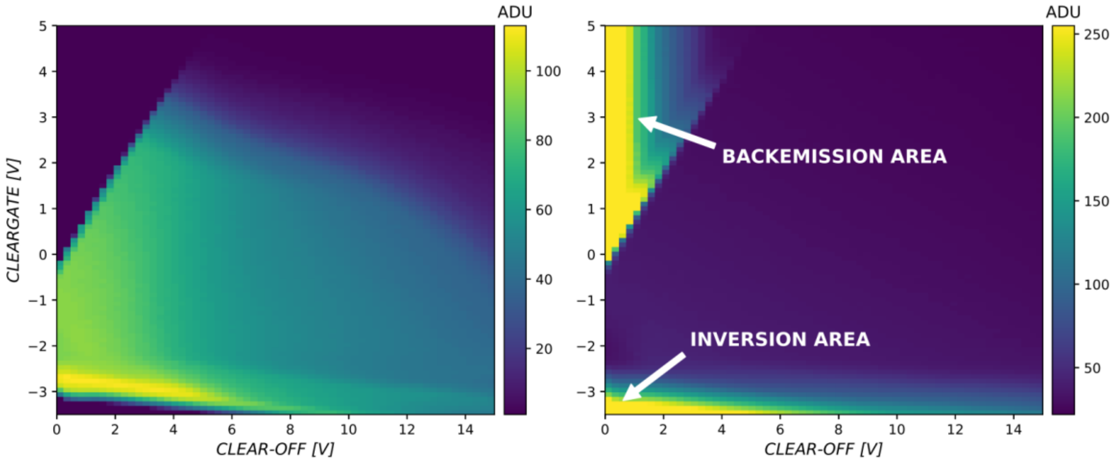

Figure 8-50: Left: Voltage sweep between cleargate and clear off, assuming a constant clear delta of +15 V. If the cleargate voltage is kept constant, then the higher the clear off voltage, the less average charge is collected in the charge storing regions (IG & OF). Right: Dark frame mean values from clear off & cleargate voltage variations. The cleargate acts as a guardian for the charge collection: if it was set too close or even above the capacitive coupled clear off voltage[54], the electrons are backemitted from the clear electrode to the charge storing regions, thereby increasing the drain current significantly (backemission area). If the cleargate was selected too negative, a parasitic channel establishes between source and drain (inversion area).

The selection of useful combinations highly depends on the operator's aspiration level, i.e. how much charge loss he is willing to accept. Anyway, without adjusting the cleargate

[53] Utilizing the full dynamic range of the DCDE.

[54] The clear off voltage has to remain at least below the internal gate potential.

voltage, the charge collection efficiency (CCE), here defined[55] as the fraction between the actual collected charge and the highest charge produced, significantly diminishes with clear off voltage increases: in case the cleargate voltage was set to -2 V, a clear off voltage of 15 V leads to a CCE of just over 40% compared to a clear off level at 0 V (see middle image of the top row in Figure 8-51).

The baseline clear off and cleargate voltage settings mark the starting point for all other voltage combinations. If a voltage was not swept, the following basis settings were applied:

- $V_G^{\text{off}} = +5\ \text{V}$
- $V_C^{\text{off}} = +1\ \text{V}$
- $V_C^{\text{on}} = +16\ \text{V}$
- $\text{clear spread} = V_C^{\text{on}} - V_C^{\text{off}} = +15\ \text{V}$
- $V_{DT} = -8\ \text{V}$
- $V_{GD} = -8\ \text{V}$
- $V_{CG} = +0\ \text{V}$
- $V_{PT} = -35\ \text{V}$

Figure 8-51 depicts the CCE for six different voltage combinations. The percentage expresses the mean charge value of all pixels in relation to the voltage combination with the highest charge. Nevertheless, the results should be treated with caution:

First of all, the pixels were not gain corrected and the diagrams represent only the mean values of all 8,192 small sensor pixels. The actual charge distribution might variate substantially between individual pixels as exemplarily shown in Figure 8-53.

Second, very large sweep ranges could directly influence the drain current via capacitive coupling. A simple back-of-the-envelope calculation should illustrate this point: since the silicon bulk is fully depleted, it can be considered as an insulator with a relative permittivity of $\varepsilon_r^{\text{Si}} = 11.68$. Sandwiched between the p-backside implant and the hole channel below the external gate, this can be again approximated by a parallel plate capacitor ($C = \varepsilon_0 \varepsilon_r A/d$). Relating the gate and bulk capacities, one calculates for a 50 µm thick sensor:[56]

Equation 8-18
$$\frac{C_{\text{gate}}}{C_{\text{bulk}}} = \frac{\varepsilon_r^{\text{SiO}_2} \cdot d_{\text{bulk}}^{\text{Si}}}{\varepsilon_r^{\text{Si}} \cdot d_{\text{gate}}^{\text{SiO}_2}} = \frac{3.9 \times 47}{11.68 \times 0.1} \approx 157$$

hence, the gate capacity is by a factor of about 157 higher than the bulk capacity. Reverting back to Equation 5-12 one can calculate the relative transconductances as

Equation 8-19
$$g_{\text{m}}^{\text{bulk}} = \frac{C_{\text{bulk}}}{C_{\text{gate}}} \cdot g_{\text{m}}^{\text{gate}} = \frac{1}{157} \times g_m^{\text{gate}}$$

[55] The more rigorous definition defines CCE as the ratio of the charge collected in the detector to the total free charge created by the ionizing event.

[56] The p-implantation on the backside has a thickness of about 3 µm, the external gate structure is negligible.

If a $g_{\mathrm{m}}^{\mathrm{gate}} = 100\mu\mathrm{S}\ [\mathrm{A/V}]$[57] is assumed and one considers only half of the voltage change because of the punch-through mechanism, it can be inferred, that a change of the punch-through voltage of around 32 V is equivalent to a gate voltage change of 0.1 V.

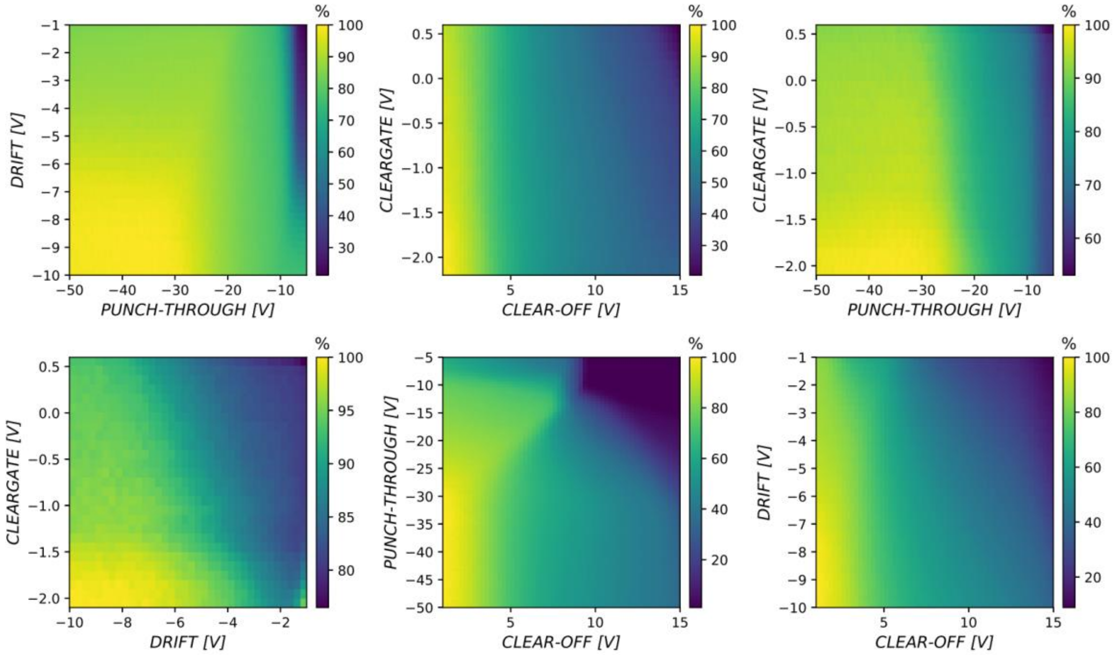

Figure 8-51: 2-D voltage sweeps across 4 DEPFET voltages: clear off, cleargate, punch-through and drift. All matrix pixels were homogeneously illuminated by a LED. The different diagrams represent the mean charge values of all pixels as a percentage of the voltage combination with the highest charge.

In a nutshell, the actual chosen voltage combination may have a substantial influence on the CCE. Special attention must be paid to the cleargate voltage which directly couples to the clear off voltage: if it was set too high or too low, the detector gets quickly expelled out of its dynamic range. By contrast, the CCE remains relatively high for a wide range of drift and punch-through voltages.

If the user might define his aspiration level for the CCE at 90% (see Figure 8-52), he would select the sensor voltage settings from the following operational voltage ranges:

- $V_C^{\mathrm{off}} < 2\ \mathrm{V}$
- $V_{DT} = -5 \text{ to } -10\ \mathrm{V}$
- $V_{CG} = -2 \text{ to } 0\ \mathrm{V}$
- $V_{PT} = -25 \text{ to } -50\ \mathrm{V}$

[57] Siemens (S) denotes the electric conductance, the reciprocal of one Ohm (Ω^{-1}).

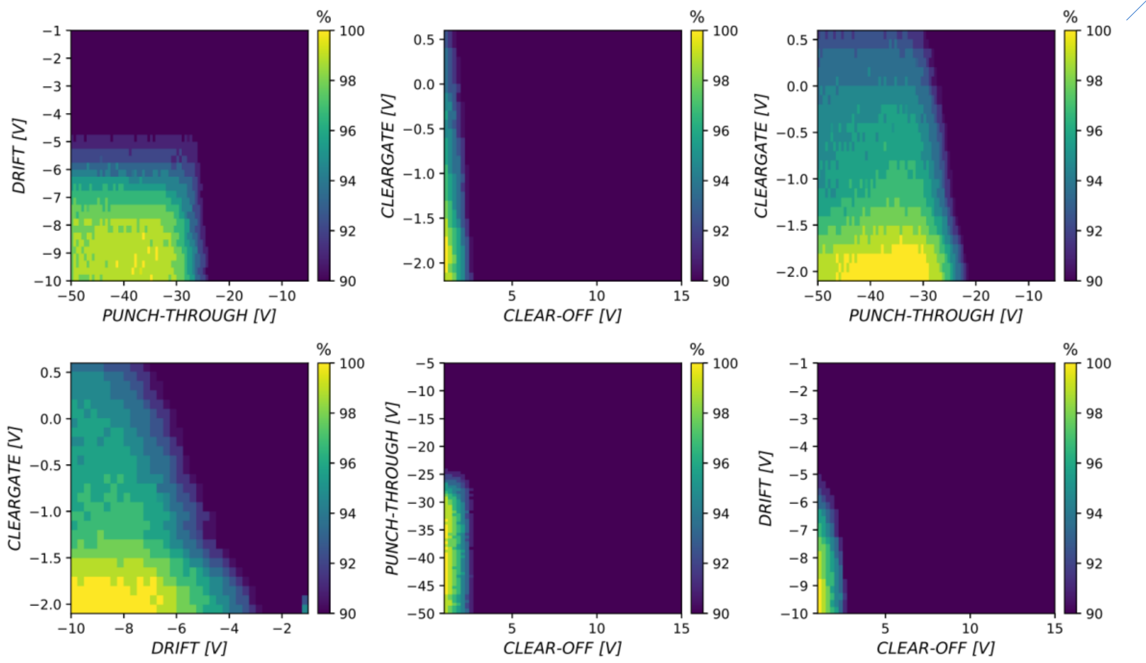

Figure 8-52: Same data as in Figure 8-51 with enhanced contrast, showing only mean charge values above 90% of the highest measured charge.

Figure 8-53 depicts a selection of 9 pixels with regards to the drift–punch-through voltage sweep. Though the mean analysis favors a range of -25 to -50 V for the punch-through voltage and -5 to -10 V for the drift voltage to achieve at least 90% of the highest charge, the optima vary strongly for the individual pixels. This can be mainly attributed to bulk doping variations.

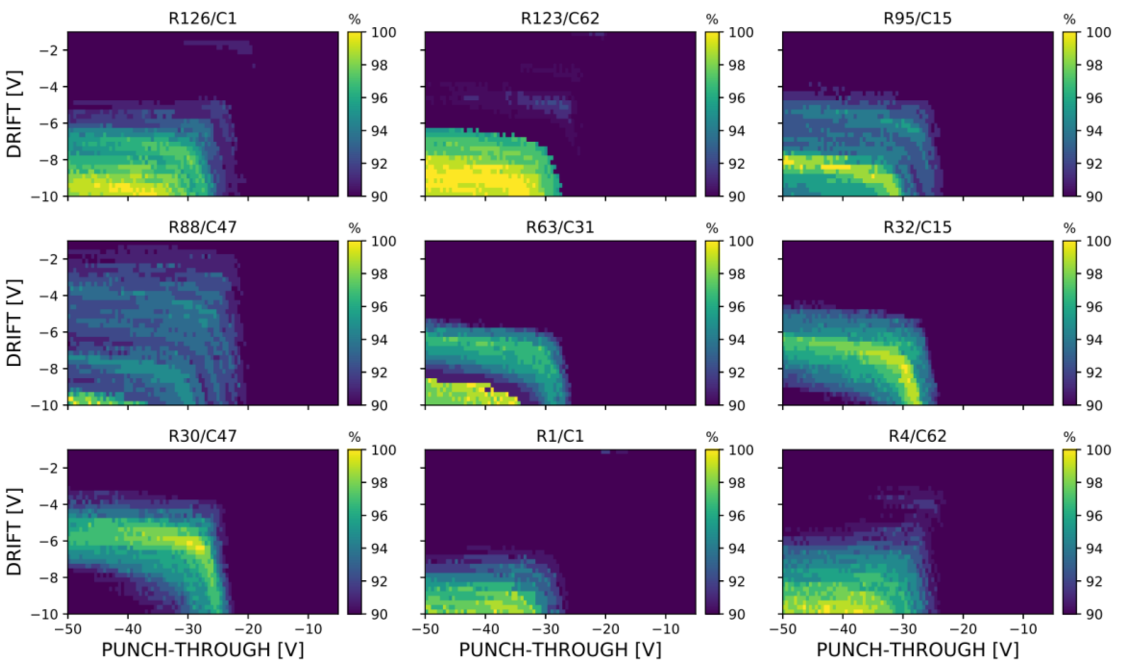

Figure 8-53: Punch-through–drift voltage sweep for a selection of individual matrix pixels. Due to different bulk dopings, the optimal charge collection occurs at different voltage levels.

9 TEM Measurement Campaigns in Hamburg

This chapter summarizes the results from two TEM campaigns in Hamburg, lasting for several days. Obviously, the small EDET system had to be subjected to a final endurance test under a transmission electron microscope. The primary goals were to verify the correct operation, the testing of the detector specifications and to gain valuable insights with respect to radiation damage.

9.1 Experimental Setup

The used JEOL-2100 TEM is equipped with a blanker, which allowed to deflect the beam electrons from the sensor, initially by manual input, later by an EDET system linked trigger pulse. The EDET hybrid board was inserted into the vacuum chamber of the TEM and connected via a glued flange with a vacuum-feedthrough PCB to the prototype DAQ and power system as shown in Figure 9-1.

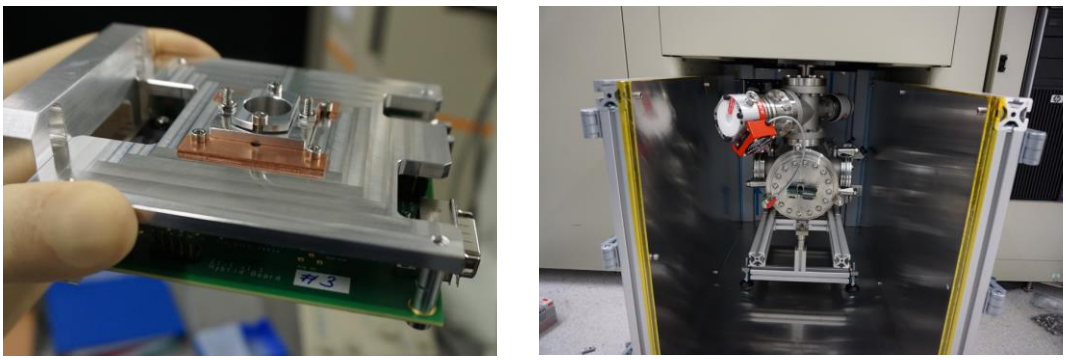

Figure 9-1: Left: EDET Hybrid Board #3 attached to a mechanical support, which serves also as a protection shield for the ASICs. Right: TEM vacuum vessel (chamber below the TEM column shown in Figure 3-1) with feedthrough PCB (mounted into the middle of the round front plate).

As exemplified in section 8.2.2.5, electrons from the TEM undergo multiple scattering, when passing through the silicon sensor. If numerous electrons strike the same entrance point successively, the corresponding electron trajectories form out a characteristic scattering cone. This cone expands with increasing sensor thickness, which deteriorates the image quality. Likewise, the problem of backscattered electrons could affect the sharpness of the detector adversely. For the final DH80k FPA a beam stop, i.e. a proper designed cavity (sloped walls coated with a low-Z material as for example carbon), fills the vacuum gap underneath the sensor, thereby contributing to the mitigation of this risk [121].

The system clock frequency[1] of the detector, which determines the frame readout speed, was slightly increased. The DCDE produced about 305,000 frames per second for a small matrix, irrespective of the effective readout capacity.

[1] 78.125 MHz

As mentioned, the original intended DHPT operation mode foresaw a first data reduction by zero suppression. Indeed, for diffraction images with occupancies lower than 3% [186], the use of the DHPT's zero suppression feature would be still a viable option. However, for scattering or shadow pictures the full raw frame data is needed.

A typical measurement sequence ("run") for the first measurements in Hamburg consisted of the following steps:[2]

- vocal start command
- start the EDET detector recording via computer script
- manual activation of a (relatively slow ~30 ms) TEM blanker (press button): deflection of the TEM electron beam (160 keV electrons) to the sensor position for usually about 200 ms (length of a TTL-pulse)
- stop the recording after about 3 seconds

Since the data transfer capacities of the actual EDET system were limited, the full frame readout speed had to be reduced significantly. At the time of writing, the maximum readout frequency was about 9,500 fps or just 3% of the DCDE intrinsic frame rate.[3] With a customized Switcher sequence, the actual frame time was effectively increased from 3.3584 µs to 26.867 µs. By this means, the share of usable data also experienced an 8-fold increase.

The only drawback from this approach was again a dysfunctional Switcher row, represented by a dark bar on the left side of Figure 9-2.[4]

During the active readout duration, on average 25,000-30,000 frames were recorded for each run, only about 1,800 (~200 ms) of them contained radiation data with varying beam intensities. The calibration of the beam intensity was made on the basis of pre-existing calibration tables and the application of different adjustment factors. The error was conservatively estimated at around $\pm 20\%$.

The second Hamburg Campaign brought some innovations, especially with respect to the triggering of the TEM beam. The MPSD team developed a new blanker which was able to deflect the TEM beam with a rise time of just 20 ns at a maximum repetition rate of 10 kHz. The blanker period was originally fixed at 105 µs and the "beam-on" time was controlled by the duty cycle as a percentage of the preset period. The blanker was able to shorten the beam-on time to very short pulses, down to 50 ns.

In order to not miss any frame and any signal, the effective frame time was further increased to 104.857 µs. This was achieved by providing the veto signal to the DHPT.[5] Originally, this feature was designed for the so-called "Gated Mode" operation, which

---

[2] 1st Hamburg campaign.

[3] Which by the way is in good accordance with the specified DHPT occupancy rate as above.

[4] The Switcher had to be kept in a parking position, while switching the additional (fictitious) 224 electrical rows.

[5] The DHPT receives all instructions from the XU1 FPGA. Other signals are for instance the global reference clock, the memory dump or the frame sync signal (FSYNC). FSYNC synchronizes the start of a new frame and resets the row counter to zero. Memory dump instructs the DHPT to release the frame data [184].

was indispensable for the BELLE II project: to keep the collider's bunch currents constant, they have to be topped off by the injection of daughter bunches at a rate of 50 Hz. The particles in the daughter bunches produce a high rate of background for a short period of time, which would saturate the occupancy of the sensor. The Gated Mode operation allows the preservation of the stored signals from collisions of the normal bunches, while protecting the pixels from background signals of the passing noisy bunches. For more about the Gated Mode see [187] [108]. In contrast to the Gated Mode operation, the veto signal was not followed by Gated Mode instructions. The Switcher was just set passive, which in turn kept the sensor active for charge collection.

Three problems were associated with this new feature: first, the veto could be only triggered after a normal (rolling shutter) frame readout period, otherwise the stored charge would have been never read out and cleared. For the charge collection, this implied a slight gradient along the readout direction, since the first line got cleared earlier and accordingly, could integrate charge for the longer remaining time interval. Second, the trigger for the TEM blanker was erroneously set too late, at point in frame time "72.1 µs", so there was only $104.857 - 72.1 = 32.757\ \mu s$ of active beam time left. Third, the second issue would have been no real issue, if the TEM blanker period was chosen shorter than the total frame period:[6] the extended duty cycle (longer than $32.757\ \mu s$) would have been recorded by the next frame until a new period starts. Only the very first frame would have been unusable.

The calibration procedure for the determination of the electron dose is described in a supplement paper to [51].

All offset corrections were carried out after the data recording.

[6] The blanker problem was detected and corrected only for the very last few runs. For most measurements, every second frame was missed.

9.2 Measurement of a TEM-MTF

A knife edge, manufactured from a 500 µm thick Titanium[7] foil was placed in close distance to the front side of the detector. To evaluate the EDET detector's MTF in a TEM, the integrating mode was chosen (in contrast to the ^{109}Cd case). Figure 9-2 presents the raw data (median value of about 1,800 frames) recorded by the sensor which was previously used for the LED-MTFs (thickness of 30 µm and a gate length of 6 µm).[8] The MTF analysis was done along the method prescribed in the preceding chapter.

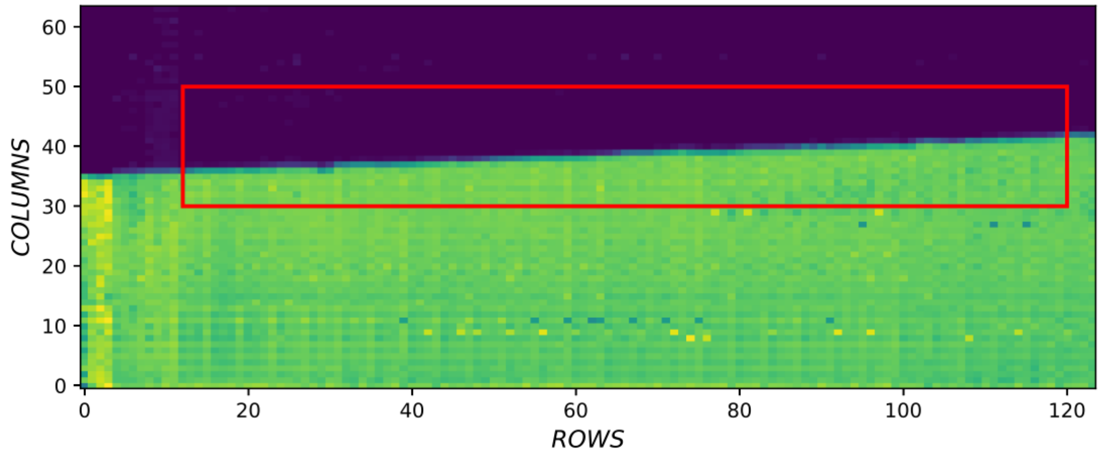

Figure 9-2: Knife edge scan on a small EDET matrix sensor, positioned into the vacuum chamber of a TEM. Due to the higher DCDE gain setting, a lower total charge was injected in order to avoid dynamic range limitations. Accordingly, the ghost charge effect played a minor role (much lower charge compared to the measurements with the 3.3 gain setting). The calculated slope angle for the slanted edge was $\theta = 2.99°$. Inert pixels were linearly interpolated.

Figure 9-3 depicts the ROI of a TEM slanted edge measurement. Apart from the interpolation of a few outliers (all outside the proximate knife edge region), no further adjustments were made.

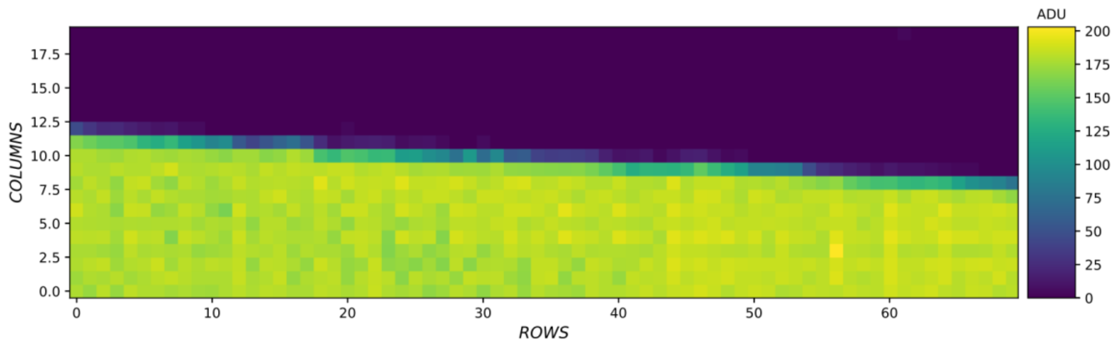

Figure 9-3: ROI of a TEM measurement with DCDE gain 11.

[7] At this dimension, 160 keV electrons should be easily stopped with an initial stopping power of over 2 MeV cm^2/g; Titanium density: 4.506 g/cm^3.

[8] As a proof, the line with the defective pixel contacts can be found at the same position.

The intensity in the bright area was not homogeneous. The slight gradient from the left to the right can be attributed to an imperfect TEM beam alignment.

It is instructive to contrast the different knife edge scans of an ideal edge with the edge gained from a TEM electron beam as is shown in Figure 9-4.

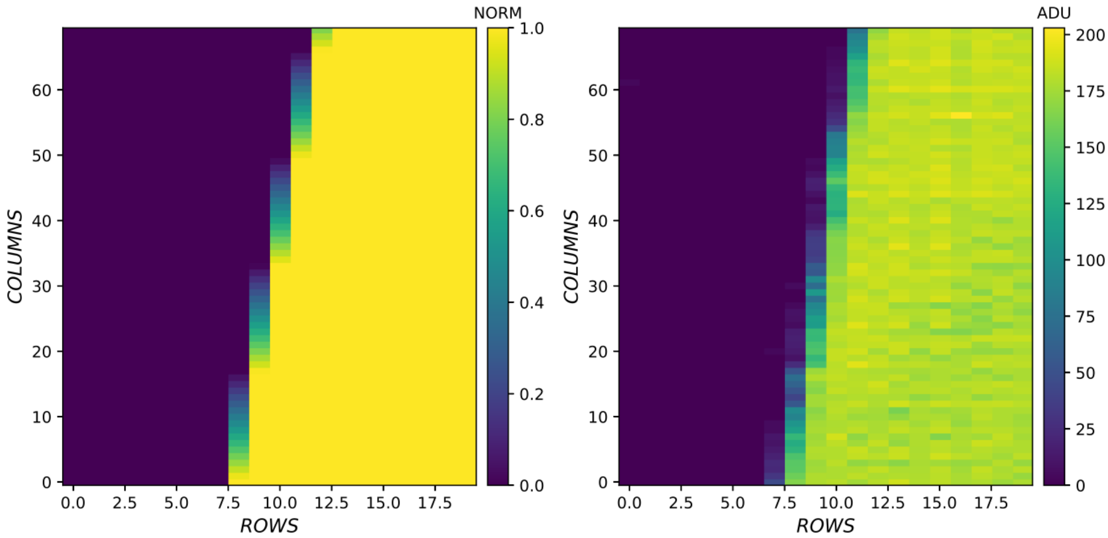

Figure 9-4: Different knife edge scans. An ideal knife edge (left) and a knife edge with a TEM beam illumination (right).

Compared to the LED measurements, the TEM edge's transition zone is characterized by much sharper contours, which is also reflected in the correspondent ESF and LSF curves as can be observed in Figure 9-5.

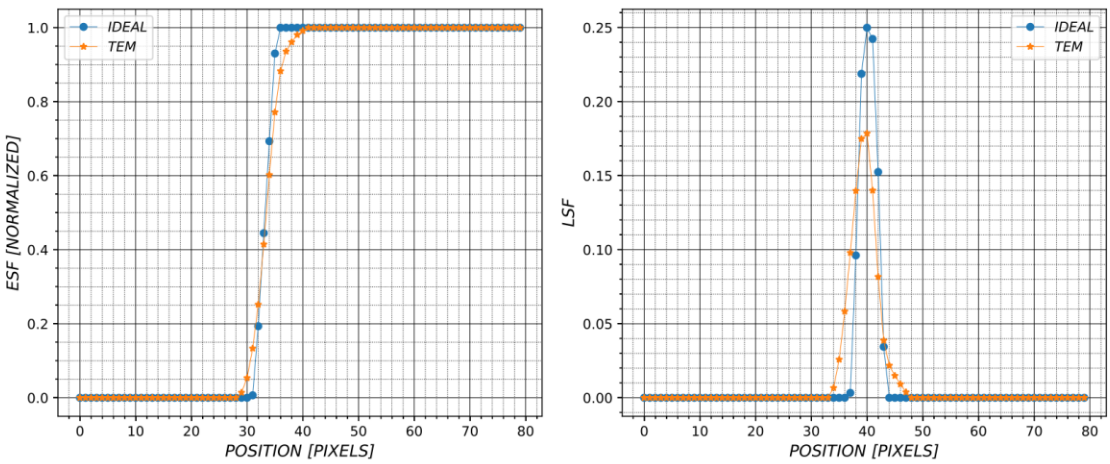

Figure 9-5: ESF and LSF curves for an ideal sensor and a TEM measurement, respectively.

The final TEM-MTF curve, presented in Figure 9-6 properly matches a comparable curve from Geant4 simulations[9], the blur length was determined at $\Lambda = 135\ \mu\mathrm{m}$. Taking into

[9] Simulation performed by I. Dourki.

account the unavoidable[10] scattering cloud within the silicon pixel, one can confidently state, that this sensor has an excellent resolution.

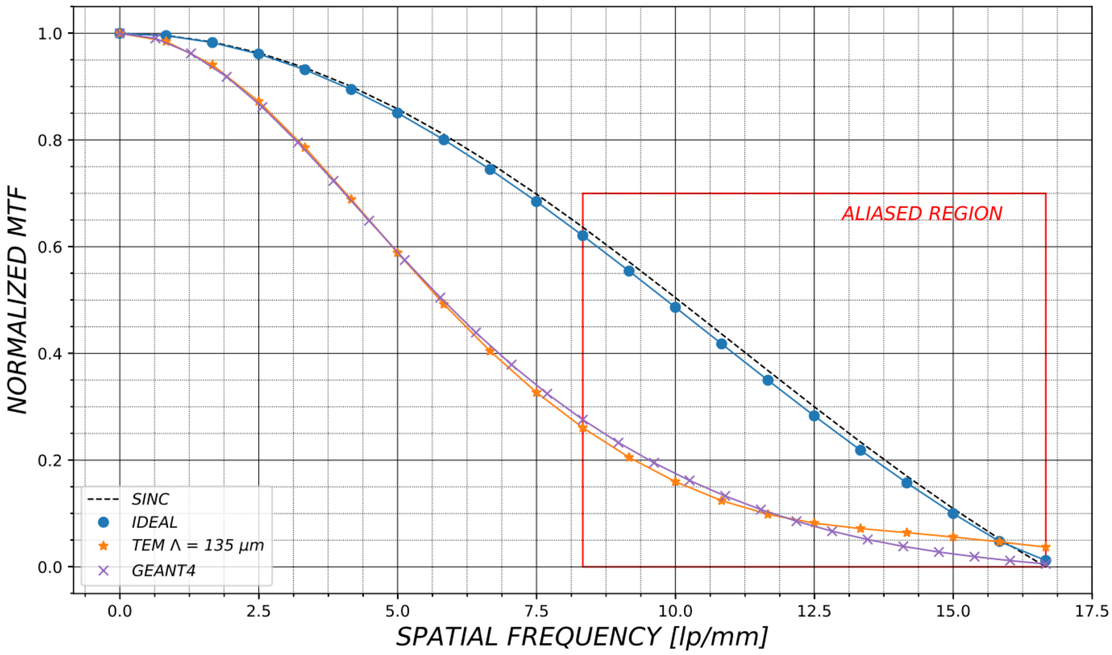

Figure 9-6: MTF curves for a simulated (Geant4) and a real environment using a TEM beam.

9.3 Radiation Effects influencing TEM measurements

Radiation damage effects for silicon detectors can roughly be classified into two categories: bulk damage, caused by the displacement of crystal atoms, and surface damage occurring in the MOSFET dielectric and the interface region.

A bulk damage in a silicon detector is characterized by the displacement of a silicon atom from its original lattice site resulting in a so-called "Frenkel pair", where the original position exhibits a vacancy and the primary knock on atom (PKA) becomes an interstitial in a nearby location [188, 189, 190, 191]. On the other hand, electrons need a kinetic energy of about 255 keV to overcome the displacement threshold energy of approximately 25 eV in order to produce a Frenkel pair. Hence, bulk damage plays only a subordinated role for TEM beam energies below 250 keV.

Surface damage is mainly caused by ionization effects in the SiO_2 layer: most of the electron hole pairs generated from ionizing radiation quickly recombine. While the highly mobile electrons move swiftly to the positive potential, the holes stay behind and are primarily attracted by the negative gate electrode. Anyhow, a few holes close to the SiO_2/Si-interface are captured by deep hole traps, where they may be kept permanently and partly compensate the external gate voltage until this process stops at a specific

[10] A tradeoff exists between the charge collection and the image resolution: the thicker the sensor, the more charge is gathered, otherwise the resolution gets worse because of electron scatterings.

saturation level. To keep the drain current constant, the negative external gate voltage has to be decreased in proportion to this opposing electric field.

An important parameter influencing surface damage is related to the potentials close to the SiO_2 layer: roughly speaking, a neutral electrical field increases the recombination rate and reduces the risk of trapped charges accordingly. More about radiation surface damage effects can be found in [192].

In the majority of all cases, the EDET sensor was exposed to the electron beam for only short time intervals. Nevertheless, some radiation damage was unavoidable and therefore, the gate voltage had to be adjusted from time to time. If there was very strong irradiation, the effects were clearly visible within one single run. For example, the general offset level of the irradiated uncovered sensor region[11] decreased significantly after employing an estimated electron flux of about 420 e^-/px/frame (160 keV electrons), as one can see in Figure 9-7. During a time span of 200 ms, close to 7,500 frames were exposed to this strong irradiation. The subsequently measured average offset level was reduced by about 12 ADU.

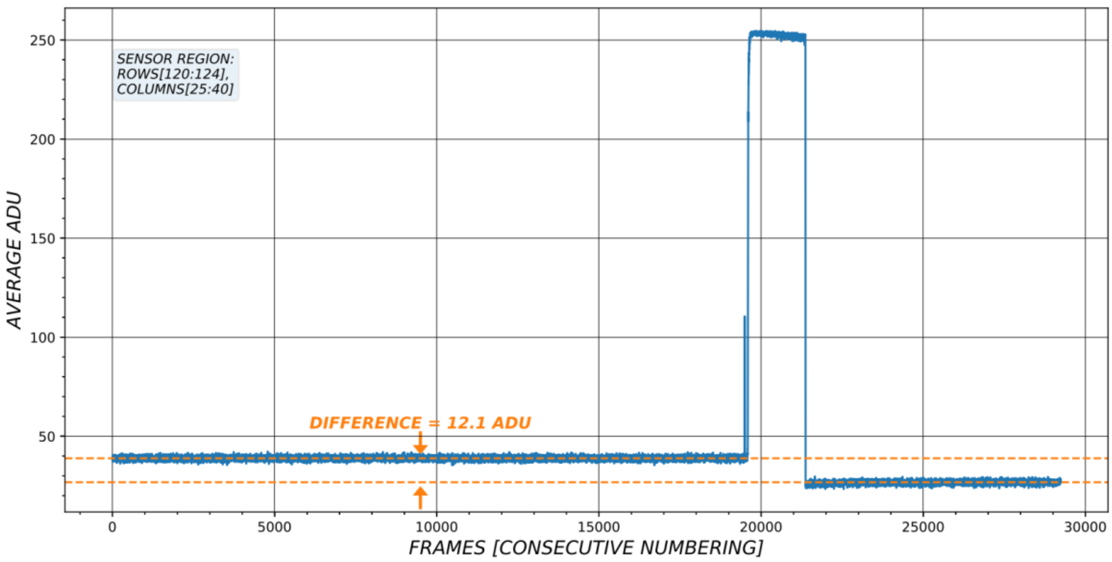

Figure 9-7: Change of the average offset level of a specific sensor region after a strong electron flux of 421 e^-/px/frame (160 keV electrons). During a time span of 200 ms about 7,5*00 frames were irradiated*.

For a plausibility check, this level shift can be compared to a large-scale radiation study performed on the PXD-DEPFET sensors for the BELLE II experiment with a total dose of 266 kGy *[193]*. To keep the overall drain–source current constant[12], the threshold limit

[11] The region of interest was restricted to only a small area for mainly two reasons: first, a good part of the sensor was permanently covered with the slanted edge mask. Second, the beam was not perfectly aligned and hence the intensity was not observed as homogeneous over the sensor area.

[12] The drain–source current was fixed at 66 mA. The module consisted of 1,000 drain lines, so the average drainline current was 66 µA (about 2/3 of the EDET baseline at 100 µA).

of the gate voltage ("gate shift") had to be permanently adjusted. The overall shape resembles a degressive growth curve, which is more pronounced toward higher radiation doses: even though a gate shift adjustment of 2 V was necessary at a cumulative dose of 8 kGy, the additional shift from 8 V to 10 V demanded more than ten times as much of irradiation (see Fig 5 of *[193]*). Figure 9-8 shows a limited section up to just 300 krad[13] of a more detailed data series.[14] The very front end was linearized, its slope exhibits a threshold voltage shift of about 23 mV per 1 krad.

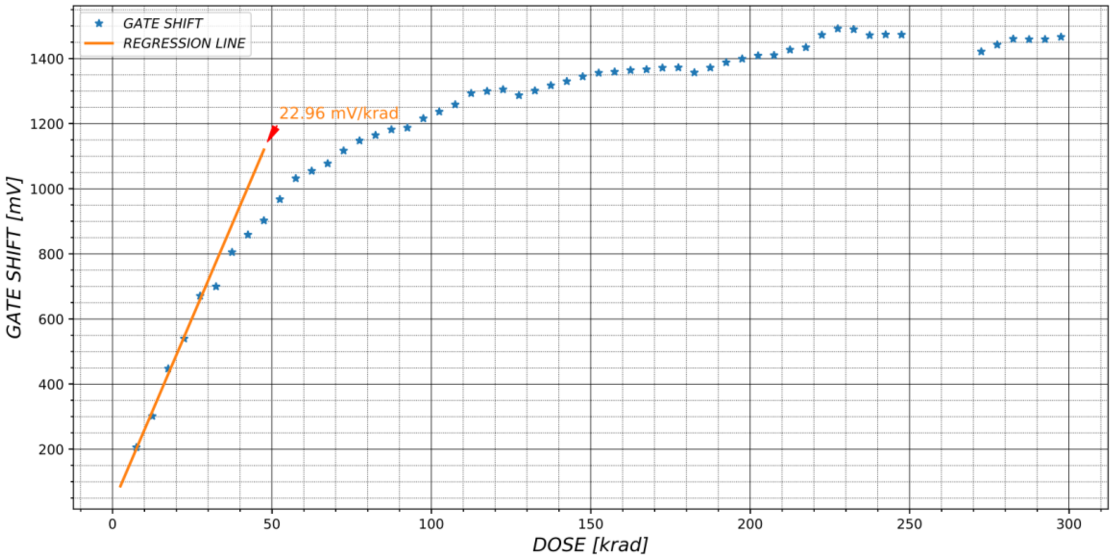

Figure 9-8: Gate voltage shift to keep the drain source constant after increased irradiation dose (data provided with kind permission from Harrison Schreeck [193]).

According to the International Commission on Radiation Units and Measurements (ICRU) the absorbed dose is defined as

Equation 9-1

$$\mathrm{D} = \frac{\mathrm{d}\bar{\varepsilon}}{\mathrm{dm}}$$

where the dose D is expressed in units of J kg^{-1} and $d\bar{\varepsilon}$ is the mean energy imparted by ionizing radiation to matter of mass dm.

To determine the mean energy loss, Equation 3-3 cannot be used. As mentioned, because of energy loss straggling this formula is inaccurate for a thin sensor. As $\kappa \ll$, the Landau equations are now better suitable, with a long distribution tail, shifting the mean to higher values. The average loss of a 160 keV electron in 100 nm thick silicon dioxide and $60 \times 60\ \mu\mathrm{m}^2$ pixel area was determined at 63 eV[15] corresponding to $1.01 \times 10^{-17}\mathrm{J}$.

[13] 100 krad = 1kGy

[14] Provided by courtesy of Harrison Schreeck.

[15] 58 eV from Geant4 simulations: I. Dourki

Accordingly[16],

$$D = \frac{420[e^-] \cdot 1.01 \times 10^{-17}\mathrm{J} \cdot 7{,}500[\mathrm{frames}]}{6 \cdot 6 \cdot 1 \times 10^{-17}\mathrm{m}^3 \cdot 2320\,\mathrm{kg/m}^3} = 38.1\frac{\mathrm{J}}{\mathrm{kg}} = 38.1\,\mathrm{Gy} = 3.81\,\mathrm{krad}$$

This would imply a total voltage shift of about $3.81\,\mathrm{krad} \times 22.96\,\mathrm{mV/krad} \approx 87\,\mathrm{mV}$. Previous measurements on the same board also performed so-called matrix transfer curves. In the course of these measurements, the gate voltages were decreased in 10 mV steps from -1 V to -4.1 V as can be seen in Figure 9-9. To consider different pixel response functions, the presented curve depicts only the mean pixel values of the selected sensor region. The gate voltage for the measurement in Figure 9-7 was fixed at -2.35 V. As can be derived from the enlarged inset axis, a change of -87 mV corresponds approximately to 11 ADU. The EDET numbers have to be adjusted for the different basic drain currents (66 µA at the BELLE radiation campaign vs 100 µA EDET standard drain current) and the different DEPFET gate lengths. The modules for the BELLE II irradiation campaign used a gate length of 3.6 µm after etching, whereas for the EDET sensor it was 4.6 µm (nominal 6 µm before etching).

Returning to Equation 4-12, $g_{m,sat}$ depends reciprocally proportional on the gate length and directly proportional to the square root of the drain current $I_{D,sat}$. Hence,

$$\frac{3.6\ \mu m}{4.6\ \mu m} \cdot \sqrt{\frac{100\ \mu A}{66\ \mu A}} \approx 0.96$$

the EDET data must be corrected to 11.6 ADU. Although this is just a back-of-the-envelope calculation, the experimental results were in good agreement. Overall, even short exposures can significantly distort the final result. The described calculation may give an estimate, how often the underlying offset levels and the gate voltages might have to be readjusted, depending on the radiation's intensity and duration.

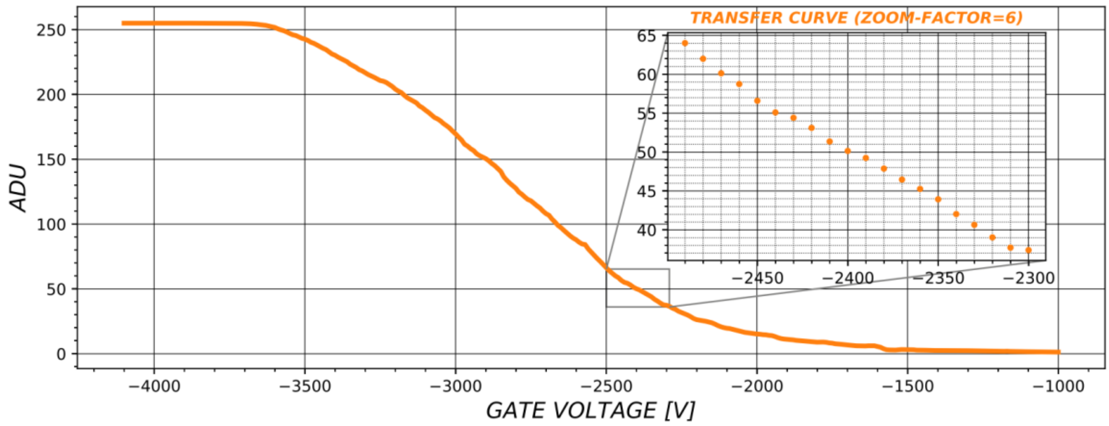

Figure 9-9: Matrix transfer curve for DCDE 3.3 gain. The curve represents the average of the selected sensor pixels.

[16] Density according to NIST data. As a compound, the two atomic numbers have to be multiplied by their weight fraction (0.53 for Oxygen, 0.47 for Silicon). Mean excitation energy is 139.2 eV.

After the first Hamburg campaign, the matrix offset values got significantly altered as shown on the top left diagram in Figure 9-10. The significant higher ADU level on the right did not experience any radiation damage since it was permanently covered by a knife edge meant to be used in a slanted edge measurement (the distinct bright spot in the middle can be attributed to a malfunctioning Switcher operation). Faintly noticeable in the low ADU area (and therefore replotted by excluding higher ADU values), one can observe a grid. It resulted from a grate, which was positioned in the TEM specimen holder, serving for the measurement of the post magnification factor (described in the next section).

Focusing one's attention on the offset distribution (colored blue in the right bottom diagram), one quickly realizes that a significant part of the matrix was not usable for further measurements. However, barring a potential necessary recalibration of all matrix pixels, the 2-bit DAC compression got all pixels back into the dynamic range of the DCDE.

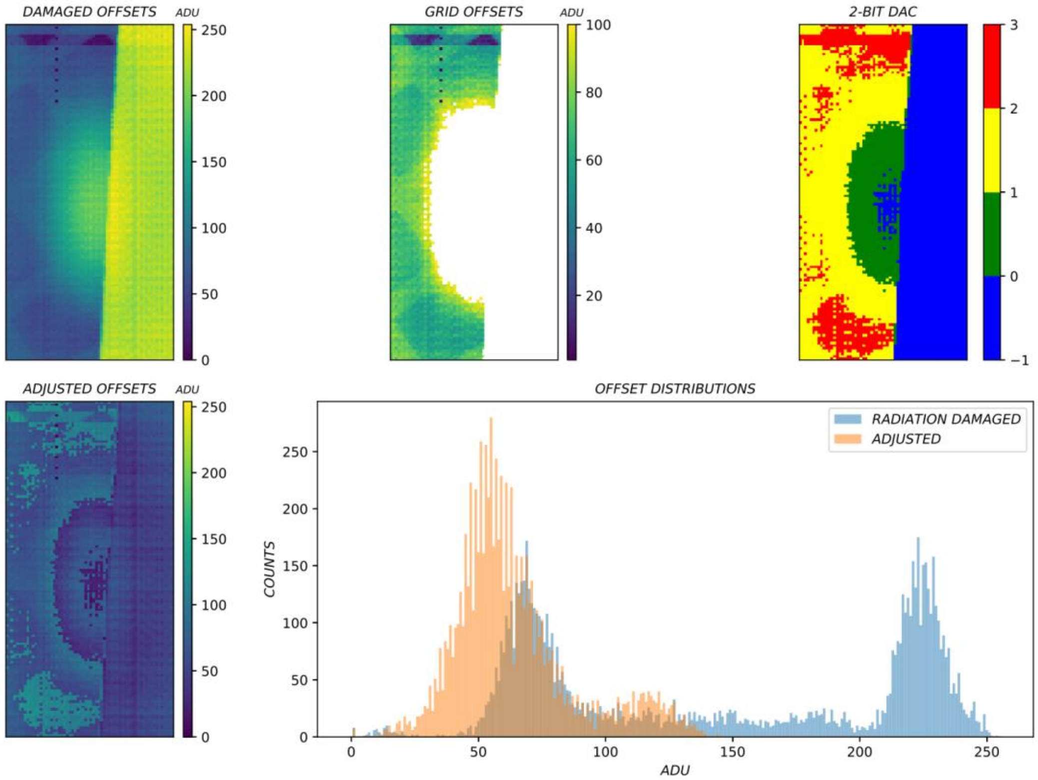

Figure 9-10: Offsets of a radiation damaged matrix before (DAMAGED OFFSETS) and after (ADJUSTED OFFSETS) 2-bit DAC adjustments. 2-BIT DAC: the colored regions indicate which pixels get 3 IPDAC (red), 2 IPDAC (yellow) 1 IPDAC (green) and no extra current (blue). The GRID OFFSETS diagram just blanks out higher ADU values in order to make the used grid better visible. The overlying offset distributions in the bottom right diagram show how much the offsets were compressed after the 2-bit DAC adjustment.

9.4 Basic Measurements

9.4.1 Determination of the Post-Magnification Factor

The actual electron intensities vary substantially with the detector's relative position to the calibration screen. To evaluate the post-magnification factor, a diffraction grating replica with known distances (25 µm mesh, hole-width 19 µm, linewidth 6 µm)[17] was placed in the TEM specimen holder [194]. The mesh is typically used for magnifications in the order of $1{,}000\times$ to $10{,}000\times$. The projected image on the EDET sensor showed a magnification[18] of about 87 compared to the nominal calibration factor of 50 in the plane of the phosphor screen, as shown in Figure 9-11. From the relation a post-magnification factor of 1.73 could be derived. Therefore, the nominal beam electron densities had to be corrected by $1/1.73^2$ (application of the squared distance law). The dose calibration was estimated to be accurate within $\pm 10\%$.

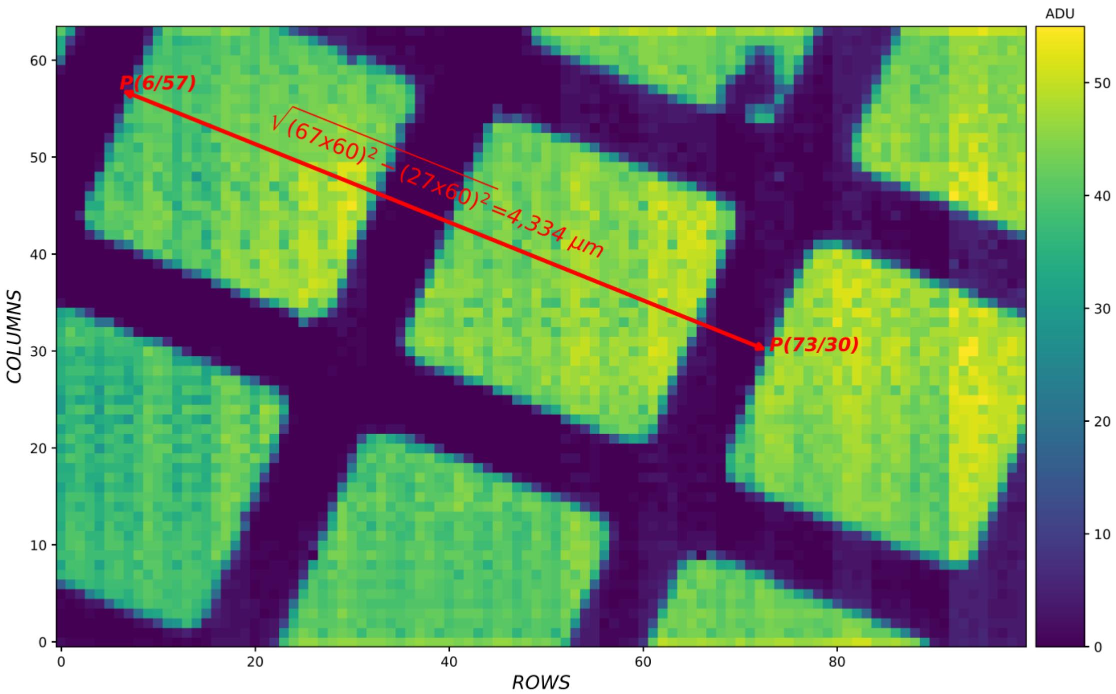

Figure 9-11: 25 µm TEM copper grid (19 µm hole width, 6 µm linewidth) projected on a small EDET sensor. The grating distance was determined by the selection of two pixel addresses and Pythagorean computation of the vector-to-vector hypotenuse. The determined spacing of 4,334 µm (50 µm in the original grid) translated into a magnification factor of 87 (the small matrix does not allow for the measurement of the recommended five line pair spacing). Cold pixels from broken drainlines were linearly interpolated in vertical direction.

[17] Average of 5 lines delivers an accuracy of 1.5%.

[18] With respect to the grating spacing.

9.4.2 Determination of TEM Pixel Charge Curves

Another experimental groundwork concerned the generation of individual pixel charge curves by increasing the TEM beam intensity. Needless to mention, the beam profile had to be made as homogeneous as possible, which mainly depended on the skills and experience of the TEM operator (correct positioning, minimum beam constriction). The intensity itself was regulated by the duty cycle of the blanker. Similar to the LED measurements, the charge curve setup started with small duty steps for the curve's front end (internal gate region) and passed on to larger steps for the overflow region (total of 39 steps). Though this approach can be readily applied for intermediate calibrations (e.g. after each necessary gate on or cleargate adjustment), the measurement itself causes additional radiation damage. To mitigate this risk, the curve could be theoretically compiled from just 4 charge points, as was shown in section 7.3.4.4. An acceptable compromise between prevention of sensor damage and required accuracy could be achieved by, for instance, 8 charge points, 3 for the IG region and 5 for the OF region.

The outcome of the first charge curve measurements is presented in Figure 9-12 and Figure 9-13. Because of the self-inflicted problems described above, the curves were not usable beyond a duty cycle of 30%. Furthermore, the reported synchronization issue led to a loss of numerous frames containing signal data, so the mean charge curve values had to be determined from just between 30 and 100 frames. The measured TEM calibration curve shows large errors. These are due to the low number of frames usable for determining the mean values and the relatively large fluctuations of the beam intensity following the Poisson statistics. As a consequence, the following images and movies are represented by uncalibrated data.

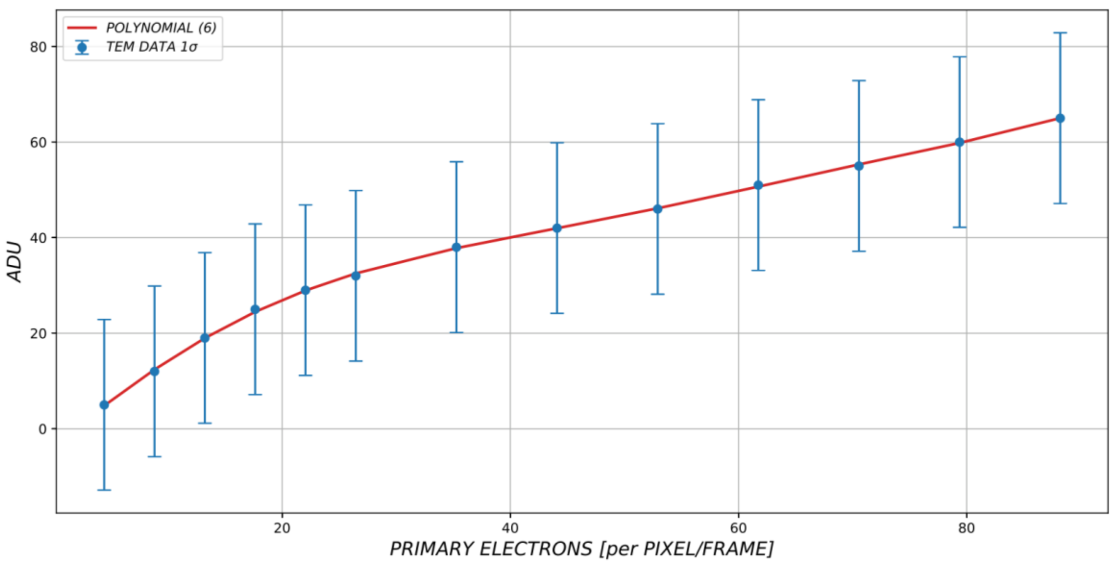

Figure 9-12: Truncated median charge curve of all small EDET matrix pixels.

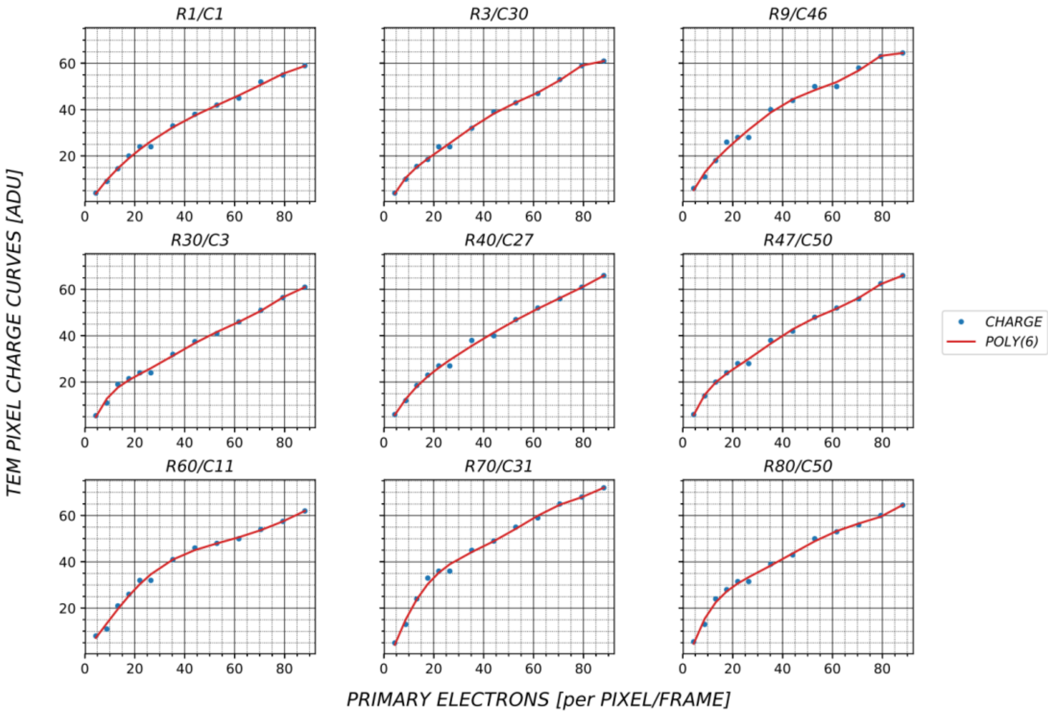

Figure 9-13: Selection of charge curves for single matrix pixels.

9.4.3 Static Images

A very simple measurement with special manufactured masks produced the following shadow images (again, cold pixels from broken drainlines were interpolated):

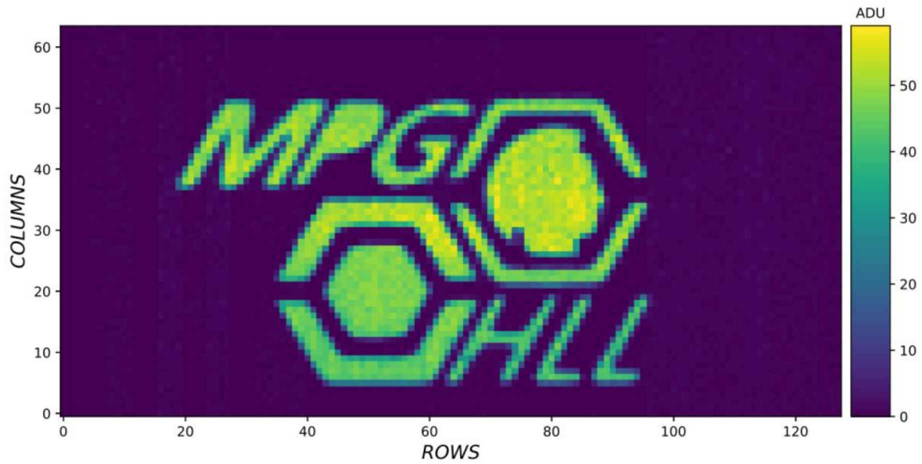

Figure 9-14: HLL Logo as a shadow picture from a small Titanium mask.

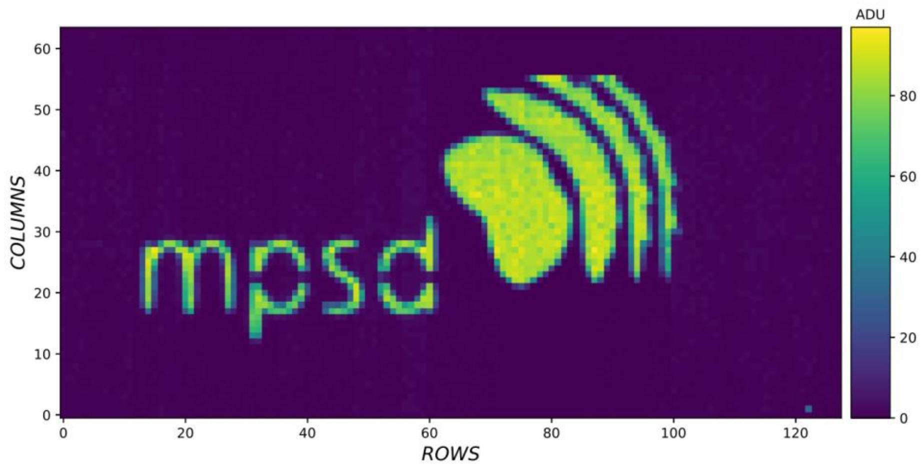

Figure 9-15: MPSD Logo as a shadow picture from a small Titanium mask.

Another static measurement concerned the magnification calibration: higher magnifications can be calibrated by polystyrene latex spheres on a diffraction grating replica as shown in Figure 9-16 [195].

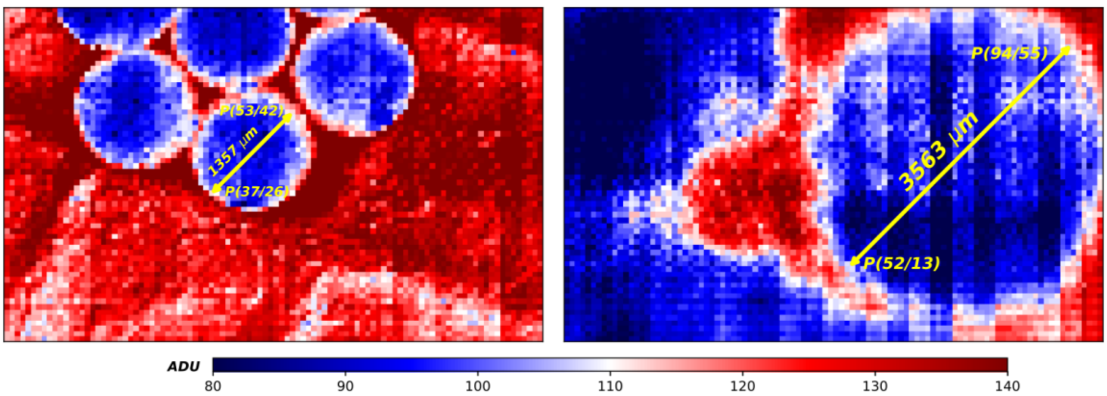

Figure 9-16: Different TEM magnifications of standardized latex spheres on a replica grating. The given pixel addresses denote start- and endpoints of the diameter vector. Left: Magnification[19] of about $\sim 5{,}200\times$*:* $\emptyset_{latexsphere} = 261\ nm$ *corresponding to 1,357 µm on the sensor. Right: Magnification of about* $\sim 13{,}650\times$*. This compares to the nominal settings of the TEM of* $3{,}000\times$ *and* $8{,}000\times$ *respectively. Factoring in the post-magnification factor of 1.73 the maximum deviations lied within 1.5%.*

The specimen contained a waffle-pattern diffraction replica grating of 2,160 lines/mm (line spacing of 463 nm), on which latex particles with a diameter of 261 nm had been placed. One could measure the magnification by either using the spacing of the grating lines (faintly visible in the left picture of Figure 9-16) or by an estimate of the diameter of the latex spheres (in µm) divided by 0.261. Due to different latex particle sizes, this method is not perfectly accurate for the determination of the instrument magnification.

[19] Ratio of the real space distance on the detector to the real space distance at the sample.

9.5 Movie Measurements

The ultimate goal of the TEM campaigns involved scientific movies, implemented by the following dynamic measurements:

In the first experiment, the electron beam induced a nucleation and growth of gold nanocrystals in a liquid cell environment [196]. The sequence of 9 frames at different points in time is depicted in Figure 9-17. The bright areas mark the pores of an anodic Aluminium oxide (AAO) [197] serving as a carrier of the liquid cell structure. The window membranes consist of Formvar, a polyvinyl resin specifically suitable for very thin slices. As one can observe, the areas of beam induced growth of gold particles (discernible by the gold dotted areas) increased continuously.

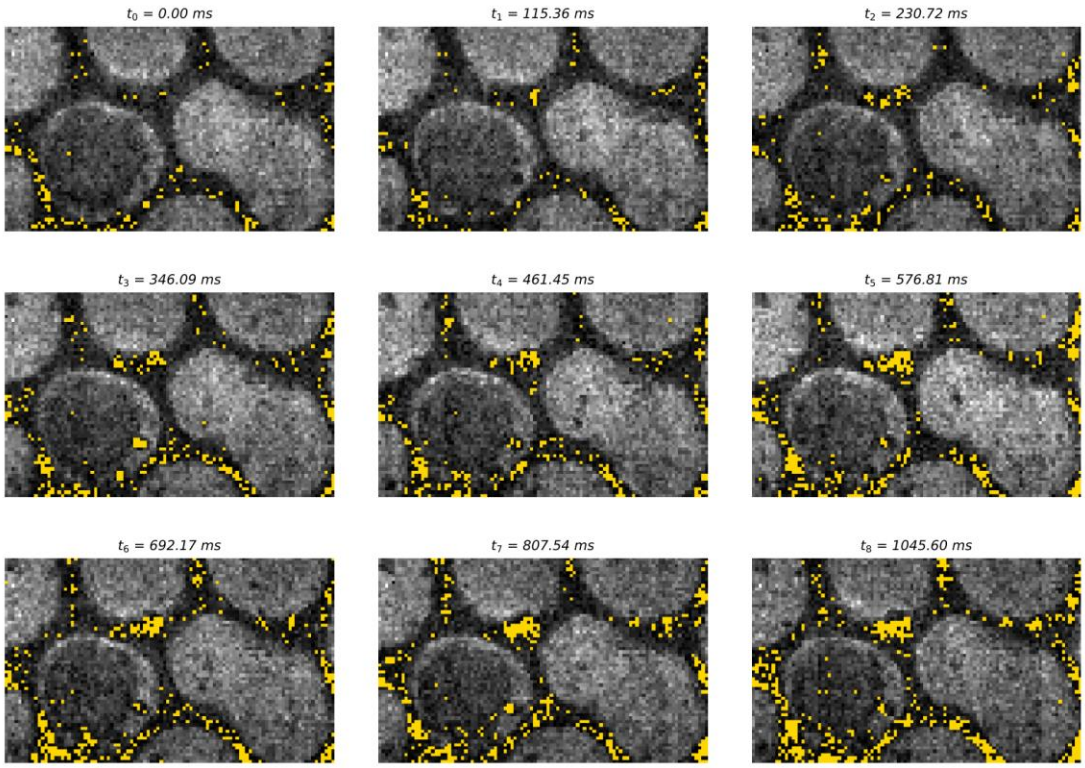

Figure 9-17: “In Situ Electrodeposition of Gold”. The illustrated sequence spanned a time interval of about 1.05 seconds and contained a total of 9,970 frames à 105.857 µs. The evolution of the gold particle growth was colored in gold.

A closer look on the recorded data revealed, that the general ADU level declined significantly because of both, a longer beam exposure (about 11,000 frames ~1.16 seconds) and a stronger intensity as shown in Figure 9-18. It is difficult to correct for this in the offline analysis, since the sensor regions were affected unequally. Hence, for the prospective run – idle operations, it is highly recommendable to record intermediary offset data after certain intervals in order to avoid some unintended effects.

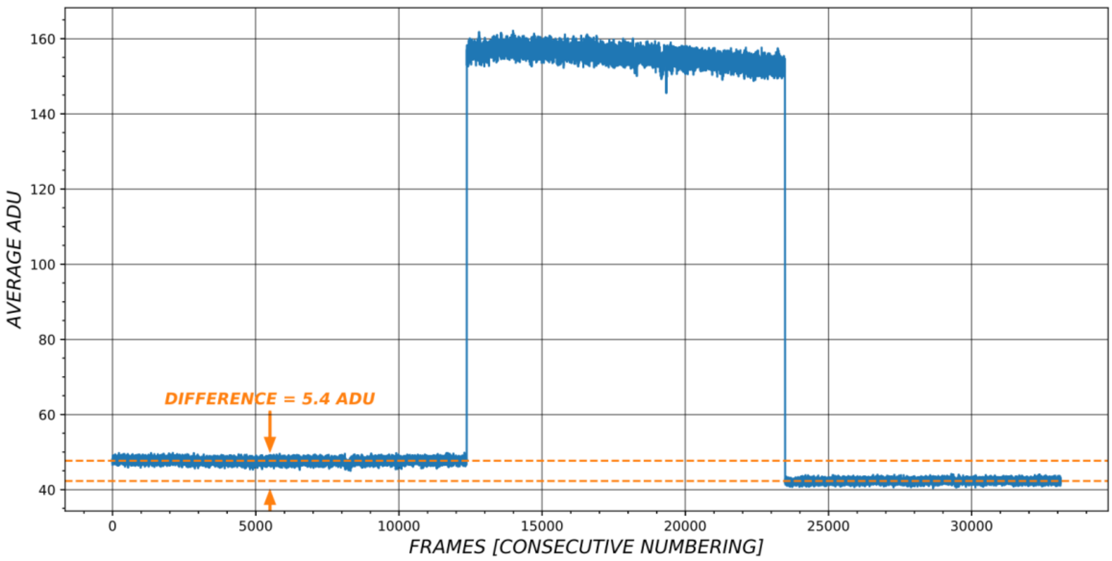

Figure 9-18: Degradation of the EDET sensor as a consequence of the In-Situ Electrodeposition of Gold.

Another measurement induced movements of Silver nanoprisms under atmospheric conditions in a Silicon nitrite environmental chamber as shown in Figure 9-19

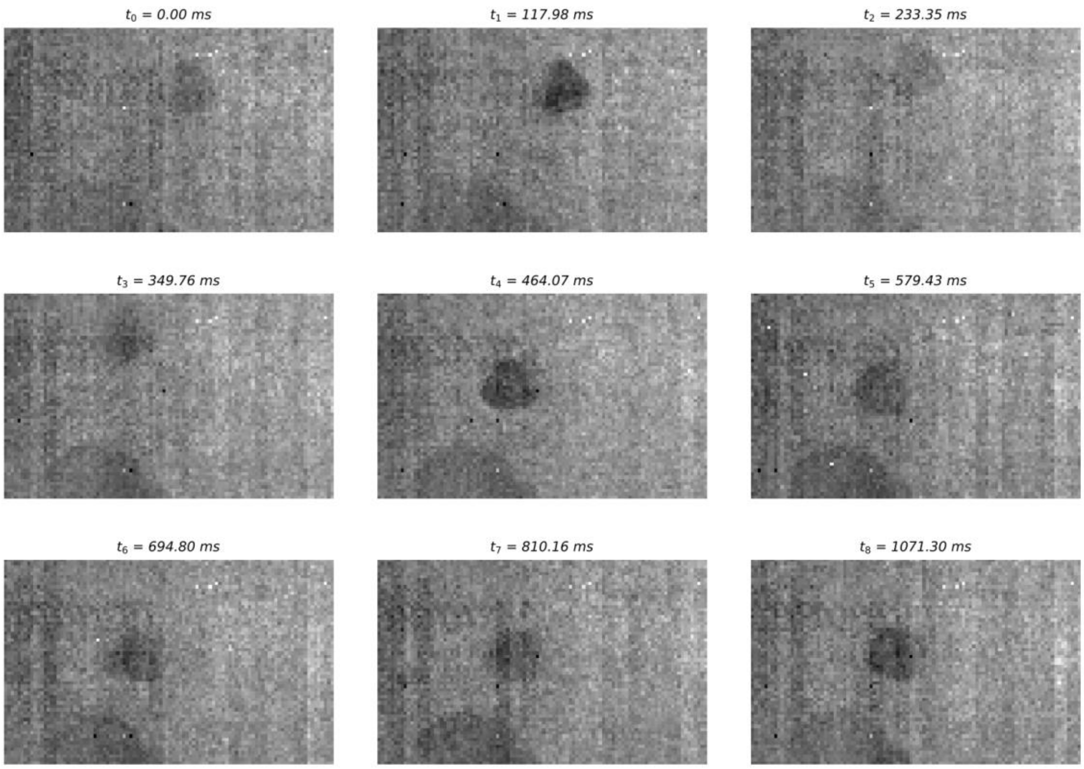

Figure 9-19: "Dancing Nanocrystal". The electron beam moves a Silver nanoprism under atmospheric conditions.

The last presented measurement in this thesis is related to the interaction between silver and ionized gas in an environmental cell as depicted in Figure 9-20. The TEM beam initially induced a volume growth by oxidation to the microstructural evolution of silver as can be observed until the third frame (top row from left to the right). Then, the grain size of the silver crystal quickly eroded by secondary electrons, accompanied by a nucleation of new silver grains. For more about the whole process read [198].

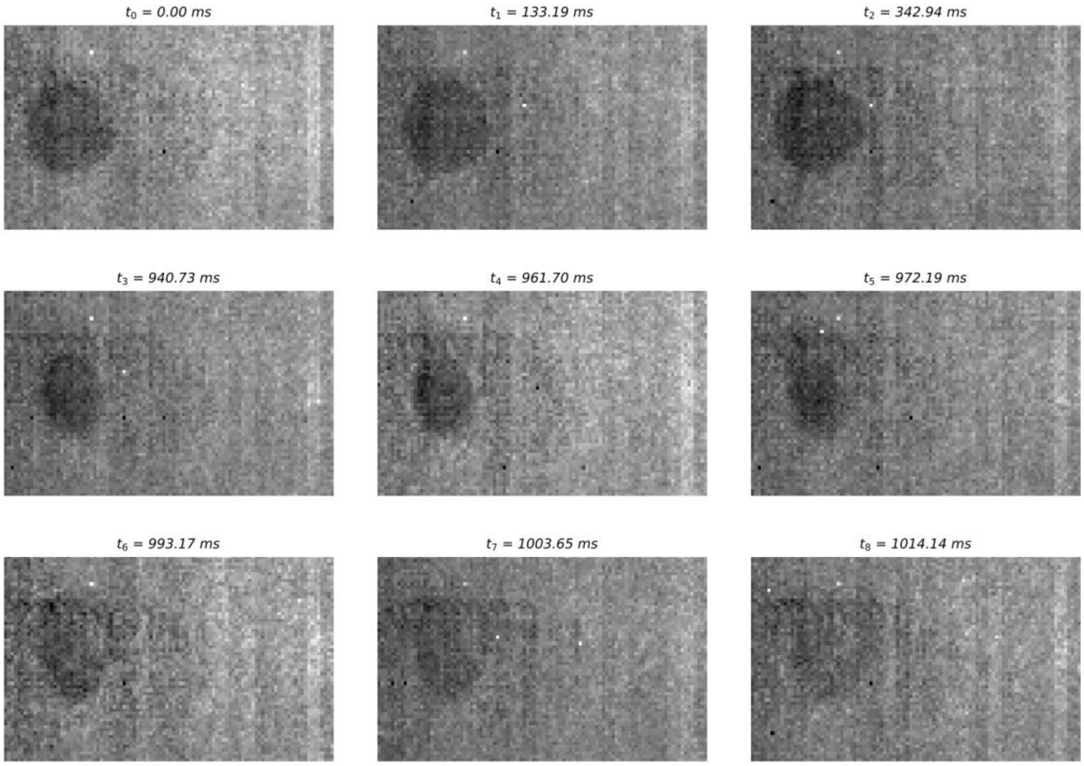

Figure 9-20: "Exploding Silver". Similar to above, the recording time (1 second) is presented in a time lapse mode showing 9 out of 10,000 frames.

10 Conclusion & Outlook

The rise of direct electron detectors significantly improved the operation of transmission electron microscopes and opened the doors for new applications. In contrast to photographic films, they allow the in-situ observation of dynamic processes. Compared to indirect detectors (CCD with a phosphor and fiber-optic coupling) they are inherently faster, deliver a better SNR and a higher resolution. Not surprisingly, as far as the aforementioned criteria are relevant for the application, direct electron detectors nowadays dominate the sale of new detectors in the TEM market.

To visualize fast dynamic processes, Halbleiterlabor der Max-Planck-Gesellschaft (HLL) and Max-Planck-Institut für Struktur und Dynamik der Materie (MPSD) undertook a common effort for a novel direct electron detector. Equipped with a high charge integration capacity, EDET will be able to record 50 frames consecutively with an unprecedented readout speed of 80 kHz. The sensor uses the DEPFET technology, a combined function of charge collection and amplification. Additionally, the new detector will offer two different operation procedures: it will be able to record traditional, low dose diffraction images (counting mode), on the other hand, TEM movies with consecutive scattering or shadow images will be possible (integration mode).

To incorporate all selection criteria into one unit, the decision was made for a two-tier structure of the sensor amplification: a strong gain for weak signals and signal compression for high intensities (non-linear pixel response). In addition, imperfections in the manufacturing process of the sensor and of the readout electronics, lead to significant pixel gain variations. Thus, it is of utmost importance, that all pixel outputs can be calibrated, that pixels react in an equal way, if exposed to an equal external stimulus. Especially with respect to biological samples it is essential, that scattering images which usually offer relative low contrast, get not distorted by differing pixel responses.

A major effort was undertaken to solve the issue of pixel calibration. In case of linear response functions this would have been a straightforward task, since a monochromatic radiation, provoking single pixel gain numbers, would do the job. However, the non-linear pixel response curve significantly adds to the complexity. All at once, a whole charge curve for every single pixel has to be determined. In the course of this scientific work it became clear, that each calibration method has its advantages and disadvantages. To get optimal results, a combination of convenient instruments must be used. For the absolute pixel calibration, a radioactive ^{109}Cd source was employed. Based on this, several methods were investigated to generate individual pixel charge curves.

A first attempt used a focused laser spot in combination with step-increased pulse frequencies. Despite the highly reliable results, this method was rejected for it was very time consuming with respect to a detector of over 1 million pixels. By contrast, a LED or also a defocused TEM beam offer widely homogeneous illuminations for all pixels at once. By gradually increasing the LED input current or, in case of the TEM beam the duty cycle, charge curves for all pixels could be simultaneously established. Finally, a specific algorithm facilitated the conversion of the individually determined pixel gains into the same common base. The whole analysis was done on a small sensor nonetheless, the developed methodology can be easily transferred to the intended large module.

In light of the major achievements with respect to the single pixel calibration, one should not forget the important groundwork, which was necessary to develop a practical system. The investigation started with the characterization of the different system parts, above all, the check of the envisaged system specifications: the readout chip (DCDE), the Switcher (steering the activation of the pixel gates and the clearing of the collected electron charge), the sensor, the power system and the DAQ system to name the main ones.

The next challenge concerned the interaction of all parts to deliver a functional system. A lot of algorithms were developed to optimize the system. Apart from an evaluation of the optimal settings for the supply voltages and the optimized register settings of the readout chips, an important task concerned the synchronization between the different parts of the readout system. Eventually, a standard measurement suite was set up for the system optimization and quality control.

Knife-edge measurements related to distinct imaging modalities (^{109}Cd source, LED and TEM beam electrons) demonstrated, that the detector exhibits an excellent resolution. The corresponding figure of merit, the modulation transfer function was determined. Deviations from an ideal MTF could be attributed to specific reasons: the geometrical experimental setup (^{109}Cd source), diffraction effects (LED) or the inevitable electron scattering within pixels (TEM) of non-zero thickness.

An unwelcome, serendipitous discovery of the MTF measurements concerned a phenomenon which was referred to as the “ghost charge” effect. It is characterized by an additional pixel current without any external charge injection. Different tailor-made tungsten masks helped to understand the nature of the ghost charge issue. By various adjustments in the system settings, especially in the DCDE, a mitigation of this effect could be achieved.

A milestone for this project was achieved by the installation of a small EDET test system on an actual TEM instrument. The results, delivered from two Hamburg campaigns were impressive and exceeded the expectations in many aspects. Knife-edge scans and other static images demonstrated both, an excellent spatial resolution and contrast of the detector. Also, first TEM movies, for example gold nanocrystal growth, had been produced.

Nevertheless, a lot of work remains to be done. First of all, the results have to be transferred to a large module, consisting of 8 DCDEs and 4 Switchers, corresponding to an increase of the sensor area by a factor of 32. This implies also an adaption of the standard optimization procedures, especially the DCDE optimization. Since the chips are bump-bonded directly onto the module, a new method of an external current source injection has to be developed. Alternatively, the injection current for the transfer curves could be also provided by the sensor: through adjustment of the gate voltages the drain currents are increased. However, one should be aware, that a transistor does not provide linear curves and in addition, potential cross talk effects within the DCDE could potentially affect the final result adversely. On the other hand, this approach is very fast and enables the optimization of all DCDE channels at once.

Furthermore, the synchronization scripts of the DAQ system must be completely reprogrammed to ensure a proper control and readout of the sensor.

The detected ghost charge issue and the large gap between DCDE gain 11.0 and gain 3.3 suggest to consider a revised version of the DCDE.

The development of the new DMC is still outstanding and will require an efficient testing, before it can be assembled to a large module. Without this chip, the envisaged frame rate of EDET will fall substantially short of expectations. While for a small matrix almost 20,000 fps are theoretically possible, for the large module this number reduces significantly to about 5,000 fps. Although this readout frequency would still be outstanding compared to other existing direct detectors, the original objectives would be certainly missed.

A specific problem for all direct electron detectors is radiation damage. The EDET sensor is particularly affected, because of the high TEM beam intensities needed for scattering images. The BELLE II irradiation campaign administered a total dose of 26,600 krad. Despite a total gate voltage shift of about 11 V (and a necessary cleargate adjustment of up to 6 V), the system performance was still pretty stable. From back-of-the-envelope calculations in section 9.3 one can infer, that in case of the base operation scenario of 100 e^-/px/frame at an energy of 200 keV, the transferred dose would amount to about 0.8 krad per 200 ms for an EDET pixel. Extrapolated to the BELLE II dose, this would correspond to 110 minutes of permanent irradiation. Hence, under consideration of a planned duty cycle of 10%, the total service life can be estimated to at least 18.5 hours on a continuous basis.

After all, there will be a point in time where a reasonable operation will no longer be possible and the sensor must be repaired. One possible method foresees a removal of the detector from the TEM and put it into a reflow oven at high temperatures [199]. This procedure exploits a phenomenon, which is commonly referred to as annealing. Annealing labels a process, where some of the trapped holes at the SiO_2/Si interface get neutralized by thermic stimulation. It strongly depends on the temperature. However, noticeable effects can only be registered at temperature levels above 250 °C. This is not recommendable for the soldering joints of the bump-bonded ASICs. Another clear disadvantage of the described approach is the loss of time. Removal and reinstallation of the detector and the necessary gas evacuation consume roughly one day. An innovative idea, developed by the collaboration, foresees a focused laser beam beneath the detector, scanning the sensitive area. Besides significant time savings, this method would also allow for higher annealing temperatures without damaging the detector electronics.

The proximate field of application for EDET will be electron beam induced chemistry and DNA origami. However, the chances are good that also other areas become highly important.

APPENDIX A JTAG

JTAG denotes an IEEE industry standard 1149.1-1990 for the testing and verification of integrated circuit (IC) designs after manufacturing [200]. Standardized test features are directly integrated into the chip's test logic. A typical JTAG interface consists of at least four pins and their corresponding logic signals:

- Test Clock (TCK)
- Test Mode Select (TMS)
- Test Data In (TDI)
- Test Data Out (TDO)
- *optional:* Test Reset (TRST)

as shown in Figure A - 1 for the EDET system architecture.

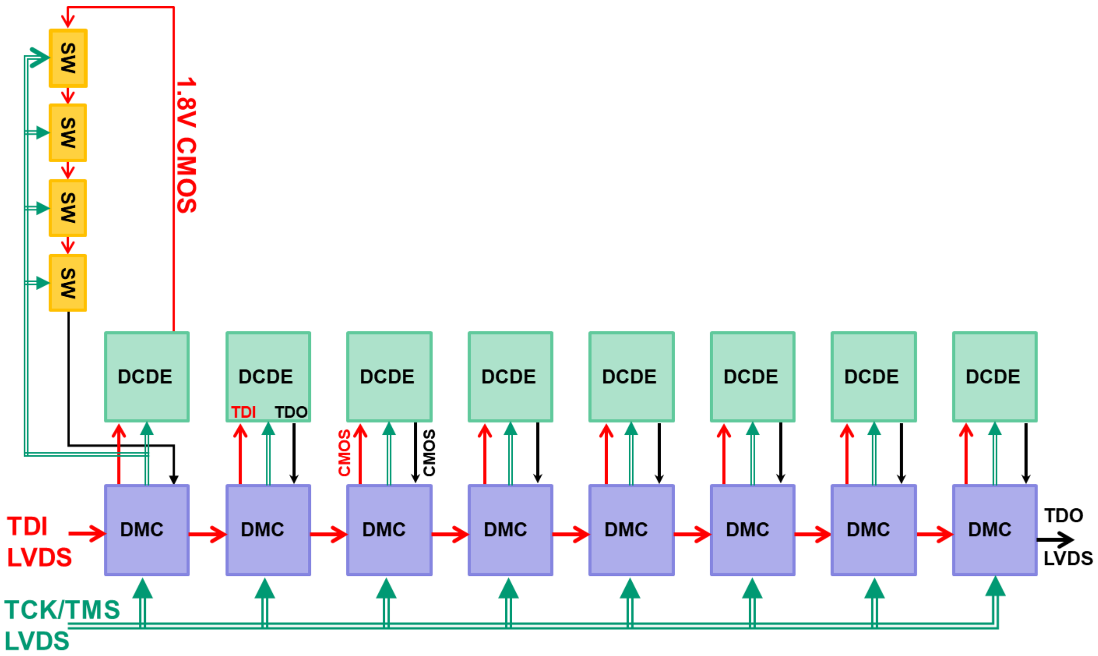

*Figure A - 1: JTAG signal flow for the EDET system architecture. The DMCs are connected by wire pairs using the Low-Voltage Differential Signal (**LVDS**) standard. The DCDEs and Switchers are connected via the single ended CMOS-standard.*

TMS and TCK are wired in parallel to all JTAG ICs, whereas TDI and TDO are connected to form a chain. Inside each IC (in our case: DCDE, DHP & Switcher) a Test Access Port (TAP) controller assumes the role of **a finite state machine** with 16 different states. The scanning unit communicates with the TAPs by manipulating TMS and TDI in conjunction with TCK, which has to toggle for anything to happen. The results are transmitted back via TDO. Each TAP-controller has one instruction register (IR) and one or multiple data registers (DR) consisting of IC specific bit-lengths. While the state machine is in the "Shift-IR" or "Shift-DR" state, 0's and 1's are read into and out of the TDI and TDO pins.

If the **boundary scan** instruction was selected, the data register chain goes through each I/O block and has access to each pin.

A Boundary Scan Description Language (BSDL) file, which describes the boundary chain for a dedicated ASIC, is usually provided by each chip designer. The FPGA (XU1-board) uses OpenOCD, a special boundary scan software that translates the BSDL code (beforehand, the BSDL code has to be converted into an OpenOCD configure file) into TAP machine code and executes tests on the connected chips, independently from their actual design. As a result, the operator gets a useful statement about the electrical connection and communication between the ASICs. Moreover, JTAG is also used to configure and control the ASICs with the required settings.

APPENDIX B EDET Standard Optimization Procedures

B.1 Delay Scan

Despite the distance between DCD and DHP is very small, the communication experiences some delays. On the one hand, the internal DHP clock controls the sampling and produces the clock signal for the DCD. On the other hand, another delay occurs between the internal DHP synchronization signal and the *row sync* signal provided to the DCD. This can be compensated by programmable delay elements in the DHP, physically implemented by inverter chains [186, 201].

The DHP contains 64 input pads, which interconnect to the output of the DCD. The 256 DCD channels are organized in 8 channel groups (0–31, 32–63, …). At the inception of a readout cycle, the full 8-bit data of the first channels (0, 32, 64, …) is sent to the DHP. The next clock cycle, the data of the second channels (1, 33, 65, …) gets transmitted and so on.

By means of an internal DCD test pattern, a 2D sweep over all possible global and local delay settings can be performed (each parameter comprises 16 configurable DAC values, so a total of 256 possible settings). The system uses signed integers, therefore the numbers range from -128 to +127 ADU. However, the word “-128” should not appear, as the ADCs in the DCD cannot produce that output code. If a transmission error occurs within one channel group, this is counted as a bit error and finally aggregated into a 2D diagram as shown in Figure B - 1.

As an example, from the test pattern channel 2 has to transfer the word “17”, corresponding to the following bit sequence with the Least Significant Bit ($\mathrm{LSB} = 2^0$) at the right side and the Most Significant Bit ($\mathrm{MSB} = 2^7$) at the left:

MSB	2^6	2^5	2^4	2^3	2^2	2^1	LSB
0	0	0	1	0	0	0	1

If now a “1” appears at the position of the MSB, this does not match with the expected number. Therefore, it is counted as a bit error. The accumulated bit errors for all channels of a channel group are finally entered into the specific global and local delay position of an MSB matrix. Needless to say, that the DCD test pattern comprises also other numbers. For example, channels 10, 42, 74, … transmit the word “-86” with a leading “1” for the MSB. In this case, a transmitted “0” for the MSB would be counted as a bit error.

As one can see, the dark blue area contains no bit errors and marks the eligible space for the delay settings.

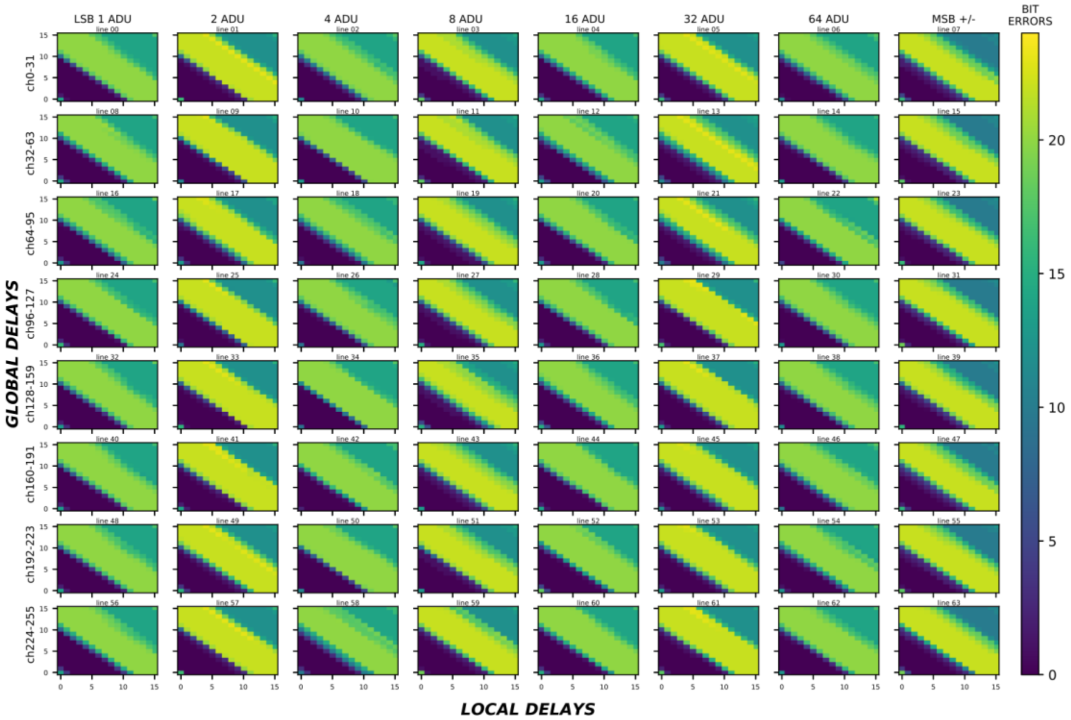

Figure B - 1: Delay Scan DHP – DCD. Each row represents one DCD channel group (à 32 channels). The 8-bit data is represented column-wise in ascending order.

B.2 ADC Transfer Curves

B.2.1 ADC Error Sources

The quantization error only depends on the available digital range. If the input current is continuous or consists of very small discrete step values, the quantization error can be calculated as [202]:

$$\frac{Q}{\sqrt{12}} \cong 0.289\ ADU$$

with Q the ideal code bin width. Apart from the quantization error, the quality of an ADC can be assessed by additional performance parameters: in electronics it is common to use the root mean square or RMS noise σ_{RMS} to assess any deviation between the output and the input signal. In addition to random noise components, it includes harmonic distortions, other spurious components and also the quantization error:

Equation B - 1
$$\sigma_{RMS} = \left[\frac{1}{n}\sum_{i=1}^{n}(y_i - \bar{y})^2\right]^{1/2}$$

with n the number of samples in the data record, y_i the sample data set and $\bar{y}$ the mean value. For the evaluation of the following transfer curves, this thesis uses the sigma noise as a performance criterion. Sigma noise refers to an aggregate number for each DCDE channel, the standard deviation of all σ_{RMS} for every current injection:

Equation B - 2
$$\sigma_{\sigma_{RMS}} = \sqrt{\frac{\sum_{i=1}^{m}\left(\sigma_i^{RMS} - \overline{\sigma^{RMS}}\right)}{m-1}}$$

for all m input current injections.

The differential nonlinearity (DNL) is defined as the difference between the specified code bin width and the ideal code bin width divided by the ideal code bin width [202]:

Equation B - 3
$$DNL_k = \frac{G \times [(T_{k+1} - T_k) - ADU]}{ADU} = \frac{G \times [T_{k+1} - T_k]}{ADU} - 1$$

where $T_{k+1} - T_k$ is the code transition level[1] for the k^{th} transition and G is the static gain determined by:

Equation B - 4
$$G = \frac{ADU(2^N - 2)}{T_{2^N-1} - T_1}$$

with N the number of digitized bits per sample for the ADC (in case of the DCDE 8-bits). In other words, DNL measures how much the actual width of each step deviates from the ideal step width.

[1] The code transition level is located between two adjacent transition points, the latter is defined as the input value that causes 50% of the output codes to be greater than or equal to the upper code of the transition [166].

An ideal converter produces a DNL of 0, or equivalently, two adjacent input code transition levels produce exactly one ADU. The DNL characterizes the ADC's precision and usually only the maximum value of all DNL_k is reported. A $DNL_k \leq -0.9$ indicates, that the ADC generates missing codes as shown in Figure B - 2: an input current change between two adjacent digital codes causes no output change. Only a significant increase of the input current causes a higher output code, with the intermediate ADUs never being measured. For the sake of completeness, if an ADC delivers a lower conversion result for a higher input stimulus, the ADC is said to react non-monotonic or inverting.

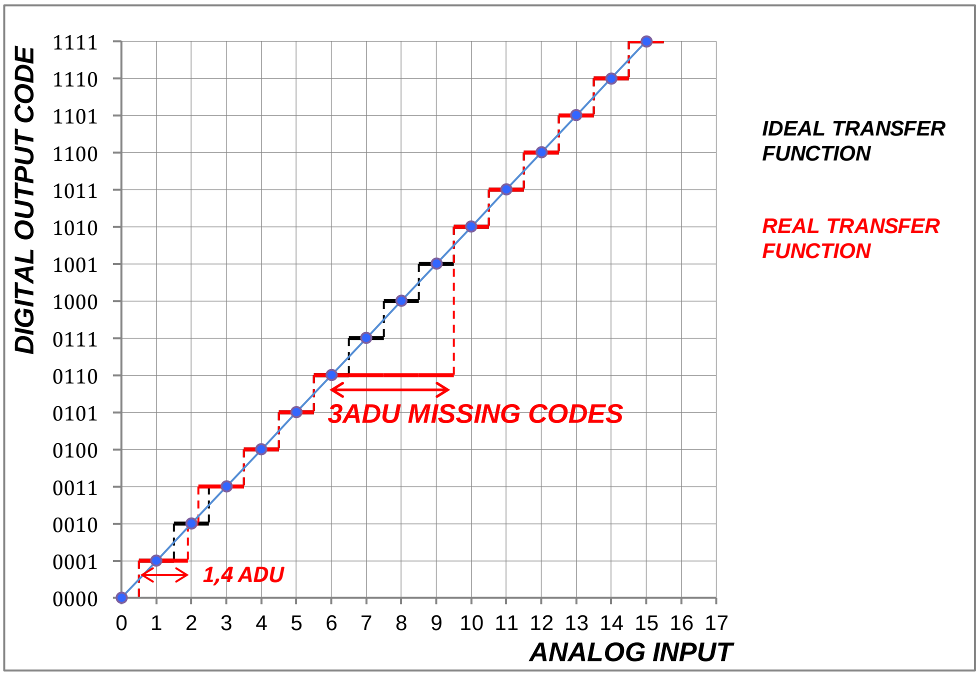

Figure B - 2: Differential Nonlinearity (DNL) of a 4-bit ADC with missing codes.

The integral nonlinearity (INL) is defined as the absolute difference between the ideal and the measured code transition levels in units of ADUs as shown in Figure B - 3. Figuratively, INL represents the curvature in the actual transfer function relative to the ideal transfer function. However, the chosen algorithm for the DCDE-INL implemented a straight-line fit to the actual transfer curve instead of an ideal expected response function.

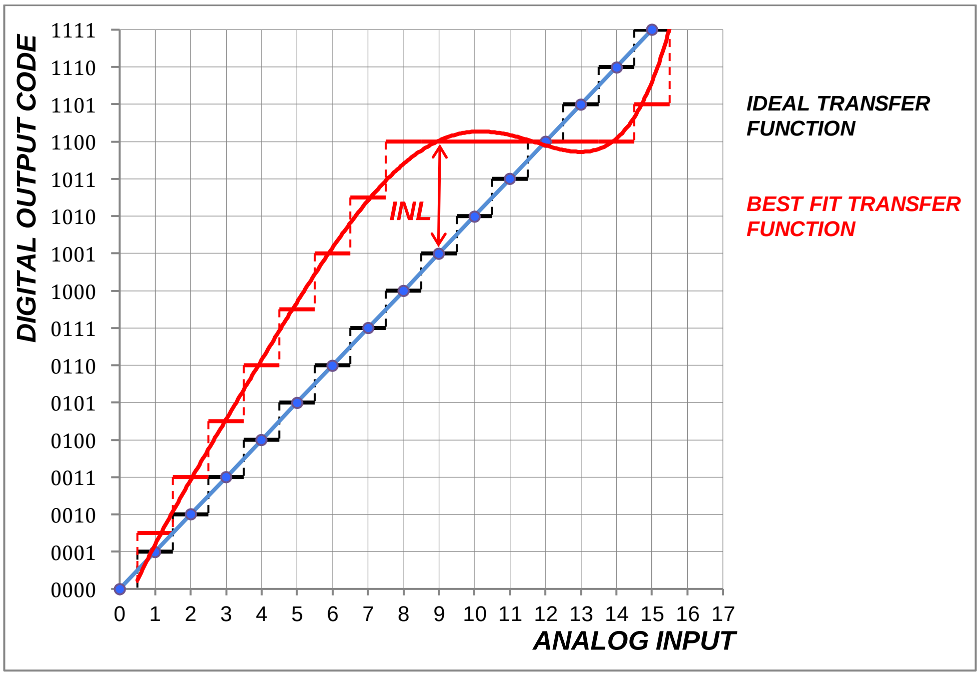

Figure B - 3: Integral Nonlinearity (INL) featuring a distinct curvature.

Again, only the maximum value of all INL_k is reported. It measures the biggest deviation of the output codes in vertical direction from a line regression, based on the underlying transfer data points.

A common problem, affecting many DCDE transfer curves, concerns some non-linear effects at both ends of the dynamic range. For that reason, the fit is performed on a restricted range between 30 and 230 ADU. As one can see, with regards to the optimized transfer curve of Figure B - 4, it does not perfectly align with the extrapolated linear regression line. Especially at the front end, a small curvature can be observed. The difference between the point on the transfer curve vertical to the intersection of the regression line with the x-axis is referred to as an independent performance parameter, the 1st endpoint error (the same methodology is applied to the 2nd endpoint).

Notwithstanding the IEEE standard, the term offset error used for this thesis is related to a missing code problem at the origin of the transfer curve. As the ADC bottom value starts at -127, which is internally translated to 1, every lowest value above 1 is considered as an offset error.

B.2.2 DCDE Settings Optimization

The determination of the optimal DCDE settings requires intuition and a lot of time. In theory, more than a dozen 7-bit DAC registers and the analog supply voltages *Refin* and *Amplow* are free adjustable. For the sake of time, a complete range scan would be highly impracticable. Fortunately, the guidance from the designer provided some initial settings for the DCDE as well as a selection of the 6 most relevant parameters: *Refin, Amplow* and the four 7-bit DCDE registers *IPSource, IPSource2, IFBPBias and IPSourceMiddle*.

Nevertheless, an entire sweep would take still too long (and conjure a serious data storage issue) since the selected DAC parameters alone would allow for 128^4 different combinations. Anyway, as a result of trial and error and long term experience the scope of that problem can be reduced by adherence to the following principles:

1. The external current injection tackles channel after channel. If an attempt is made to find optimal settings for all channels, the required time increases by a factor of 256. On the other hand, one should be aware if the optimization focuses on just one particular channel, the performance of all other channels can significantly deteriorate.
2. To assess the quality of a transfer curve, several performance criteria should be applied. The four primarily used are (in descending order of importance, view of the author): missing codes, noise, DNL and offset error. The hierarchy is important, since oftentimes one parameter gets optimized at the expense of the other ones.
3. The range of the supply voltages *Refin* and *Amplow*[2] should be kept within a narrow band between 700-800 mV and 200-400 mV respectively. Outside this range some unwelcome effects occur. As an example, the right diagram of Figure B - 4 depicts a transfer curve, where *AmpLow* was obviously chosen too high: the DCDE would lose considerably in dynamic range by an increased offset level of over 30 ADU.

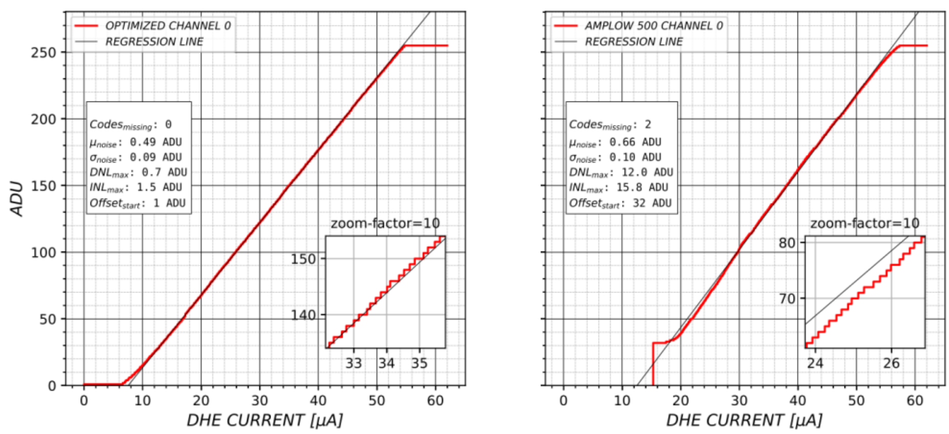

Figure B - 4: Left: Optimized ADC curve, AmpLow set at 300 mV. Right: High AmpLow level of 500 mV leads to a significant narrowing of the dynamic range.

4. All four mentioned DAC register values should be fixed above DAC 50. For most of the analyzed DCDE chips, the optimum settings range between DACs 70 and 90. Figure B - 5 depicts the missing code values of a particular DCD channel with respect to 16,200 different combinations. The moving average (orange curve) combines in each case 100 values and moves down with increasing *IPSource,* until it reaches a bottom at DAC 85 for *IPSource*.

[2] *AmpLow* is mainly responsible for draining the current.

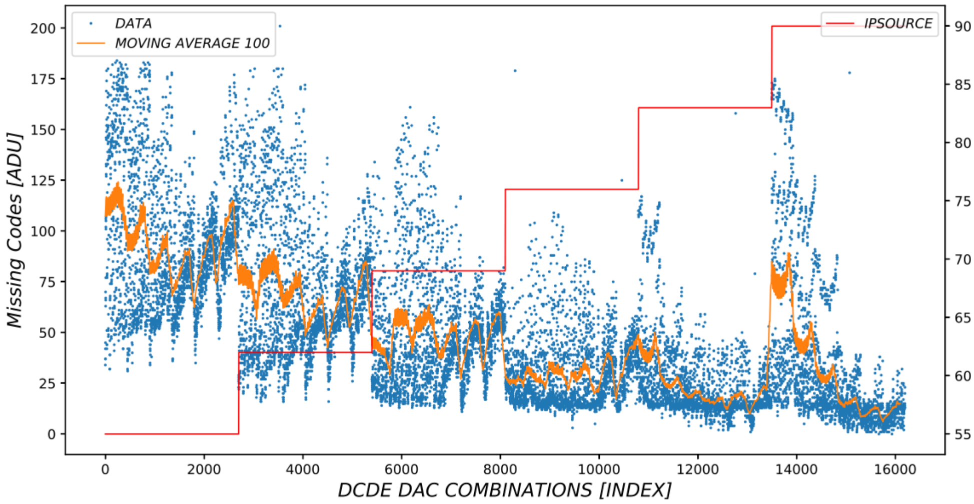

Figure B - 5: Impact of several DCDE settings variations on the missing codes criterion. The blue dots mark 16,200 collected results. The orange curve compounds averages of 100 values. The step curve in red indicates the respective levels of IPSource (right hand scale).

This analysis can be done for all other performance criteria, DCDE parameters, channels and DCDEs. An example, an impact study of *IPSource2* on all described performance parameters is presented in Figure B - 6.

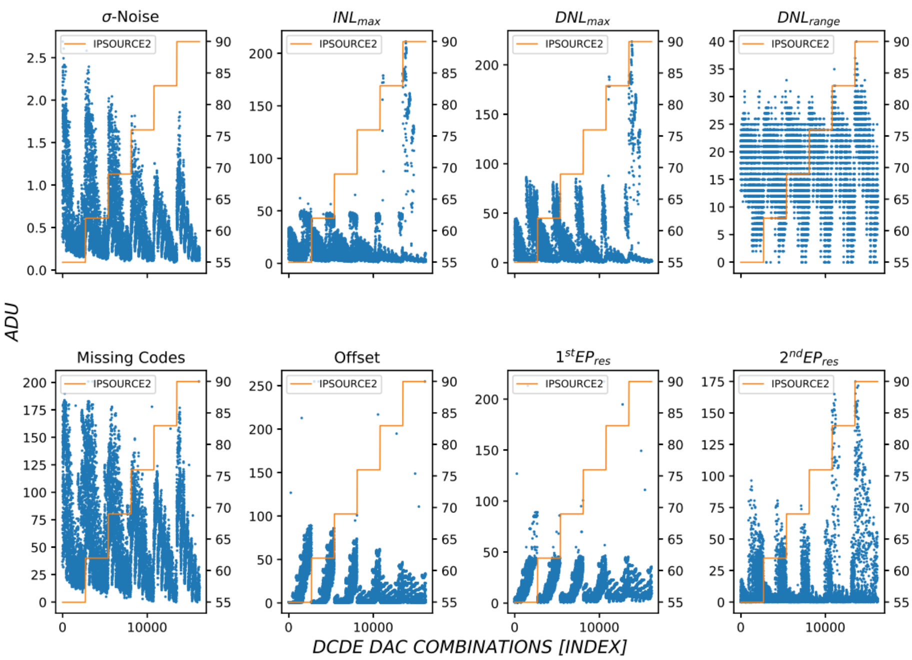

Figure B - 6: Effect of IPSource2 on different performance parameters. Again, a preference for higher DAC values is observable with respect to missing codes (e.g. for a DAC of 55, not any combination hits the ideal situation with 0 missing codes. If choosing a DAC of 85, a lot of 0 missing code events occur and the maximum is limited at 125). In turn, at 90 DAC the overall dispersion widens significantly.

5. The transfer curves do not react very sensitive to small voltage/DAC changes, so 50 mV steps for the supply voltages and DAC step changes of 7 are sufficient.
6. Several local minima for the performance criteria can exist. Figure B - 7 depicts a single step DAC-sweep of the *IPSource2* register for a specific DCDE and channel. As one can see, especially with respect to noise, INL, DNL and missing codes, two minima are observable. Accordingly, constraining the set space around past optimal settings with reasonable step sizes can save a lot of time.

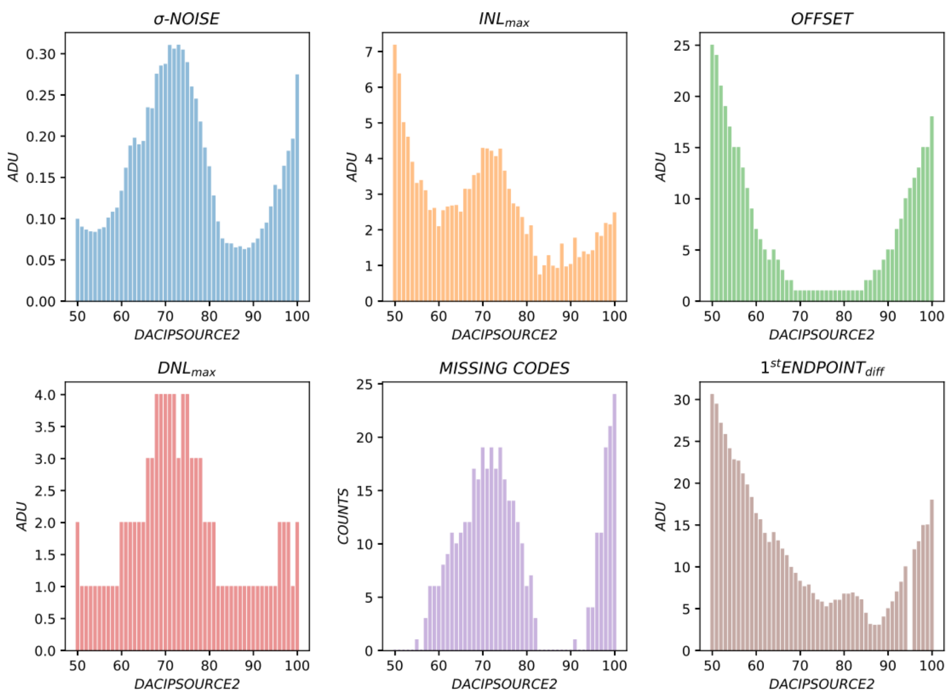

Figure B - 7: Sweep of IPSource from 50 to 100 in single DAC steps for a particular DCDE channel.

7. The outcomes between high (33.0) and low (3.3) DCDE gains are quite similar, albeit slightly worse for the low DCDE gain. As a consequence, the optimization of the low gain settings will do.
8. Because of the Nyquist theorem, the high granular input current step sizes can be significantly enlarged to half of the digitized output steps, which again saves a lot of time.

The operator might evaluate on the above criteria and the available time for the final optimization procedure. For this thesis, a relative generous duration was selected and the following approach was adopted:

I. DAC steps external current source: 20 DAC[3] (from 0 to 65,000 for a DCDE gain of 3.3), that means 3,250 increasing current injections. Each current was measured 256 times (→ σ_{RMS}^{256}→$\sigma_{\sigma_{RMS}}^{3,250}$).

II. Standard settings for all DCDE channels and determination of the "worst" channel with the highest count of missing codes. In case of Figure B - 8, channel 243 exhibited the worst missing codes result.

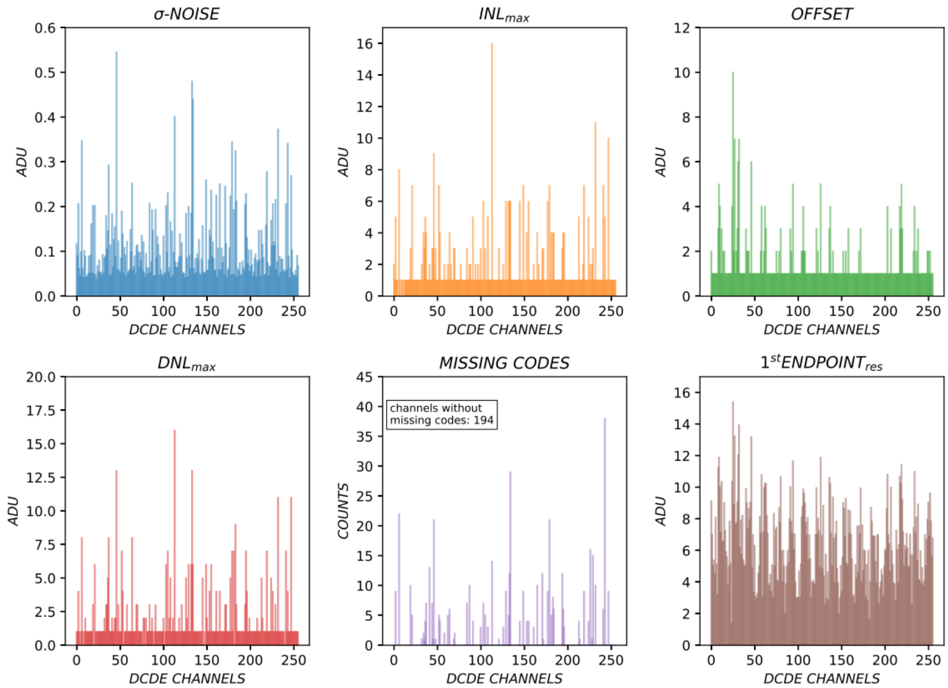

Figure B - 8: Result of all 256 DCDE transfer curves on 6 performance criteria before optimization. Channel 243 was selected for a single channel optimization procedure, because of its highest missing code count of 37 (the same channel was not the worst with respect to other performance criteria)

III. A sweep was performed on the selected bad channel with the following sweep values (start / end /step width): *IPSource* 55/90/7, *IPSource2* 55/90/7, *Amplow* 200/400/50, *Refin* 700/800/50, *IFBPBias* 55/90/7, *IPSourceMiddle* 60/88/7, in total 16,200 setting combinations. The performance parameters must not be fixed too low in order to avoid adverse effects from pure single channel optimization: e.g. noise ≤ 0.14, DNL ≤ 2.0, missing codes ≤ 10, offset value ≤ 5. Only sweep combinations passing the performance criteria were stored (trade-off between quantity and quality, heavily depending on the performance parameter limits: a passage of at least 1,000 combinations should be envisaged for the first optimization round).

[3] From section 6.3.1.3: one DAC step of the used external current source corresponds to about 3.82 nA. 20 DAC steps amount to 76.4 nA. The typical ADU value, expressed as a current for the DCDE 3.3 gain is 670 nA, equivalent to almost 9 external current step increases. Hence, a step increase to 80 DAC would still comply with the Nyquist rule and consume only 25% of the original time.

IV. The remaining combinations were applied bit by bit to the other DCDE channels, still complying with the requirement to pass the limits. The process stopped, if there was only one or no combination left. If too many combinations remained, the process was repeated at stricter performance parameter values. Figure B - 9 and Figure B - 10 show a “bad” and a “good” curve before and after optimization.

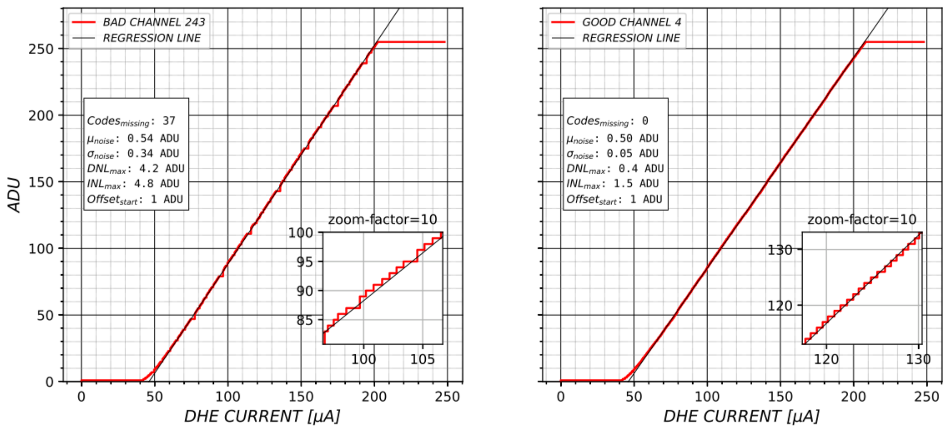

Figure B - 9: Left: DCDE channel 243 with a lot of missing codes before settings optimization. Right: several channels (exemplary channel 4) already meet the performance criteria.

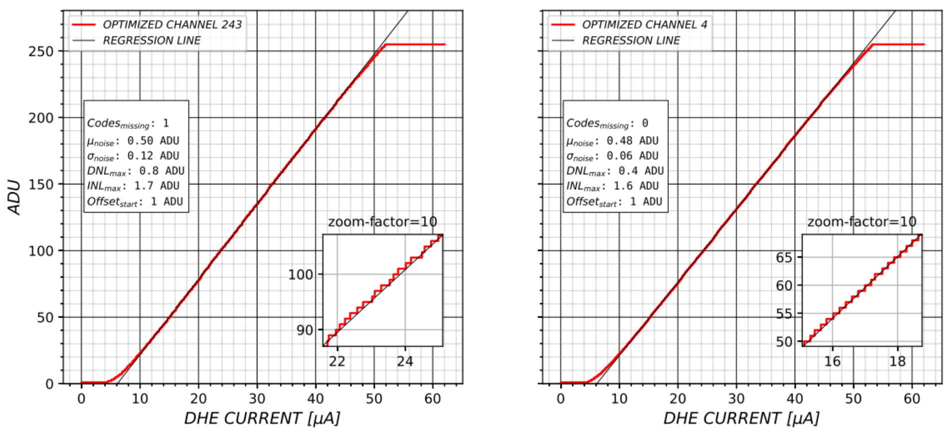

Figure B - 10: Left: same channel as above after optimization. Right: channel 4 remains by and large unaffected by the optimization procedure.

The final result from the whole optimization procedure can be studied in Figure B - 11. As one can see, missing codes were significantly reduced, as well as all other criteria were positively affected.

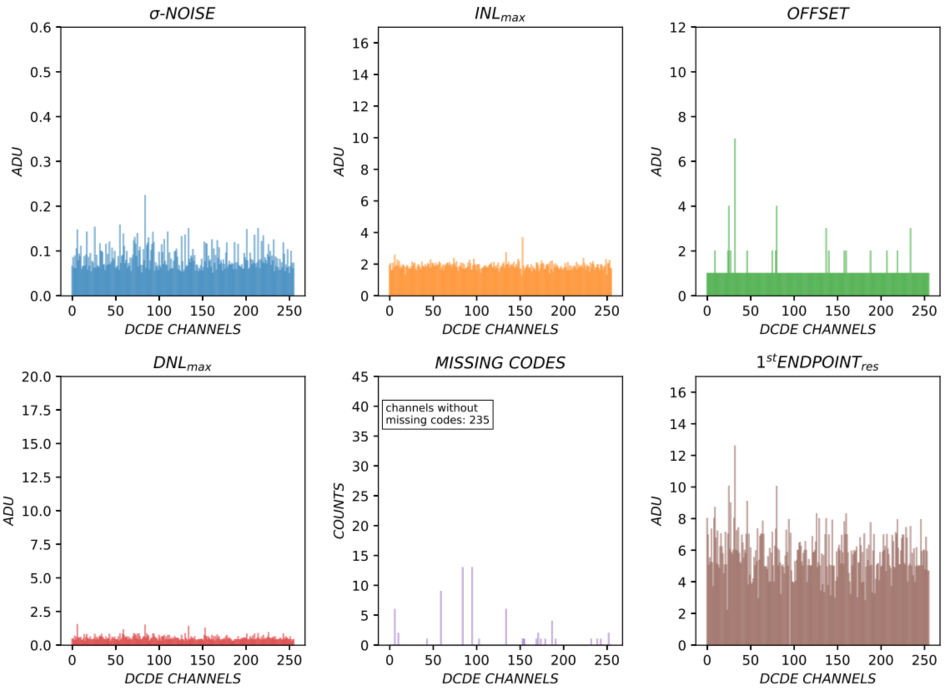

Figure B - 11: Result of all 256 DCDE transfer curves on 6 performance criteria after optimization. All criteria show significantly improved results.

B.3 Sampling Point Analysis

The readout of one electrical row comprises exact 32 clock cycles. Contingent on the selected clock frequency, this period takes either 104.95 or 128 ns.[1] The sampling interval covers exact 8 clock cycles. In the meantime, the raw drain current charges a current memory cell (a capacitor is used as the memory element [119] and a transconductor converts the voltage into a current). A system of pipelined comparators finally converts the current into an ADU output value. The start of the sampling period can be switched by changing the phase of the Switcher signals.

To ensure that the sampling period does not take place during the clear cycle, a laser or LED illuminated the sensor while the Switcher phases (32 clock cycles) were shifted successively bit by bit. The resulting net charge allows for an exact determination of the Switcher phases which must be avoided, as shown in Figure B - 12.

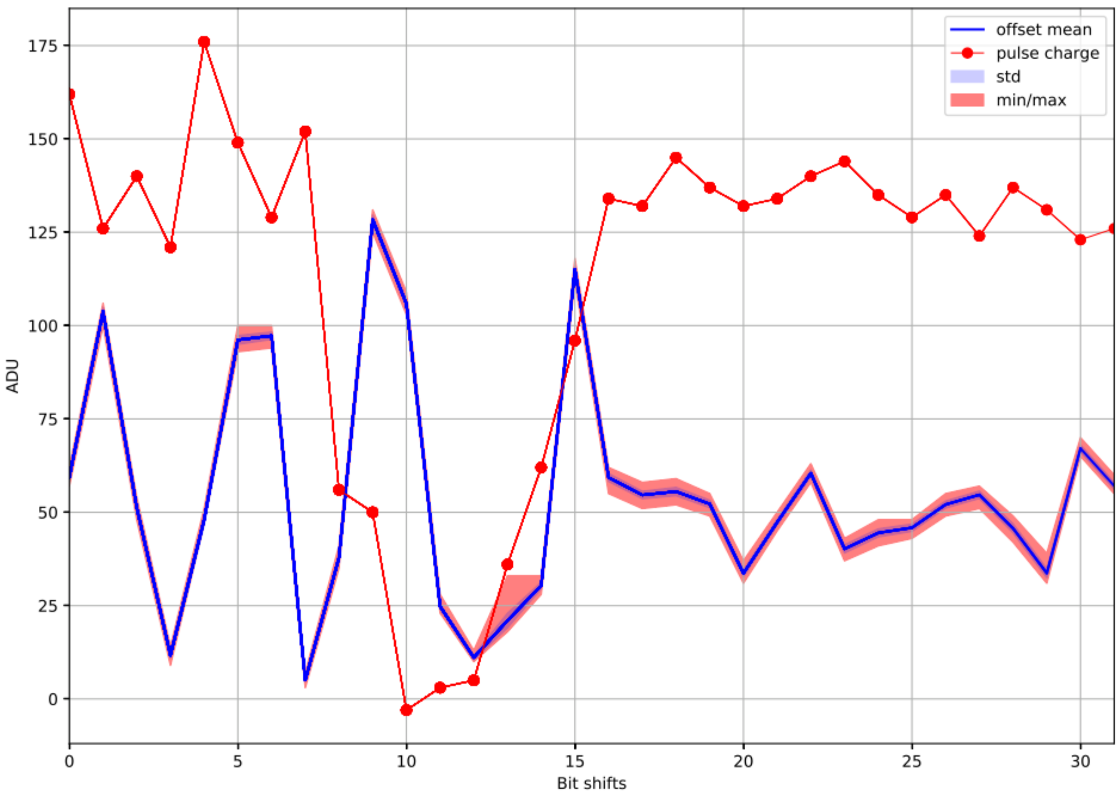

Figure B - 12: Sampling point scan on a specific EDET pixel using a 3.3 DCDE gain. The Switcher phases 8 to 15 should be avoided, since parts or the total charge would be cleared away (red line connecting charge data points). The plot also shows the mean (dark blue), standard deviation (light blue) and the minimum and maximum values (light red) for 30 recorded frames. Of special note are the strong changes of the DC level, especially during the clear and gate on period. However, the deviations are relatively small within a narrow band.

[1] 102.4 ns, if using the actual XU1 board clock frequency.

B.4 Offset Compression

The 2-bit DCDE register I_{DAC} enables the injection of a configurable extra current *IPDAC* to the drain current before it flows to the transimpedance amplifier. The objective behind, attempts to narrow the offset distribution by adding an additional current to each pixel individually. Depending on the pixel's relative position within the dynamic range, it gets 0, 1, 2 or 3 times of the *IPDAC* current to narrow down the distribution as shown on the left diagram of Figure B - 13. The elevated, compressed offset values must be usually restored to the dynamic range with help of the global current sink *VnSubIn* (with a potential of up to 200 µA).[1] The offset correction values are stored pixel for pixel within the DHP/DMC memory.

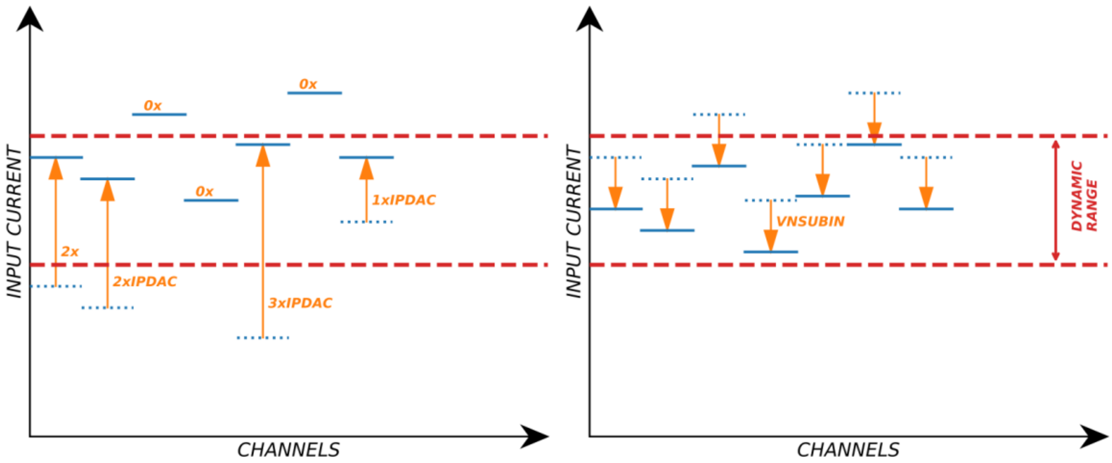

Figure B - 13: Left: The individual pixel ADUs are compressed with help of the 2-bit DAC register I_{DAC}. Right: The global current sink VnSubIn compensates the raised pixel currents back into the dynamic range of the DCDE.

For the determination of the correct I_{DAC} values, a relative simple approach was implemented. As shown in Figure B - 14, the overall ADU-span of the offset distribution is sectioned into quartiles: the quarter with the lowest pixel values gets an $I_{DAC} = 3$, the second lowest quarter gets 2 and so on. This method implicitly assumes, that the I_{DAC} and *IPDAC* values are equally distant (which is not the case by contemplating Figure B - 15). A more sophisticated approach can be found in [129].

[1] The smaller and more precise current source *VpAddIn* is used for the fine-tuning.

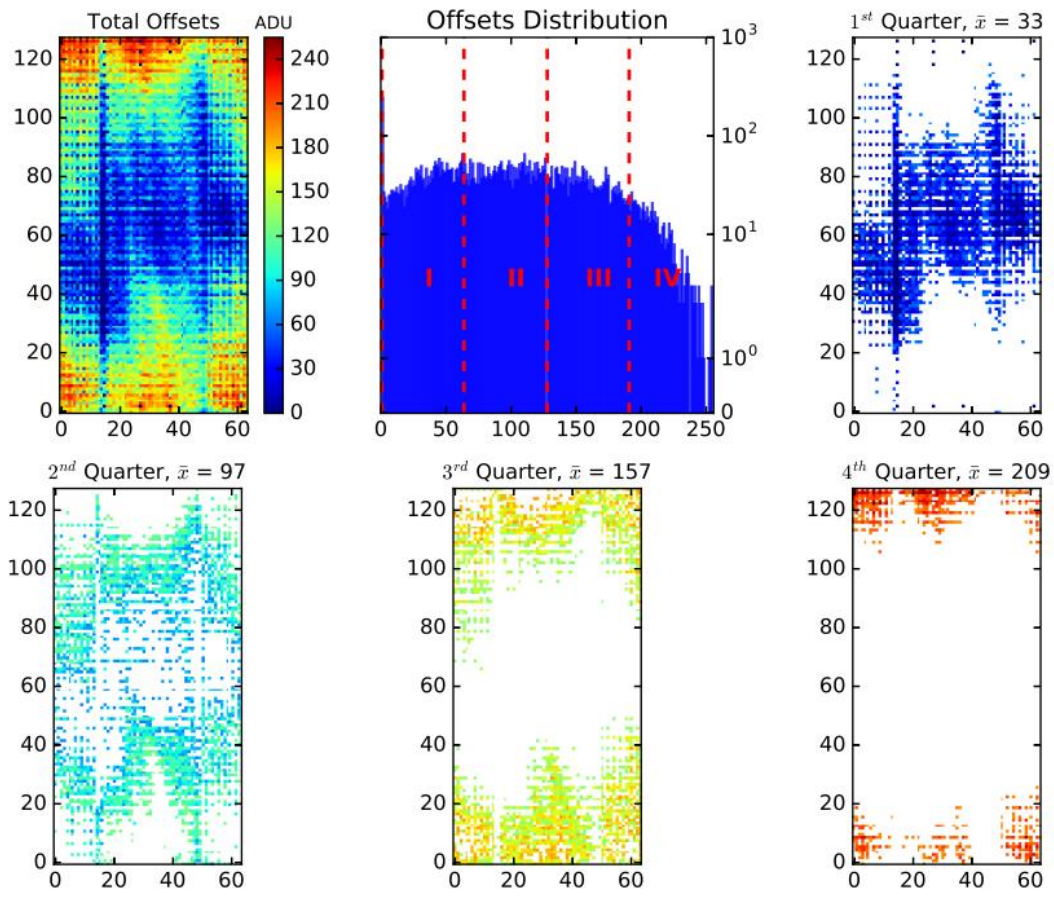

Figure B - 14: Segregation of the offset distribution into 4 same ADU-length sections. The lowest quarter gets an additional current injection of three times of the global current source IPDAC. The fourth quarter with its mean already at 209 ADU gets no extra current.

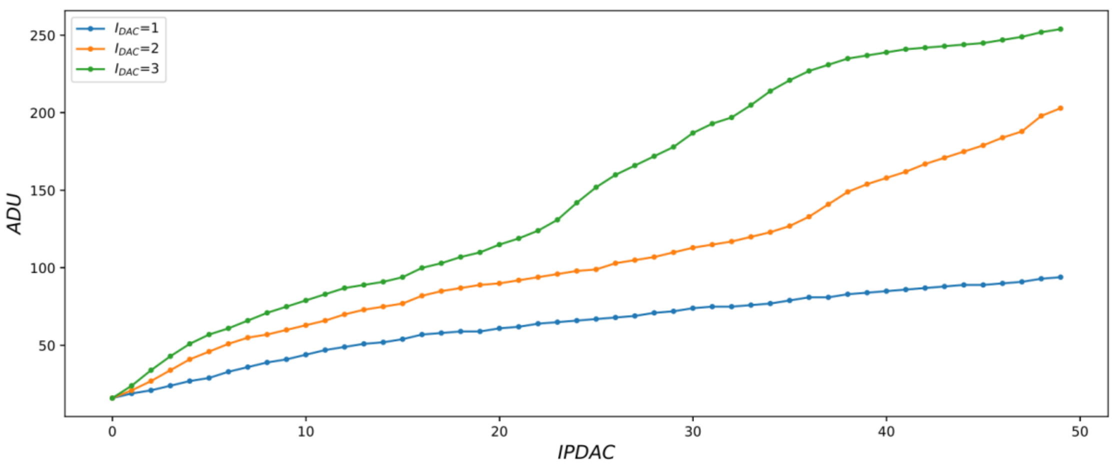

Figure B - 15: Stepwise increase of IPDAC for the I_{DAC} settings 1,2 and 3 (DCDE Gain 1.7). Ideally, the curves would resemble to straight lines, diverging only in their slopes by the aforementioned factors.

The I_{DAC} data is transferred from the DHP/DMC memory by means of a 32 stages deep deserializer chain [119] for each of the 8 ADC channel pairs within the DCDE. Similar to the delay settings for the clock and the synchronization signal between DHP/DMC and DCDE, a correct delay scan must be performed. The average *IPDAC* current steps amount to about ≈ 2 µA. Comparing this number to the spread of a typical offset distribution of about 30 µA one easily calculates, that this step increases were chosen too strong, since already with an I_{DAC} of 3 and an *IPDAC* of 5, the lowest pixel ADU would jump to the other end of the distribution. This way, the full range of the 7-bit IPDAC will never be utilized and the benefit of this operation is significantly reduced. Nevertheless, a remarkable reduction of the offset spread can be achieved as can be observed in Figure B - 16.

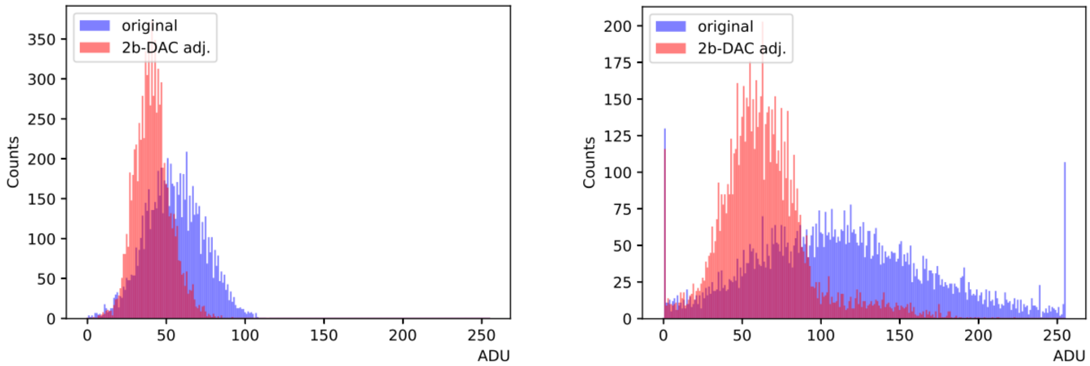

Figure B - 16: Offset compression for different DCDE gain settings: Gain 3.3 (left) and Gain 33.0 (right).

APPENDIX C Gaussian Beam Properties

In the process of focusing/defocusing, the beam radius changes its size. If the beam radius is sufficiently close to the z-axis but far from the origin, a so-called paraxial approximation can be applied. A wave propagation is considered to be paraxial, if the spherical wave resembles a planar wave which is approximately the case at a distance far from the origin so that $\sqrt{\rho^2} = \sqrt{x^2 + y^2} \ll z$. Only rays sufficiently close to the optical axis of the system are considered. The Gaussian beam is an important solution of the paraxial approximation.[1] Gaussian beams keep their properties with exception to their evolving parameters [140]:

- The intensity distribution in any transverse plane is a circularly symmetric Gaussian function centered around the beam axis.
- The width of this function has a minimum value at the beam waist and gradually expands in both directions.
- The wavefronts are approximately planar near the beam waist and undergo a modification to spherical far from the beam waist.

The complex amplitude $U(\boldsymbol{r})$ of a Gaussian beam is [140]:

Equation C - 1
$$U(\boldsymbol{r}) = A_0 \frac{w_o}{w(z)} e^{-\frac{\rho^2}{w^2(z)}} e^{-jkz - jk\frac{\rho^2}{2R(z)} + j\zeta(z)}$$

A_0 is a constant, $w(z)$ is a measure of the beam width, $R(z) = z[1 + (z_0/z)^2]$ an expression for the wavefront radius of curvature and $\zeta(z) = \tan^{-1} z/z_0$. $w(z)$ assumes its minimum value at $z = 0$ at the beam waist, which is denoted by $w_0 = \sqrt{\lambda z_0/\pi}$.

Another figure of merit, referred to as the Rayleigh range[2] z_0, characterizes the distance where the area of the beam spot is twice as large as the corresponding area at the waist position. Under a different perspective one can also say, that z_0 addresses a range where the beam does not diverge significantly.

Equation C - 2
$$z_0 = \frac{\pi w_0^2}{\lambda}$$

With that two parameters, one can calculate the beam radius $w(z)$ and the distance z from waist at z_0 according to the following formula:

Equation C - 3
$$w(z) = w_0 \sqrt{1 + \left(\frac{z}{z_0}\right)^2}$$

The beam width is by a factor of $\sqrt{2}$ larger than the width at the beam waist. The optical intensity $I(\boldsymbol{r}) = |U(\boldsymbol{r})|^2$ is a function of the axial positions z and ρ:

[1] Helmholtz equation.

[2] Also called depth-of-focus or confocal parameter if taken in both directions from the focused position.

Equation C - 4
$$I(\rho,z) = I_0 \left[\frac{w_0}{w(z)}\right]^2 e^{-\frac{2\rho^2}{w^2(z)}}$$

The integration of the optical intensity over any transverse plane yields the total optical power:

Equation C - 5
$$P = \int_0^\infty I(\rho,z) 2\pi\rho d\rho = \frac{1}{2} I_0 (\pi w_0^2)$$

which is independent of z and half the peak intensity multiplied by the beam area. If I_0 is expressed in terms of P, Equation C - 4 can be rewritten as:

Equation C - 6
$$I(\rho,z) = \frac{2P}{\pi w^2(z)} e^{-\frac{2\rho^2}{w^2(z)}}$$

On the beam axis at the location $z = z_0$ the exponent is 0 and the intensity declines to half of the peak intensity. At a radial distance of $\rho = w(z)$ the intensity drops to $1/e^2$ compared to its peak value on the beam axis, hence it transmits ≈86.5% of the total power within a circle of radius $w(z)$. At 1.5 $w(z)$ and 2 $w(z)$ the intensities tumble to $1/e^{4.5} \approx 1.1\%$ and $1/e^8 \approx 0.03\%$ respectively.

The beam half-angle divergence θ_0 is defined by

Equation C - 7
$$\theta_0 = \frac{w_0}{z_0} = \frac{\lambda}{\pi w_0}$$

Hence, the divergence angle is directly proportional to the wavelength and indirect proportional to the beam's waist. A Gaussian beam characterizes an ideal situation which only can approximately been met.

According to ISO Standard 11146 the so called beam propagation factor M^2 measures the quality of an optical beam by its profile deviation from a Gaussian form (angular divergence).

Equation C - 8
$$M^2 = \frac{w_0\theta_0}{\lambda/\pi}$$

APPENDIX D Cd-109 Source Geometry

A realistic simulation of the modulation transfer function implies, that the main influencing parameters (especially the source geometry, the geometry of the experimental set-up and the interaction with matter) are well understood. To minimize self-attenuation, the used ^{109}Cd source was electroplated at a thickness of just 10.5 nanometers on a 0.127 mm silver foil.[1] The top side was backed up by a second foil. The disk diameter of the embodied sandwich structure is 6.35 mm. To protect the source and the user, the radioactive substance was sealed into a stainless steel capsule with a tungsten plug to the closed side and a beryllium window to the capsule's opening with a diameter of 5.08 mm. The 1.02 mm thick beryllium window serves as a filter to prevent electrons from escaping.

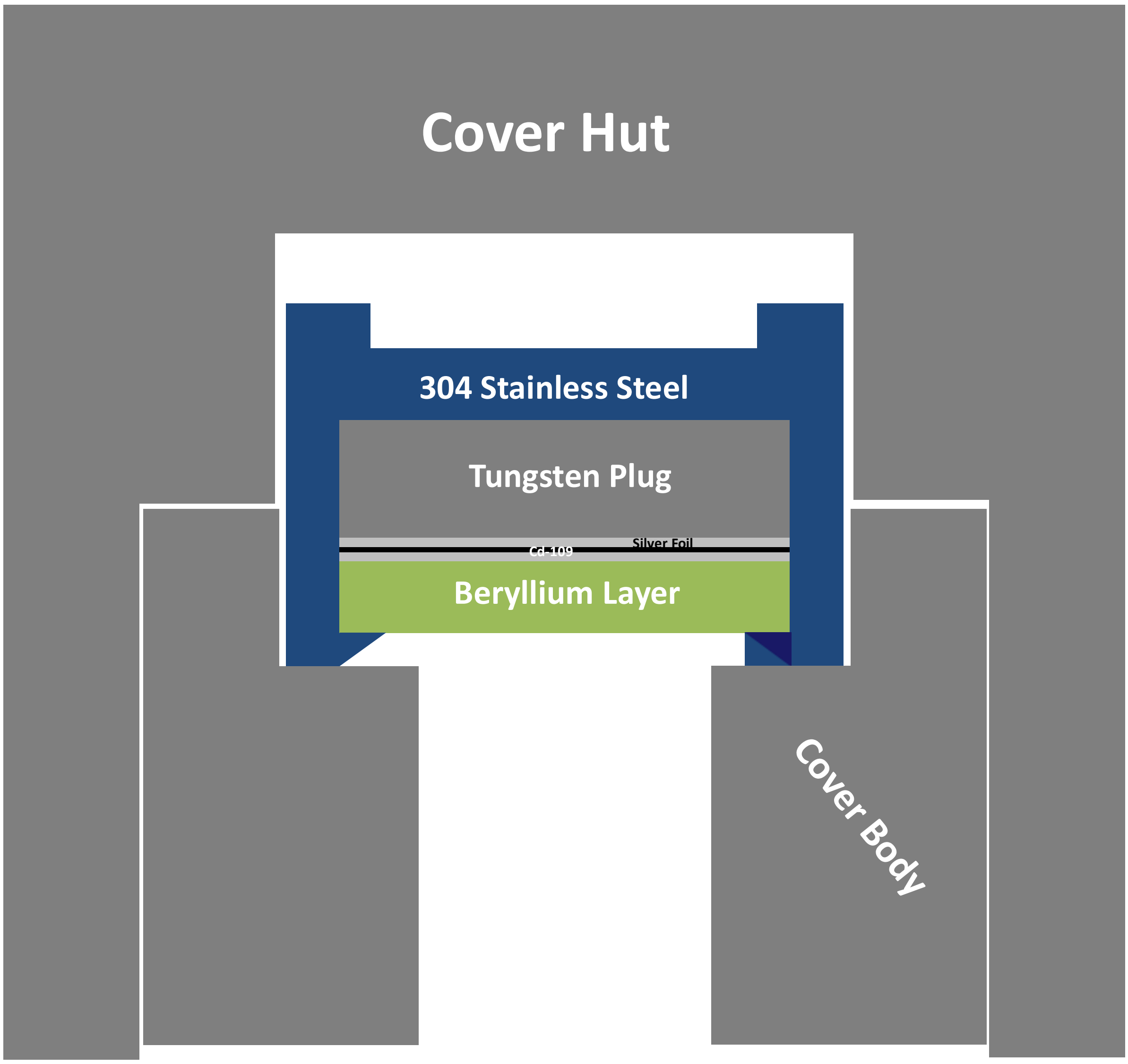

Figure D - 1: Capsule with a ^{109}Cd sealed source embedded in a protective tungsten holder with collimator.

As shown in Figure D - 1 the capsule itself is embedded into a source holder, made from tungsten, consisting of a screw-on type cover hut and a cover body. The walls of the tungsten holder are at least 3 mm thick. The collimator pipe extends the source – opening distance of 7.1 mm. The pure pipe length is 5.3 mm and the pipe's diameter amounts to 4.3 mm.

For a point Q lying on the axis of a thin disk-shaped radioactive source an analytical solution exists. As shown in Figure D - 2 the radioactive disk can be fragmented into infinitesimal rings with a thickness of dr' and a circumference of $2r'\pi$.

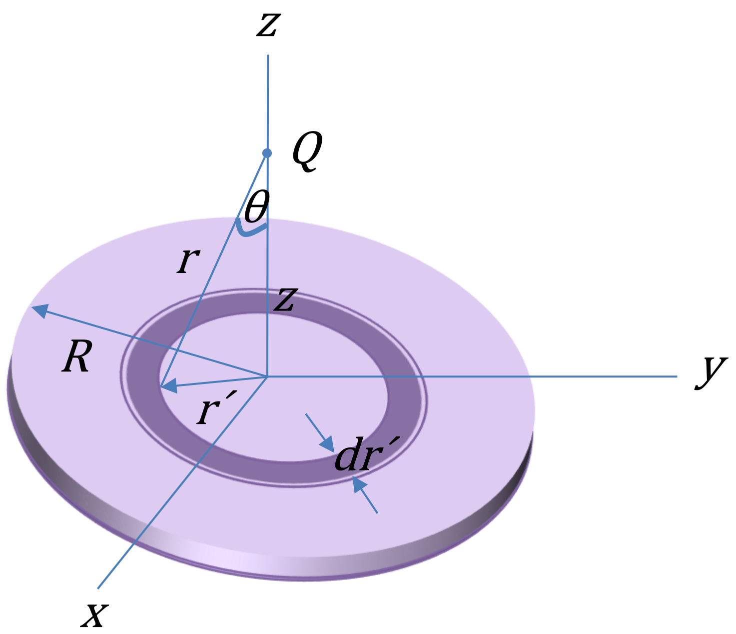

Figure D - 2: Schematics of radioactive disk source's exposure on point Q

The intensity decreases according to the inverse square law, hence the intensity I_Q at point Q is given by:

Equation D - 1
$$I_Q = a \cdot 2\pi \int_0^R \frac{r'dr'}{(r'^2 + z^2)} = a \cdot \pi \cdot ln\left(\frac{R^2 + z^2}{z^2}\right)$$

with $a = A/R^2\pi$ denoting the activity per disk area. Note some similarities to Coulomb's law, although Coulomb's law calculates the force between two point charges leading to a different, indefinite integral. At a distance 4 times the source diameter, the deviation from a point source is well below 1% (0.77%). However, for off-axis points there is no analytical solution and the source intensity has to be determined numerically. Again, the source can be decomposed into small rings. Since the disk features circular symmetry, it is sufficient to calculate just one line from an arbitrary chosen off-axis point to the center axis of the disk in a parallel plane with distance z. The geometry is presented in Figure D - 3.

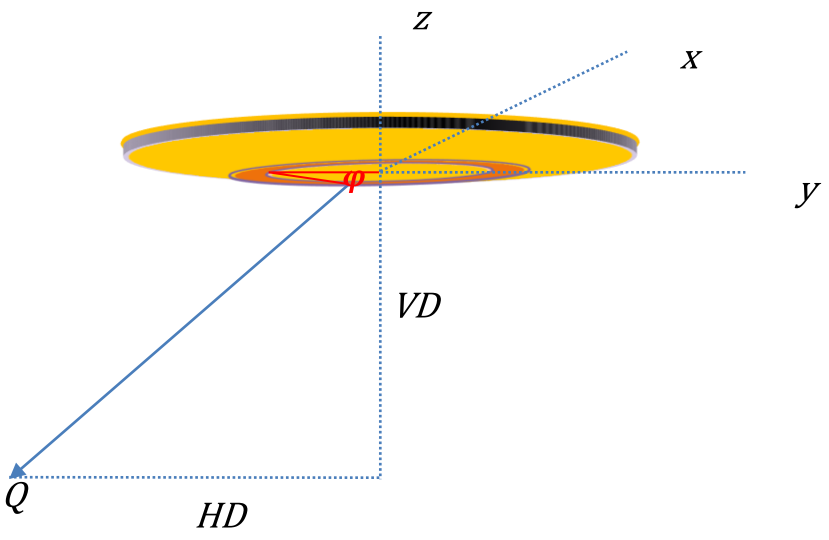

Figure D - 3: Schematics for the off-axis source intensity determination. The radioactive source's disk geometry is decomposed into small rings of thickness d. *The rings themselves are decomposed into small segments* dq. *φ measures the angle between the intensity line projected onto the disk and the small ring segment.* HD *marks the horizontal distance from the perpendicular axis of the plane to the center of the disk.* VD *describes the vertical distance from the measurement plane to the parallel disk plane.*

Without any barrier, the intensity for a specific point Q along the intensity line can be calculated according to the following equation:

Equation D - 2

$$I(Q) = \sum_{r_{i=1}}^{R} \left(2 \cdot \frac{r_i}{r_i - r_{i-1}} - 1\right) \sum_{j=0}^{2\pi} w \cdot \frac{1}{\left(VD^2 + \left(\overline{HD} - r_i \cdot \cos^2 \varphi_j\right) + \left(r_i \cdot \sin^2 \varphi_j\right)\right.}$$

The total disk radius is separated into m equally spaced small rings over an interval of $[R/m\,, R]$. The most inner circle is split up into n evenly spaced angle segments over an interval of $[0, 2\pi]$. To keep the angle segment area constant, the total number of angle sections has to be increased by an expression inserted before the second summation sign in Equation D - 2. Since this expression contains an arithmetic progression of odd numbers the general weight factor is $w = 1/(m^2 \cdot n)$.

Until now, the capsule and the tungsten holder geometry have not been taken into account. As shown in Figure D - 4, depending on the position of the charge point Q along the charge line, more or less charge is shielded off.

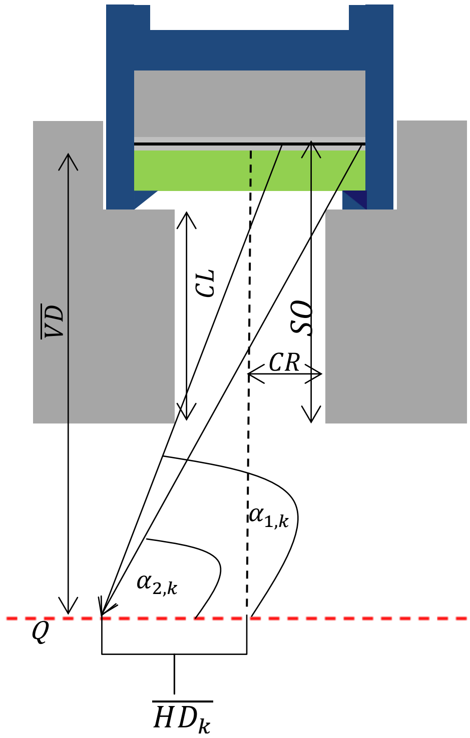

Figure D - 4: [109]Cd source geometry for charge collection points outside the collimator area. CR denotes the collimator radius of 2.15 mm, CL the collimator length until the first edge serving as the fundament for the cadmium capsule and SO the source to the collimator's opening distance. α_1, α_2 span the angle for the part of the disk area contributing to the charge point Q. The non-contributing part must be considered by a correction factor to Equation D - 2.

The minimum angle to register any charge is

Equation D - 3
$$\alpha_{min} = \tan^{-1}\left(\frac{SO}{R_{disk} + CR}\right)$$

As a logical consequence, a selected charge point $\overline{VD}/\tan\alpha > \overline{HD} + R_{disk}$ belongs to the inactive shadow area.

The charge line is likewise segmented into equally spaced l sections over an interval of $[\overline{HD}, 0]$. If $Q_k = \overline{HD} - \overline{HD_k}$, $k \in [0, l]$ lies outside the collimator area, the formulas for the two angles spanning the contributing area are

Equation D - 4
$$\alpha_{1,k} = \tan^{-1}\left(\frac{\overline{VD} - SO}{\max(Q_k - CR,\ 0.00001)}\right)$$

The maximum in the denominator should avoid an undesired division by 0.

Equation D - 5
$$\alpha_{2,k} = \tan^{-1}\left(\frac{\overline{VD} - SO + CL}{Q_k + CR}\right)$$

The next step determines the sagitta (height) of the circular segment area which is not contributing to the charge point because of shielding geometries:

Equation D - 6
$$h_{1,k} = R_{disk} - CR + \frac{SO}{\tan \alpha_{1,k}}$$

Equation D - 7
$$h_{2,k} = max\left(0, \quad R_{disk} - CR - \frac{SO - CL}{\tan \alpha_{2,k}}\right)$$

To determine the size of the shielded disk area, an intermediary step calculates the opening angle of the corresponding circle segment:

Equation D - 8
$$\theta_{1/2,k} = 2 \cdot \cos^{-1}(1 - h_{1/2,k}/R_{disk})$$

The shielded circular segment areas are then calculated by Equation D - 9, normalized by the total area of the radiative disk to get the correction factors:

Equation D - 9
$$corr_{1/2,k} = \frac{\frac{R_{disk}^2}{2} \cdot (\theta_{1/2,k} - \sin \theta_{1/2,k})}{R_{disk}^2 \pi}$$

The total correction factor is $corr_k = 1 - corr_{1,k} - corr_{2,k}$ which has to be multiplied to Equation D - 2.

If Q_k lies within the collimator area, Equation D - 4 has to be slightly adjusted

Equation D - 10
$$\alpha_{1,k} = \tan^{-1}\left(\frac{\overline{VD} - SO + CL}{CR - Q_k}\right)$$

The comparison with a real measurement is presented in Figure D - 5. Except for the different pixel gains, the simulated data produces an intensity ring structure with similar shades. At this point, it is easy to simulate different source sensor distances and integrate additional geometrical barriers like especially a knife edge.

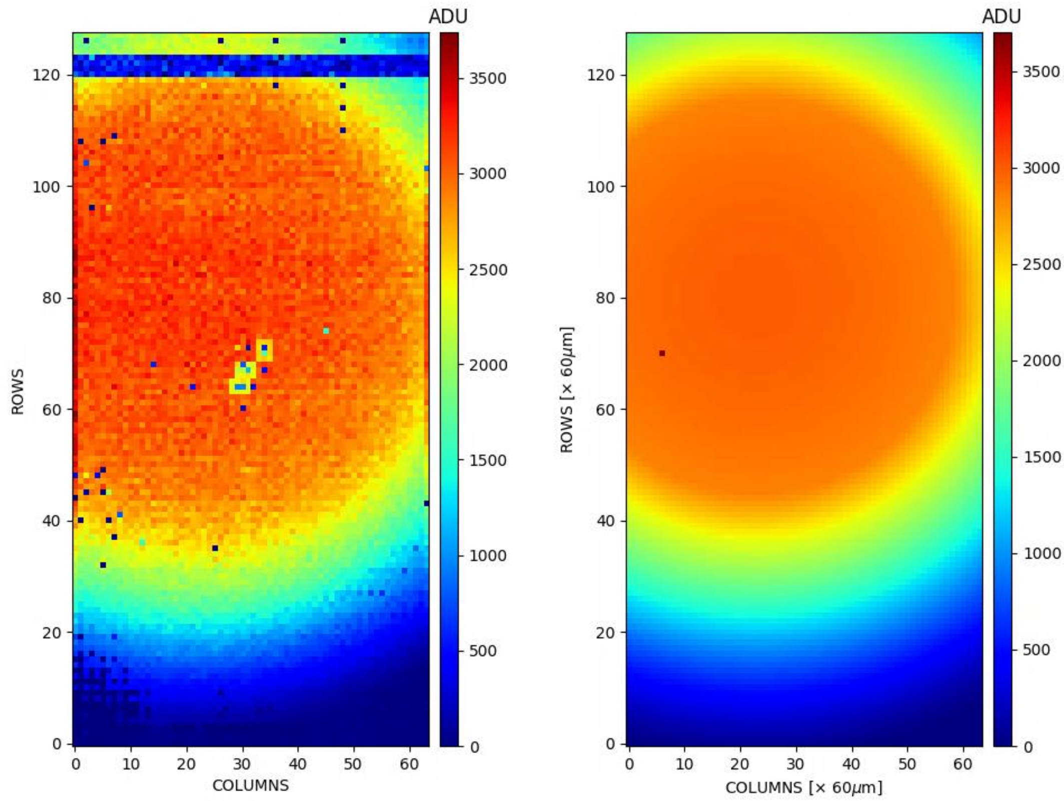

Figure D - 5: Comparison of ^{109}Cd source intensities: real data (left, including a broken Switcher line on top) and simulated data (right). Except for the different pixel gains, the simulated data reproduces quite well the real data.

APPENDIX E Diffraction

Light as a macroscopic figure can be well described by the Maxwell equations. It obeys the rules of electromagnetic radiation (Planck, Wien, Boltzman and Kirchhoff laws). If striking an edge, the wave nature of light causes it to spread out as it propagates (diffraction). The Huygens principle considers every point on a wave front as a source of spherical wavelets. The secondary wavelets, emitted from different points mutually interfere to produce the travelling wave.

The same principles are also applicable to single photons, the elementary quantum mechanical particles of light with mass zero and to mass particles like electrons. The dual nature is apparent: Compton scattering and the photoelectric effect confirm the particle nature of photons and electrons, while other observations like diffraction, interference and polarization reject it and support their wave characterization. The diffraction pattern from Young's slit experiments (and later for electrons by Davisson and Germer [203]) clearly prove, that photons can be mathematically treated as a composition of isotropic point sources with equal amplitude and spacing, in professional terminology as a linear **antenna array** [204].

Even though the receiver (R) in Figure E - 1 is located in the obstructed region of a knife edge (assumed of negligible thickness), it receives the vector sum of the Huygens secondary waves from the imaginary plane (P) above the knife edge.

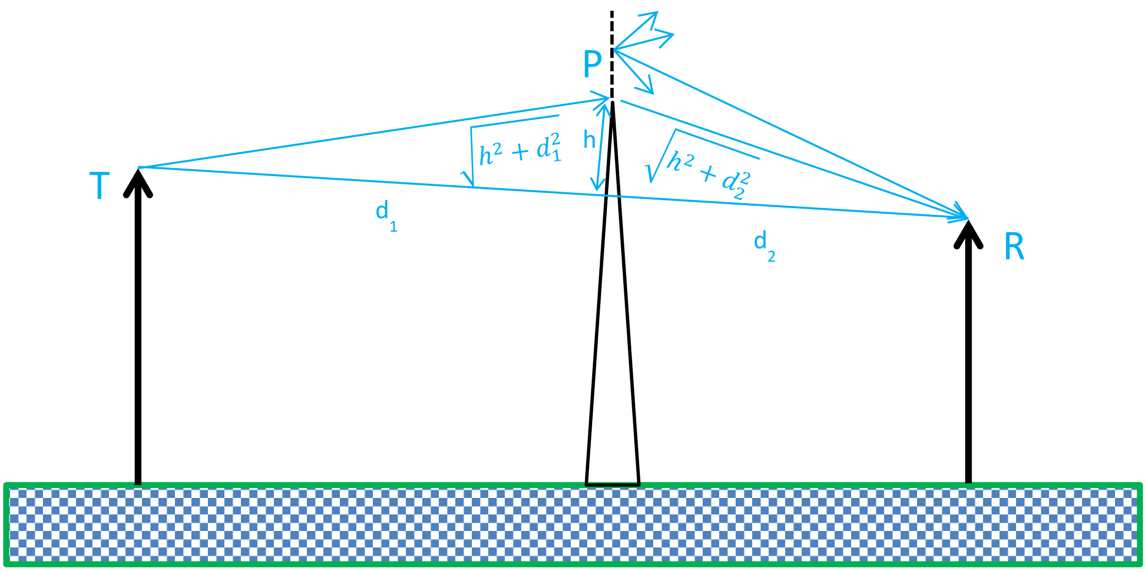

Figure E - 1: Line-of-Sight (LOS): diffraction allows X-rays to propagate behind obstructions where there is no line-of-sight. LOS refers to the direct path $d_1 + d_2$ from the transmitter (T) to the receiver (R).

The shortest distance between the transmitter (T) and the receiver is called the line-of-sight (LOS) which is blocked by the knife edge at a distance d_1, the length from the obstacle to the receiver is denoted by d_2. The contribution to the total field from the first wavelet at the tip of the knife edge can be calculated as follows [205] :[1]

the excess path length is:

Equation E - 1

$$\Delta = \sqrt{d_1^2 + h^2} + \sqrt{d_2^2 + h^2} - (d_1 + d_2) \approx \frac{h^2}{2}\frac{(d_1 + d_2)}{d_1 d_2}$$

The approximation uses a Taylor expansion $\sqrt{1+x^2} \approx 1 + x^2/2$ and is only true for $h \ll d_1, d_2$. From the law of Cosines h can be easily determined:

Equation E - 2

$$b^2 = a^2 + c^2 - 2ac \cdot \cos\beta$$

$$\beta = \cos^{-1}\left(\frac{b^2 - a^2 - c^2}{-2ac}\right)$$

$$h = a \cdot \sin\beta$$

$$h = a \cdot sin\left(\cos^{-1}\left(\frac{b^2 - a^2 - c^2}{-2ac}\right)\right)$$

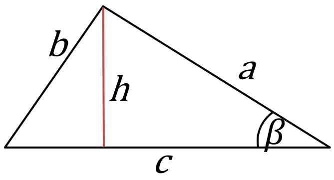

The phase difference, expressed in terms of the wavenumber κ is:[2]

Equation E - 3

$$\phi = \kappa\Delta = \frac{2\pi}{\lambda}\frac{h^2}{2}\frac{(d_1 + d_2)}{d_1 d_2} = \frac{\pi}{2}\nu^2$$

with

Equation E - 4

$$\nu = h\sqrt{\frac{2(d_1 + d_2)}{\lambda d_1 d_2}}$$

the Fresnel-Kirchoff diffraction parameter. Essentially, ν corresponds to the difference between the LOS level and the obstacle height multiplied by a frequency dependent scalar. If the tip of the obstructing knife-edge is above the direct LOS path, ν and h are positive and negative when below. To include all other Huygen sources above the knife edge, their relative intensity contribution has to be integrated from $\nu \ to\ \infty$. The resulting complex Fresnel integral $F(\nu)$ can only be solved numerically.

The diffraction loss $J(\upsilon)$ (dB) depends on the magnitude $|F(\upsilon)|$ of the normalized electric field produced at the receiver relative to the LOS path [206]. The International Telecommunication Union (ITU-R) provides an approximate calculation which is solely dependent on the diffraction parameter υ [207]:

Equation E - 5

$$J(\upsilon) = 6.9 + 20\log\left(\sqrt{(\upsilon - 0.1)^2 + 1} + \upsilon - 0.1\right)$$

$$\upsilon > -0.5\sqrt{2}$$

[1] It is assumed that the polarization of these waves remains unchanged.

[2] The phase difference is also referred to as the electrical length of the path difference.

Alternatively, the following piecewise function approximation for the diffraction loss can be made [208]:[3]

Equation E - 6
$$J(\upsilon) = \begin{cases} 0 : \upsilon < -1 \\ 20\log(0.5 - 0.62\upsilon) : -1 \le \nu \le 0 \\ 20\log(0.5 \cdot e^{-0.95\upsilon} : 0 \le \upsilon \le 1 \\ 20\log(0.4 - \sqrt{0.1184 - (0.38 - 0.1\upsilon)^2} : 1 \le \upsilon \le 2.4 \\ 20\log\left(\frac{0.225}{\upsilon}\right) : \upsilon > 2.4 \end{cases}$$

If the obstruction is very close to the receiver $(d_1 \gg d_2)$:

Equation E - 7
$$\upsilon = h\sqrt{\frac{2(d_1 + d_2)}{\lambda d_1 d_2}} \approx h\sqrt{\frac{2}{\lambda d_2}}$$

Solving when $\nu = -1$:

Equation E - 8
$$h_{cr} = -\sqrt{\frac{\lambda d_2}{2}}$$

delivers the critical obstacle height. The negative value indicates, that the obstruction is below the LOS path and only minimal diffraction effects occur. A value of zero means that the tip of the obstruction, T and R are all in line and the electrical field strength is reduced by one half.

[3] The original diffraction model by William C.Y. Lee can be found in [185].

Glossary

Annealing: wafer annealing is a heating process, that activates ion-implanted dopants, reduces structural defects and stress, and reduces interface charge at the silicon-silicon dioxide interface.

Antenna Array: expression from the radio-communication industry referring to a combination of radiating elements usually identically designed. The electrical fields of different radiators add up linearly in a vector sense to the total far field. The energy distribution of an individual element is different from the far field of an isolated individual element, because of interference. The latter depends on the spacing, geometry and electrical phase of each element in the antenna array. Accordingly, three elements enter into the field equation: an element factor, defining the far field of an isolated single element; a distance factor, representing the free space propagation of the wave and an array factor, modifying the radiation pattern of the isolated element by placing it into an array [209].

Astigmatism: if an electromagnetic lens does not have perfect axial symmetry, a circular image of the electron source deforms to an ellipse image.

Backscattered Electrons (BSE): these electrons are scattered by high angles in such a way, that they even reverse their travel direction. If the surface of a solid object is bombarded by electrons, it emits secondary electrons. Since elements with high atomic numbers backscatter electrons more strongly, this can be used for compositional surface analyses (scanning electron microscopy). However, electrons backscatter also within the silicon substrate or from the detector housing, thereby contributing to the detector noise. Measures like thinning down the silicon substrate (“backthinning”) and equipment of the detector housing with low Z-materials significantly reduce the effect of backscattered electrons on the detector’s performance.

Boundary Scan Chain: method for testing off-chip interconnections based on IEEE Standard 1149.1

Cascode: two-stage amplifier frequently consisting of two transistors.

Chromatic Aberration: an energy spread of the incident electron beam or an energy loss induced by inelastic scattering, when electrons pass through a specimen, cause the electron rays to be focused differently. Thus, a blurred image is produced on the image plane.

CMOS: Complementary Metal-Oxide-Semiconductor, integrating both NMOS and PMOS circuits. Since only one of these transistor types is on at any given time, CMOS chips require significant less power, making them very popular for integrated circuits.

Common Mode: the common mode noise represents a row-wise correlated pulse height variation of the DEPFET Matrix, originating from low-frequency baseline fluctuations (e.g. RF pickup in the matrix, readout chip or PCB as well as variations of the supply voltages) [210]. The common mode correction for the DHPT’s zero suppression mode is described in [120].

Crosstalk: in electronics, crosstalk (XT) is a disturbance caused by the electric or magnetic fields of one circuit or channel, creating an undesired effect in an adjacent circuit or channel (electromagnetic interference).

DAC settings: Digital-to-Analog Converters convert digital data to an analog signal. The DCDE has 25 current-mode DACs (7-bits each) that generate bias currents (turned into voltages via resistors or diode connected transistors) for the analog channels. The DAC bits are stored in a JTAG accessible global configuration register.

Depletion Zone: if p-type and n-type doped silicon is brought together, the mobile charge carriers (electrons and holes) diffuse away, leaving back a depletion region with ionized donor or acceptor impurities. In the equilibrium state, the generated electrical field across the p-n-junction prevents holes and electrons to drift to the n-region and p-region respectively. The extension of the depletion region depends on the corresponding doping concentration between n-type and p-type semiconductors. If the p-type material (anode) of the p-n-junction is forward biased (positive voltage) the electrical field gets smaller.

Electron Capture: a parent nucleus may capture one of its own electrons, thereby changing a nuclear proton to a neutron and simultaneously emitting an electron neutrino.

Enclosed (design) Transistors: standard CMOS processes use p-type substrate wafers. Strong irradiation may lead to bulk and surface damages and provoke short circuits in the design. The effect is strongly pronounced under thick oxide regions, where leakage currents appear close to the interface. Especially nMOS transistors with a classical rectangular form suffer from shallow surface channels, if they are separated only by lightly doped p-type silicon. Moreover, the charge accumulated at the ends of polysilicon gates may prevent them to be switched off completely. This is, why the use of enclosed NMOS transistor gates (“enclosed” means a circular design of the polysilicon gate) and p-type guard-rings of increased doping were introduced, especially for high energy physics experiments [211].

Field of View: denotes the solid angle through which a camera is sensitive to electromagnetic radiation.

Finite State Machine: describes an abstract computation model. The actual condition represents exactly one of a finite number of states. The change to another state is called a transition. The JTAG standard uses a finite machine of 16 states controlled by TCK and TMS.

Infiniband Cable: Infiniband is a computer-networking communications standard. It currently provides the fastest transfer rates available for copper cables.

JTAG: the Joint Test Action Group originally developed the standard IEEE 1149.1 for testing finished printed circuit boards after manufacture. Nowadays, JTAG protocols allow the programming, debugging and testing of integrated circuits, processors and FPGAs.

LVDS Cable: twisted pair copper cable, consuming low power and running at high speeds using a specific technical standard, that specifies the electrical characteristics of a differential, serial communications protocol.

Multiflash: (by Gus Kayafas) "In 1949, Edgerton brought his strobes and other equipment to Longwood Cricket (and Tennis) Club to photograph the touring tennis stars. He was given a few minutes with each in an anteroom before they went out for their matches. The outstanding American tennis player, Gussie Moran tosses the ball into a perfect parabola for a power serve. Moran was especially well-known for her sense of fashion style and her outfits - she refused to wear Doc's black kimona, used to reduce overexposure on the body. In typical inventive reaction, he determined that he would photograph action outside of her brilliantly white clad body. In so many of Edgerton's best photographs, what seems like a perfect balance and form was a product of anticipation, timing, and much effort. Edgerton's ability to reveal the surprise of content with beautiful form that allowed the viewer to discover more than simple visceral pleasure. This image came from a remarkable group made at Longwood including Gonzales and Kramer. LIFE published many of them.

***The multiflash is** simply a strobe firing in rapid succession, either timed electronically in regular intervals or released in manually timed, slower, or irregular intervals. Problems to contend with range from the potential melting or explosion of the flashtube from overheating to the variation in the range of illumination of the areas that receive many flashes of exposure (such as a background or relatively stationary body) or merely one flash (such as a ball or arm). The flash must also be able to recycle quickly enough. Synchronization is also more complex because the flash must end at the appropriate moment as well as begin at the right time. Finally, the rate of flashing must be timed to separate or crowd the individual exposures as best suits the image.*

Records of the paths of movement during a period of time shown simultaneously in one frame allow an understanding of motion and the interaction of all the parts. Sometimes the information can be literally evaluated, for example, how the space between images of a tennis racket is greater before the impact and transfer of momentum, than after the impact when the racket slows. Sometimes the insight is less literal, but certainly as clear; for example, in the comparison of the graceful golf swing of a professional as compared to the awkward stroke of a duffer."

Occupancy: defined as the fraction of pixels or channels hit in each triggered event.

Punch-Through: punch-through denotes a short-channel effect (occurring whenever the channel length is of the same order of magnitude as the depletion layer widths) in a MOSFET, where the depletion layers around the drain and source regions merge into a single depletion region. The field underneath the gate can no longer be effectively controlled by the gate, but becomes strongly dependent on the drain–source voltage. Hence, punch-through causes a rapidly increasing parasitic current with increasing drain-source voltage. This effect is undesirable, as it increases the output conductance and limits the maximum operating voltage of the device.

Photopeak: arises when the gamma ray deposits all of its energy in the detector. The most likely interaction is the photoelectric effect, where an incident gamma essentially gives all its energy to eject an inner shell electron from one of the silicon atoms. The ejected electron exhibits a significant kinetic energy which is lost via exciting and ionizing additional silicon atoms.

Printed Circuit Board: thin board made of layers of conductive and non-conductive laminate material. Conductive tracks, pads and other features are etched or “printed” onto the PCB board, connecting different components such as transistors, resistors and integrated circuits.

Radiation Length: mean distance over which a high-energy electrons loses all but $1/e$ of its energy by electromagnetic interaction (bremsstrahlung) or where a high-energy photon loses $7/9$ of the mean free path for pair production. It is measured in $g \cdot cm^{-2}$.

Rolling Shutter: sequential row-wise read out of the EDET matrix.

SMU: the Source Measurement Unit is a power sourcing instrument, that provides voltage, current sourcing and measurement at high precision.

Spherical Aberration: the most important defect of the objective lens. It describes an effect, where rays or electrons away from the optical axis are not focused but slightly shifted from the image plane. As a result, a circular blurred image is produced on the image plane.

Stokes Shift: related to the fluorescence process, addressing the energy difference between an absorbed photon of higher energy and the emitted photon of lower energy.

Transimpedance Amplifier: converts the drain current of the EDET matrix to a voltage for the later analog to digital conversion.

Transfer Curve (Transfer Function): relates the input signal to the generated digital output code. The transfer function looks like a staircase, in which each tread represents a particular digital output code and each riser represents a transition between adjacent codes. These transitions are not sharply defined, but resemble a probability function in which the ADC converts more and more frequently to the next higher output code as the input current slowly increases.

Waist: measure of the beam size at focused position, where the beam width is smallest.

Wehnelt Cylinder: shape of a topless, hollow cylinder. Biased to a negative voltage, the Wehnelt cylinder surrounds the tip of a thermionic electron gun. It operates as a convergent electrostatic lens, focusing the electron beam through the bottom hole of the cylinder.

Bibliography

[1] SADROZINSKI, Hartmut, „Particle Detector Applications in Medicine," *Nucl. Instrum. Methods Phys. Res. A, Vol. 732,* 2014.

[2] DOSANJH, Manjit, From Particle Physics to Medical Applications, Bristol: IOP Publishing Ltd., 2017.

[3] YAJNIK, Santosh, Proton Beam Therapy - How Protons are Revolutionizing Cancer Treatment, New York: Springer Science+Business Media, 2013.

[4] NUNES, Marcos d'Avila, Protontherapy versus Carbon Ion Therapy - Advantages, Disadvantages and Similarities, Springer International Publishing Switzerland, 2015.

[5] CLOUGH, R.N. et al., „Direct Detectors for Electron Microscopy," *J. Phys: Conf. Ser. 522 012046,* 2014.

[6] BELLE II COLLABORATION, The PXD Whitebook, Z. Dolezal, C. Kiesling, C. Lacasta & H.G. Moser, Sep 2012.

[7] AMINI, K. and BIEGERT, J., „Ultrafast electron diffraction imaging of gas-phase molecules," 2020.

[8] KING, Wayne E. et al., „Ultrafast electron microscopy in materials science, biology, and chemistry," *J. Appl. Phys. 97,* p. 111101, 04 Feb 2005.

[9] CARTER, C. Barry and WILLIAMS, David B. (Editors), Transmission Electron Microscopy: Diffraction, Imaging, and Spectrometry, Springer International Publishing Switzerland, 2015.

[10] MILO, Ron and PHILLIPS, Rob, Cell Biology by the numbers, Draft, July 2015.

[11] TURKOWYD, Bartosz et al., „From single molecules to life: microscopy at the nanoscale," *Analytical and Bioanalytical Chemistry,* September 2016.

[12] MILLER, Dwayne R.J. et al., „'Making the molecular movie': first frames," in *Foundations of Crystallography, Acta Crystallographica Section A*, Singapore, International Union of Crystallography, 2009.

[13] ROSS, Frances M., „In Situ Transmission Electron Microscopy," in *in: Science of Microscopy, Vol. 1, HAWKES, Peter W. and SPENCE, John C.H. (Ed.)*, Springer, 2007, pp. pp. 445-534.

[14] HEO, Jaeyoung et al., „In-situ electron microscopy mapping of an order-disorder transition in a superionic conductor," *Nature Communications 10:1505,* 2019.

[15] SUN, Ke et al., „The Oxygen Reduction Reaction of Metallic Nanoparticles during Catalyzed Oxidation," *Nature, Scientific Reports, 7:7017,* 2017.

[16] WU, Jianbo et al., „In Situ Environmental TEM in Imaging Gas and Liquid Phase Chemical Reactions for Materials Research," *Advanced Materials No. 28,* pp. pp. 9686-9712, 2016.

[17] TAI, Kaiping et al., „Catalyzed oxidation for nanowire growth," *Nanotechnology, Vol. 25,* 2014.

[18] WOEHL, Taylor J. et al., „Direct in Situ Determination of the Mechanmisms Controlling Nanoparticle Nucleation and Growth," *ACS Nano, Vol. 6, No. 10,* pp. pp. 8599-8610, 2012.

[19] VISWANATHA, R. and SARMA, D.D., „Growth of Nanocrystals in Solution," in *in: Nanomaterials Chemistry: Recent Developments and New Directions; RAO, C.N.R., MÜLLER, A. and CHEETHAM, A.K. (Ed.)*, 2007, pp. pp. 139-168.

[20] WANG, Gang et al., „Colloidal synthesis of Au nanomaterials with a controlled morphology and crystal phase vie [Au(I)-oleylamine] complex," *J. Mater. Chem. A, 9,* pp. pp. 19534-19553, 2021.

[21] N. e. a. THANH, „Mechanisms of Nucleation and Growth of Nanoparticles in Solution," *Chemical Reviews Vol. 114,* pp. pp. 7610-7630, 2014.

[22] JIN, Rongchao et al., „Photoinduced Conversion of Silver Nanospheres to Nanoprisms," *Science, Vol. 294, No. 5548,* pp. pp. 1901-1903, 2001.

[23] AHMADI, TS et al., „Shape-Controlled Synthesis of Colloidal Platinum Nanoparticles," *Science, Vol. 272, No. 5279,* pp. pp. 1924-1925, 1996.

[24] MIRKIN, Chad A. et al., „Plasmon-Mediated Synthesis of Silver Cubes with Unusual Twinning Structures Using Short Wavelenght Excitation," *small, No. 11,* pp. pp.1947-1953, 2013.

[25] SMITH, Lisa, „Wavelength-Dependent Shapeshifting: Plasmon-Mediated Growth Control," *Advanced Science News,* 10 January 2013.

[26] SUTTER, P. et al., „In Situ Electron Microscopy of Plasmon-Mediated Nanocrystal Synthesis," *Journal of the American Chemical Society, Vol. 139,* pp. pp. 6771-6776, 2017.

[27] SCHULTZ, S. et al., „Single-target molecule detection with nonbleaching multicolor optical immunolabels," *Proc. Natl. Acad. Sci. USA, Vol 97,* pp. pp. 996-1001, 2000.

[28] Hu, Bo et al., „Structural remodeling of bacteriophage T4 and host membranes during infection initiation," *PNAS,* pp. pp. E4918-E4928, 2015.

[29] EVANS, James E. et al., „Visualizing macromolecular complexes with in situ liquid scanning transmission electron microscopy,“ *Micron 43,* pp. pp. 1085-1090, 2012.

[30] Z. HAN, „In situ Electron Microscopy of Complex Biological and Nanoscale Systems: Challenges and Opportunities,“ *Frontiers in Nanotechnology, Vol. 2,* Dec 2020.

[31] ROTHEMUND, Paul W.K., „Folding DNA to create nanoscale shapes and patterns,“ *Nature, Vol. 440,* pp. pp.297-302, 2006.

[32] KESKIN, Sercan et al., „Visualization of Multimerization and Self-Assembly of DNA-Functionalized Gold Nanoparticles Using In-Liquid Transmission Electron Microscopy,“ *J. Phys. Chem. Lett., Vol. 6,* pp. pp. 4487-4492, 2015.

[33] YAO, Guangbao et al., „Gold-Nanoparticle-Mediated Jigsaw-Puzzle-like Assembly of Supersized Plasmonic DNA Origami,“ *Angew. Chem. Int. Ed., Vol. 54,* pp. pp. 2966-2969, 2015.

[34] HOPPE, Sarah M. et al., „In-Situ Transmission Electron Microscopy of Liposomes in an Aqueous Environment,“ *Langmuir Vol. 29,* pp. pp. 9958-9961, 2013.

[35] SCHNEIDER, Nicholas M. et al., „Electron-Water Interactions and Implications for Liquid Cell Electron Microscopy,“ *J. Phys. Chem. C. ,Vol. 118, No. 38,* pp. pp. 22373-22382, 2014.

[36] DE JONGE, Niels et al., „Live Cell Electron Microscopy Is Probably Impossible,“ *ACS Nano Vol. 10,* pp. pp. 9061-9063, 2016.

[37] ROTTENFUSSER, Rudi et al., „Numerical Aperture and Resolution,“ ZEISS, [Online]. Available: https://www.zeiss.com/microscopy/int/solutions/reference/basic-microscopy/numerical-aperture-and-resolution.html. [Zugriff am 23 06 2021].

[38] DAVIDSON, Michael W., „Microscopy - The Source for Microscopy Education: Resolution,“ Nikon, [Online]. Available: https://www.microscopyu.com/microscopy-basics/resolution. [Zugriff am 23 June 2021].

[39] KISIELOWSKI, C. et al., „Detection of Single Atoms and Buried Defects in Three Dimensions by Aberration-Corrected Electron Microscope with 0.5-A° Information Limit,“ *Micros. Microanal. 14,* pp. 469-477, 2008.

[40] LUO, Zhiping, A Practical Guide to Transmission Electron Microscopy, Vol I+II, New York: Momentum Press, 2016.

[41] EGERTON, Ray F., Physical Principles of Electron Microscopy, An Introduction to TEM, SEM and AEM, Springer Science+Business Media Inc., 2005.

[42] REIMER, Ludwig and KOHL, Helmut, Transmission Electron Microscopy, Physics of Image Formation, 5th Edition, Münster: Springer Science+Business Media LLC, 2008.

[43] HAWKES, Peter W. and SPENCE, John C.H. (Ed.), Springer Handbook of Microscopy, Springer Nature Switzerland, 2019.

[44] WILLIAMS, David B. and CARTER, C. Barry, Transmission Electron Microscopy Part 1: Basics, 2nd Edition, New York: Springer Science+Business Media LLC, 2009.

[45] WATT, Ian, The Principles and Practice of Electron Microscopy, 2nd Edition, Cambridge University Press, 1997.

[46] FLORES-MANCERA, Miguel Angel et al., „Electron Inelastic Mean Free Paths for LiF, CaF2, Al203, and Liquid Water from 433 keV down to the Energy Gap,“ *ACS Omega,* pp. pp. 4139-4147, March 2020.

[47] RING, E.A. et al., „Silicon nitride windows for electron microscopy of whole cells,“ *Journal of Microscopy,* 19 July 2011.

[48] MUELLER, C. et al., „Nanofluidic Cells with Controlled Pathlenght and Liquid Flow for Rapid, High-Resolution In Situ Imaging with Electrons,“ *The Journal of Physical Chemistry Letters, 4,* pp. pp. 2339-2347, June 2013.

[49] VENEGAS-FOJAS, D. et al., „Multi-window Transmission Electron Microscopy liquid cell to improve imaging performance,“ *MikroSystemTechnik Kongress,* pp. pp. 492-495, October 2017.

[50] DE JONGE, Niels et al., „Practical Aspects of Transmission Electron Microscopy in Liquid,“ in *Advances in Imaging and Electron Physics Vol 186*, Elsevier Ltd., 2014, pp. pp. 1-37.

[51] AZIM, Sana et al., „Environmental Liquid Cell Technique for Improved Electron Microscope Imaging of Soft Matter in Solution,“ *Microscopy and Microanalysis Vol. 27,* pp. pp. 44-53, 2021.

[52] McMULLAN, G. et al., „Detective quantum efficiency of electron area detectors in electron microscopy,“ *Ultramicroscopy 109,* pp. pp. 1126-1143, 2009.

[53] HART, James L. et al., „Direct Detection Electron Energy-Loss Spectroscopy: A Method to Push the Limits of Resolution and Sensitivity,“ *Nature, Scientific Reports No.7,* 2017.

[54] TURCHETTA, R. et al., „CMOS Monolithic Active Pixel Sensors (MAPS): Developments and future outlook,“ *Nuclear Instruments and Methods in Physics Research A 582,* pp. pp. 866-870, 2007.

[55] McMULLAN, G. et al., „Direct Electron Detectors,“ in *Methods in Enzymology*, 2016, p. July.

[56] TURCHETTA, R., „CMOS Monolithic Active Pixel Sensors (MAPS) for scientific applications,“ in *LHC Electronics Workshop*, CERN, 2003.

[57] LIANG, Jin et al., „Applications of direct detection device in transmission electron microscopy,“ *Journal of Structural Biology, 161,* pp. pp. 352-358, 2008.

[58] WATANABE, T. et al., „A Radiation-Hardened CMOS Image Sensor With Pixels Exhibiting a Negligibly Small Dark-Level Increase During Ionizing Radiation,“ *IEEE Transactions on Nuclear Science, Vol. 67, No. 8,* pp. pp. 1835-1845, 2020.

[59] HAWKES, Peter W. (Ed.), Advances in Imaging and Electron Physics, Elsevier Inc., 2015.

[60] SCHWANK, Jim, „U.S. Department of Energy, Office of Scientific and Technical Information, Sandia National Laboratories,“ 2007. [Online]. Available: https://www.osti.gov/servlets/purl/1147853. [Zugriff am 29 June 2021].

[61] KUIJPER, Maarten, „FEI's direct electron detector developments: Embarking on a revolution inc cryo-TEM,“ *Journal of Structural Biology 192,* pp. pp. 179-187, 2015.

[62] DIRECT ELECTRON, „www.directelectron.com,“ [Online]. Available: https://www.directelectron.com/products/de-16/. [Zugriff am 28 June 2021].

[63] BARNABY, D.A. Levin, „Direct detectors and their applications in electron microscopy for materials science,“ *Journal of Physics: Materials No. 4,* 2021.

[64] GATAN - AMETEK, „Improving DQE with Counting and Super-Resolution,“ [Online]. Available: https://www.gatan.com/improving-dqe-counting-and-super-resolution. [Zugriff am 25 02 2022].

[65] MIR, J.A. et al., „Characterisation of the Medipix3 detector for 60 and 80 keV electrons,“ *Ultramicroscopy 182,* pp. pp. 44-53, 2017.

[66] BALLABRIGA, Rafael, The Design and Implementation in 0.13 µm CMOS of an Algorithm Permitting Spectroscoping Imaging with High Spatial Resolution for Hybrid Detectors, CERN, 2010.

[67] NGUYEN, Kayla, New imaging capabilities for materials enabled by the electron microscope pixel array detector (EMPAD), Cornell University, 2018.

[68] PLOTKIN-SWING, Benjamin et al., „Hybrid pixel direct detector for electron energy loss spectroscopy,“ *Ultramicroscopy 217,* 2020.

[69] BALLABRIGA, Rafael, „12th International Workshop on Radiation Imaging Detectors," in *Characterization of the Medipix3 pixel readout chip*, Robinson College, Cambridge U.K., 2010.

[70] SCHOLZE, F. et al., Determination of the electron-hole pair creation energy for semiconductors from the spectral responsivity of photodiodes, Nucl. Instr. Meth. Phys. Res. A 439.

[71] ZYLA, P.A. et al., „Passage of particles through matter," Particle Data Group, [Online]. Available: https://pdg.lbl.gov/2021/reviews/contents_sports.html. [Zugriff am 07 2021].

[72] LEROY, Claude and RANCOITA, Pier-Giorgio, Principles of Radiation Interaction in Matter and Detection, 4th Edition, Singapore: World Scientific Publishing Co. Pte. Ltd., 2016.

[73] STERNHEIMER, R.M., „The Density Effect for the Ionization Loss in Various Materials," *Physical Review, Vol. 88, No. 4,* pp. pp. 851-858, Nov 1952.

[74] STERNHEIMER, R.M. et al., „Density Effect for the Ionization Loss of Charged Particles in various Substances," *Atomic Data and Nuclear Data Tables 30,* pp. pp. 261-271, 1984.

[75] STERNHEIMER, R.M. et al., „Density effect for the ionization loss of charged particles in various substances," *Physical Review B, Vol. 26, No. 11,* pp. pp. 6067-6075, Dec 1982.

[76] SELTZER, S.M and BERGER, M.J., „Bremsstrahlung Spectra from Electron Interaction with screened atomic Nuclei and orbital Electrons," *Nuclear Instruments and Methods in Physics Research B12,* pp. pp. 95-134, 1985.

[77] PRATT, H. et. al., „Bremsstrahlung Energy Spectra from Electrons of kinetic Energy 1 keV < T1 < 2000 keV incident on neutral Atoms 2 < Z < 92," *Atomic Data and Nuclear Data Tables 20,* pp. pp. 175-209, 1977.

[78] MCCALL, Gene, „Calculation of X-ray bremsstrahlung and characteristic line emission produced by a Maxwellian electron distribution," *J. Phys. D: Appl. Phys., 15,* pp. pp. 823-831, 1982.

[79] KRAMERS, H.A., „XCIII. On the theory of X-ray absorption and of the continuous X-ray spectrum," *The London, Edinburgh, and Dublin Philosophical Magazine and Journal of Science,* pp. pp. 836-871, 1923.

[80] BERGER, Martin J. and SELTZER, Stephen M., „Tables of Energy Losses and Ranges of Electrons and Positrons," Washington D.C. 1964, NASA-SP-3012.

[81] BOSCHINI, M.J. et al., „Nuclear and non-ionizing Energy-Loss of Electrons with low and relativistic Energies in Materials and space Environment," in *Proceedings*

of the 13th ICATPP Conference on Astroparticle, Particle, Space Physics and Detectors for Physics Applications, Como, Italy, 2011.

[82] LANDAU, L., „On the Energy Loss of Fast Particles by Ionization, J. Phys. U.S.S.R, 19, 77, 1944,“ in *in: Collected Papers of L.D. Landau*, Pergamon Press, 1965, pp. pp. 201-205.

[83] BICHSEL, Hans, „Straggling in thin silicon detectors,“ *Rev. Mod. Phys, Vol. 60, No. 3,* July 1988.

[84] VAVILOV, P.V., „Ionization Losses of High-Energy Heavy Particles,“ *J. Exptl. Theoret. Phys. (U.S.S.R.), 32,* pp. pp. 920-923, April 1957.

[85] LEO, W.R., Techniques for Nuclear and Particle Physics Experiments, A How-to Approach, 2nd Edition, Berlin Heidelberg: Springer-Verlag, 1993.

[86] ROSSI, Bruno, High-Energy Particles, Prentice Hall, 1952.

[87] KÖLBIG, K.S. and SCHORR B., „A Program Package for the Landau Distribution,“ *Computer Physics Communications 31,* pp. pp. 97-111, 1984.

[88] BÖRSCH-SUPAN, Wolfgang;, „On the Evaluation of the Function <Landau distribution> for Real Values of Lambda,“ *Journal of Research of the National Bureau of Standards,* pp. pp. 245-250, 1961, Vol. 65B, No.4.

[89] WILKINSON, D.H., „Ionization energy loss by charged particles Part I. The Landau distribution,“ *Nuclear Instruments and Methods in Physics Research A 383,* pp. pp. 513-515, 1996.

[90] KÖLBIG, K.S. and SCHORR B., „Asymptotic Expansions for the Landau Density and Distribution Functions,“ *Computer Physics Communications 32,* pp. pp. 121-131, 1984.

[91] AHMED, Syed Naeem, Physics and Engineering of Radiation Detection (Second Edition), Ontario: Elsevier, 2015.

[92] SCHORR, B., „Programs for the Landau and the Vavilov Distributions and the corresponding Random Numbers,“ *CERN-Data Handling Divsion,* August 1973.

[93] CHIBANI, Omar, „New Algorithms for the Vavilov Distribution Calculation and the Corresponding Energy Loss Sampling,“ *IEEE Transactions on Nuclear Science, Vol 45, No. 5,* pp. pp. 2288-2292, October 1998.

[94] ROTONDI, Alberto et al., „Fast Calculation of Vavilov Distribution,“ *Nuclear Instruments and Methods in Physics Research, B47,* pp. pp. 215-223, 1990.

[95] TALMAN, Richard, „On the Statistics of Particle Identification using Ionization,“ *Nuclear Instruments and Methods 159 ,* pp. pp. 189-211, 1979.

[96] WILKINSON, D.H., „Ionization energy loss by charged particles, Part II: Effects of atomic structure," *Nuclear Instruments and Methods in Physics Research A, 401,* pp. pp. 263-274, 1997.

[97] HAWKES, SPENCE (Editors), Handbook of Microscopy, Springer Nature Switzerland AG, 2019.

[98] WANG, Zhong Lin, Elastic and Inelastic Scattering in Electron Diffraction and Imaging, New York: Springer Science+Business Media, 1995.

[99] JABLONSKI, A. et al., NIST Electron Elastic-Scattering Cross-Section Database - Version 4.0, Gaithersburg: National Institute of Standards and Technology, 2016.

[100] WALKER, D.W., „Relativistic effects in low energy electron scattering from atoms," *Advances in Physics, 20,,* pp. pp. 257-323, 1971.

[101] DESCLAUX, J.P., „A Multiconfiguration Relativistic Dirac-Fock Program," *Computer Physics Communications 9^,* pp. pp. 31-45, 1975.

[102] INKSON, B.J., „Scanning electron microscopy (SEM) and transmission electron microscopy (TEM) for materials characterization," in *Materials Characterization using Nondestructive Evaluation (NDE)*, Elsevier Ltd., 2016, pp. pp.17-43.

[103] LENZ, Friedrich, „Zur Streuung mittelschneller Elektronen in kleinste Winkel," *Zeitschrift für Naturforschung,* pp. pp. 185-204, 1954.

[104] SANTOS, J.P. et al., „Cross sections for K-shell ionization of atoms by electron impact," *J. Phys. B: Atomic, Molecular and Optical Physics 36,* pp. pp. 4211-4224, 2003.

[105] LLOVET, Xavier et al., „Cross Sections for Inner-Shell Ionization by Electron Impact," U.S: Secretary of Commerce on behalf of the United States, 2014.

[106] BURHOP, E.H.S., „Le Rendement de Fluorescence," *Le Journal de Physique et le Radium,* pp. pp. 625-629, July 1955.

[107] MPI-SD & HLL, „Proposal for development of advanced electron detectors for UED and DTEM," 2013.

[108] MÜLLER, Felix, Characterization and Optimization of the Prototype DEPFET Modules for the Belle II Pixel Vertex Detector, München, 2017.

[109] EL HAGE, Krystel et al., „Implications of short time scale dynamics on long time processes," *Structural Dynamics 4,* 2017.

[110] KEMMER, J. and LUTZ, G., „New Detector Concepts," *Nuclear Instruments and Methods in Physics Research A253,* pp. pp. 365-377, 1987.

[111] TSIVIDIS, Y., Operation and Modeling of the MOS Transistor, 2nd edition Oxford University Press, 1999.

[112] LUTZ, G., Semiconductor Radiation Detectors - Device Physics, Munich: Springer Verlag, 1999.

[113] M. PREDIKAKA, Characterization of a novel DePFET based sensor for an ultra-fast Transmission Electron Microscopy application, at the time of writing unpublished thesis.

[114] SZE, S. and NG, K., Physics of Semiconductor Devices, 3rd edition: John Wiley & Sons, 2007.

[115] RICHTER, Rainer, „Revision of DEPMOS basic equations," Munich, Halbleiterlabor, April 2021.

[116] LUTZ, G., Semiconductor Radiation Detectors - Device Physics, Munich: Springer Verlag, 1999.

[117] FISCHER, P. et al., „Steering and Readout Chips for DEPFET Sensor Matrices," Mannheim.

[118] FISCHER, P., PERIC, I., KREIDL, C., SwitcherB18 (Gated Mode) Reference Manual, University Heidelberg, Feb 2014.

[119] PERIC, Ivan, Production ASICs: DCDB4.1 and DCDB4.2 Reference Manual, Karlsruhe, June 2017.

[120] LEMARENKO, Mikhail and GERMIC, Leonard, DHPT 1.0 Manual, Bonn, 2015.

[121] DOURKI, Ibrahym, Development of a Novel Electron Detector with 80 kHz Frame Rate for Imaging Applications: Simulation of the Detector Response and First Experimental Rsults, Hamburg, 2019.

[122] D. GITARIC, „CAD Designs".

[123] ENCLUSTRA FPGA SOLUTIONS, „Mercury+ XU1," [Online]. Available: https://www.enclustra.com/en/products/system-on-chip-modules/mercury-xu1.

[124] KOCH, Manuel, Development of a Test Environment for the Characterization of the Current Digitizer Chip DCD2 and the Depfet Pixel System for the Belle II Experiment at SuperKekB, Bonn, 2011.

[125] FISCHER, Peter et al., SwitcherB18 (Gated Mode) - Reference Manual, Heidelberg, 2015.

[126] DOLEZAL, Z. and UNO, S. (Editors), Belle II Technical Design Report, October: KEK Report 2010-1, 2010.

[127] BLAJ, G. et al., „Robust Pixel Gain Calibration with Limited Statistics," *SLAC-PUB-17459,* 2017.

[128] E. &. ZIEGLER, „www.ezag.com," [Online]. [Zugriff am 01 03 2021].

[129] LÜTTICKE, Florian, Development of Pixel Modules for the Belle II Detector, Bonn, 2017.

[130] NIST XCOM DATABASE, „https://www.nist.gov/pml," [Online]. Available: https://physics.nist.gov/cgi-bin/Xcom/xcom2. [Zugriff am May 2021].

[131] BÉ, M. and SCHÖNFELD, E., CD-109 Table de Radionucléides, LNE-LNHB/CEA, Mai 2014.

[132] FANG, J. et al., „Understanding the Average Electron-Hole Pair-Creation Energy in Silicon and Germanium Based on Full-Band Monte Carlo Simulations," *IEEE Transactions on Nuclear Science,* pp. pp. 444-451, Vol. 66, No. 1, January 2019.

[133] BEVELACQUA, Joseph J., Contemporary Health Physics: Problems and Solutions, WILEY-VCN Verlag, 2009, second Edition.

[134] LEMARENKO, M., GERMIC, L., DHPT 1.0 Manual, Version 0.1, February 26, 2015.

[135] STUDNA, D.E. and ASPNES, A.A., „Dielectric functions and optical parameters of Si, Ge, GaP, GaAs, GaSb, InP, InAs, and InSb from 1.5 to 6.0 eV," *Physical Review B,* pp. pp. 985-1009, Volume 27, Number 2, 15 January 1983.

[136] SONY, „IMX219PQH5-C Datasheet".

[137] HAMAMATSU, „Datasheet," [Online]. Available: https://www.hamamatsu.com/eu/en/product/type/S4584-06/index.html. [Zugriff am 08 03 2021].

[138] RP PHOTONICS ENCYCLOPEDIA, [Online]. Available: https://www.rp-photonics.com/gaussian_beams.html. [Zugriff am 09 03 2021].

[139] HILL, Dan, „How to Convert FWHM Measurements to 1/e-Squared Halfwidths, Radiant Zemax Knowledge Base," Radiant Zemax Knowledge Base, 04 04 2007. [Online].

[140] SALEH, B. and TEICH, C., Fundamentals of Photonics, John Wiley & Sons, 2nd edition, 2007.

[141] T. L. GMBH. [Online]. Available: https://www.topag.de/products/laser-beam-shaping/top-hat-beam-shaper/gth-4-2.2. [Zugriff am Feb 2021].

[142] OSRAM, „www.osram-os.com," [Online]. Available: https://www.osram.com/ecat/Platinum%20DRAGON%C2%AE%20SFH%204235

/com/en/class_pim_web_catalog_103489/prd_pim_device_2219732/. [Zugriff am 11 03 2021].

[143] HALBRITTER, H. et al., „High-Speed LED Driver for ns-Pulse Switching of High-Current LEDs," *IEEE Photonics Technology Letteres Vol. 26, No. 18,* September 15 2014.

[144] WIKIPEDIA, „Lambert's cosine law," [Online]. Available: https://en.wikipedia.org/wiki/Lambert's_cosine_law. [Zugriff am 23 03 2021].

[145] NAGEL, James R., „Light extraction by Lambertian sources from light emitting diodes," *Proceedings of SPIE,* February 2013.

[146] HAMAMATSU, „Opto-semiconductor handbook, Chapter 02 Si photodiodes," [Online]. Available: https://www.hamamatsu.com/sp/ssd/doc_en.html. [Zugriff am 12 03 2021].

[147] LANCASTER, Jack L. and HASEGAWA, Bruce, Fundamental Mathematics and Physics of Medical Imaging, CRC Press, 2017.

[148] DANCE, D.R. et al. (ED.), Diagnostic Radiology Physics, A Handbook for Teachers and Students, Vienna: IAEA, 2014.

[149] FERETTI, Andrea, „D-5.2: Comparative study of silicon sensors for direct electron measurements in Electron Microscopes," 675587 STREAM ITN Deliverable Report, 2018.

[150] OPTIKOS CORPORATION, „How to Measure MTF and other Properties of Lenses," 16 July 1999. [Online]. Available: www.optikos.com. [Zugriff am 01 04 2021].

[151] ESTRIBEAU, M. and MAGNAN, P., „Fast MTF measurement of CMOS imagers using ISO 12333 slanted-edge methodology," *Proceedings of SPIE Vol. 5251,* pp. pp. 243-249, 19 February 2004.

[152] BOSTAN, G. et al., „The slanted-edge method application in testing the optical resolution of a vision system," *Journal of Optoelectronics and Advanced Materials Vol. 21, No. 1-2,* pp. pp. 22-34, January - February 2019.

[153] IMATEST LLC, „Sharpness: What is it and How it is Measured - Documentation Current v2020.2," [Online]. Available: https://www.imatest.com/docs/sharpness/. [Zugriff am 09 04 2021].

[154] EHSAN, S., FLYNN, M.J. and REIMANN, D.A, „A method for measuring the presampled MTF of digital radiographic systems using an edge test device," *Med. Phys. 25,* pp. pp. 102-113, January 1998.

[155] NEUMANN, Anke, Verfahren zur Auflösungsmessung digitaler Kameras, Köln, 2003.

[156] IMATEST LLC, „Slanted-Edge versus Siemens Star: A comparison of sensitivity to signal processing," [Online]. Available: https://www.imatest.com/2014/10/slanted-edge-versus-siemens-star/. [Zugriff am 08 03 2022].

[157] OLSON, J. T., ESPINOLA, R. L. and JACOBS, E.L., „Comparison of tilted slit and tilted edge superresolution modulation transfer function techniques," *Optical Engineering 46(19,* 1 Januar 2007.

[158] KOHM, K. (ORBIMAGE), „Modulation Transfer Function Measurement Mehtod and Results for the Orbview-3 high Resolution Imaging Satellite".

[159] REICHENBACH, Stephen E. et al., „Characterizing digital image acquisition devices," *Optical Engineering, Vol. 30, No. 2,* pp. pp. 170-177, February 1991.

[160] Syed Naeem Ahmed, Physics and Engineering of Radiation Detection (Second Edition), Ontario: Elsevier, 2015.

[161] SMITH, Stephen W., Digital Signal Processing - A Practical Guide for Engineers and Scientists, Elsevier, 2003.

[162] HASCHKE, Michael, Laboratory Micro-X-Ray Fluorescence Spectroscopy, Berlin: Springer International Publishing, 2014.

[163] KRAUSE, M.O., „Atomic radiative and radiationless yields for K and L shells," *Journal of Physical and Chemical Reference Data Vol. 8, No. 2,* pp. pp. 307-327, 1979.

[164] LAWRENCE BERKELY NATIONAL LABORATORY, „X-Ray Data Booklet," [Online]. Available: https://xdb.lbl.gov/. [Zugriff am 16 04 2021].

[165] DAOUDI, Salim, „New K-shell fluorescence yields Curve for elements with 3 < Z < 99," *Journal of the Korean Physical Society, Vol. 67, No. 9,* pp. pp. 1537-1543, 2015.

[166] TIWARI, M.K., „Development of a total reflection X-ray fluorescence spectrometer for ultra-trace element analysis," *Bull. Mater. Sci. Vol 25, No. 5,* pp. pp. 435-441, October 2002.

[167] HONSBERG, Christiana and BOWDEN, Stuart, „https://www.pveducation.org/," [Online]. Available: https://www.pveducation.org/pvcdrom/materials/optical-properties-of-silicon. [Zugriff am 3 November 2021].

[168] MYKLEBUST, R.L and NEWBURY, D.E., „Monte Carlo Electron Trajectory Simulation of Beam Spreading in thin Foil Targets," *Ultramicroscopy 3,* pp. pp. 391-395, 1979.

[169] DROUIN, Dominique et al., „CASINO V2.42 - A Fast and Easy-to-use Modeling Tool for Scanning Electron Microscopy and Microanalysis Users," *Scanning Vol. 29,* pp. pp.92-101, 2007.

[170] DEMERS, H. et al., „Simulating STEM Imaging of Nanoparticles in Micrometers-Thick Substrates," *Microscopy and Microanalysis, Vol. 16, Issue 6,* pp. pp. 795-804, December 2010.

[171] DEMERS, Hendrix et al., „Three-dimensional electron microscopy simulation with the CASINO Monte Carlo software," *Scanning, Vol 33,* pp. pp.135-146, 2011.

[172] MITJA, C., ESCOFET, J., TACHO, A. and REVUELTA, R., „Slanted Edge MTF," [Online]. Available: https://imagej.nih.gov/ij/plugins/se-mtf/index.html.

[173] MITRE. [Online]. Available: http://www2.mitre.org/tech/mtf/.

[174] BURNS, R. David. [Online]. Available: http://losburns.com/imaging/software/SFRedge/index.htm.

[175] BURNS, Peter D and WILLIAMS, Don, „Refined Slanted-Edge Measurement for Practical Camera and Scanner Testing," in *Proc. IS&T 2002 PICS Conference*, pp. 191-195, 2002.

[176] VIALLEFONT-ROBINET, Francoise et al., „Comparison of MTF measurements using edge method: towards reference data set," *Optics Express, Optical Society of America,* pp. pp.33625-33648, 2018, 26.

[177] KOREN, Norman, „Resolution and MTF curves in scanners and sharpening," [Online]. Available: http://www.normankoren.com/Tutorials/MTF2.html. [Zugriff am 23 04 2021].

[178] LIU, Hong et al., „Step by step analysis toward optimal MTF algorithm using an edge test device," *Journal of X-Ray Science and Technology 17,* pp. pp. 1-15, 2009.

[179] SAMEI, Ehsan et al., „Comparison of edge analysis techniques for the determination of the MTF of digital radiographic systems," *Phys. Med. Biol. 50,* pp. pp. 3613-3625, 2005.

[180] IMATEST, „LSF corretion factor for slanted-edge MTF measurements," 01 04 2015. [Online]. Available: https://www.imatest.com/2015/04/lsf-correction-factor-for-slanted-edge-mtf-measurements/. [Zugriff am 21 04 2021].

[181] KNOPF, Jochen, Development, Characterization and Operation of the DCDB, the Front-End Readout Chip for the Pixel Vertex Detector of the Future BELLE-II Experiment, Mannheim, 2011.

[182] GATTI, E. and REHAK, P., „Semiconductor Drift Chamber - An Application of novel charge Transport Scheme," *Nuclear Instruments and Methods in Physics Research 225,* pp. pp. 608-614, 1984.

[183] FIORINI, C. et al., Single-Side Biasing of Silicon Drift Detectors with Homogeneous Light-Entrance Window, IEEE Transactions on Nuclear Science, Vol. 47, No. 4, Aug 2000.

[184] PETROVICS, Stefan, Neutron Irradiations and Punch-Through Biasing Studies with DEPFETs for BELLE II, Master Thesis LMU Munich, 2012.

[185] AVELLA, Paola and RICHTER, Rainer, Pilot run - matrix measurements after first metal, Prag: 7th Belle II VXD workshop, Jan 2015.

[186] GERMIC, Leonard, Data Handling Processor and Signal Transmission in the Belle II DEPFET Pixel Detector, Bonn, 2018.

[187] PRINKER, Eduard, „Testing of the Gated Mode for the Belle II Pixel Detector," Munich, 2015.

[188] LINDSTRÖM, Gunnar, „Radiation damage in silicon detectors," *Nuclear Instruments and Methods in Physics Research A 512,* pp. pp. 30-43, 2003.

[189] MOLL, Michael, Radiation Damage in Silicon Particle Detectors - microscopic defects and macroscopic properties, Hamburg, 1999.

[190] WUNSTORF, R., „Systematische Untersuchungen zur Strahlenresistenz von Silizium-Detektoren für die Verwendung in Hochenergiephysik-Experimenten," Interner Bericht, DESY, 1992.

[191] GÖSSLING, C. et al., „Influence of Surface Damage on Highly Segmented Silicon Detectors," Il Nuovo Cimento, Vol. 112 A, N. 11, Universität Dortmund, 1999.

[192] WÜSTENFELD, Jens, Characterisation of Ionisation-Induced Surface Effects for the Optimisation of Silicon-Detectors for Particle Physics Applications, Dortmund, 2001.

[193] SCHREECK, Harrison et al., „Effects of gamma irradiation on DEPFET pixel sensors for the BELLE II experiment," *Nuclear Inst. and Methods in Physics Research, A959,* 2020.

[194] PLANO GmbH, „www.plano-em.de," TEM Kalibrierungs-Netzchen aus Kupfer, 1000 mesh, 28 September 2021. [Online]. Available: https://www.plano-em.de/tem-kalibrierung-netzchen-grid-aus-kupfer.

[195] TED PELLA. INC., „www.tedpella.com," Magnification Calibration Latex Spheres on Diffraction Grating Replica, Product No. 603, Technical Notes, 28 September

2021. [Online]. Available: https://www.tedpella.com/technote_html/603%20TN.pdf.

[196] YANG, Jie et al., „In Liquid Observation and Quantification of Nucleation and Growth of Gold Nanostructures Using in Situ Transmission Electron Microscopy,“ *The Journal of Physical Chemistry C, 121,* pp. pp. 7435-7441, 2017.

[197] LIM, Siew Yee et al., „Engineering of Hybrid Nanoporous Anodic Alumina Photonic Crystals by Heterogenous Pulse Anodization,“ *Nature, Scientific Reports 8:9455,* 2018.

[198] SUN, Li et al., „In Situ Transmission Electron Microscopy Observation of Silver Oxidation in Ionized/Atomic Gas,“ *Langmuir,* pp. pp. 14201-14206, July 2011.

[199] HENSEL, Martin, Optimization of the radiation tolerance and annealing of radiation damage on active pixel sensors for application as direct electron detectors, München: LMU, 2015.

[200] PARKER, Kenneth P., The Boundary-Scan Handbook, New York: Spring Science+Business Media, 1992.

[201] GERMIC, Leonard, DHPT Operation Document - A User friendly Look-up document v. 1.1, Bonn, 2016.

[202] IEEE STD 1241-2000, IEEE Standard for Terminology and Test Methods for Analog-to-Digital Converters, Institute of Electrical and Electronics Engineers, Inc., Dec 2000.

[203] DAVISSON, C.J. and GERMER, L.H., „Reflection of Electrons by a Crystal of Nickel,“ *Proceedings of the National Academy of Sciences of the United States of America. Vol 14,* pp. pp. 317-322, 1928.

[204] HODGE, John C., „Photon diffraction and interference,“ in *Blue Ridge Community College*, Flat Rock, 2018.

[205] HUM, Sean Victor, „ECE422 - Radio and Microwave Wireless Systems - Diffraction,“ [Online]. Available: https://www.waves.utoronto.ca/prof/svhum/ece422.html. [Zugriff am 09 04 2021].

[206] GYASI-AGYEI, Amoakoh, „Wireless Internet of Things - Principles and Practice,“ Nr. World Scientific, 2020.

[207] INTERNATIONAL TELECOMMUNICATION UNION, „Propagation by Diffraction Recommendation P.526-15,“ 10 2019. [Online]. Available: https://www.itu.int/rec/R-REC-P.526-15-201910-I/en. [Zugriff am 14 04 2021].

[208] NWOKONKO, Swinton C. et al., „Remodelling of Lee's Knife Diffraction Loss Model as a Function of Line of Site Percentage Clearance,“ *International Journal of Theoretical and Applied Mathematics Vol. 3, No. 4,* pp. pp. 138-142, 2017.

[209] YOUNIS, Marwan & ABADPOUR, Sevda, Advanced Radio Communication I, Lecture Notes, Karlsruhe: Institut für Hochfrequenztechnik und Elektronik, 2018/19.

[210] KOHRS, R., Development and Characterization of a DEPFET Pixel Prototype System for the ILC Vertex Detector, Bonn University: Doctoral Thesis, 2008.

[211] MEROLI, S., Radiation damage for silicon detectors, http://meroli.web.cern.ch/meroli/lecture_radiation_damage_silicon_detector.html.

[212] NISTIR 5632, Tables of X-Ray Mass Attenuation Coefficients and Mass Energy-Absorption Coefficients, http://www.nist.gov/pml/data/xraycoef/.

[213] YADAV, Amit et al., „AlGaInP red-emitting light emitting diode under extremely high pulsed pumping," *Proc. of SPIE Vol 9768,* February 2016.

[214] THERMO FISHER SCIENTIFIC, „Electron Microscope Pixel Array Detector (EMPAD), Datasheet," [Online]. Available: https://assets.thermofisher.com/TFS-Assets/MSD/Datasheets/EMPAD-Datasheet.pdf. [Zugriff am 02 July 2021].

[215] TALMAN, Richard, „On the Statistics of Particle Identification using Ionization," *Nuclear Instruments and Methods 159,* pp. pp. 189-211, 1979.

[216] RICHTER, Rainer, „Revision of DEPMOS basic equations," Munich, Halbleiterlabor, 2021.

[217] RANCOITA, P.G. SEIDMAN, A., „Silicon Detectors in High-Energy Physics: Physics and Applications," *Rivista del Nuovo Cimento Vol 5, No 7,* July 1982.

[218] PAGNUTTI, Mary A. et al., „Laying the foundation to use Raspberry Pi 3 V2 camera module imagery for scientific and engineering purposes," *Journal of Electronic Imaging,* pp. pp. 013014-1 to 012014-13, Vol. 26(1), Jan/Feb 2017.

[219] MOLL, Michael, „Displacement Damage in Silicon Detectors for High Energy Physics," *IEEE Transactions on Nuclear Science, Vol. 65, No. 8,* pp. pp.1561-1582, August 2018.

[220] MOLL, M., Radiation Damage in Silicon Particle Detectors, Hamburg, 1999.

[221] MASAOKA, K. et al., „Modified slanted-edge method and multidirectional modulation transfer function estimation," *Optics Express, Vol. 22, No. 5,* March 2014.

[222] LUO, Zhiping, A Practical Guide to Transmission Electron Microscopy, Volume II: Advanced Microscopy, New York: Momentum Press, 2016.

[223] LI, X. et al., „Electron counting and beam-induced motion correction enable near-atomic-resolution single-particle cryo-EM," *Nature Methods, Vol. 10,* pp. pp. 584-590, May 2013.

[224] LI, Tiecheng et al., „Comparison of different analytical edge spread function models for MTF calculation using curve-fitting," *Proc. SPIE,* 7489, 74981H (2009).

[225] LESSER, Michael, „Silicon sensor quantum efficiency, reflectance, and calibration," *Proc. SPIE 9154, High Energy, Optical, and Infrared Detectors for Astronomy VI, 915411,* 21 July 2014.

[226] LEMARENKO, Mikhail et al., DHP 0.2 Manual, Bonn, 2012.

[227] LEMARENKO, Mikhail et al., Data Handling Processor - Manual, v. 1.0, Bonn: SI LAB, 2016.

[228] LEE, William C.Y., Mobile Communications Engineering, New York: Mc-Graw-Hill, 1985.

[229] KHANNA, V.K., Fundamentals of Solid-State Lighting, CRC Press, 2014.

[230] KESKIN, Sercan and DE JONGE, Niels, „Reduced Radiation Damage in Transmission Electron Microscopy of Proteins in Graphene Liquid Cells," *Nano Letters Vol. 18,* pp. pp. 7435-7440, 2018.

[231] IMATEST LLC, „Sharpness," [Online]. Available: https://www.imatest.com/solutions/sharpness/. [Zugriff am 09 April 2021].

[232] M.-S. &. HLL, „Proposal for development of advanced electron detectors for UED and DTEM," 2013.

[233] HAYWARD, E., Photonuclear Reactions, NBS Monograph 118, 1970.

[234] EVENSON, Zachary (Ed.), Topics in Appllied Physics, 1973-2021, 153 Volumes.

[235] EHSAN, S., FLYNN, M.J. and REIMANN, D.A., „A method for measuring the presampled MTF of digital radiographic systems using an edge test device," *Medical Physics, Vol. 25, No. 1,* pp. pp. 102-113, January 1998.

[236] DOURKI, Ibrahym, Development of a Novel Electron Detector with 80 kHz Frame Rate for Imaging Applications: Simulation of the Detector Response and First Experimental Results, Hamburg, 2019.

[237] DATTA, A. et al., „A data reduction and compression description for high throughput time-resolved electron microscopy," *Nature Communications Vol 12, 664,* January 2021.

[238] CLOUGH, R.N. et al., „Direct Detectors for Electron Microscopy," *J. Phys. Ser. 522 012046,* 2014.

[239] BUHR, Egbert et al., „Accuracy of a simple method for deriving the presampled modulation transfer function of a digital radiographic system from an edge image," *Medical Physics 30,* pp. pp. 2323-2331, September 2003.

[240] AOUDE, Rafael and PITZL, Daniel, „Study of CMS Pixel Sensors," DESY, September.

[241] NIST, „X-Ray Mass Attenuation Coefficients," [Online]. Available: https://physics.nist.gov/PhysRefData/XrayMassCoef/chap2.html. [Zugriff am 12 07 2021].

[242] KNOPF, J., FISCHER, P., KREIDL, C. and PERIC, I., A 256 channel 8-Bit current digitizer ASIC for the Belle-II PXD, Aachen: Topical Workshop on Electronics for Particle Physics, 2010.

[243] JESPERS, B. and GINETTI, P., A CMOS 13-b Cyclic RSD A/D Converter, IEEE Journal of Solid-State Circuits, Vol. 27, No. 7, July 1992.

[244] AUST, C., A Low-Power, Variable-Resolution Analog-to-Digital Converter, U. o. V. Thesis, Hrsg., 2000.

[245] AGILENT TECHNOLOGIES, Agilent 33250 80 MHz Waveform Generator - User's Guide, 2003.

[246] CARUSONE, T., JOHNS, D., MARTIN, K., Analog Integrated Circuit Design, John Wiley & Sons Inc., 2nd edition, 2012.

[247] PELGROM, M., Analog-to-Digital Conversion, 2010: Springer Science+Business Media B.V..

[248] BERGER, C., Elementarteilchenphysik, Aachen: Springer Verlag, Feb 2006.

[249] BROWN, S. and ROSE, J., Architecture of FPGAs and CPLDs: A Tutorial, Department of Electrical and Computer Engineering University of Toronto.

[250] PERIC, Ivan, ASICs for Belle II DEPFET Pixel Detector, internal paper.

[251] SANDOW, C. et al., Clear-performance of linear DEPFET devices, Nucl. Instr. Meth. in Phys. Res. A 568, July 2006.

[252] PERIC, Ivan et al., DCD - The Multi-Channel Current-Mode ADC Chip for the Readout of DEPFET Pixel Detectors, IEEE Trans. Nucl. Sci., Vol. 57, No. 2, Apr 2010.

[253] PERIC, Ivan, DCD & Switcher Redesign Status, Seeon: 19th International Workshop on DEPFET Detectors and Applications, May 2015.

[254] PERIC, Ivan, DCD History, internal paper, 2014.

[255] PERIC, Ivan, DCD4_Pipeline Mismatch, University of Heidelberg, 2014.

[256] PERIC, Ivan et al., DCDB and SWITCHERB, the Readout ASICs for Belle II DEPFET Pixel Detector, IEEE Nuclear Science Symposium Conference Record, N31-5, 2011.

[257] PERIC, Ivan et al., DCD-Bv4-Pipeline Reference Manual, University of Heidelberg, Jan 2015.

[258] ATRIS, Y., Design of RSD-Cyclic and Hybrid RSD-Cyclic/Sigma-Delta ADCs, W. S. U. Thesis, Hrsg., 2007.

[259] LEUTZ, H. et al., Electron capture ratios in Cd-109 and internal conversion coefficients in Ag*-109, University of Heidelberg: Nucl. Phys. 63, 1965.

[260] MAZZIOTTA, M., Electron-hole pair creation energy and Fano factor temperature dependence in silicon, Nucl. Instr. Meth. Phys. Res. A 584, 2008.

[261] AGARWAL, A. and LANG, J., Foundations of Analog and Digital Electronic Circuits, San Francisco: Elsevier, 2005.

[262] CORDES, K.-H., WAAG, A. and HEUCK, N., Integrierte Schaltungen, Grundlagen - Prozesse - Design - Layout, Pearson Studium, 2011.

[263] RUMMEL, Stefan, Investigation of DEPFET as Vertex Detector at IL - Intrinsic properties, radiation hardness and alternative readout schemes, Munich, 2009.

[264] JAEGER, R. and BLALOCK, T., Microelectronic Circuit Design, McGraw-Hill Companies Inc., 4th edition 2011.

[265] FEHER, J., Introduction to Digital Logic, Textbook Equity Edition 2014, 2010.

[266] GLOBISCH, S. et al., Lehrbuch Mikrotechnologie, Munich: Carl Hanser Verlag, 2011.

[267] SCHOLZE, F. et al., Mean energy required to produce an electron-hole pair in silicon for photons of energies between 50 and 1500 eV, 1998: Journal of Applied Physics, Vol. 84, No. 5.

[268] PANDA, S., Microelectronics and Optoelectronics Technology, New Dlhi: University Science Press, 2009.

[269] PERIC, Ivan, New DCD Chips, Ringberg: 13th International Workshop on DEPFET Detectors and Applications, June 2013.

[270] FROUGNY, C., On-the-Fly Algorithms and Sequential Machines, Proc. 13th IEEE Symp. Computer Arithmetic 260, 1997.

[271] DAUBERT, S.J. and VALLANCOURT, D., Operation and analysis of current copier circuits, IEE Proceedings, Vol. 137, No. 2, Apr 1990.

[272] KANAYA, K. and OKAYAMA, S., Penetration and energy-loss theory of electrons in solid targets, J. Phys. D: Appl. Phys., Vol. 5, 1972.

[273] ROSSI, L. et al., Pixel Detectors - From Fundamentals to Applications, Springer Verlag, 2006.

[274] RITTER, Andreas, Radiation Hardness Studies for DEPFETs in Belle II, Technische Universität München, 2013.

[275] ALIG, R. et al., Scattering by ionization and phonon emission in semiconductors, Physical Review B, Vol. 22, No. 12, 1980.

[276] KREIDL, Christian, Steering electronics, module design and construction of an all silicon DEFET module, Thesis: University of Mannheim, 2011.

[277] FIEZ, T., Switched-Current Circuit Design Issues, IEEE Journal of Solid State Circuits, Vol. 26, No. 3, Mar 1991.

[278] PERIC, Ivan, Switcher - ASIC Review, Oct 2014.

[279] KESTER, W. (ED.), The Data Conversion Handbook, Analog Devices Inc., 2005.

[280] TEXAS INTRUMENTS, Understanding Data Converters - Application Report, SLAA013, 1995.

[281] KING, Wayne E. et al., „Ultrafast electron microscopy in materials science, biology, and chemistry,“ *J. Appl. Phys. 97,* p. 111101, 04 Feb 2005.

[282] GREEN, Martin A. and KEEVERS, Mark J., „Optical properties of intrinsic silicon at 300 K,“ *Progress in Photovoltaics, Vol. 3, Issue 3,* pp. pp. 189-192, 1995.

[283] NIST ESTAR DATABASE, „https://www.nist.gov/pml,“ [Online]. Available: https://physics.nist.gov/PhysRefData/Star/Text/ESTAR.html.

[284] AIP, Journal of Applied Physics, „Overview - Focus and Coverage,“ [Online]. Available: https://aip.scitation.org/jap/info/focus.

[285] LEE, Young Pak Lee et al. (Series Editors), „Topics in Applied Physics - Book series,“ [Online]. Available: https://www.springer.com/series/560/editors.

[286] CHO, Hoduk et al., „The Use of Graphene and Its Derivatives for Liquid-Phase Transmission Electron Microscopy of Radiation-Sensitive Specimens,“ *Nano Letters Vol. 17,* pp. pp. 414-420, 2017.

[287] KESKIN, Sercan and DE JONGE, Niels, „Reduced Radiation Damage in Transmission Electron Microscopy of Proteins in Graphene Liquid Cells,“ *Nano Letters Vol.18,* pp. pp. 7435-7440, 2018.

Acronyms

ADC	Analog to Digital Converter
ADU	Analog Digital Unit ≡ LSB
AEM	Analytical Electron Microscopy
AES	Auger-Electron Spectroscopy
ASIC	Application Specific Integrated Circuit
ASM	All Silicon Module
BELLE	is not an acronym meaning beauty in French – studying b quarks
BSDL	Boundary Scan Description Language
BSE	Backscattered Electrons
CAD	Computer Aided Design
CCD	Charge Couple Device
CCE	Charge Collection Efficiency
CG	Cleargate
CHC	Charge Handling Capacity
CMC	Current Memory Cell
CMOS	Complementary Metal Oxide Semiconductor
DAC	Digital to Analog Converter
DAQ	Data Acquisition system
DC	Direct Current
DCD-B	Drain Current Digitizer for Belle II
DEPFET	Depleted P-Channel Field Effect Transistor
DHP	Data Handling Processor
DLSP	Double-L Shaped Patch Panel
DMC	Digital Movie Chip
DNL	Differential Nonlinearity
DR	Data Register
DSLR	Digital Single Lens Reflex
DUT	Device Under Test
EELS	Electron Energy Loss Spectroscopy
FIR	Finite Impulse Response Filter

FOV	Field of View
FPA	Focal Plane Array
FPGA	Field Programmable Gate Array
fps	frames per second
HLL	Halbleiterlabor der Max-Planck-Gesellschaft
IC	Integrated Circuit
ICRU	International Commission on Radiation Units and Measurements
IEEE	Institute of Electrical and Electronics Engineers
IMPF	Inelastic Mean Free Path
INL	Integral Nonlinearity
IR	Instruction Register
JTAG	IEEE 1149.1 Standard Test Access Port and Boundary Scan Architecture
LASER	Light Amplification by Stimulated Emission of Radiation
LC-EM	Liquid Cell Electron Microscopy
LED	Light Emitting Diode
LHC	Large Hadron Collider
LSB	Least Significant Bit
LVDS	Low Voltage Differential Signaling
MAPS	Monolithic Active Pixel Sensors
MBM	MIC Brain Module
MC	Monte Carlo Simulation
MHM	MIC Housekeeping Module
MIC	Module Interface Circuitry
MOSFET	Metal Oxide Semiconductor Field Effect Transistor
MPM	MIC Power Module
MPMS	MIC Power Module Stack
MPSD	Max-Planck-Institut für Struktur und Dynamik der Materie
MSB	Most Significant Bit
MSM	MIC Service Module
OpenOCD	Open On-Chip Debugger
PCB	Printed Circuit Board

PKA	Primary Knock on Atom
PMOS	p-channel MOSFET
PSF	Point Spread Function
PSU	Power Supply Unit
PT	Punch-Through
PXD	Pixel Detector
RAM	Random Access Memory
RC	Resistor Capacitor
REM	Reflection Electron Microscopy
RF	Radio Frequency
ROI	Region Of Interest
SEM	Scanning Electron Microscope/Microscopy
SMU	Source Measurement Unit
SNR	Signal to Noise Ratio
SoC	System on a Chip
STEM	Scanning Transmission Electron Microscope/Microscopy
SVD	Silicon Vertex Detector
TAP	Test Access Port
TCK	Test Clock
TDI	Test Data In
TDO	Test Data Out
TEM	Transmission Electron Microscope/Microscopy
TIA	Transimpedance Amplifier
TMS	Test Mode Select
TRST	Test Reset
TTL	Transistor-Transistor-Logic
UDP	User Data Protocol
UED	Ultrafast Electron Diffraction
VIC	Vacuum InterConnect
VXD	VerteX Detector (SVD+PXD)
XEDS	X-ray Energy Dispersive Spectroscopy
XU1	Xilinx Ultrascale+^{TM}

Acknowledgements

First of all, I would like to thank Prof. Dr. Christian Kiesling for granting me the opportunity as a PhD candidate, for taking over the necessary supervisory activities and for his invaluable instructions. Moreover, he insisted that also TEM results must be included into this thesis. Though this claim extended the planned completion once more, I deeply appreciate it with the benefit of hindsight.

I very much like to remember a situation in Vienna, when Prof. Kiesling and Prof. Dr. Jochen Schieck pushed me to consider a doctorate in physics. At this time, I just finished my bachelor thesis and considered this idea as completely unrealistic. Why? After the completion of my PhD in business I sincerely swore to never try it again… Many thanks again to Prof. Kiesling and Prof. Schieck for their encouraging words.

Special thanks go to Dr. Jelena Ninkovic and Dr. Johannes Treis for all the support, challenging questions, important comments, profound inputs and helpful advices to my scientific work. They spent numerous hours on a regular basis for guidance and discussion. Thank you for your patience. I appreciate that as a high privilege.

For the daily operation, one person I owe a deep debt of gratitude: Christian Koffmane. He had always an open ear for my problems. He is well respected both internally and to the BELLE 2/EDET community as a trouble shooter. Most of the time he finds a solution, even if the situation looks hopeless. Without his help, many achievements of this thesis would have been not realized. Thank you Christian for all your patience, the extensive knowledge transfer and your invaluable guidance.

I would also like to sincerely thank Rainer Richter, the chief-designer of the DEPFET matrices. With his profound knowledge he helped me to understand some of my measurement results and suggested new testing methods.

Science lives from knowledge transfers and the mutual exchange of ideas. Special thanks to our HLL experts Laci Andricek, Dr. Peter Lechner, Dr. Florian Schopper, Dr. Andreas Wassatsch and Dr. Alexander Bähr.

I am also very thankful to Mikhail Polovykh and Dr. Andrey Vostrukhin for their unconventional ideas and support and for providing the whole EDET readout software. Many thanks to Martin Hensel for his great support in programming situations where I got stuck. Martin has also programmed the whole system control framework.

A special thank goes to Thomas Selle. He was organizing all Hamburg campaigns, providing the corresponding photos and he was working tirelessly and with great precision.

A person I would like to thank specifically is my colleague Mitja Predikaka. We worked in the same room, we exchanged a lot of ideas and had great fun together. Thank you Mitja for all your support and time.

I also want to express my gratitude to all other Semiconductor Laboratory people for providing me an excellent working environment and all necessary facilities, especially Danilo Mießner for his excellent assembling work on the Hybrid boards as well as his solid patience and expertise for repairing damaged boards.

Thank you Martin Soyer, for providing technical aids as for example the LED holder, Mark Matiaske for the sensor masks, Silvia Krivokuca for the ASIC bonding and Gerhard Liemann for his steady support. In this list I also like to thank Raik Lehmann for ensuring the supply of an invaluable treasure for all thesis writing students: the provision and maintenance of the coffee machine.

Special thanks to Vladimir Travalja for the great IT-support.

I would also greatly acknowledge our collaborators at MPSD in Hamburg headed by Dr. Sascha Epp. Sascha was very supportive, especially during our Hamburg TEM campaigns and contributed a lot of rewarding comments. Many thanks to Dr. Günther Kassier for all the helpful inputs to this thesis as well as for operating the TEM and to Djordje Gitaric for providing the CAD designs of the EDET detector. Above all, sincere thanks to Dr. Ibrahym Dourki, pioneering the first thesis about the EDET project. Ibrahym performed all the Geant4 simulations mentioned in this thesis. Thank you Ibrahym for all your effort!

Particular thanks go to Prof. Dr. Ivan Peric (University of Karlsruhe) for his important inputs and very helpful remarks related to the DCDE, to Dr. Florian Lütticke and Botho Paschen (University of Bonn) for their great support and to Dr. Harrison Schreeck (University Göttingen) for the detailed radiation damage data.

I do not want to forget Gus Kayafas, President of Palm Press Inc. who contributed this wonderful stroboscopic image and an associated caption. My sincere thanks for that.

Last but not least, I especially want to thank my friends and my family for all their encouragement and patience, while working on this thesis.

I regret, in all sincerity, if I have forgotten somebody to mention. Thank you all, who have contributed to this thesis.